Studies on Er_2O_3/Dy_2O_3 doped zinc borotellurite glasses

A

Thesis

Submitted for the partial fulfillment of the requirements for the award of

Doctor of Philosophy

THAPAR INSTITUTE
OF ENGINEERING & TECHNOLOGY
(Deemed to be University)

By

Sandeep Kaur
(Registration No. 901612025)

Under the guidance of

Dr. O.P. Pandey
Senior Professor and Head
School of Physics and Material Science
Thapar Institute of Engineering & Technology
Patiala, Punjab-147004

Dr. Neetu Chopra
Associate Professor
P.G. Department of Physics
Kanya Maha Vidyalaya
Jalandhar, Punjab-144004

October, 2022

DEDICATION

In loving memory of my Grandparents

Sardarni Sant Kaur
&
Sardar Lachhman Singh

AND

Sardarni Dalip Kaur Chawla
&
Sardar Gurcharan Singh Chawla

Declaration

This is to certify that the present thesis entitled, **"Studies on Er_2O_3/Dy_2O_3 doped zinc borotellurite glasses"** submitted for the partial fulfillment for the award of the degree of **DOCTORATE OF PHILOSOPHY (Ph.D.)** in School of Physics and Materials Science, Thapar Institute of Engineering & Technology, Patiala, Punjab is a genuine documentation of my own work carried out under the supervision of **Dr. O.P. Pandey** and **Dr. Neetu Chopra**. The matter presented in this thesis has not been submitted in part or full to any other institute/university for the award of any other degree.

Date: 7th October 2022

Sandeep Kaur

This is to certify that the above statement made by the candidate is true to the best of my knowledge.

Dr. O.P. Pandey
Senior Professor and Head
School of Physics and Material Science
Thapar Institute of Engineering & Technology
Patiala (Punjab)

Dr. Neetu Chopra
Associate Professor
P.G. Department of Physics
Kanya Maha Vidyalaya
Jalandhar (Punjab)

Scanned with CamScanner

Table of Contents

Index

ACKNOWLEDGEMENT

This thesis has not been possible without the help of the people I met and worked with them during my Ph.D work. It is matter of pride and honor for me to acknowledge all those people who helped me directly or indirectly during my Ph.D work.

First and foremost, I would like to thank my research supervisors, **Dr. O.P. Pandey** and **Dr. Neetu Chopra**. Without their assistance and dedicated involvement in each and every step throughout the process, this thesis would have never been accomplished. I was able to overcome all the difficulties that I had to face during my Ph. D work. Thanks to my supervisors. I would like to thank them for their unwavering support and understanding over past five years. My thesis has taken good shape because of their help and suggestions in formatting the entire thesis**.** All the achievements I have accomplished so far, I owe all of them. I am extremely thankful to DST-SERB for providing me financial grant **(EMR/2015/0002045)** to carry out my thesis work.

I would also like to show gratitude to my doctoral committee members, including **Dr. Kulvir Singh**, **Dr. B. C. Mohanty** and **Dr. Haripada Bhunia**. They raised many precious and critical points in our discussions during the progress monitoring meetings and I hope that I have managed to address several of them here. All the faculties and staff of SPMS are acknowledged who never turned me down whenever I approached for any help.

I owe my humble and sincere thanks to **Dr. (Prof.) C.K. Jayasankar**, Department of Physics, Sri Venkateshwara University, Tirupati for his guidance and support. His helpful suggestions and comments have provided guidance leading to the completion of my thesis work. I am extremely grateful to Sir that he allowed me to sit in his lab and to learn about radiative parameters from himself and his students as well. I owe you a lot sir. I also would like to thank **Mr. Nilesh Kulkarni and Mr. Rudheer Bapat** for offering their helping hand in instrumentation during my stay at TIFR, Mumbai. I owe a big thanks to SAIF, Labs Chandigarh for providing FESEM facilities.

It is my privilege to thank **Prof. Prakash Gopalan**, Director, Thapar Institute of Engineering & Technology, Patiala for providing me resources in the institution and needful help during the various stages of my work.

I am profoundly obliged to **Dr. (Prof.) Atima Sharma Dwivedi,** Principal, Kanya Maha Vidyalaya, Jalandhar, for her constant encouragement and needful help during the various stages of my work. I am also very thankful to **Dr. Gopi Sharma**, **Mrs. Parminder Kaur Cheema,** Head Department of Physics, Kanya Maha Vidyalaya, Jalandhar and **Dr. Manmohan Singh** for their whole-hearted support and blessings.

Getting through my dissertation required more than academic support, and I have many, many people to thank for listening to and, at times, having to tolerate me over the past few years. I cannot begin to express my gratitude and appreciation for their friendship. I am extremely thankful to my seniors and lab mates **Dr. Rameez Ahamd Mir, Dr. Piyush Shrama, Dr. Ruby Priya, Dr. Shivani Singla, Mr. Sanjay Upadhyay** and **Mr. Puneet Sharma**. Thanks for standing by me.

Most importantly, none of this could have happened without my family. I would love to write thanks to My tough but Sweet & Soft father **(Sardaar Satpal Singh)** and My emotional but Strong mother **(Sardarni Jatinder Kaur)**. Thank you for your love, support and endless naggings. Above all, I would like to thank you for raising and loving me no matter how much of a bad daughter I am. Also, to my sister **(Anmolpreet Kaur)** and my BABY brother **(Upinderdeep Singh)** with whom I fight all the time but still love them the most. They were always there to uplift my spirits whenever I was sad. Thank you, my quirky family. Every time I was ready to quit, you did not let me and I am forever grateful.

A journey is easier when you travel together. Words fail to express my appreciation for my husband **(Maninder Bir Singh**), for his support and generous care during the last few months of my PhD life. He was always beside me during the happy and hard moments to cheer and motivate me. Thank you doesn't seem sufficient for my mother-in-law **(Sardarni Narinder Pal Kaur)**, but it is said with appreciation and respect. I would like to grab this opportunity and thank my sister-in-law as well **(Mrs. Babbanpreet Kaur)** for her support, encouragement, care and understanding. This dissertation stands as a testament to your unconditional love and encouragement.

Sandeep Kaur

List of Publications

From Ph.D. Work

1. **S. Kaur,** O.P. Pandey, C.K. Jayasankar, N. Chopra, **(2022)** Exploring thermal, optical, structural and luminescent properties of gamma irradiated Dy^{3+}doped tellurite glasses: Photon shielding properties, Radiation Physics and Chemistry, **110375**
2. **S. Kaur,** O.P. Pandey, C.K.Jayasankar, N. Chopra, **(2021)** Effect of gamma irradiation on physical, optical, spectroscopic and structural properties of Er^{3+}-doped vitreous zinc borotellurite, Journal of Luminescence, **235, 118031**
3. **S. Kaur**, O.P. Pandey, C.K. Jayashankar, N. Chopra, **(2020)** Influence of heat treatment on spectroscopic and structural properties of vitreous Er^{3+} -doped zinc borotellurite, Journal of Non Crystalline Solids, **530, 119842**
4. **S. Kaur**, O.P. Pandey, C.K. Jayashankar, N. Chopra, **(2019)** Spectroscopic, thermal and structural investigations of Dy^{3+} activated zinc borotellurite glasses and nano glass ceramics for white light generation, Journal of Non Crystalline Solids, **521**, **119472**

Other Publications

5. S. Singla, **S. Kaur**, N. Mahendru, O. P. Pandey, N. Chopra, G. Sharma, **(2022)** Enhanced photoluminescence in Dy^{3+}/Au co-doped Bismuth Borosilicate Glass, Optical Materials, **126, 112236**
6. S. Singla, R. Priya, **S. Kaur**, O.P. Pandey, **(2020)** Blue light excited novel Eu doped $CaGd_2ZnO_5$ nanophosphors: Structural and photoluminescent properties, Optik-International Journal for Light and Electron Optics, **216**, **164830**
7. R. Priya, **S. Kaur**, U. Sharma, O.P. Pandey, S. J. Dhoble, **(2020)** A review on recent progress in rare earth and transition metals activated SrY_2O_4 phosphors" Journal of Materials Science: Materials in Electronics, **31**, **13011-13027**
8. N. Chopra, **S. Kaur**, M. Kaur, S. Singla, Ritika, G. Sharma, M. S. Heer, **(2018)** Optical, Physical and structural properties of Er^{3+} doped low phonon energy vitreous matrices: ZnO-B_2O_3-TeO_2, Physica Status Solidi (a), **1700934 (1-7)**

Book Chapter

1. R. Priya, S. Bhatia, **S. Kaur**, V. Dubey and O.P. Pandey, Synthesis of rare-earth-activated phosphors, Rare-Earth-activated phosphors, Elsevier, **(2022)**, ISBN: 978-0-323-89856-0

Papers published as conference proceedings

1. N. Chopra, **S. Kaur**, O.P. Pandey, S. Sharma, Physical, optical and structural characterizations of Dy^{3+}- glasses, **(2021)** IOP Conference Series Materials Science and Engineering 1114(1):012098, doi: 10.1088/1757-899X/1114/1/012098

2. **S. Kaur**, O.P. Pandey, Gopi Sharma, Manmohan S. Heer, Neetu Chopra, Optical and thermal characterization of Dy^{3+} doped sodium borotellurite glasses, **(2018)** ISBN No. 978-93-87276-93-2 in National conference on Emerging Scenario in Basic and Applied Sciences for sustainable development.

List of Conferences

1. **S. Kaur,** O. P. Pandey, Neetu Chopra, **(2019)**, Optical, thermal and structural characterization of Dy^{3+} doped sodium borotellurite glasses, *Nanostructured Materials: Structure, Properties and Applications (NSNM-19)* at Kanya Maha Vidyalaya, Jalandhar.

2. **S. Kaur**, O.P.Pandey, Gopi Sharma, Manmohan S. Heer, Neetu Chopra, **(2018)** "Optical, thermal and structural characterization of Dy^{3+} doped zinc borotellurite glasses" *National conference on Materials Science Application in Energy and Environment'* 17, March 2018 at DAV College, Jalandhar, India. Presented under Poster Presentation.

3. **S. Kaur**, O.P.Pandey, Gopi Sharma, Manmohan S. Heer, Neetu Chopra, **(2018)**, "Optical and thermal characterization of Dy^{3+} doped sodium borotellurite glasses" *National conference on Emerging Scenario in Basic and Applied Sciences for sustainable development' April 5,2018* at DAV College, Bathinda, India.

4. **S. Kaur,** O.P. Pandey, Neetu Chopra, **(2018)**, Optical, thermal and Structural characterization of Dy^{3+}doped zinc borotellurite glasses, *International conference on Science, Technology and Applications of Rare Earths,* September 2018 at Tirupati.

5. **S. Kaur**, Shivani, Venu Gopal Achanta, Neetu Chopra, Gopi Sharma **(2017)**, Characterization of Dy^{3+} doped bismuth borosilicate glasses, *International Conference on Advances in Glass Science and Technology,* 23-25 January at CGCRI Kolkata.

Tutorials/Fellowships

1. ICG-CGCRI Tutorial organized by international commission on glass at CSIR-Central glass & Ceramic Research Institute from 19 to 21 January, 2017.

2. Participated in 2nd ICG-CGCRI online tutorial from January 18-27, 2021 and won second prize in group project.

3. Visiting Fellow, ENEA Advanced Technological Physics, Italy from 15 November, 2019 to 15 May, 2020

List of Figures

Chapter 1
Introduction

Chapter 3
Materials and Methods

Chapter 4
Results and Discussion I
Effect of heat treatment on $(70\text{-}x)TeO_2\text{-}20B_2O_3\text{-}10ZnO\text{-}xEr_2O_3$ glasses

Chapter 5
Results and Discussion II
Effect of heat treatment on (70-x)TeO_2-20B_2O_3-10ZnO-xDy_2O_3 glasses

Chapter 6
Results and Discussion III
Effect of gamma irradiation on $(70-x)TeO_2$-$20B_2O_3$-$10ZnO$-xEr_2O_3 glasses

Chapter 7
Results and Discussion IV
Effect of gamma irradiation on $(70\text{-}x)TeO_2\text{-}20B_2O_3\text{-}10ZnO\text{-}xDy_2O_3$ glasses

Chapter 8
Conclusions and Future Perspectives

List of Tables

Chapter 1
Introduction

Chapter 2
Literature Survey

Chapter 3
Materials and Methods

Chapter 4
Results and Discussion I
Effect of heat treatment on (70-x)TeO_2-20B_2O_3-10ZnO-xEr_2O_3 glasses

Chapter 5
Results and Discussion II
Effect of heat treatment on (70-x)TeO_2-20B_2O_3-10ZnO-xDy_2O_3 glasses

Chapter 6
Results and Discussion III
Effect of gamma irradiation on $(70\text{-}x)TeO_2\text{-}20B_2O_3\text{-}10ZnO\text{-}xEr_2O_3$ glasses

Chapter 7
Results and Discussion IV
Effect of gamma irradiation on $(70\text{-}x)TeO_2\text{-}20B_2O_3\text{-}10ZnO\text{-}xDy_2O_3$ glasses

Chapter 8
Conclusions and Future Perspectives

SUMMARY

Rare earth (RE^{3+}) elements are well known for their exceptional properties and industrial applications. They play important role in the modern optoelectronic industries. RE doped glasses have many applications such as in high power lasers and as radiation shielding materials. Most of the glass lasers use RE^{3+} ions as active sites because of low coupling of the RE^{3+} with the host vibrations. The host required for laser applications must have very less phonon energy. For this purpose tellurite glasses are considered as excellent choice because of their least phonon energy amongst all the other oxide glasses. The present work deals with the preparation of Er_2O_3/Dy_2O_3 doped zinc borotellurite glasses. The effect of different processing conditions like heat treatment and gamma irradiation on the structural, optical and luminescent properties of such glasses is studied in detail. The entire thesis is divided into eight chapters; the outline of each chapter is given below:

Chapter 1 The optical properties of the RE doped glasses are important for their applications. The present chapter describes the luminescence properties of materials and their associated mechanisms. Since the work deals with tellurite and borate glasses a brief introduction of glasses and their properties which get affected by heat treatment and gamma irradiation have been presented in this chapter.

Chapter 2 summarizes the literature review on the tellurite glasses. This chapter gives introduction about the work done by different researchers to prepare pure tellurite glasses. It also discusses about the discrepancies found in various parameters like transition temperature and density of pure TeO_2 glasses. In continuation it discusses about the mixed former and effect of modifiers on the tellurite glasses. This chapter also gives information about the effect of dopants like rare earths and metal nano particles on the luminescent properties of the tellurite glasses. Discussion about the effect of heat treatment and gamma irradiation on different properties of TeO_2 glasses is also done in this chapter. After analyzing the work done so far, the gaps in study has been highlighted and accordingly, the objectives of the present study are proposed.

Chapter 3 gives the details about sample preparation and the various characterizations done in the present study. The chapter discusses about the preparation of Er_2O_3/Dy_2O_3 doped zinc borotellurite glasses in detail. The parameters adopted for characterization techniques such as X-ray diffraction (XRD), differential thermal analysis (DTA), field emission scanning

electron microscopy (FESEM), UV-Vis-NIR absorption spectroscopy, Photoluminescence (PL) spectroscopy are given in this chapter.

Chapter 4 illustrates the spectroscopic studies of erbium zinc borotellurite glasses and glass-ceramics. The concentration of Er_2O_3 is varied from 0 to 2.5 mol%. In order to convert the glasses to glass ceramics, thermal studies are done to choose a temperature range for heat treatment. In order to optimize time and temperature, glass sample with 0.5 mol% Er_2O_3 is given heat treatment at 375, 400 and 450 ^oC for 2, 4 and 6h. Since the maximum PL intensity has been observed for the sample heat treated at 400 ^oC for 4h, all the glasses are heat treated at 400 ^oC for 4h. Further, the effect of heat treatment on the structural and various radiative properties on the glasses is discussed in detail.

Chapter 5 discusses about the spectroscopic, thermal and structural properties of Dy_2O_3 on the zinc borotellurite glasses and glass-ceramics using DTA, XRD, FESEM, Raman spectroscopy, UV-Vis-NIR spectroscopy, PL, and decay time measurements. The optimization of the thermal parameters in order to covert glasses into glass ceramics is done as explained in the Chapter 4.

Chapter 6 discusses about the effect of 50 kGy gamma irradiation on the thermal, structural and spectroscopic properties of the Er_2O_3 doped glasses. The chapter also discusses it's applications as shielding material and shielding properties of the present glasses in detail.

Chapter 7 discusses about the effect of 50 kGy gamma irradiation on the thermal, structural and spectroscopic properties of the Dy_2O_3 doped glasses. The chapter further discusses about the effect of increasing Dy_2O_3 concentration on the shielding properties of the present glasses in detail.

Chapter 8 summaries the results obtained in the Chapter 4, 5, 6 and 7. The effect of different processing conditions like heat treatment and gamma irradiation on the spectroscopic properties of Er_2O_3/Dy_2O_3 doped glasses is discussed and compared. At the end suggestions for the future work is also given in this chapter.

INTRODUCTION

Overview

The glasses with rare earth doping are very interesting materials for opto-electronic devices because of their emission characteristics. RE-doped glasses are considered as suitable materials for frequency up-converters, lasers, fibers, amplifiers, optical, temperature sensors and optical limiters etc. This chapter is divided into three sections. First section is about basics of the luminescence. The second section deals with the rare earth spectroscopy. Finally, third section is devoted to the introduction of glasses and effect of different processing conditions like heat treatment and gamma irradiation on the glasses.

1.1 Introduction

Spectroscopy is an analytical technique to characterize materials by absorption, reflection, emission and scattering of electromagnetic radiation in a material. The spectroscopic investigations contribute to our present day knowledge about the properties of atoms and molecules. The emission and absorption spectrum helps to study the molecular/atomic structure of a material. For instance, the atoms are uniformly arranged in a long-range order in crystals and sort or medium range order in glasses or other amorphous materials. This property of the solids can be used to analyze the solids with the help of solid state spectroscopy. Over the years, luminescent materials have played an important role in photonic devices such as lasers, communication, nuclear shielding and so on [1-3]. The introduction of luminescent ions into different matrices is considered as vital aspect in the advancement of optical devices. Such materials are potential materials for temperature sensors, near infrared (NIR) lasers and fiber amplifiers etc. [2-5]. The spectroscopic properties of the luminescent materials depend on their vicinity or host composition. The addition of different modifiers and dopants can modify their spectroscopic properties. In other words, the neighboring ligand fields have an extensive influence on the absorption and emission characteristics of rare earth ions in a host matrix.

1.2 Introduction to luminescence

Luminescence is light emission phenomenon that occurs because of different allowed electronic transitions. When a photon is made to fall on an atom or ion it goes to a higher energy state. The unstable atom/ion comes back to the ground state after certain time period. The energy radiated by the atoms/ions is lower than the incident energy. **Table 1.1** represents different types of excitation that could be achieved with different excitation modes.

Table 1.1: Different types of luminescence

Type of Luminescence	Source of Excitation
Electro-luminescence	Due to presence of strong current
Photo-luminescence	Due to absorption of photons
Cathodo-luminescence	Due to cathode rays
Chemi-luminescence	Because of chemical reactions
Radio-luminescence	Due to irradiation by high−energy particles
Bio-luminescence	Light produced by biological systems
Thermo-luminescence	Due to gradual heating of a material

1.2.1 Mechanism

Excitation: In luminescence mechanism the activator (luminescent) ion absorbs the energy in lower energy state (E1) and goes to the excited state (E2) as explained in **Fig. 1.1**. It is worth noting that the host materials do not participate in luminescence, but holds the activator ions. On the other hand, activator ions absorb the energy and emits radiatively or non-radiatively.

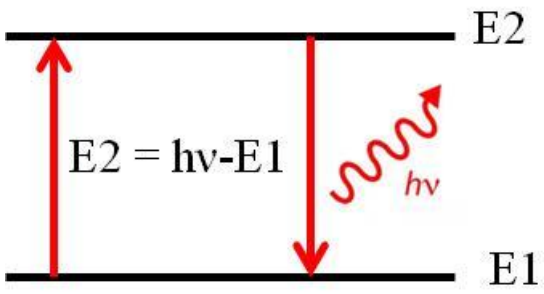

Fig. 1.1: Excitation and emission process.

Emission: On absorbing photon, atoms/ions moves from lower energy state to higher energy state. After spending a certain lifetime in the excited state, ions comes back to lower excited state by giving off energy in the form of photon or via non-radiative emission **(Fig. 1.1)**. These two emission processes are competitive. Thereby to prepare a luminescent material the non-radiative emission loss should be minimized. The said emission transitions depend upon, excited states decay time and emission crosssection of activator ion. In case of rare earths, the majority of transitions occur in the visible region, are from 4f-4f configuration.

1.3 Rare earth (RE) spectroscopy

The RE^{3+} elements were first discovered in 1787 when an unusual black mineral was found in Ytterby, Sweden. The RE ions exist in either RE^{3+} or RE^{2+} states. The trivalent state is the most stable and therefore predominant oxidation state for all RE ions [6,7]. The RE^{3+} ions have noble gas xenon configuration, and additional 4f electrons. Since, these elements have similarities in their electron configuration, so most of their physical properties are similar. When RE ion is doped in any host lattice it acts as optically active center (activator) and exhibit luminescence on excitation.

1.3.1 Photoluminescence in rare earth ions

After the material absorbs photons, the resulted emission in the form of light is known as Photoluminescence. When light of required energy falls on a material, it absorbs photons and

goes to the excited state. The atoms/ions return to the ground state after a certain period of time, and in case of radiative relaxation, the emitted light is the photoluminescence.

1.3.1.1 Rules for f-f transitions

The 4f-electrons present in RE-ions are protected by 5s/5p valence electrons. The electronic transitions happening in the RE ions are characterized as three types (a) electric-dipole (ED), (b) electric-quadruple (EQ) and (c) magnetic-dipole (MD) transitions [8]. **Table 1.2** gives the constraints or selection rules for the said transitions.

Table 1.2: Selection rules for 4f-4f transitions in RE- ions [8]

Transition	Parity	ΔS	ΔL	ΔJ(0≠0)
ED	opposite	0	≤ 6	≤ 6
EQ	same	0	$0, \pm 1, \pm 2$	$0, \pm 1, \pm 2$
MD	same	0	0	$0, \pm 1$

ED transitions: The interactions between active ion and electric field vector through an electric-dipole results in the ED transitions. The non-centro-symmetrical interactions in these transitions allow the combination of energy states of contradictory parity [8].

EQ transitions: EQ transitions have quadrupolar nature. It comprises of four point charges with net charge and dipole moment zero. The electric quadruple has even parity. These transitions are weaker than ED and MD transitions [8].

MD transitions: MD transitions are due to the interaction between active ion and magnetic field component.

1.3.1.2 Splitting of energy levels in RE ions

When RE ion is doped in a particular matrix, it interacts with its surrounding through Coulomb potential. For a solid host matrix, the Hamiltonian model is used.

$$H_{ion} = H_{CO} + H_{ES} + H_{SO} + H_{CF} \quad \textbf{(1. 1)}$$

Where, H_{CO} represents coulombic interactions between the RE-ions, H_{ES} denotes electrostatic forces of interaction between electrons of RE-ions and H_{SO} is the measure of spin-orbit interaction. Also, another factor H_{CF} is considered in the Hamiltonian due to the perturbation induced in crystal-field because of host matrix. The energy levels are denoted as $^{2S+1}L_J$ [8].

1.3.2 Factors affecting photoluminescence in RE ions

1.3.2.1 Concentration Quenching

When activator or luminescent ions are added in a material, the intensity of emitted light should increase. This occurs because of the increase in absorption of the light by activator/luminescent ions. In practice this happen up-to a particular doping concentration only. After that the emission intensity starts decreasing. This phenomenon is known as concentration quenching. It happens due to following reasons:

An increase in number of activator or luminescent ions results into increase in non-radiative transfer of energy (W_{NR}). Also due to large number of activator ions present in a system, distance between two ions decreases, which increases the chances of high values of W_{NR}. Because of this, the luminescent ion starts acting as sink or traps leading to reduction of emitted light. The quenching can also happen without the actual energy transfer but via cross-relaxation.

1.3.2.2 Hypersensitive transitions

In RE ions there are certain transitions which are affected by surrounding environment. These transitions are known as hypersensitive transitions and follow constraint rules of Electric Quadruple transitions [9-11]. Different transitions in RE ions are given in the following **Table 1.3**.

Table 1.3: Observed Hypersensitive transitions in RE^{3+} ions

Ln^{3+}	**Transition**	**≈Energy ($x10^3$ cm^{-1})**
$Pr^{3+}(4f^2)$	$^3H_4 \rightarrow {}^3P_2$	5.20
$Nd^{3+}(4f^3)$	$^4I_{9/2} \rightarrow {}^4G_{5/2}$	17.30
$Pm^{3+}(4f^4)$	$^5I_4 \rightarrow {}^5G_2, {}^5G_3$	18.00
$Sm^{3+}(4f^5)$	$^6H_{5/2} \rightarrow {}^6F_{1/2}$ $^6H_{5/2} \rightarrow {}^6P_{7/2}$	6.40 26.60
$Eu^{3+}(4f^6)$	$^7F_1 \rightarrow {}^5D_1$ $^7F_0 \rightarrow {}^5D_2$ $^7F_2 \rightarrow {}^5D_0$	18.70 21.50 16.30
$Gd^{3+}(4f^7)$	$^8S_{7/2} \rightarrow {}^6P_{7/2}, {}^6P_{5/2}$	32.50
$Dy^{3+}(4f^9)$	$^6H_{15/2} \rightarrow {}^6F_{11/2}$ $^6H_{15/2} \rightarrow {}^4I_{15/2}, {}^4G_{11/2}$	7.70 23.40
$Ho^{3+}(4f^{10})$	$^5I_8 \rightarrow {}^5G_6$ $^5I_8 \rightarrow {}^3H_6$	22.10 27.70

Ln^{3+}	Transition	≈Energy ($x10^3$ cm^{-1})
$Er^{3+}(4f^{11})$	$^4I_{15/2} \rightarrow {}^2H_{11/2}$ $^4I_{15/2} \rightarrow {}^4G_{11/2}$	19.20 26.40
$Tm^{3+}(4f^{12})$	$^3H_6 \rightarrow {}^3F_4$ $^3H_6 \rightarrow {}^3H_4$ $^3H_6 \rightarrow {}^1G_4$	5.90 12.70 21.30

1.3.2.3 Non-Radiative Transitions

In the said transitions the emitted light is lost in the form of heat. This happens because of the variations in ligand field. These variations result into energy transfer from the excited ion to host matrix leading to lose of energy in the form of heat. The said transitions are classified as: (i) co-operative upconversion and (ii) Cross-relaxations [12]. In order to minimize the non-radiative de-excitation, it is always preferred that the active ions should be surrounded by a host having low phonon energies.

1.3.3 Upconversion (UC) Emission

UC emission is basically an example of anti-stokes process which involves transformation of more than one low-energy photon to higher-energy photon. It is possible in RE^{3+}- ions with metastable and long-lived intermediate levels. The up-conversion-processes occur through different ways: excited-state-absorption (ESA), two-photon-absorption (TPA) and energy transfer up-conversion (ETU) [11,12].

Excited state absorption (ESA): ESA process requires absorption of two (or more) photons by RE- ions sequentially. The ions present in ground state (GS), it goes to meta-stable (MS) state through ground state absorption (GSA). When another photon is absorbed by that ion, it further goes to higher excited state (ES) as shown in **Fig. 1.2 (a)**. The excited ion eventually comes back to the GS by giving off up-conversion luminescence.

Two photon absorption (TPA): In TPA, an ion in the GS absorbs two photons simultaneously and goes to an excited state via virtual state. The virtual state is shown by the dashed line in **Fig. 1.2 (B)**.

Energy transfer up-conversion (ETU): The sensitized ETU is the most efficient up-conversion mechanism. In ETU process, there is a cross-relaxation between ions in their excited states. In this case, one ion absorbs energy and passes on to the other ion which is already in the excited state as shown in **Fig. 1.2 (C)**.

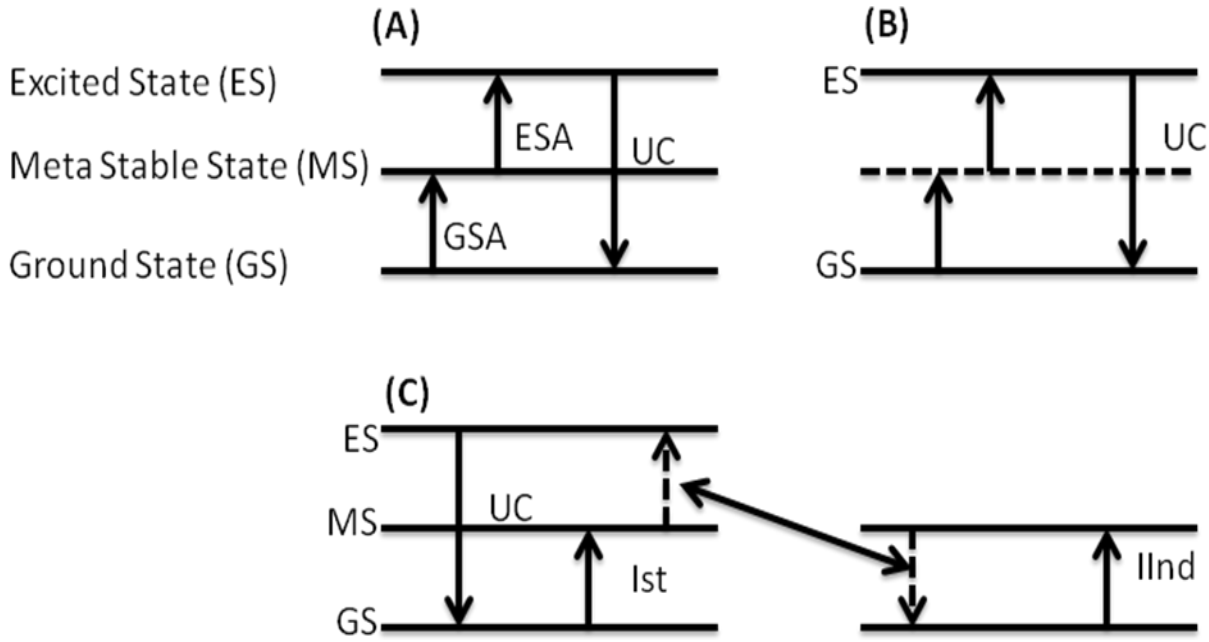

Fig. 1.2: Schematic representation of the up-conversion emission by different mechanisms

1.4 Introduction to Glasses

Glass is a non-crystalline solid that undergoes a phenomenon called glass transition [13,14]. The glass transition occurs from viscous liquid to glass and the corresponding temperature is called as glass transition temperature (T_g) [14,15]. Glass is known as thermodynamically metastable state due to quenching of arrangement of the atoms during the preparation. **Fig. 1.3** shows a V-T graph corresponding to crystals and glassy phases. When a material undergoes cooling from an initial state *A*, volume of the material decreases gradually with decrease in temperature. In the case of slow cooling, the atoms have sufficient time to arrange themselves in an orderly arrangement and crystallization takes place at T_m. The volume of the slow cooled material decreases sharply to point *B* and follows the path *BC* with further decrease in temperature. However, if the cooling rates are very high, the atoms do not have sufficient time to arrange themselves in an orderly fashion, hence the crystallization is avoided. The volume of the super-cooled liquid decreases along ADF/E route. The materials exhibit glassy nature below transition temperature only. If the glassy materials are re-heated well above T_g it can be transformed into crystalline materials.

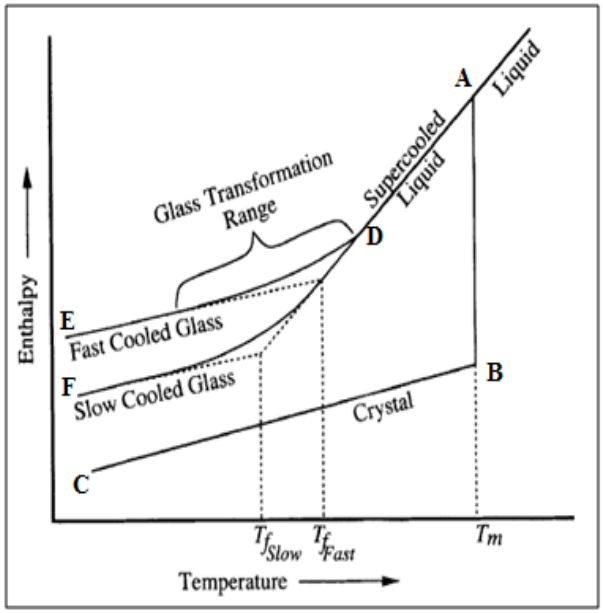

Fig. 1.3: Effect of temperature on enthalpy glass and crystals [14]

1.4.1 Tellurite glass

Recently, tellurite (TeO_2) glasses are gaining interest of glass scientist because of their different properties e.g. phonon energy (780 cm^{-1}), low glass melting temperatures, good chemical stability, high refractive index and durability [16-18]. These distinctive properties make TeO_2 glasses as a possible host material for applications in different opto-electronic devices [17,18].

Structure of tellurite glasses

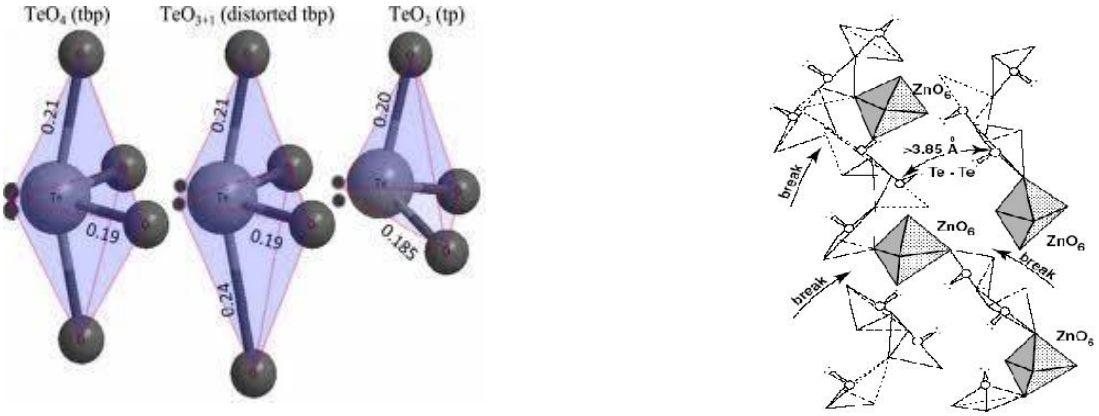

Fig.1.4: (a) Different structural units present in tellurite glass and (b) Predicted model of zinc tellurite glass [19,20]

It has been observed that the building units present in TeO_2 glasses are trigonal pyramidal TeO_3 groups and trigonal bi-pyramidal TeO_4 **(Fig 1.4 (a)).** These structural units are highly

asymmetrical and have a large variation in bond lengths because of the presence of lone pair in one of the equatorial sites. The lone pair repels oxygen atoms strongly which constrains the structure. With addition of modifiers/dopants (**Fig. 1.4 (b) and 1.5)** in tellurite glasses, there is a conversion of units with bridging oxygens (BOs) (TeO_4) to units having non-bridging oxygens (NBOs) (TeO_{3+1}) groups. The TeO_{3+1} units have two terminal Te-O bonds [19].

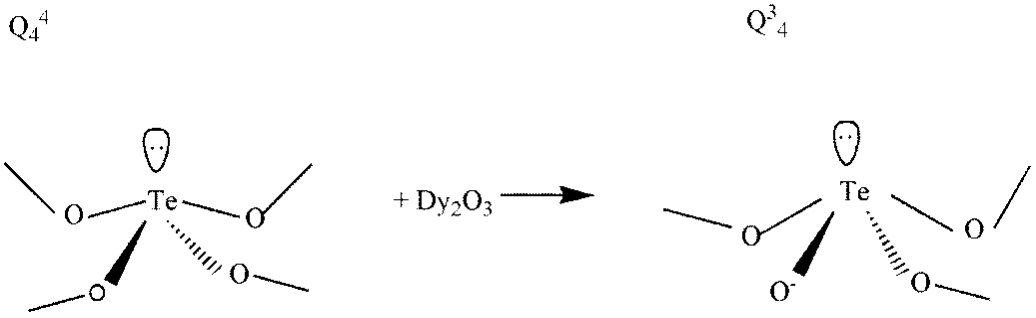

Fig. 1.5: Possible structural variations induced in TeO_2 glasses with Dy_2O_3. Where Q_4^4 superscript gives the number of BOs and subscript gives number of NBOs.

1.4.2 Borate Glasses

Borate glasses comprises of B_2O_3 as glass former. The structure of borate glass is believed to consist of boroxol rings as shown in **Fig 1.6**. It consists of three B-O triangles joined together [14,21]. Borate glasses are potential candidates for opto-electronic devices having RE-elements. It is because of the presence of different poly-borate groups which are stable and well defined. **Fig 1.7** shows different structural groups comprising of borate glasses. The addition of borate in the TeO_2 glasses helps to improve stability of glass structure.

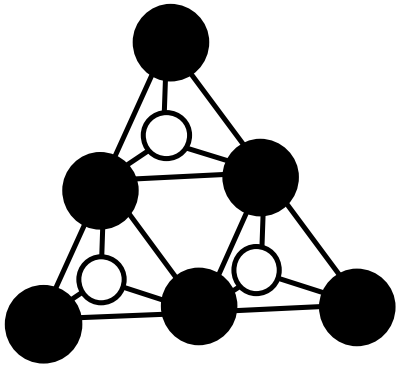

Fig. 1.6 Boroxol ring structure [14]

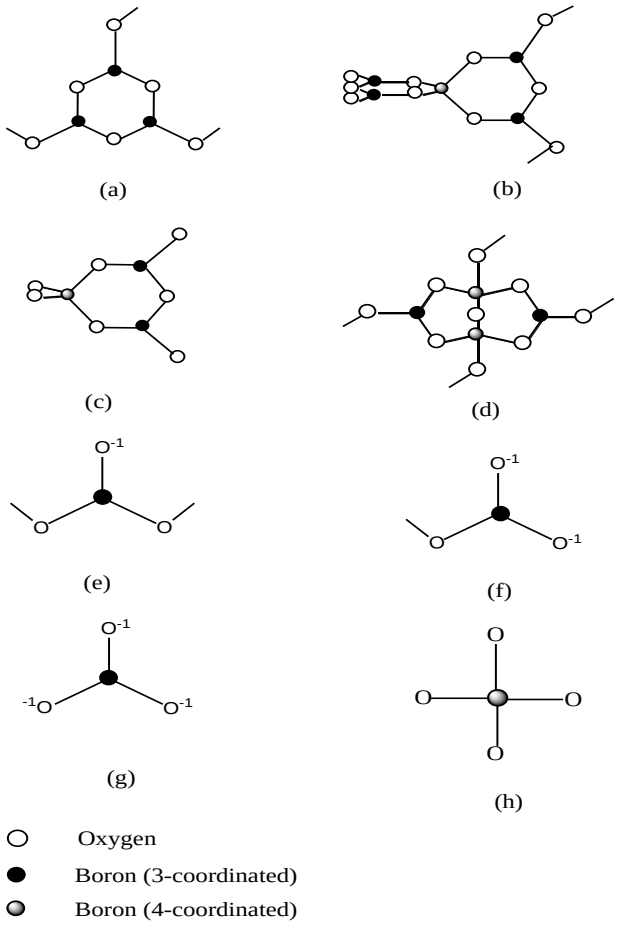

Fig. 1.7 Structural groups present in alkali borate glasses

1.4.3 Importance of RE doped glasses

Rare earths (RE^{3+}) are known for their exceptional spectroscopic characteristics and applications in opto-electronic industries [22-27]. The glass phosphors use RE^{3+} ions as active ions, because of low coupling of the RE^{3+} with the host matrix vibrations. It results in decrease of non-radiative energy loss [28-31]. This leads to increase in the efficiency of laser active medium. RE^{3+} ions acquire the non-symmetrical sites in the glasses. Hence, the site-to-site variations in the in-homogeneous broadening of the absorption and emission spectra (also known as Stark Splitting) and non- exponential decay curves or the radiative transition probability depends upon the host glass composition and its preparation technique. In case of high phonon energy, the non-radiative emissions are higher.

1.4.4 Glasses to Glass-Ceramics

The science and technology continuously call for novel materials with excellent thermodynamic and spectroscopic properties to achieve new functionality. Glass Ceramics

(GCs) are hetro-phase complex materials. GCs are formed by controlled heat treatment of glasses, which leads to nucleation and crystallization in glass matrix. GCs consist of micro or nano-sized crystalline phase and residual glass phase.

***Preparation routes of Glass-Ceramics*:** The crystallization in glasses is a two step transformation: nucleation stage and crystal growth stage. In nucleation, small volumes of crystallites are produced in the parent glass. It is followed by crystal growth, in which atoms/molecules move from glass-crystal interface to the crystallite sites. The schematic of glass ceramics formation is shown in **Fig 1.8**.

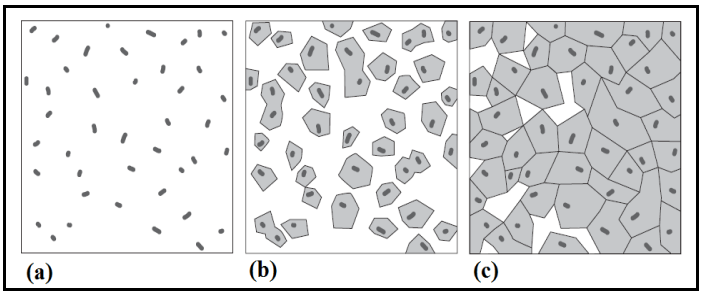

Fig. 1.8 Conversion of glasses to glass-ceramics by heat treatment [32]

The GCs are obtained by various methods. These are discussed in brief as follows:

Single Stage Method: Single stage method is applied when there is considerable overlap between the crystal growth rates and nucleation rate curves. **Fig 1.9** represents a case in which this method has been illustrated. The single stage heat treatment is done at temperature T_{NG}. The glass ceramics for the present study are prepared by this method.

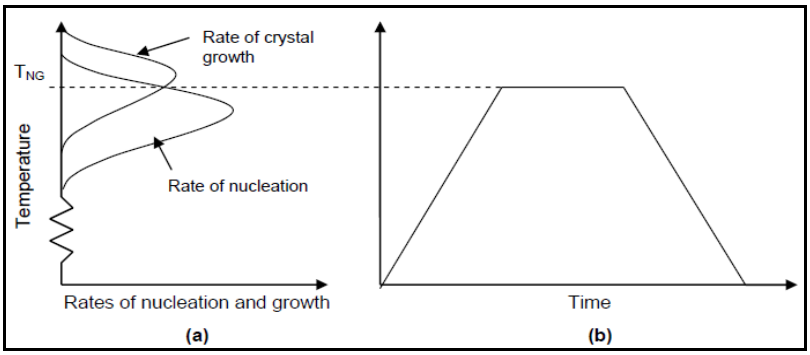

Fig. 1.9 (a) Schematic of nucleation and crystal growth on temperature in a glass matrix, (b) Schematic of heat treatment done via single stage method [33]

Two Stage Method: Two stage methods are employed when extent of overlap in nucleation and crystal growth rate curve is very less [33]. This method requires heating of samples in two steps to achieve ceramization.

1.4.5 Gamma ray interactions with matter

Gamma rays are ionizing electromagnetic radiations produced from radioactive decay of atomic nuclei. Gamma rays on interaction with matter may produce charged particles such as positrons and free electrons. There are three dominant photon interaction processes that can happen when gamma rays interact with matter [53-55]. These processes are discussed below:

Photoelectric Absorption (PA): In this particular process gamma ray photons interact by means of K-shell electrons of an atom. The gamma photon is absorbed by the K-shell electrons. The energy absorbed is partly used to knock-off an electron and rest of the part goes as kinetic energy. Binding energy of a particular shell acts as threshold energy for this process. The photon absorption is dominant process at low photon energies for elements having large atomic numbers.

Compton Scattering (CS): Another possibility of gamma ray interaction with matter is inelastic/incoherent scattering of gamma photons. This is known as Compton scattering. As a result of Compton scattering, energy goes to an electron partially and remaining to photon which is elastically or in-elastically scattered. This process results is independent of Z and a gradual decreases in its value is observed with the increasing photon energy.

Pair Production (PP): It involves induction of e^-/hole pair by means of absorption of γ-photons completely. It is more pronounced in elements having high Z.

The atomic cross-section for these processes in principle increases with increasing Z. Consequently, heavy metals are relatively more effective for shielding and detection of gamma radiations as compared to lighter elements. Moreover, it is observed that cross-section of PA and CS decreases and of PP increases with increasing energy. As a result, the total absorption of gamma rays in an element has a region of lowest and highest transparency at some energy. This may act as a window through which gamma rays may escape from a given shielding material. Therefore, it is always preferred to use mixtures of different materials for gamma rays shielding to close the window.

Studies on the changes in optical properties yield valuable information regarding the radiation induced defect centers and development of structural models. The detailed review on the progress in the field of rare earth doped borotellurite glasses is discussed in the next chapter.

References

1. N. Hirosaki, R. Xie, K. Inoue, T. Sekiguchi, B. Dierre, and R. Xie , Appl. Phys. Lett., 2007, 061101, 2-5

2. A.A. Talin, K.A. Dean and J.E. Jaskie, Solid State Electron., 2001, 45, 936-976

3. G. Li, X. Xu, C. Peng, M. Shang, d. Geng, J. Chen and J. Lin, Fluoresc. Lumin. Mater., 2011, 19, 3020-3028

4. C.S. Kamal, T. K. V. Rao, t. Samuel, P. V. S. Reddy, J. B. Jasinski, Y. Ramakrishna, M. C. Rao, RSC Adv, 2017, 7, 44915-44922

5. I. V. B. Maggay and W. R. Liu, J. Nanosci. Nanotechnol., 2018, 18, 3-10

6. B.G. Wybourne, (1978), Spectroscopic properties of rare earths, Interscience Publishers, New York

7. F.A. Cotton, G. Wilkinson, Advanced inorganic chemistry (A Wiley Interscience Publication, New York, (1988) 960

8. B. Henderson, G.F. Imbusch, Optical spectroscopy of inorganic solids, Oxford University Press, 2006.

9. J. Solé, L. Bausa, D. Jaque, An introduction to the optical spectroscopy of inorganic solids, John Wiley & Sons, 2005

10. S. Dai, C. Yu, G. Zhou, J. Zhag, G. Wang, L. Hu, J. Lumin. 117 (2006) 39.

11. X. Wang, Q. Nie, T.Xu, S. Dai, X. Shen, L. Liu, J. Opt. Soc. Am. 24 (2007) 972.

12. C. K. Jorgensen, B. R. Judd, Mol. Phys. 8 (1964) 28

13. Am. Soc. Testing Mater., ASTM C 162-56, ASTM stand. Part 13,1965

14. J. E. Shelby, (2005), Introduction to Glass Science and Technology, Second Edition, The Royal Society of Chemistry, Cambridge, UK

15. R.W. Douglas, S. Frank (1972), A History of glassmaking, Foulis Co., London

16. B. C. Bunker, G. W. Arnold and J. A. Wilder, J. Non-Cryst. Solids 64 (1984)291.

17. S. Kim and T. Yoko, J. Am. Cer. Soc 78 (1995) 1061.

18. L. C. Courrol, L. V. G. Tarelho, L. Gomes, N. D. Vieira, Jr. F. C. Cassanjes, Y. Messaddeq and S. J. L. Ribeiro, J. Non-Cryst. Solids 284 (2001) 217.

19. V. Kozhueharov, H. Burger, S. Neov and B. Sidzhimov, Polyhedron, 5 (1986) 771-777.

20. S. Manning, H. E. Heidepriem and T. M. Monro, Opt. Mater., 2(2012) 140-152.

21. V.V. Tarsov, Problems in the Physics of Glass, Stroiizdat, Moscow, 1979.

22. I. Arul Rayappan, K. Marimuthu, S. Surendra Babu , M. Sivaraman, J. Lumin., 130 (2010) 2407-2412.

23. M. V. S. Kumar, D. Rajesh, A. Balakrishna and Y. C. Ratnakaram, J. Mol. Struct., 1041 (2013) 100-105.

24. R. V. Kumar, S.B. Rai, Sol. State. Commun., 132 (2004) 647-652.

25. P. Chimalawong, K. Kirdsiri, J. Kaewkhao, P. Limsuwan, Procedia Engin., 32 (2012) 690 – 698.

26. C.K. Jayasankar, M.F. Reid, F.S. Richardson, Phys. Stat. Sol. (b), 155(2) (1989) 559-569.

27. C.K. Jayasankar, K. R. Setty, P. Babu, Th. Troster, W.B. Holzapfel, Phys. Rev. B., 69 (2004) 214108 (1-7).

28. K. S. Lim, N. Vijaya, C.R. Kesavulu ,C.K. Jayasankar, Opt. Mater., 35(8) (2013)1557-1563.

29. C.K. Jayasankar, V. Venkatramu, S. Surendra Babu, P. Babu, J. Alloys Compds., 374 (2004) 22-26.

30. C.R. Kesavulu ,C. K. Jayasankar, Mater. Chem. Phys., 130 (2011) 1078-1085.

31. S. Selvi, G. Venkataiah, S. Arunkumar, G. Muralidharan, K. Marimuthu, Physica B, 454 (2014) 72-81.

32. M. Yamane and Y. Asahara, (2000), Glasses for Photonics, Cambridge University Press, UK.

33. W. Hölland and G. H. Beall, (2002), Glass-Ceramic Technology, The American Ceramic Society, U.S.A.

34. P. Babu, K. Hyuk Jang, Ch. S. Rao, L. Shi, C. K. Jayasankar, V. Lavín, H. J. Seo, Opt. Express, 19 (2011) 1836-1841.

35. M. Jayasimhadri, L.R. Moorthy, K. Kojima, K. Yamamoto, N. Wada, J. Phys. D: Appl. Phys., 39 (2006) 635-641

36. C. Yu, J. Zhang, L. Wen, Z. Jiang, Mater. Lett., 61(2007) 3644-3646.

37. O. Maalej, M. El Jouad, N. Gaumer, S. Chaussedent, B. Boulard, M. D. B. Ameur, M. D. B. Tijani, J. Non. Cryst. Solids, 420 (2015) 48-54.

38. J. Xie, Q. Zhang, Y. Zhuang, X. F. Liu, M. Guan, B. Zhu, R. Yang, J. Qiu, J. Alloys Compd., 509 (2011) 3032-3037.

39. P. Babu, K. H. Jang, E. S. Kim, L. Shi, R. Vijaya, V. Lavin, C.K. Jayasankar, H. J. Seo, J. Non. Cryst. Solids, 350 (2010) 236-243.

40. R. Bagga, V. G. Achanta, A. Goel, J. M.F. Ferreira, N. P. Singh, D. P. Singh, M. Falconieri, G. Sharma, Mater. Sci. Eng., B 178 (2013) 218-224.

41. Z. Pan, A. Ueda, R. Mu, S.H. Morgan, J. Lumin. 126 (2007) 251-256.

42. I. Jlassi, H.Elhouichet, S.Hraiech, M.Ferid J. Lumin. 132 (2012) 832-840.

43. S. Marjanovic, J. Toulouse, H. Jain, C. Sandmann, V. Dierolf, A.R. Kortan, N. Kopylov, R.G. Ahrens, J. Non-Cryst. Solids 322 (2003) 311-318.

44. S. Xu, D. Fang, Z. Zhang, Z. Jiang, J. Solid State Chem. 178 (2005) 2159-2162.

45. R. J. Amjad, M.R. Sahar, S. K. Ghoshal, M.R. Dousti, S.Riaz, B.A.Tahir, J. Lumin. 132 (2012) 2714-2718.

46. S.K. Singh, N.K. Giri, D.K. Rai, S.B. Rai, Solid State Sci. 12 (2010) 1480-1483.

47. A. Jha, P. Joshi, S. Shen, Opt. Express 16 (2008) 13526-13533.

48. H. Lin, S. Jiang, J. Wu, F.Song, N. Peyghambarian, E.Y.B. Pun, J. Phys. D: Appl. Phys. 36 (2003) 812-817.

49. V. K. Tikhomirov, D. Furniss, A. B. Seddon, J. Mater. Sci. Lett., 21(2002) 293-295. .

50. Y. Guo, G. Gao, M. Li, L. Hu, J. Zhang, Mater. Lett. 80 (2012) 56-58.

51. F. Yang, C. Liu, D. Wei, Y. Chen, J. Lu, S.Yang, Opt. Mater. 36 (2014) 1040-1043.

52. P.H. González, I.R. Martín, L.L. Martín, S.F.L .Luis, C.P. Rodríguez, V. Lavín, Opt. Mater. 33 (2011) 742-745.

LITERATURE SURVEY

Overview

Tellurite (TeO_2) glasses are promising host materials for rare earth doping because of several promising properties. The optical properties of TeO_2 glasses are important for several applications like laser technology and optical communication networks. Present chapter deals with the literature review on the tellurite glasses. The synthesis of pure TeO_2 glass and the discrepancies reported for different parameters like transition temperatures and density have been discussed. A detailed discussion about the effect of other glass formers and modifiers on the preparation and properties of TeO_2 glasses has been presented in this Chapter. Discussion about the effect of different parameters like heat treatment and gamma irradiation on TeO_2 glasses is also done in this chapter. After analyzing the work done so far, the gaps in the study have been highlighted and accordingly the objectives of the present study have been proposed.

2.1 Introduction

The first well planned study on tellurite (TeO_2) glasses was done by Stanworth [1] in 1952. Until today TeO_2 glasses are providing new prospects to fabricate optoelectronic devices [2-4]. Tellurite glass former have attracted interest of glass scientist because of its better optical, physical and radiative properties when compared to other oxide glasses. Tellurite glasses are preferred because of their advantages such as: wide transmission, low melting point (< 800 ^oC), lowest phonon energy among oxide glass hosts, high chemical stability, solubility of RE^{3+} ions and refractive index [5,6]. In consequence of said properties strong emission and large quantum efficiencies are expected from the TeO_2 glasses doped with RE elements [7-10]. Owing to these properties, tellurite glasses are considered as promising materials for lasers, sensors, electronic devices, and for optical amplifiers. Tellurite is an intermediate/conditional glass former hence pure TeO_2 glass is prepared by some special quenching techniques. Some of the work is presented here.

Sarjeant et al. [11] have prepared the blobs of pure glassy TeO_2 by using splat quenching. While, Kim et al. [12] prepared pure TeO_2 glass by quenching the glass melt in NaCl, ethanol and ice mixture at a very low temperature of -10 °C. In order to prepare flaky glass in large quantities twin-roller technique was employed by Barney et al. [13]. Tagiara et al. [14] prepared TeO_2 glass with intermittent quenching. The crucible containing glass melt was removed from furnace and stirred until it became viscous. Further glass melt was promptly quenched by dipping the base of crucible in and out of water.

Since the fundamental properties of glasses like density (ρ) and T_g are sensitive to composition and thermal record, the complexities in glass preparation lead to disagreeable results of T_g and ρ. Also, the density of pure tellurite glass shows a large deviation as observed from different studies. For instance, it varies from 4.80 to 5.62 g/cm^3 as reported in different studies [14-19]. Also, different studies in relation to pure TeO_2, reported different T_g values varying from 303.1 to 385 ^oC [14-19].

2.2 Consequence of composition on the properties of TeO_2 glasses

To encounter the above mentioned problems some modifications in terms of glass compositions of the glasses has been made and studied.

2.2.1 Mixed network former effect

To prepare tellurite glasses by conventional melt-quenching, the addition of glass-forming oxides like GeO_2, P_2O_5 and B_2O_3 etc. can be an option [20-25]. In this regard, borate is a potential former because of its good thermal and optical properties along with its glass forming ability [26]. The introduction of borate to tellurite glasses results into increased refractive index. Rada et al. [27] prepared TeO_2-B_2O_3 glasses, in a ceramic crucible by melt-quenching technique. Structural studies of TeO_2-B_2O_3 glass confirm that glasses with higher B_2O_3 content have appearance of discrete vibrational bands [27]. This may be because of increase in structural units containing NBOs. Ahmed et al. [28] prepared GeO_2-TeO_2 glasses with the help of melt quenching at 1400 ^oC. The as-prepared samples were found to have a compact structure. The absorption bands were found to be broad and strong. Rinke et al. [22] prepared sodium phosphate tellurite glasses by melt-quenching. Structure of obtained glasses consisted of collection of interlinked anionic $P^{(2)}$ tetrahedra and neutral $TeO_{4/2}$ anti-prisms. The clustering of sodium cations was also observed in structural studies. The results suggest that sodium ions behave differently in the present glass than in other oxide glasses.

2.2.2 Effect of modifiers

Addition of alkali/alkaline earths metal ions to tellurites leads to rupture of glass structure, hence transforming TeO_4 to TeO_{3+1} structural groups. Agammy et al. [29] reported on structure of NaF–TeO_2 glasses. The studies suggest that, in samples with the modifier concentration ≤10 mol%, the modifier convert TeO_4 units into $TeO_{3/2}F$ and $Na^+[TeO_{3+1}]^-$ units. Whereas, at concentration higher than 10 mol% NaF partially forms crystalline phases. Jiusti et al. [26] studied the T_g of alkali ($Li_2O/Na_2O/K_2O/Rb_2O/Cs_2O$) tellurites. It decreases with an increase in alkali concentration from 0 to 30 molar percent. On the other hand, metal oxides like SrO/MgO/BaO/CaO had the opposite effect on the properties of samples. Tellurite glasses, containing ZnO were reported by several researchers [30-35]. An inconsistency in trends of transition temperature and density is observed with varying ZnO content. Some studies suggests a decrease in T_g with increasing in ZnO concentration [17,30,35] whereas other studies reported increase in T_g with ZnO addition [24,25,33,37]. A variation in the density of ZnO-TeO_2 glasses is also reported [24,25,34,35,38,39].

It is observed that the relation between structure and observed trend in T_g of tellurites is complex, because of their structural complexity. Sekiya et al. [39] suggested that on addition of modifiers to the TeO_2 glasses, some Te_{eq}-O_{ax}-Te, (where, eq = equatorial and ax = axial sites) bonds are broken, and non-bridging-oxygens (NBOs) are formed. Hence, it can be said that many structural rearrangements are possible with addition of modifier causing contrast in results.

2.2.3 Addition of dopants

2.2.3.1 RE-doping in glasses

The introduction of RE^{3+} ions into vitreous matrices is considered as vital aspect in the advancement of glass materials based optical devices, for instance temperature sensors and near infrared (NIR) lasers etc. [40-43]. One of the important approaches to obtain fiber lasers is the use of upconversion (UC) processes in order to obtain the NIR to visible laser emission. The UC in Er^{3+} ions is possible due to the existence of metastable energy levels. To broaden the applications of TeO_2 glasses some modifications in terms of doping has been done. Glass phosphors mostly use RE^{3+} ions as activators, because of low coupling of the RE^{3+} with the host vibrations. This in turn decreases the loss in the form of heat and hence improves the quantum efficiency of emitting level.

Zhou et al. [40] have reported on the fluorescence behaviour of Tm^{3+}-doped tellurite glasses. The emission at 1.20 μm emission has been observed corresponding to Tm^{3+}: $^1G_4$-$^3H_4$ transition. The respective emission cross-section has been calculated to be 0.47×10^{-20} cm^2. Due to effective population inversion in $^1G_4$ and $^3H_4$ levels, a positive gain band was achieved at relatively low Tm^{3+} dopant concentration.

Linganna et al. [41] prepared Nd^{3+} doped P_2O_5-TeO_2 glasses by melt-quenching. Figure of merit (FOM) for transition $^4F_{3/2}$ - $^4I_{11/2}$ was higher than other reported glasses doped with Nd^{3+} [39]. Hence, the said glasses have the potential to act as laser medium at 1060 nm.

Selvi et al. [42] worked on Dy^{3+} doped boro-tellurite phosphate glass and reported that decay time of $^4F_{9/2}$ excited state decreased with the increasing Dy^{3+} amount. Hazlin et al. [43] studied the optical as well as structural characteristics of tellurite glasses doped with Dy^{3+}. An increase energy gap and decrease in Urbach energy was observed with increase in Dy^{3+} content. Glasses doped with Er^{3+} are known to give visible (553 nm) and NIR (1.53 μm) emission. In addition, the erbium doped glasses show the upconversion. Pandey et al.

[44], studied photon downshifting in tungsten tellurite glasses. The prepared glasses showed an enhancement of 14.2 times in NIR region after further doping with Yb^{3+}. The results suggested that the prepared samples can be used as luminescent coating solar cells to enhance its efficiency [44]. Umar et al. [45] observed that with the increasing Er^{3+} ion content, there is an increase in density, molar volume, energy gaps, molar refraction and transmission coefficient. The emission characteristics of some rare earth doped glasses are given in **Table 2.1**.

Table 2.1: PL characteristics of some rare earth doped glasses

Glass Composition (mol%)	**Synthesis method**	**Dopant**	**Excitation wavelength**	**Emission Transitions (ground state-excited state)**
$95SiO_2$-$5Pr(NO_3)_3$ [46]	Sol-gel method	Praseodymium (Pr)	450 nm	495, 540, 615 and 650 nm ($^3P_0$-$^3H_4$, $^3P_1$-$^3H_5$, $^1D_2$-$^3H_4$ and $^3P_0$-$^3F_2$)
57ZrF-36BaF_2-1LaF_3-3EuF_3-3AlF_3 [47]	Sol-gel method	Europium (Eu)	394 nm	579, 591, 612, 655 and 702 nm ($^5D_0$-$^7F_{0,1,2,3\ and\ 4}$)
$5La_2O_3$-$95TeO_2$ [48]	Melt-quenching	Lanthanum (La)	325 nm	325, 405, 447, 538 and 582 nm (intrinsic defects)
$25Bi_2O_3$-$5B_2O_3$-(70-*x*)P_2O_5-*x*CeF_3 [49]	Melt-quenching	Cerium (Ce)	317 nm	360 nm (5D - 4F)
x(Pr_6O_{11})-100-x(SLS-ZnO) [50]	Melt-quenching technique	Praseodymium (Pr)	444 nm	530, 556, 613 and 650 nm (^3P_o - $^3H_{4,\ 5,\ 6}$, $^3F_2$)
$40Bi_2O_3$–20BaO–(40-x)B_2O_3 [51]	Melt-quenching technique	Neodymium (Nd)	585 nm	900, 1060 and 1345 nm ($^4F_{3/2}$- $^4I_{9/2,\ 11/2\ and\ 13/2}$)
20PbO-5CaO-5ZnO-10NaF-59B_2O_3-Sm_2O_3 [52]	Melt-quenching technique	Samarium (Sm)	402 nm	565, 602, 648 and 710 nm ($^4G_{5/2}$-$^6H_{5/2,\ 7/2,\ 9/2\ and\ 11/2}$)
20PbO-5CaO-5ZnO-10NaF- 59B_2O_3-1Tb_2O_3 [52]	Melt-quenching technique	Terbium (Tb)	378 nm	418, 442 and 458 nm ($^4F_7$-$^5D_1$ $^7F_6$ – $^5D_{3,4}$)
(70-x)TeO_2-20B_2O_3-xDy_2O_3 [53]	Melt-quenching	Dysprosium (Dy)	383 nm	484, 576 and 664 nm ($^4F_{9/2}$-$^6H_{15/2\ ,13/2\ and\ 11/2}$)
$(Sb_2O_3)_{90-x}$-$(Na_2O)_{10}$-$(ZnO)_x$ [54]	Melt-quenching technique	Erbium (Er)	514.5 nm	550, 670, 850, 980, and 1530 nm ($^4F_{9/2}$- $^4I_{15/2}$, $^4S_{3/2}$- $^4I_{13/2}$, $^4S_{3/2}$- $^4I_{13/2}$, $I_{11/2}$- $^4I_{15/2}$, $^4I_{13/2}$- $^4I_{15/2}$)
60TeO_2–30ZnF_2–10NaF [55]	Physical and chemical dehydration	Holmium (Ho)	1163 nm	2.85 mm ($^5I_6$-$^5I_7$)

2.2.3.2 Metallic doping in glasses

The metal nanoparticles (np) doped in a rare earth glass results in an increment in the emission intensity making nps as ideal sensitizers. This is due to local surface plasmon resonance. Hua et al. [56] studied Dy^{3+} doped silver tellurite glasses and observed an increase of 29% in the luminescence intensity. Similar results were obtained by Mahraz et al. [57] with Ag doping in the Er^{3+} -borotellurite glasses. Mawlud [58] studied the comparison between Ag and Au np doping in Sm^{3+}-ZnO-NaO-TeO_2 glasses. It was observed that luminescence intensity increased with the introduction of metal nps (gold and silver) in the glass. The samples having Au nano-particles had higher lifetime as compared to the Ag counterpart.

2.3 Factors affecting the spectroscopic properties of RE-doped glasses

2.3.1 Effect of heat treatment

The demand for optical and electronic sources having high efficiency and minimal environmental hazard is increasing. In this context, glass-ceramics formed by controlled nucleation of glasses with the advantages of both glass and crystal are potential materials. GCs exhibit combined properties of glasses such as (i) optical transparency (ii) formability into various shapes (iii) different possible compositions (iv) gas and liquid impermeability (v) hardness, with distinctive characteristics of polycrystalline materials called ceramics and crystalline materials such as optical activity.

Heat treatment of the glasses at particular temperature leads to a transformation of glassy material to the glass-ceramic. It is interesting to study the crystallites of nano/micrometer size induced in a glass matrix as it is expected that these crystals may give rise to excellent properties. Rajesh et al. [59] studied the influence of $NaYF_4$ nanocrystals on radiative parameters of the oxy-flouro tellurite glasses doped with Nd_2O_3. The results reveal that increasing Nd^{3+} concentration had a negative effect on the nano-crystalline phase as first crystalline peak decreased accordingly. The emission intensity of band centered at 1060 nm enhanced after ceramization due to occupancy of the Nd^{3+} in $NaYF_4$ nano-crystalline phase.

Walas at el. [60] prepared Eu^{3+} doped tellurite glass ceramics by heat treatment. The analysis of the emission spectra confirmed that lifetime and emission of glass ceramics were higher than of pristine glasses. In another study Bolundut et al. [61] observed similar

results in Sm^{3+}:Ag lead TeO_2 glass samples. In a study Kumar et al. [62] observed an enhancement in the green upconversion because of crystallization in tellurite glass having co-doping of Er^{3+} and Yb^{3+}. Bi-exponential character in decay curves was also observed in the heat treated samples. Similar results were observed by Ennouri et al. [63] because of precipitation of $ErPO_4$ crystals in the P_2O_5-TeO_2 glasses by heat treatment. Joshi et al. [64] reported the effect of ceramization on oxy-halide tellurite glasses having co-doping of Yb^{3+} and Er^{3+}. The observed results explained that emission efficiency of the samples increased drastically after heat treatment. Kaur et al. [53] reported a decrease in the emission intensities in Dy^{3+} doped TeO_2 samples as well as lifetime values after heat treatment due to increased energy transfer rates. Similar results were observed by Babu et al. also [65].

2.3.2 Effect of gamma irradiation

When gamma rays interact with materials there is formation of large number of optical defects. These defects include electrons/hole pairs which are either pre-existing in the glass or are created by the gamma irradiation [66,67]. These defects may give rise to absorption band known as radiation induced band.

Alaily et al. [66] explained the effect of irradiation on the phosphate glasses doped with Sm_2O_3. The irradiation of the glasses with γ-rays leads to the creation of large number of electrons due to photo-generation process. The so produced electrons are either trapped in the preexisted defects or cause new hole-centers in the glass structure. The study suggested that presence of Sm^{3+} ions can reduce the effect of irradiation in the glass matrix. Kaur et al. [67] studied the spectroscopic properties of the zinc borotellurite glasses doped with Er_2O_3 after 50 kGy irradiation. The results concluded that the spectroscopic parameters got marginally modified due to gamma irradiation. Also the shielding properties of the glasses were improved with the increasing rare earth concentration. The glasses with rare earth doping showed less changes in their properties after gamma irradiation which indicates that doped glasses have resistant against gamma radiation in comparison to undoped glass sample [67]. Some characteristic physical, optical and thermal properties of irradiated glass samples are given in **Table 2.2**.

Table 2.2: Characteristic properties of some gamma irradiated samples

Properties	**$20PbF_2$-$20TeO_2$-$57.5B_2O_3$-2.5 Sm_2O_3[68]**	**$10ZnO$-$5Na_2O_3$-$10Bi_2O_3$-$73.5B_2O_3$-$1.5Eu_2O_3$ [69]**	**$78TeO_2$-$20B_2O_3$-$10ZnO$-$2Er_2O_3$ [67]**
Density (gm/cc)	4.27	3.514	4.82
Refractive Index	1.761	2.30	2.40
T_g (^oC)	407	-	375
T_c (^oC)	606	-	444
T_m (^oC)	710	850-900	750
Radiation applied	150kGy	50kGy	50kGy
Radiation induced Absorption	The intensity of the absorption peaks decreased after γ-irradiation	1.The absorbance increased significantly after irradiation in the NIR region but marginally in the UV-Vis region 2.Low Eu_2O_3 [0.1 mol%] content has two extra absorption bands at 520 and 660 nm	The absorption increases by 15% on an average from UV-Vis-NIR region.
Change in Density	4.30 (Increased)	3.484 (Decreased)	4.8244 (Increased)
Change in RI	1.808 (Increased)	2.35 (Increased)	2.42 (Increased)
Change in Hardness	3.98 (Increased)	4 5.994 (Decreased)	-
Change in Tg	370 (Decreased)	-	365 (Decreased)
Change in PL	Increased	-	Decreased upto 40%
Change in Structure	Marginal increase in structural units with Non Bridging Oxygen's observed	Increase in RI values after gamma irradiation is observed due to formation of electron/hole pairs	Increase in structural units with Non Bridging Oxygen's

2.4 Gaps in the Study

The literature review suggested the preparation of pure TeO_2 glasses requires special quenching techniques. However, the addition of glass formers and modifiers not only helps in the formation of TeO_2 glass by conventional methods but also improves the optical properties. In addition, doping of these glasses with RE^{3+} ions makes them important in the field of opto- electronics. But there are few reports on the studies of the mixed former effect of borate and tellurium glass composites so far. Also, there is vast variation in their measured PL characteristics for the same concentration of dopants. Glasses are also potential materials in the field of radiation shielding. There are only few reports on impact

of gamma irradiation on spectroscopic properties of zinc borotellurite glasses doped with rare earth elements.

Considering these gaps following objectives of the present work has been planned.

2.5 Objectives

1. To prepare Er_2O_3/ Dy_2O_3 doped TeO_2-B_2O_3-ZnO glasses via melt-quenching technique.

2. To study the thermal properties of the as-prepared glasses as a function of rare-earth doping concentration.

3. To study the effect of variation in rare-earth doping concentration on photoluminescence property of glasses and glass ceramics.

4. To study the effect of gamma irradiation on the structural and spectroscopic properties of the as prepared glasses.

References

1. J.E. Stanworth, Nature 169 (1952) 581–582; J.E. Stanworth, J. Soc. Glass Technol. 38 (1954) 425–435.

2. F. Goutaland, M. Mortier, B. Capoen, S. Turrell, M. Bouazaoui, A. Boukenter and Y. Ouerdan, Opt. Mater. 28 (2006) 1276-1279.

3. D. Zheng, H. Da-gui and Z. De-yin, J. Electron. Sci. Technol. *China* 4 (2006) 144-147

4. C. Sumalatha, R._Doddoji, M. Venkateswarlu, P. Rekha Rani, K.Swapna, Sk. Mahamuda and A.S.Rao, Spectrochim. Acta A Mol. Biomol. Spectrosc. 240 (2020) 118568.

5. R. Sharma, A. Prasad, S. Kaur, N. Deopa, R. Rani , M. Venkateswarlu and A.S. Rao, J. Non. Cryst. Solids 516 (2019) 82-88.

6. N.S. Tagiara, D. Palles, E.D. Simandiras, V. Psycharis, A. Kyritsis and E.I. Kamitsos, J. Non-Cryst. Solids 457 (2017) 116–125.

7. K. S. R. Krishna Reddy, K. Swapna, Sk. Mahamuda, M. Venkateswarlu, A.S. Rao and G. V. Prakash, Opt. Mater., 85 (2018) 200-210.

8. R. Kaur, A. Khanna, M. G. Barriuso, F. González and B. Chen, Mater. Res. Bull., 106 (2018) 288-295.

9. G. Devarajulua, P. S. Prasad, N. J. Sushma, C. M. Reddy, S. Chourasia, B. D. P. Raju, Ceram. Int. 43 (2017) 16076-16083

10. Hirdesh and Atul Khanna, J. Lumin. 204 (2018) 319-326

11. P.T. Sarjeant, R. Roy, J. Am. Ceram. Soc. 50 (1967) 500–503.

12. S.H. Kim, T. Yoko, S. Sakka, J. Am. Ceram. Soc. 76 (1993) 2486–2490.

13. E.R. Barney, A.C. Hannon, D. Holland, N. Umesaki, M. Tatsumisago, R.G. Orman, S. Feller, J. Phys. Chem. Lett. 4 (2013) 2312–2316.

14. N.S. Tagiara, D. Palles, E.D. Simandiras, V. Psycharis, A. Kyritsis, E.I. Kamitsos, J. Non-Cryst. Solids 457 (2017) 116–125.

15. E. Lambson, G. Saunders, B. Bridge, R. El-Mallawany, J. Non-Cryst. Solids 69 (1984) 117–133.

16. R. El-Mallawany, J. Non-Cryst. Solids 379 (2013) 177–179.

17. H.A.A. Sidek, S. Rosmawati, B.Z. Azmi, A.H. Shaari, Adv. Condens. Matter Phys. 2013 (2013), 783207.

18. R.K. Ramamoorthy, A.K. Bhatnagar, J. Alloys Compd. 623 (2015) 49–54.

19. A.G. Kalampounias, G. Tsilomelekis, S. Boghosian, J. Chem. Phys. 142 (2015) 154503.

20. F.A. A. Wahab, A. Abdallah, H. A. Maksoud, J. Non. Cryst. Solids 545 (2020) 120170.

21. A. Osaka, Q. Jianrong, Y. Miura, T. Yao, J. Non-Cryst. Solids 191(1995) 339-345.

22. M. T. Rinke, L. Zhang, H. Eckert, Chem. Phys. Chem. 8(2007) 1988 – 1998.

23. F. Wang, J. Dai, L. Shi, X. Huang, C. Zhang, X. Li, L. Wang, Mater. Lett. 67 (2012) 196–198.

24. N. Mochida, K. Takahashi, K. Nakata, S. Shibusawa, J. Ceram. Soc. Jpn. 86 (1978) 316–326.

25. H. Bürger, K. Kneipp, H. Hobert, W. Vogel, V. Kozhukharov, S. Neov, J. Non-Cryst Solids 151 (1992) 134–142.

26. J. Jiusti, E. D. Zanotto, S. A. Feller, H. J. Austin, H. M. Detar, I. Bishop, D. Manzani, Y. Nakatsuka, Y. Watanabe, H. Inoue, J. Non-Cryst. Solids 550 (2020) 120359.

27. S. Rada, M. Culea, E. Culea, J. Non-Cryst. Solids 354 (2008) 5491–5495.

28. M. M. Ahmed, C. A. Hogarth, M. N. Khan, J. Mater. Sci. 19 (1984) 4040-4044.

29. E.F.El Agammy, H. Doweidar, K. El-Egili, R. Ramadan, M. Jaremko, A. H. Emwas, Ceram. Int. 46 (2020) 18551–18561.

30. E. Stavrou, C. Tsiantos, R.D. Tsopouridou, S. Kripotou, A.G. Kontos, C. Raptis, B. Capoen, M. Bouazaoui, S. Turrell, S. Khatir, J. Phys. Condens. Matter 22 (2010)

31. 195103.

32. D. Dutta, M.P.F. Graca, M.A. Valente, S.K. Mendiratta, Solid State Ionics 230 (2013) 66–71.

33. A. Kaur, A. Khanna, C. Pesquera, F. González, V. Sathe, J. Non-Cryst. Solids 356 (2010) 864–872.

34. J.G. Thorbahn, J.W. Zwanziger, J. Non-Cryst. Solids 381 (2013) 48–53.

35. S. Sakida, J. Jin, T. Yoko, Phys. Chem. Glasses 41 (2000) 65–70.

36. R.K. Ramamoorthy, A.K. Bhatnagar, J. Alloys Compd. 623 (2015) 49–54.

37. H. Matsumoto, T. Mabuchi, Y. Shigesato, I. Yasui, Jpn. J. Appl. Phys. 35 (1996) 694–698.

38. T. Komatsu, N. Ito, T. Honma, V. Dimitrov, Solid State Sci. 14 (2012) 1419–1425.

39. T. Sekiya, N. Mochida, A. Ohtsuka, J. Non-Cryst. Solids 168 (1994) 106–114.

40. B. Zhou, H. Lin, E. Y. B. Pun, Optics Express 18 (2010) 18805-18810.

41. K. Linganna, R. Narro-García, H. Desirena, E. De la Rosae, Ch. Basavapoornima, V. Venkatramu, C.K. Jayasankar, J. Alloys Comps., 264 (2016) 322-327.

42. S. Selvi, G. Venkataiah, S. Arunkumar, G. Muralidharan, K. Marimuthu, Physica B, 454 (2014) 72-81.

43. M. N. Ami Hazlin, M.K. Halimah, F.D. Muhammad, J. Lumin., 196 (2018) 498-503.

44. A. Pandey, R. E. Kroon, V. Kumar, H. C.Swart, J. Alloys Compds., 657 (2016) 32-36.

45. S.A. Umar, M.K. Halimah, K.T. Chan, A.A. Latif, J. Non. Cryst. Solids, 471 (2017) 101-109.

46. A. L. Fanai, U. Khan, S. Rai, J. Non. Cryst. Solids, 503–504 (2019) 89–93.

47. M. Dejneka, E. Snitzer, R. E. Riman, J. Non. Cryst. Solids, 202 (1996) 23–34.

48. R. Kaur, A. Khanna, J. Lumin., 225 (2020) 117375.

49. N. Chanthima, T. Sareein, Y. Tariwong, J. Kaewkhao, N. Sangwaranatee, Appl. Mech. Mater., 879 (2018) 22–26.

50. N. Mohamed, J. Hassan, K. A. Matori, R. S. Azis, Z. A. Wahab, Z. M. M. Ismail, N. F. Baharuddin, S. S. A. Rashid, Results Phys., 7 (2017) 1202–1206.

51. R. Ruamnikhom, P. Limsuwan, M. Horprathum, N. Chanthima, H. J. Kim, S. Ruengsri, J. Kaewkhao, Adv. Mater. Sci. Eng. 2014 (2014) 751973 (1-5).

52. C. Madhukar Reddy, B. Deva Prasad Raju, N. John Sushma, N. S. Dhoble, S. J. Dhoble, Renew. Sustain. Energy Rev., 51 (2015) 566–584.

53. S. Kaur, O. P. Pandey, C. K. Jayasankar and N. Chopra, J. Non. Cryst. Solids, 521 (2019) 119472.

54. J. Zavadil, Z. G. Ivanova, P. Kostka, M. Hamzaoui and M. T. Soltani, 611 (2014)

111–116.
55. J. He, Z. Zhou, H. Zhan, A. Zhang and A. Lin, J. Lumin., 145 (2014) 507–511.
56. C. Hua, L. Shen, E. Y. B. Pun, D. Li, H. Lin, Opt. Mater. 78 (2018) 72-81.
57. Z. A. S. Mahraz, M.R. Sahar, S.K. Ghoshal, J. Alloys Compds., 649 (2015) 1102-1109.
58. S. Q. Mawlud, Spectrochimica Acta Part A: Mole. Biomol. Spectra 209 (2019) 78–84.
59. D. Rajesh, A.S.S. de Camargo, J. Lumin. 207 (2019) 469–476.
60. M. Walas, T. Lewandowski, A. Synak, M. Łapinski, W. Sadowski, B. Koscielska, J. Alloys Compds. 696 (2017) 619-626.
61. L. Bolundut, P. Pascuta, E. Culea, M. Bosca, L. Pop, R. Stefan, J Mater Sci 55 (2020) 9962–9971.
62. J. S. Kumar, K. Pavani, M.P.F. Graça, M.J. Soares, J. Alloys Compds, 617 (2014) 108-114
63. M. Ennouria, I. Jlassia, E. Habibb, G. Bernard, J. Lumin., 216 (2019) 116753.
64. C. Joshi, R. N. Rai, S.B. Rai, J. Quant. Spectros. Radia. Trans. 113 (2012) 397–404.
65. P. Babu, K. Hyuk Jang, Ch. S. Rao, L. Shi, C. K. Jayasankar, V. Lavín, H. J. Seo, Opt. Express, 19 (2011) 1836-1841.
66. N.A. El-Alaily, O.I. Sallam, F.M. Ezz-Eldin, J. Non. Cryst. Solids, 523 (2019) 119604.
67. S. Kaur, O.P. Pandey, C.K. Jayasankar, N. Chopra, J. Lumin., 235 (2021) 118031.
68. A. Wagh, V. Hegde, C.S. Dwaraka Viswanath, G. Lakshminarayana, Y. Raviprakash, S. D. Kamath, J. Lumin., 199 (2018) 87–108.
69. A. Wagh, K. Manjunath, V. Hegde, S. D. Kamath, Optik, 160 (2018) 298–306.

Experimental

Overview

This chapter describes the procedures adopted to prepare glasses and glass ceramics of different compositions**.** Various techniques used to analyze these glasses and glass ceramics has also been presented. The thermal, morphological, structural and luminescent properties have been studied by means of differential thermal analysis, field emission scanning electron microscopy, Raman and emission spectroscopy respectively. Operating conditions of these instruments along with associated theories used to calculate optical and radiative parameters has been presented at their respective places.

3.1 Experimental

3.1.1 Precursors used:

The precursors used for sample preparation are TeO_2, H_3BO_3, ZnO, Er_2O_3 and Dy_2O_3 procured from Sigma Aldrich having minimum 99.99% purity. All the chemicals were used after heating them at 100^oC to remove the absorbed water.

3.1.2 Preparation of samples

Erbium doped glasses and glass ceramics: Er^{3+}-doped zinc borotellurite samples were synthesized by means of melt-quenching method. A batch of 25 g was prepared by taking the oxides as precursors in stoichiometric amounts. The precursors were further mixed with the help of pestle mortar to achieve homogeneous batch. The mixed oxides were transferred to alumina crucible. The crucible containing the batch was melted in a furnace at 850 ^oC for 1 hour. The glass melt was stirred in the furnace to remove the trapped gases to achieve homogeneity. After melting, the molten mass was poured on the brass mould and transferred to the preheated furnace for annealing at 300 ^oC for 2 hours. The annealing was done to remove the internal stresses. Samples were left for overnight in the furnace to come back to room temperature on their own. The as-prepared samples were finally cut into pieces of 1cm×1cm each having approximate thickness of 2mm. The glass pieces were polished for further studies. One set of the sample was termed as pristine glass sample (as-prepared). The other two sets of the samples were used for preparing the glass ceramics and also for gamma irradiation studies. In order to obtain the glass ceramics (GC), the second set of as-prepared samples were given heat treatment at 375^oC, 400^oC and 450^oC for 2h, 4h and 6h respectively. Further the optimized conditions to achieve glass ceramics were finalized after characterizing these samples. The glass ceramics were coded as $TBZEr_xGC$ (where x = 0.0, 0.5, 1.0, 2.0, 2.5). **Table 3.1** gives their sample ID and composition.

Table 3.1 Chemical composition of $TBZEr_x$ samples

Sample ID	TeO_2 (mol%)	B_2O_3 (mol%)	ZnO (mol%)	Er_2O_3 (mol%)
$TBZEr_{0.0}$	70.0	20.0	10.0	0.0
$TBZEr_{0.5}$	69.5	20.0	10.0	0.5
$TBZEr_{1.0}$	69.0	20.0	10.0	1.0
$TBZEr_{2.0}$	68.0	20.0	10.0	2.0
$TBZEr_{2.5}$	68.5	20.0	10.0	2.5

Dysprosium doped glasses and glass ceramics: Dy^{3+}-doped zinc borotellurite glasses ($TBZDy_x$) and glass ceramics ($TBZDy_xGC$) were obtained by varying Dy_2O_3 concentration at the cost of tellurite, keeping borate and zinc oxide constant **(Table 3.2)**. These samples were prepared using same synthesis method as explained earlier. In order to obtain their heat treated derivatives (glass-ceramics), the prepared glass samples were heat treated for 4 hours in the furnace at 400^oC (optimized conditions).

Table 3.2 The chemical composition of $TBZDy_x$ samples

Sample code	TeO_2 (mol%)	B_2O_3 (mol%)	ZnO (mol%)	Dy_2O_3 (mol%)
$TBZDy_{0.0}$	70.0	20.0	10.0	0.0
$TBZDyr_{0.5}$	69.5	20.0	10.0	0.5
$TBZDy_{1.0}$	69.0	20.0	10.0	1.0
$TBZDy_{2.0}$	68.0	20.0	10.0	2.0
$TBZDy_{2.5}$	68.5	20.0	10.0	2.5

3.1.2.1 *Energy Dispersive Spectroscopy (EDS) of the prepared glasses:*

In order to check the composition of the prepared glasses, EDS analysis was done. The EDS analysis of $TBEr_{2.5}$ and $TBZDy_{2.5}$ are shown in **Fig. 3.1 (a,b).** It is observed from the EDS spectra **(Fig. 3.1)** that all the precursors of the glass are present. The absence of alien elements including Al indicates the non-reactive nature of the present glasses with alumina.

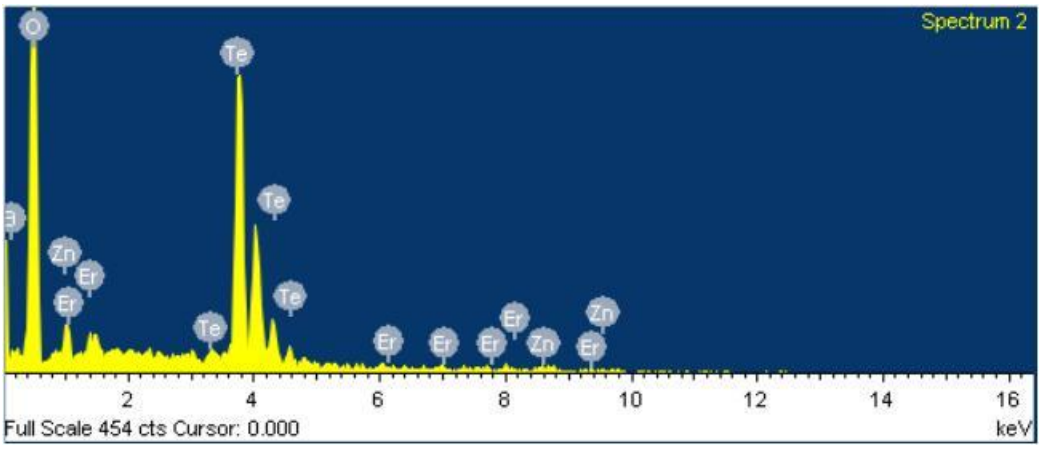

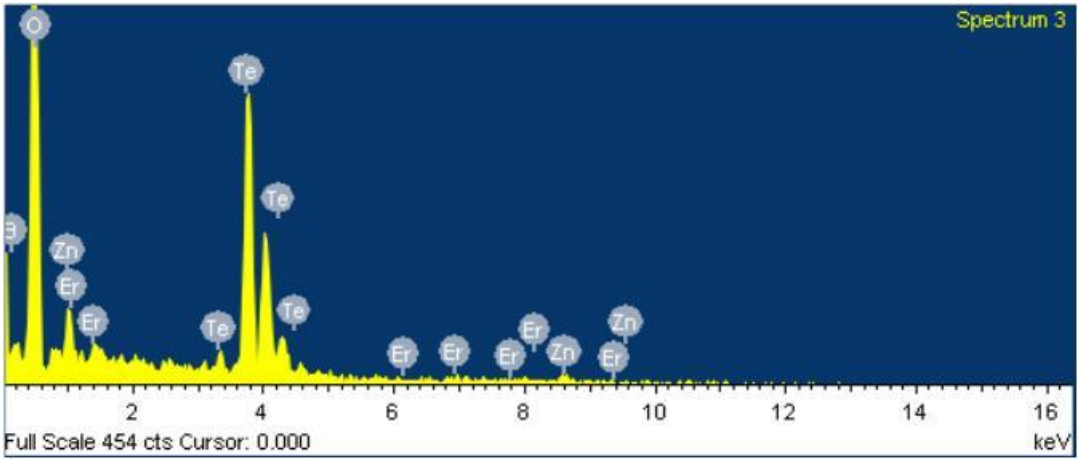

Fig. 3.1 (a): EDS spectra of $TBZEr_{2.5}$ at different locations

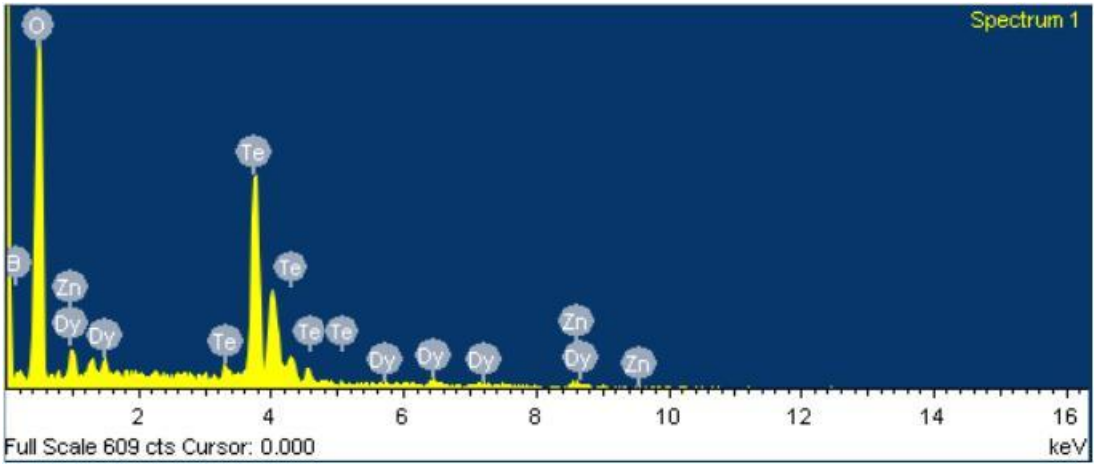

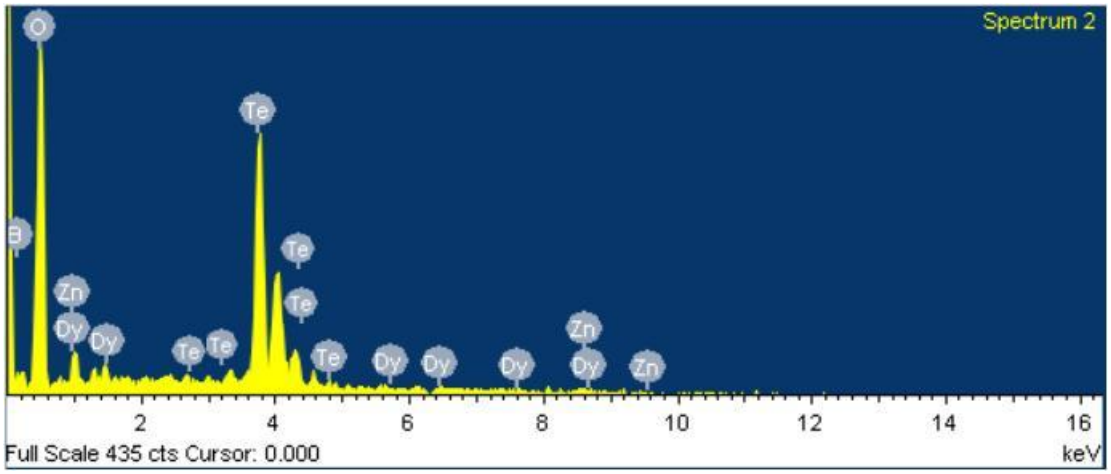

Fig. 3.1 (b): EDS spectra of $TBZDy_{2.5}$ at different locations

In order to verify the elemental composition, the amounts taken in mol% of all the compounds are converted into wt%. The nominal values of elemental wt% are compared

with the experimental data obtained from EDS. A comparison between nominal elemental composition and observed elemental composition is given in **Table 3.3 (a, b)**.

Table 3.3 (a): Nominal elemental and obtained elemental composition of $TBZEr_{2.5}$ glass

Element	Nominal elemental composition (Wt%)	Observed elemental composition (Wt%)	Absolute Error%
Te	61.81	61.79	0.03
O	24.40	24.52	0.49
B	3.10	3.08	0.64
Zn	4.68	4.64	0.84
Er	6.01	5.97	0.66
Total	100%	100%	2.66%

Table 3.3 (b): Nominal elemental and obtained elemental composition of $TBZDy_{2.5}$ glass

Element	Nominal elemental composition (Wt%)	Observed elemental composition (Wt%)	Absolute Error%
Te	61.91	61.89	0.03
O	24.44	24.55	0.45
B	3.11	3.08	0.96
Zn	4.70	4.67	0.63
Dy	5.84	5.81	0.51
Total	100%	100%	2.58%

It is worth noting from **Table 3.3 (a) and (b)** that there is no significant variation in the nominal and observed elemental composition of the prepared glasses. Similar observations were made for other glass samples also.

3.1.3 Gamma irradiation of glass samples

The third set of the as-prepared RE-doped zinc borotellurite glasses were further subjected to 50 kGy gamma ray dose using a ^{60}Co radioisotope. The irradiated samples were denoted as $TBZEr_x50kGy$, where x= 0.0, 0.5, 1.0, 2.0 and 2.5 mol % Er^{3+} and $TBZDy_x50kGy$, where x= 0.0, 0.5, 1.0, 2.0, 2.5 mol%.

3.1.4 Characterization Techniques

The thermal, structural, optical and spectroscopic properties of the prepared samples were done using different techniques. A brief description of the studies is given below:

X-ray diffraction (XRD)

The amorphous/ crystalline nature of all the prepared samples was done with the help of X-ray diffraction technique (XRD). All the samples were characterized with the help of Panalytical X' Pert Pro diffractometer. The X-Ray tube was operated at 30 kV and 10 mA with Cu K_α (1.5405 Å) source with Ni filter. The XRD patterns were recorded in the range of $20° \leq 2\Theta \leq 70°$ with a step size of 0.0131° and scan speed of 19.68 s with a total scan time of 15 min. The samples were rotated with the frequency of 10 Hz. The Joint Committee on Powder Diffraction Standards (JCPDS) database now called International Center for Diffraction Data (ICDD) was referred for identifying the phase observed after the heat treatment.

Differential Thermal Analysis (DTA)

The thermal properties of glass samples were studied with the help of Differential thermal analysis (DTA) using Netzsch DSC404F3. The studies were done on 100 mg of powdered sample in nitrogen atmosphere in a Pt crucible. The heating rate was kept at 5^oC/min. The temperature measurement sensitivity of equipment is $\pm 1^oC$.

Field Emission Scanning Electron Microscopy (FESEM)

The morphological studies were done with the help of FESEM Hitachi SU8000 operating at 15 kV using back scattered and secondary electron imaging. FESEM images of polished samples were taken after gold sputtering. Quantitative elemental analyses were carried out with an energy dispersive X-ray (EDS) spectrometer attached to FESEM Hitachi SU8000.

Raman Spectroscopy

The Raman spectra of glasses were recorded by Renishaw In-Via Reflex micro-Raman spectrometer equipped with a CCD detector using 514 nm argon ion laser (50 mW) and 2400 lines/mm diffraction grating using ×50 objective. The glasses were scanned between 0-1200 cm^{-1} with exposure time of 10 s and 10 accumulations for each sample. The calibration of the spectrometer was done with silicon before taking measurements. Measurements were carried out in an un-polarized mode in the back scattering geometry.

Fourier Transform Infrared Spectroscopy

Fourier Transform Infrared Spectroscopy (FTIR) is used to study the modification in basic structural units. The FTIR spectrum of the prepared glasses is collected at room

temperature in absorption mode from 400-1500 cm^{-1} range using IRAffinity-1 (Shimadzu Co., Japan). The instrument is equipped with 'DRS-8000A Diffuse Reflectance Spectroscopy' powder sample assembly. A fine mixture of 1 mg of sample and 100 mg of KBr obtained in agate mortar was loaded on DRS attachment and the spectra were recorded. Each spectrum was recorded with a resolution of 2 cm^{-1} and represents an average of 16 scans. Normalized spectrum of blank KBr of each sample was studied using IRsolution software.

UV-Vis-NIR Spectroscopy

To study the optical properties e.g. absorption coefficient, band gap and refractive index the absorbance spectra of all the samples were recorded. The studies were carried out using double beam spectrometer from Cary 5000 UV-VIS-NIR spectrometer in the range of 400-2000 nm with a resolution of 1 nm. The scan rate was kept 300 nm/min with a slit width of 5 nm.

Photoluminescence (PL) Spectroscopy

The emission spectra of the glasses were recorded with the help of FLS-980 fluorescence spectrometer (Edinburgh) equipped μs Xe lamp as the excitation source and PMT as detector.

The excitation spectra were taken at 552 nm for the Er^{3+}- doped glass samples. The emission spectra of the Er^{3+} glasses were recorded at 380 nm and 980 nm excitation wavelength. The decay curves for Er^{3+}- glasses were recorded at 380 nm excitation (552 nm emission) and 980 nm excitation (1554 nm emission), respectively.

For the dysprosium doped samples, excitation spectra were recorded in the wavelength range of 300-500 nm at 575 nm emission. The emission spectra of the same were recorded in 450-700 nm range at 383 nm excitation. The fluorescence lifetime measurements of the Dy^{3+}- glasses were done at 383 nm excitation and 575 nm emission.

3.2 Theory

Density

The density of the prepared glasses was calculated using following formula [1]

$$\rho = \frac{W_a}{W_a - W_b}\rho_l \qquad (3.1)$$

where, W_a is the weight of glass sample in air, W_b is its weight in ethanol and ρ_l is the density of the ethanol (0.789 g/cc) at room temperature (maintained at 20^oC). No

significant variation in the laboratory temperature has been observed. The measured weights are accurate upto ±0.01 mg. All the measurements were repeated five times in order to reduce experimental error. The average of these five measurements is the density of the sample whereas the standard deviation on five measurements is the relative error associated with them.

X-Ray diffraction (XRD) studies

The crystallite size has been calculated with the help of Debye-Scherer formula [2] given by

$$D = \frac{0.9\,\lambda_{inc}}{\beta Cos(\theta)} \tag{3.2}$$

Where, D is the crystallite size, λ_{inc} is the incident wavelength (1.5405 Å), θ is the Bragg angle and β is the full width at half maxima of the diffraction line.

Absorption spectroscopy

Absorption spectroscopy allows the determination of band gaps, refractive index oscillator strengths and Judd- Ofelt (JO) parameters of the prepared samples.

Band Gap and Refractive index

The optical band gap (direct and indirect band gap) values in the present study have been determined by applying the relation proposed by Davis and Mott as given in equation **(3.3)** [3].

$$h\upsilon\alpha(\upsilon) = B\,(h\upsilon - E_{opt})^{n} \tag{3.3}$$

where, hυ is photon energy, α(υ) is the absorption coefficient, n is the index number (n=2 for indirect transitions and n=1/2 for direct transitions), B is a constant related to the extent of band tailing and E_{opt} is the optical energy gap.

The refractive index of the prepared glass samples is measured using Dimitrov and Sakka relation [4] given by equation **(3.4)**

$$\frac{n^2-1}{n^2+2} = 1 - \sqrt{\frac{E_{opt}}{20}} \tag{3.4}$$

where, n is refractive index and E_{opt} is optical energy band gap.

Oscillator strengths of absorption bands

The experimental oscillator strength (f_{exp}) is calculated as follows [5]

$$f_{\exp} = \frac{2.303mc^2}{N_{AV}\pi e^2}\int \varepsilon(\upsilon)d\upsilon = 4.318\times10^{-9}\int \varepsilon(\upsilon)d\upsilon \tag{3.5}$$

Where, m and e are the mass and charge of an electron, N_{AV} is the Avogadro's number, ε(υ) is the molar absorptivity of a band at wavenumber υ (cm^{-1}). The molar absorptivity at a given wavenumber is calculated from the Beer-Lambert's law as given below [5]

$$\varepsilon(\upsilon) = \frac{1}{Cl} \log \frac{I_0}{I} \tag{3.6}$$

Where, C is the concentration of the RE^{3+} ions (mol/cm^3), *l* is the thickness of the sample (cm) and $\log \frac{I_o}{I}$ is the absorptivity or optical density.

Judd-Ofelt theory

According to the Judd-Ofelt (JO) theory, the oscillator strength (f_{cal}) for the absorption band can be estimated as follows [6,7]

$$f_{cal} = \frac{8\pi^2 mc\nu}{3h(2J+1)} \quad \frac{(n^2+2)^2}{9n} \quad \sum_{\lambda=2,4,6} \Omega_\lambda (\psi J \| U^\lambda \| \psi' J')^2 \tag{3.7}$$

Where, *h* is the Planck's constant, n is refractive index, $(n^2+2)^2/9n$ is the Lorentz local field correction for the absorption band. $\|U^\lambda\|$ are the doubly-reduced matrix elements, J and J' are the total angular momentum of ground and excited states [8].

The JO intensity parameters obtained from least squares fit by equating the equations **(3.5)** and **(3.7).** The root mean square deviations (δ_{rms}) between the experimental and calculated oscillator strengths given by the relation

$$\delta_{rms} = \left[\frac{\Sigma \left(f_{\exp} - f_{cal} \right)^2}{N} \right]^{1/2} \tag{3.8}$$

Where, f_{exp} is the experimental oscillator strength, N is the number of absorption transitions used in the fit.

Emission Spectroscopy

The different radiative parameters are calculated with the help of Emission spectroscopy using Füchtbauer-Ladenburg (FL) theory [5] and McCumber (MC) theory [9].

Füchtbauer-Ladenburg (FL) theory

According to the FL theory the radiative transition probability (A_R) is given by [5]

$$A_R(\Psi J, \Psi' J') =$$

$$\frac{64\pi^4 \nu^3}{3h(2J+1)} \left(\frac{n(n^2+2)^2}{9} e^2 \sum_{\lambda=2,4,6} \Omega_\lambda (\Psi J \| U^\lambda \| \Psi' J')^2 + n^3 \frac{e^2 h^2}{16\pi^2 m^2 c^2} (\Psi J \| L + 2S \| \Psi' J')^2 \right) \tag{3.9}$$

Where υ is the frequency, J and J' are the total angular momentum of excited and ground state respectively, e and m are the charge and mass of electron and n is the refractive index. The total radiative transition probability (A_T) can be obtained by [5]

$$A_T(\Psi J) = \sum_{\Psi J} A_R\left(\Psi J, \Psi' J'\right) \tag{3.10}$$

The calculated branching ratio (β_R) values is given by [5]

$$\beta_R(\Psi J, \Psi' J') = \frac{A(\Psi J, \Psi' J')}{A_T(\Psi J)} \tag{3.11}$$

The radiative lifetime (τ_R) of an excited level is given as [5]

$$\tau_R(\Psi J) = \frac{1}{A_T(\Psi J)} \tag{3.12}$$

The peak stimulated emission cross-section (σ_{emi}) is represented as [5]

$$\sigma_{emi} = \frac{\lambda_p^4}{8\pi c n^2 \Delta\lambda_{eff}} A_R(\psi J, \psi' J') \tag{3.13}$$

Where, λ_p is the peak wavelength and $\Delta\lambda_{eff}$ is its effective line-width.

McCumber (MC) Theory

McCumber (MC) theory [9] uses reciprocity relations between the Einstein coefficients to give the absorption and stimulated emission probabilities. According to the MC theory the absorption cross-section is given by [9]

$$\sigma_{abs} = \frac{2.303 \log \frac{I_o}{I}}{Nt} \tag{3.14}$$

Where, $\log \frac{I_o}{I}$ is the absorbance, t is the thickness of the sample and N is the concentration of RE (ions/cm^3)

Emission cross-section is given by [9]

$$\sigma_{abs} = \sigma_{emi}(\vartheta) \exp\left(\frac{h\vartheta - E_o}{K_B T}\right) \tag{3.15}$$

From $\sigma_{abs}(\lambda)$ and $\sigma_{emi}(\lambda)$ values, the room temperature gain coefficient is studied by using the relation [9]

$$G(\lambda, P) = P\,\sigma_{emi}(\lambda) - (1-P)\,\sigma_{abs}(\lambda) \tag{3.16}$$

Color Co-ordinates

The CIE 1931 color-coordinate (x, y) are determined by using following formulas [10]

$$x = \frac{X}{X+Y+Z} \tag{3.17}$$

$$y = \frac{Y}{X+Y+Z} \tag{3.18}$$

where, X, Y and Z are the tristimulus values of the source.

The correlated colour temperature (CCT) and calculated using the color coordinates by the McCamy empirical formula [11]

$$CCT = -449n^3+3525n^2-6823n+5520.33 \tag{3.19}$$

$n = (x-x_e) / (y-y_e)$ is the inverse slope line and ($x_e = 0.332$, $y_e = 0.186$) is the epi-centre.

Decay dynamics

Single-exponential decay

The luminescence intensity as a function of time can be described by the following relation [12]

$$I(t) = I_O \, exp\left(\frac{t}{\tau_o}\right) \tag{3.20}$$

where I_0 is the initial emission intensity, when t = 0. The value τ_0 represents the lifetime of the excited state.

Non-exponential decay

In such case, the experimental lifetime (τ_{exp}) is determined by using the following formula [12]

$$\tau_{exp} = \frac{\int t\, I(t)dt}{\int I(t)dt} \tag{3.21}$$

where $I(t)$ is intensity as a function of time.

Inokuti - Hirayama (IH) model

Inokuti and Hirayama [12] modified the theory to account for energy transfer between the 4f- 4f electrons of RE^{3+} ions. The modified theory can be described by the formula [12]

$$I(t) = I_0 \exp\left\{-\frac{t}{\tau_0} - Q\left(\frac{t}{\tau_0}\right)^{3/S}\right\} \tag{3.22}$$

where, t is the time after excitation, τ_0 is the intrinsic decay time of the donors in the

absence of acceptors. Q is the energy transfer parameter defined as [12]

$$Q = \frac{4\pi}{3}\Gamma\left(1-\frac{3}{S}\right)C_{DA}R_0^3 \tag{3.23}$$

Q depends on the gamma function Γ(x), which is equal to 1.77 for dipole-dipole (S = 6). R_0 is the critical transfer distance defined as the donor-acceptor separation for which the rate of energy transfer between a donor and acceptor is equal to the rate of intrinsic decay, τ_0^{-1}. The dipole-dipole interaction parameter C_{DA} is related to R_0 as [12]

$$C_{DA} = R_0^S \tau_0^{-1} \tag{3.24}$$

The non-radiative transition rate (W_{NR}) can be evaluated from the fluorescence and radiative lifetimes of the $^4F_{3/2}$ emitting level from the following expression [12]

$$W_{NR} = \frac{1}{\tau_{exp}} - \frac{1}{\tau_{rad}} \tag{3.25}$$

The quantum efficiency (η) is defined as the ratio of the number of photons emitted to the number of photons absorbed and is given by [12]

$$\eta = \frac{\tau_{exp}}{\tau_{rad}} \text{ x } 100 \tag{3.26}$$

Shielding parameters

The characteristic shielding properties for the as-prepared glasses has been computed using the PSD/Phy-X software [13].

For the multi-component system, the mass attenuation coefficient (MAC) can be given by the following equation [13]

$$\frac{\mu}{\rho} = \Sigma_i W_i \left(\frac{\mu}{\rho}\right)_i \tag{3.27}$$

where, $\left(\frac{\mu}{\rho}\right)_i$ gives the mass attenuation coefficient, ρ is the density of the material and W_i is the weight fraction of the i^{th} element in the sample.

The Half Value Layer (HVL) is defined [13]

$$\text{HVL} = \frac{\ln 2}{\mu} = \frac{0.693}{\mu} \tag{3.28}$$

Another parameter dependent on MAC is mean free path (MFP). It can be determined by the following equation [13]

$$\text{MFP} = \frac{1}{\mu} \tag{3.29}$$

In order to specify atomic number at different energies for materials containing more than one element, following equation is used [13]:

$$Z_{eff} = \frac{\sum_i f_i A_i (\frac{\mu}{\rho})_i}{\sum_j f_j \frac{A_j}{Z_j} (\frac{\mu}{\rho})_j} \quad (3.30)$$

where, Z_i and A_i are the atomic number and atomic weight of the i^{th} element and f_i is the fractional abundance of the i^{th} element w.r.t number of total elements present in the material. The error estimated in the values of MAC, HVL, MFP and Z_{eff} is not more then ±2.5% .

References

1. M.S. Sajna, S. Thomas, K.A. Ann Mary, C. Joseph, P.R. Biju, N. V. Unnikrishnan, J. Lumin., 159 (2015), 55–65.

2. R. Bagga, V. G. Achanta, A. Goel, J. M.F. Ferreira, N. P. Singh, D. P. Singh, M. Falconieri, G. Sharma, Mater. Sci. Eng., B 178 (2013), 218-224.

3. J. Tauc, Amorphous and liquid semiconductors, first ed., Plenum, London, 1974.

4. Z.A.S. Mahraz, M.R. Sahar, S.K. Ghoshal, J. Mol. Struct., 1072 (2014), 238-241.

5. C. Gorller-Walrand, K. Binnemans, Spectral intensities of f-f transitions in Handbook on the Physics and Chemistry of Rare Earths edited by K.A. Gscheneidner Jr. and L. Eyring (North Holland, Amsterdam, 1998), 25 (1998)101-264.

6. B.R. Judd, Phys. Rev., 127 (1962), 750-761.

7. G.S. Ofelt, J. Chem. Phys., 37 (1962), 511-520.

8. W.T. Carnall, P.R. Fields, K. Rajnak, J. Chem. Phys., 49 (1968), 4424-4442.

9. D.E. McCumber, Phys. Rev. A 136 (1964) 954-957.

10. Recueil des Travaux et Compte Rendu des Séance, Commission Internationale de l'Eclairage, Huitieme Session, Cambridge, September 1931, The University Press, Cambridge, 1932, pp. 19–32 Resolution 2 (1932).

11. C. S. McCamy, COLOR research and application 17, (1992)142-144.

12. M. Inokuti, F. Hirayama, J. Chem. Phys., 43 (1965), 1978-1989.

13. E, Şakar, Ö. Özpolat, B. Alım, M.I. Sayyed, M. Kurudirek, J. Phys. Chem. Solids, 166 (2020), 108496

Effect of heat treatment on (70-x) TeO_2-$20B_2O_3$-10ZnO-xEr_2O_3

Overview

The present chapter deals with the spectroscopic studies of erbium zinc borotellurite glasses and glass ceramics. The as-prepared samples are prepared via melt-quenching. Thermal studies are done to choose a temperature range for heat treatment. To optimize time and temperature conditions, glass sample with 0.5 mol% Er_2O_3 is given heat treatment at 375, 400 and 450 ^oC for 2, 4 and 6h. Since the maximum PL intensity has been found at 400 ^oC for 4h, all the glasses are given heat treatment at 400 ^oC for 4h. The CIE chromaticity coordinates for prepared samples lies in green region. An increase in the emission intensity, lifetime and up-conversion intensity is observed after ceramization.

4.1 Introduction

The introduction of RE^{3+} ions into different vitreous matrices is considered as a vital aspect in the advancement of glass lasers [1-8]. One of the important approaches to obtain stimulated emission in glass lasers is the use of up-conversion (UC) processes. The Up-conversion in RE^{3+} ions is possible due to the existence of metastable energy levels [9-16]. It is worth noting that optical properties of rare earth ions are environment dependent. In other words, the neighboring ligand fields in any host matrix have an extensive influence on the emission cross-section. Tellurite based glasses are known for their lowest phonon energy amongst the oxides, which is favorable for Up-conversion [13-16]. Heat treatment of the glasses is also a good option to achieve low phonon energies for UC [9,11]. Several reports suggest that properties like luminescence quantum yields, broad bandwidths and attenuation coefficients of the oxyfluoride glass systems get improved when nanocrystals are present in the systems [2,5,6,14,29], hence, improving their potential as new functional materials in the field of photonics. Jlassi et. al [3] and Jha et al. [14], prepared sodium tellurite glasses and glass ceramics (GC). In their work, emission and the upconversion emission intensity obtained from the glass ceramics was higher than that of the precursor glass.

The aim of this chapter (i) to prepare zinc borotellurite glasses doped with Er_2O_3 ($TBZEr_x$, x = 0,0.5,1.0,2.0,2.5) and glass ceramics ($TBZEr_xGC$, x = 0,0.5,1.0,2.0,2.5) (ii) to explore their structural properties through XRD and FESEM, (iii) to determine forbidden gap energy and order of disorderedness (ΔE) through absorption spectroscopy, (iv) to calculate Judd-Ofelt (JO) parameters, (v) Determining radiative properties and (vi) finally to study the visible and NIR emission characteristics, up-conversion and lifetime characteristics of the $TBZEr_x$ and $TBZEr_xGC$.

4.2 Physical studies

4.2.1 Appearance

The photographs of the present samples are given in **Fig. 4.1 (a)** and **(b)**. It is apparent from the photographs that the as-prepared glasses are transparent. However, the glass ceramics become opaque after the heat treatment.

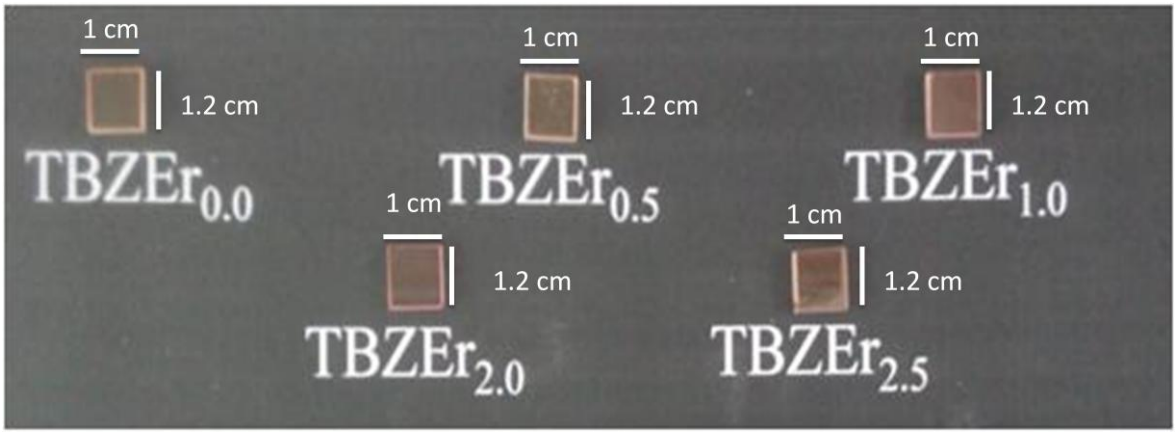

Fig.4.1 (a): Photograph of Er_2O_3- doped zinc borotellurite glasses

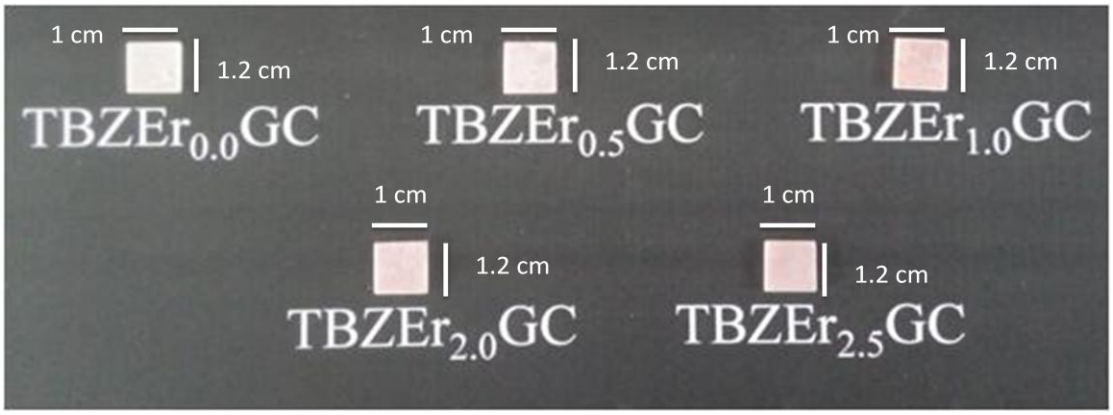

Fig. 4.1 (b): Photograph of Er_2O_3- doped zinc borotellurite glass ceramics

4.2.2 Density

Table 4.1 gives the density of the prepared samples. It is clear that density increases with increasing Er_2O_3 concentration. An increase in density with RE addition may be due to addition of high molecular weight compound, Er_2O_3 (382.5g/mol) in place of comparatively lighter compound, TeO_2 (159.6 g/mol). The RE^{3+} ions goes into the interstitial spaces within the glass network, increasing the packing density of the glass structure and decreasing the molar volume [18].

Table 4.1: Density of prepared samples

Sample ID	Density (g/cm^3)±2%
$TBZEr_{0.0}$	4.72
$TBZEr_{0.5}$	4.79
$TBZEr_{1.0}$	4.86
$TBZEr_{2.0}$	4.90
$TBZEr_{2.5}$	4.95

Sample ID	Density (g/cm^3)±2%
$TBZEr_{0.0}GC$	4.87
$TBZEr_{0.5}GC$	4.92
$TBZEr_{1.0}GC$	4.97
$TBZEr_{2.0}GC$	4.99
$TBZEr_{2.5}GC$	5.04

It is also worth noting that the density of the glasses increases after heat treatment. This may be because of increase in rigidity of samples after ceramization.

4.3 Thermal properties of the as-prepared glasses

To study the thermal temperatures of the as-prepared glasses differential thermal analysis (DTA) was carried out. The DTA curves of $TBZEr_x$ glasses are given in **Fig. 4.2**. The observed values of thermal temperatures are given in **Table 4.2.** It is found that T_g increases from 364 to 378 ^oC, T_{c1} from 424 to 449 ^oC and T_{c2} from 455 to 481 ^oC with an increase in Er^{3+} mol% from 0.0 to 2.5%. The trend of increase in the value of T_g, T_{c1} and T_{c2} is in agreement with the earlier reported works [26,27].

This variation is because due to introduction of Er_2O_3, Te-O and B-O bonds are replaced by Er-O bonds [26, 27]. Since the Te-O and B-O bonds are weaker (377kJ/mol and 536 kJ/mol, respectively) than Er-O bond (606kJ/mol), the network connectivity in the glass matrix becomes stronger. **Table 4.2** shows that with the increase in the T_g, T_{c1} and T_{c2} values, ΔT (T_g-T_{c1}) also increases, which further indicates an increase in glass stability against devitrification.

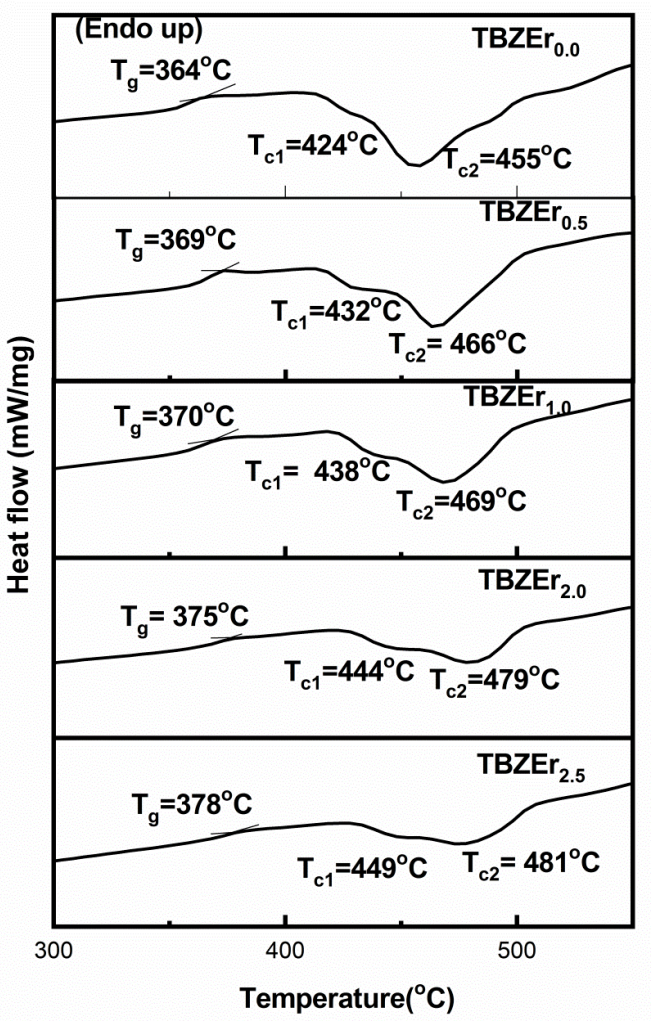

Fig. 4.2: DTA thermograph of as prepared glass samples

Table 4.2: Thermal parameters of $TBZEr_x$ glasses

Sample ID	T_g±1 (^oC)	T_{c1}±1 (^oC)	T_{c2}±1 (^oC)	$\Delta T=T_{c1}-T_g$ (^oC)
$TBZEr_{0.0}$	364	424	455	60
$TBZEr_{0.5}$	369	432	466	63
$TBZEr_{1.0}$	370	438	469	68
$TBZEr_{2.0}$	375	444	479	69
$TBZEr_{2.5}$	378	449	481	71

4.4 Structural and morphological studies

4.4.1 X-ray diffraction (XRD)

4.4.1.1 XRD of as-prepared glass samples

The X-ray diffractograms of all $TBZEr_x$ samples are shown in the **Fig. 4.3 (a)**. No bragg peaks are observed in present glasses hence confirms the amorphous nature of all as-prepared samples.

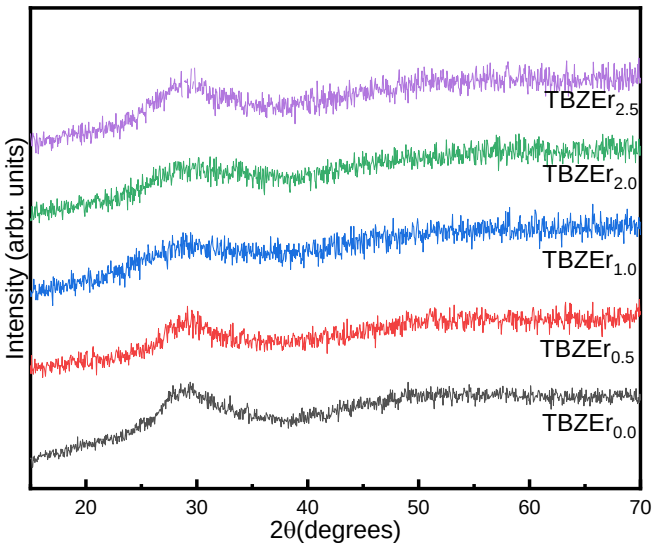

Fig. 4.3 (a): X-ray diffractograms of the as-prepared $TBZEr_x$ glasses

4.4.1.2 Optimization of time and temperature for producing glass ceramics

From the DTA studies which are presented in **Fig. 4.1**, the T_g has been observed in the range of 364 to 378 ^oC and T_{c1} in the range of 424 to 449 ^oC. In order to convert the glasses into glass ceramics $TBZEr_{0.5}$ glass is given heat treatment at 375, 400 and 450 ^oC for 2, 4 and 6 h respectively. The obtained X-ray diffractograms are given in **Fig. 4.3 (b – d)** respectively.

The XRD diffractograms of $TBZEr_{0.5}$ glass heat treated at 375 ^oC for 2, 4 and 6h respectively are shown in **Fig. 4.3 (b)**. The heat treated $TBZEr_{0.5}$ samples show background due to the presence of residual amorphous phase. It was observed that the prepared samples show some crystallization. The Bragg's peaks are observed due to the formation of α-TeO_2 (para-tellurite) phase.

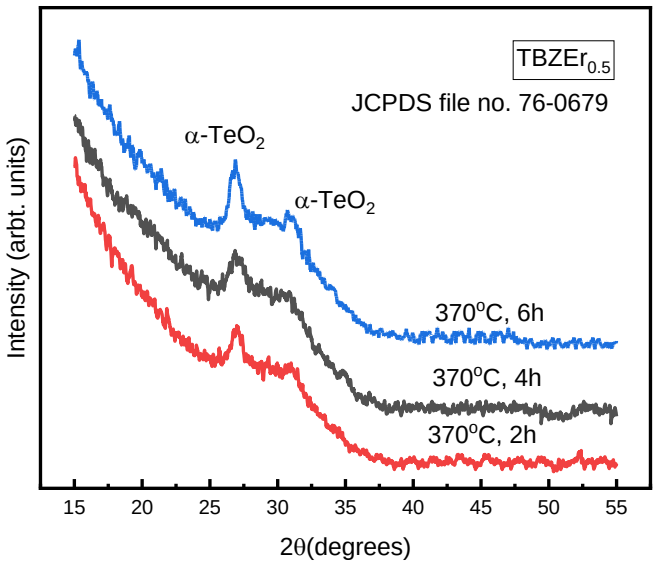

Fig. 4.3 (b): X-ray diffractograms of $TBZEr_{0.5}$ at 370 ^oC for 2, 4 and 6h

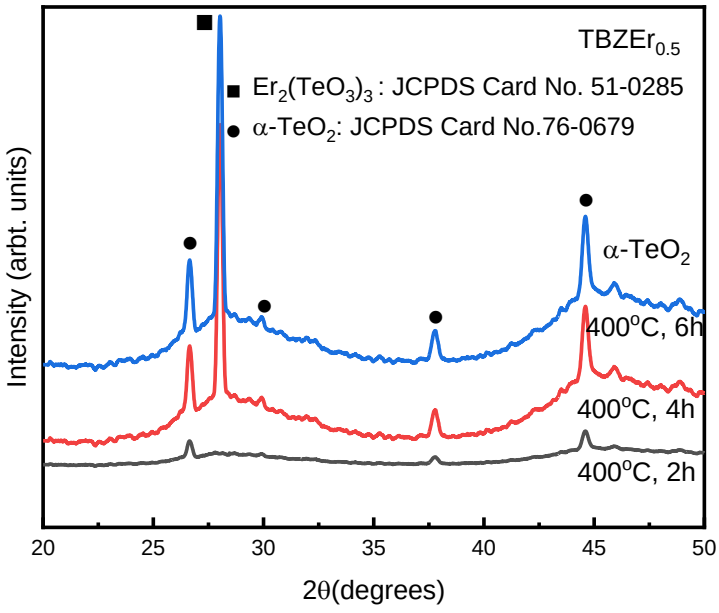

Fig. 4.3 (c): X-ray diffractograms of $TBZEr_{0.5}$ at 400 ^oC for 2, 4 and 6h

XRD diffractograms of $TBZEr_{0.5}$ samples heat treated at 400^oC for 2, 4 and 6h are shown in **Fig. 4.3(c)**. It is observed that along with α-TeO_2, another phase at 2θ = 28.14^o due to

monoclinic $Er_2(TeO_3)_3$ appears. This indicates the presence of Er^{3+}- ions has facilitated formation of $Er_2(TeO_3)_3$ phase. With an increase in time the intensity of $Er_2(TeO_3)_3$ phase also increases.

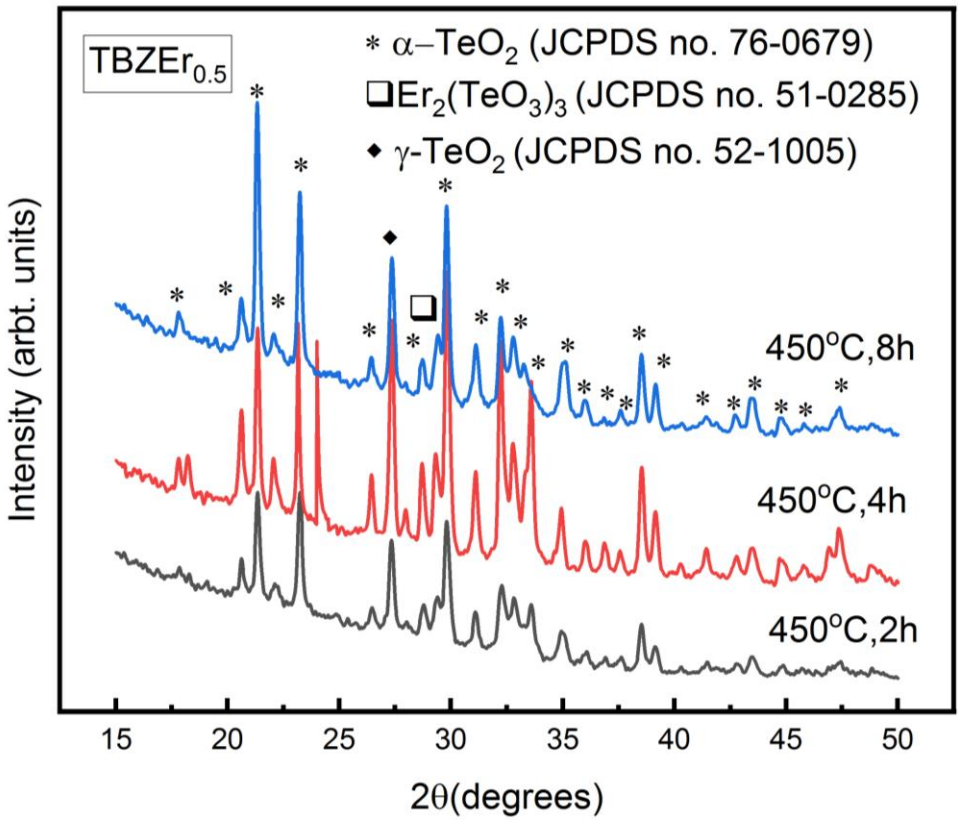

Fig. 4.3 (d): X-ray diffractograms of $TBZEr_{0.5}$ at 450 ^oC for 2, 4 and 6h

The $TBZEr_{0.5}$ glass has been further heat treated at 450 ^oC for 2, 4 and 6h. The observed XRD diffractograms of $TBZEr_{0.5}$ glass heat treated are shown in **Fig. 4.3 (d)**. From the above results, it can be seen that samples heat treated at 450 °C for 2, 4 and 6h are highly crystalline, with very small content of amorphous phase.

In the present study the focus is the radiative characteristics of the glasses and glass ceramics. To optimize the conditions for heat treatment (temperature and time) the emission spectra of all the above studied samples has been taken and shown in **Fig. 4.3 (e).** It has been observed that out of all the trials, sample heat treated at 400 ^oC for 4h has highest emission intensity. Therefore, in the order to prepare GC with crystalline phases dispersed into amorphous matrix, all the RE-doped samples are given heat treatment at 400 ^oC for 4h.

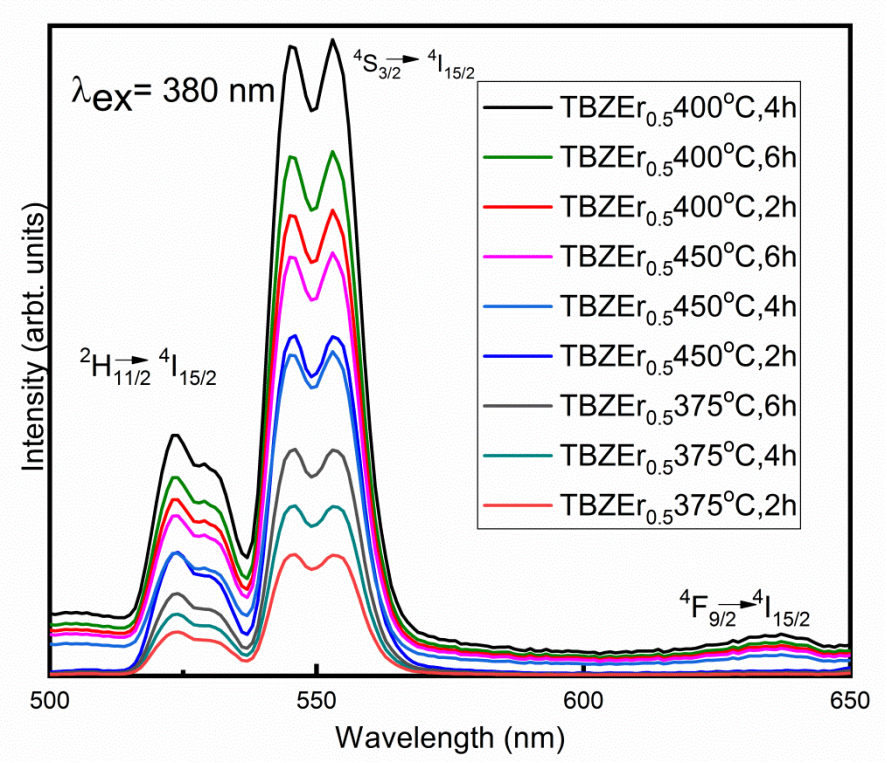

Fig. 4.3 (e): Visible emission observed in $TBZEr_{0.5}$ sample at 375, 400 and 450 ^oC for 2, 4 and 6h

4.4.1.3 Effect of heat treatment on glasses with increasing RE concentration

Fig. 4.3 (f) shows the XRD diffractograms of $TBZEr_x$ glasses after heat treatment at 400 ^oC for 4h. The JCPDS database has been referred for identifying crystalline phases of observed peaks. The primary crystalline phase formed in $TBZEr_{0.0}GC$ sample after heat treatment is α-TeO_2 (paratellurite) phase (JCPDS file no. 76-0679) with tetragonal crystal structure. Whereas, it is clear from **Fig. 4.3 (f)** that samples containing Er_2O_3 (≥ 0.5 mol%) favors the formation of monoclinic $Er_2(TeO_3)_3$ phase (JCPDS file no. 51-0285) along with α-TeO_2 phase. This is clear evidence that incorporation of erbium ions has led to formation of crystalline phases. The size of crystallites formed has been calculated with help of Debye-Scherer formula [5]. The crystallite sizes for the optimized values of time and temperature (400 ^oC, 4h) are given in **Table 4.3**. The average crystallite size in the prepared $TBZEr_xGC$ has been found to be 24 nm.

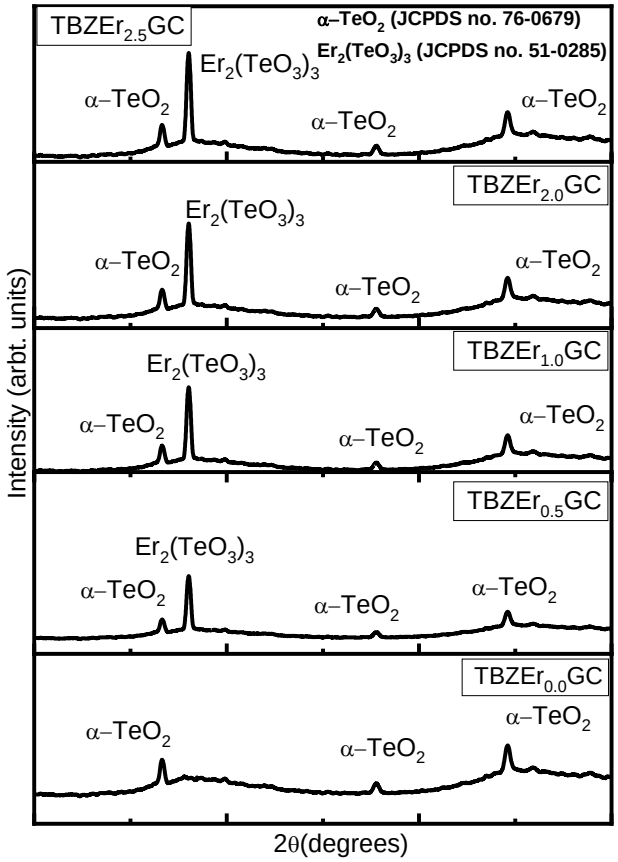

Fig. 4.3 (f) X-ray diffractograms of $TBZEr_xGC$ after heat treatment at 400 ^oC for 4h

Table 4.3: Average crystallite size (nm) ± 5 nm in glass ceramics

Sample ID	**Crystallite Size** ± 5 nm
$TBZEr_{0.0}GC$	21
$TBZEr_{0.5}GC$	25
$TBZEr_{1.0}GC$	30
$TBZEr_{2.0}GC$	34
$TBZEr_{2.5}GC$	42

4.4.2.1 Raman spectroscopy

The de-convoluted spectra of glass samples are shown in **Fig. 4.4 (a)**. The de-convoluted bands are found at around 614, 662, 716, and 764 cm^{-1}. The bands centered at approximately 716 and 764 cm^{-1} are due to TeO_{3+1} trigonal pyramid (tp) unit's symmetric bending and stretching vibrations. The said units contain non-bridging oxygens (NBOs). Other two bands centered at 614 and 662 cm^{-1} are due to TeO_4 trigonal bipyramidal (tbp)

unit's asymmetric bending and stretching vibrations. These units contain bridging oxygens (BOs) respectively [25, 26, 56]. **Fig. 4.4 (b)** shows the variation in the structural units with increasing RE- content. With increasing RE content, intensity of peaks at 614 and 662 cm^{-1} decreases w. r. t. to the peak at 716 and 764 cm^{-1} **(Fig. 4.4 (b)).** This indicates that addition of rare earth ions to TeO_2 glass results in breakage of Te-O-Te bond linkages and thus leads to systematic conversion of Q^4_4 to Q^3_4 structural groups via formation of TeO_{3+1} units [47]. Thus, there is a decrease of TeO_4 polyhedra structural units with BO and increase in TeO_4 structural units with NBOs [25].

Raman spectra of glass ceramics are shown in **Fig. 4.4 (c)**. The Raman bands get narrower due to heat treatment of the samples. The Raman bands at about 653, 614, 415 and 801 cm^{-1} are ascribed to α-TeO_2 [47]. No significant change is observed in the spectra after heat treatment with changing rare earth content.

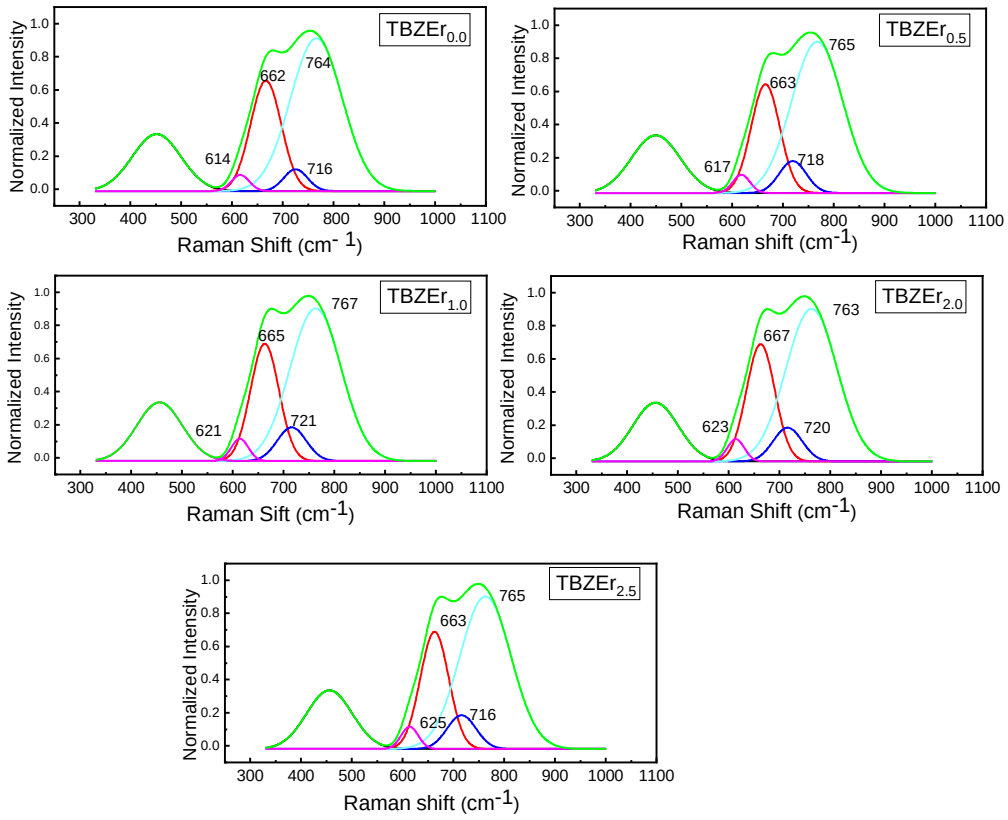

Fig. 4.4 (a): Raman spectra of Er^{3+}-doped zinc borotellurite glasses

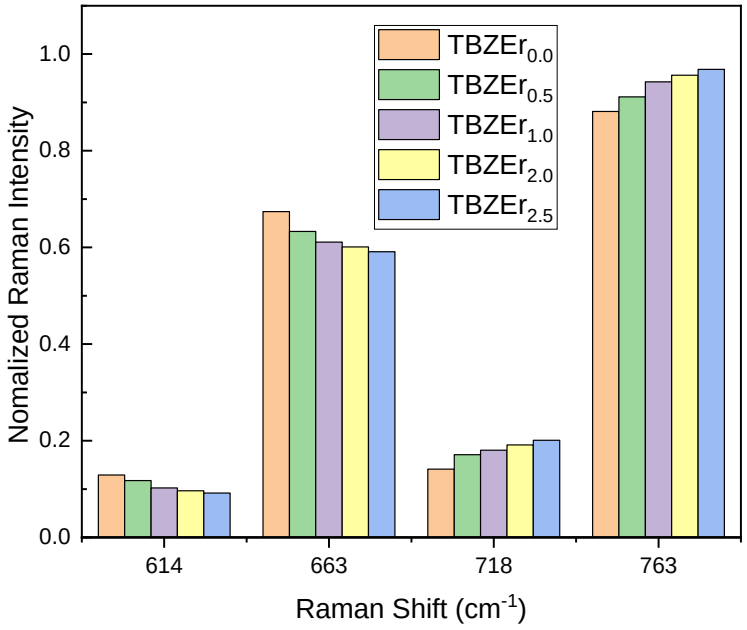

Fig. 4.4 (b): Normalized intensities of the raman bands after de-convolution at different RE- concentrations

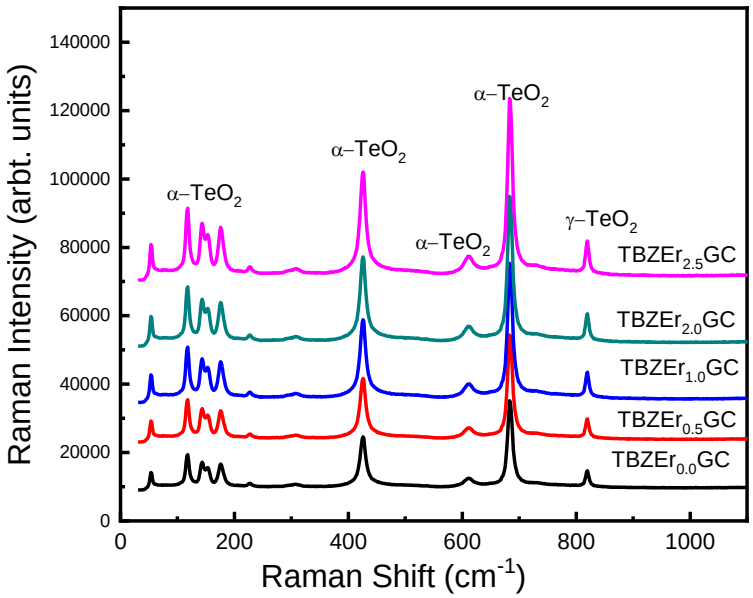

Fig. 4.4 (c): Raman spectra of glass ceramics

4.4.4.2 Fourier Transform Infrared Spectroscopy (FTIR):

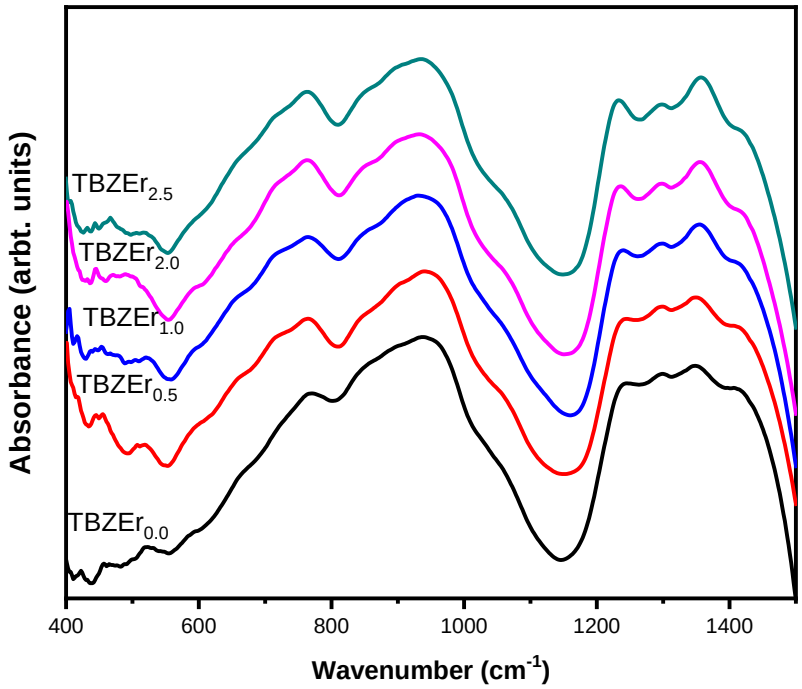

Fig.4.5 (a): Infrared Absorbance Spectra of the prepared glass system

Fig.4.5 (a) gives the FTIR spectra of Er^{3+} -doped zinc borotellurite glasses. The vibrational modes associated are divided into three distinct wavenumber regions 1500-1200 cm^{-1}, 1100-800 cm^{-1} and 800-680 cm^{-1} respectively. The vibrational bands in 800-680 cm^{-1} wavenumber are due to structural units consist of TeO_3 and TeO_4 units. The band observed at 770cm^{-1} is attributed to vibrations of tetraborate and TeO and TeO^- bonds of trigonal pyramidal TeO_3 units. The intermediate region (1100-800 cm^{-1}) is assigned to B-O stretching vibrations of BO_4 tetrahedra of pentaborate, tetraborate and diborate structural units. The higher (1500-1200 cm^{-1}) wavenumber region belongs to stretching vibrations of B-O bond in BO_3 units. Bands centered at 1350 cm^{-1} becomes prominent for high content of Er^{3+}. The structural units observed for the present glasses are tabulated in **Table 4.4.**

Table 4.4: Functional vibration groups (in cm^{-1}) of Er^{3+} doped zinc borotellurite glasses at different molar fractions

S.No.	$TBZEr_{0.0}$	$TBZEr_{0.5}$	$TBZEr_{1.0}$	$TBZEr_{2.0}$	$TBZEr_{2.5}$	Assignment of bands
1.	770 cm^{-1}	770 cm^{-1}	770cm^{-1}	770cm^{-1}	770cm^{-1}	TeO and TeO^- bonds of TeO_3 units
2.	870-1180 cm^{-1}	870-1180 cm^{-1}	870-1180 cm^{-1}	870-1180 cm^{-1}	870-1180 cm^{-1}	B-O stretching vibrations of BO_4 tetrahedra due to B-O vibrations of pentaborate, tetraborate and diborate structural units
3.	1219-1258 cm^{-1}	1219-1258 cm^{-1}	1219-1258 cm^{-1}	1219-1258 cm^{-1}	1219-1258 cm^{-1}	Stretching vibrations of BO_3 tetrahedra due to B-O involving mainly the linkage of oxygen connecting different groups.
4.	1271-1316 cm^{-1}	1271-1316 cm^{-1}	1271-1316 cm^{-1}	1271-1316 cm^{-1}	1271-1316 cm^{-1}	Assigned to stretching vibrations of the B-O of trigonal $(BO_3)^{3-}$ units in metaborated, pyroborates and orthoborates
5.	1350 cm^{-1}	1350 cm^{-1}	1350 cm^{-1}	1350 cm^{-1}	1350 cm^{-1}	Due to anti- symmetric stretching vibrations with three NBO's of B-O-B groups.

In order to understand the effect of rare earth concentration on the structural units deconvolution of the present graphs has been done. Fig. 4.5 (b) shows the variation in intensities with the increase in RE concentration. It is clear from Fig. that the addition of Er^{3+} at the cost TeO_2 leads to an increase in structural groups with NBO's. Fig. 4.5(c) represents the FTIR spectra of Er^{3+} doped zinc borotellurite glass ceramics. It is to note that after heat treatment there are significant number of changes observed in the FTIR spectra. The formation of sharper and narrower vibrational bands observed after heat treatment are due to the devrification of the glasses. Apart from this, formation of new structural units at 1218 and 1335 cm^{-1} is observed. Also, bands at 579 and 622 cm^{-1} became more prominent due to heat treatment.

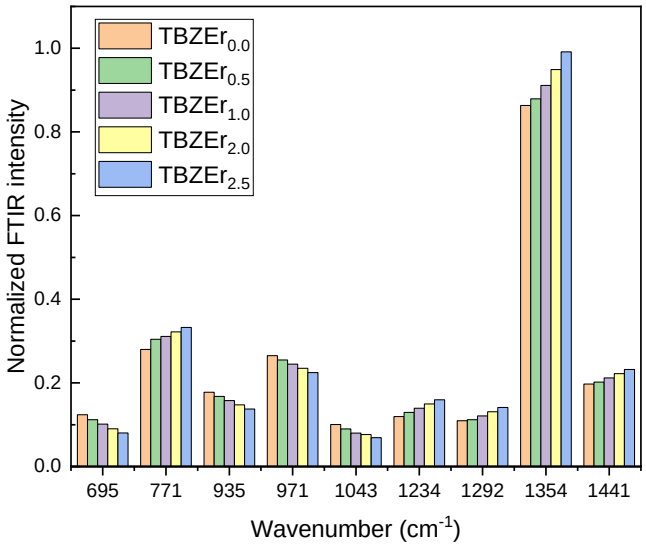

Fig. 4.5(b): Normalized FTIR intensities of the prepared glasses

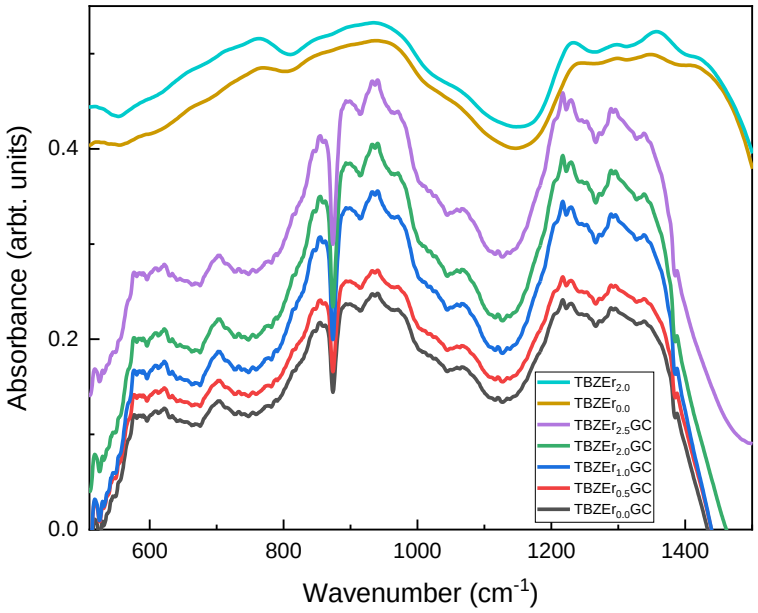

Fig. 4.5(c): Infrared absorbance spectra of the Er^{3+}-zinc borotellurite glass ceramics

4.4.3 Field emission scanning electron microscopy (FESEM):

The micrographs of glasses are given in **Fig. 4.6 (a)**. These micrographs show that the surface of the glasses is clean. There is no crystalline phase present in the matrix of glass.

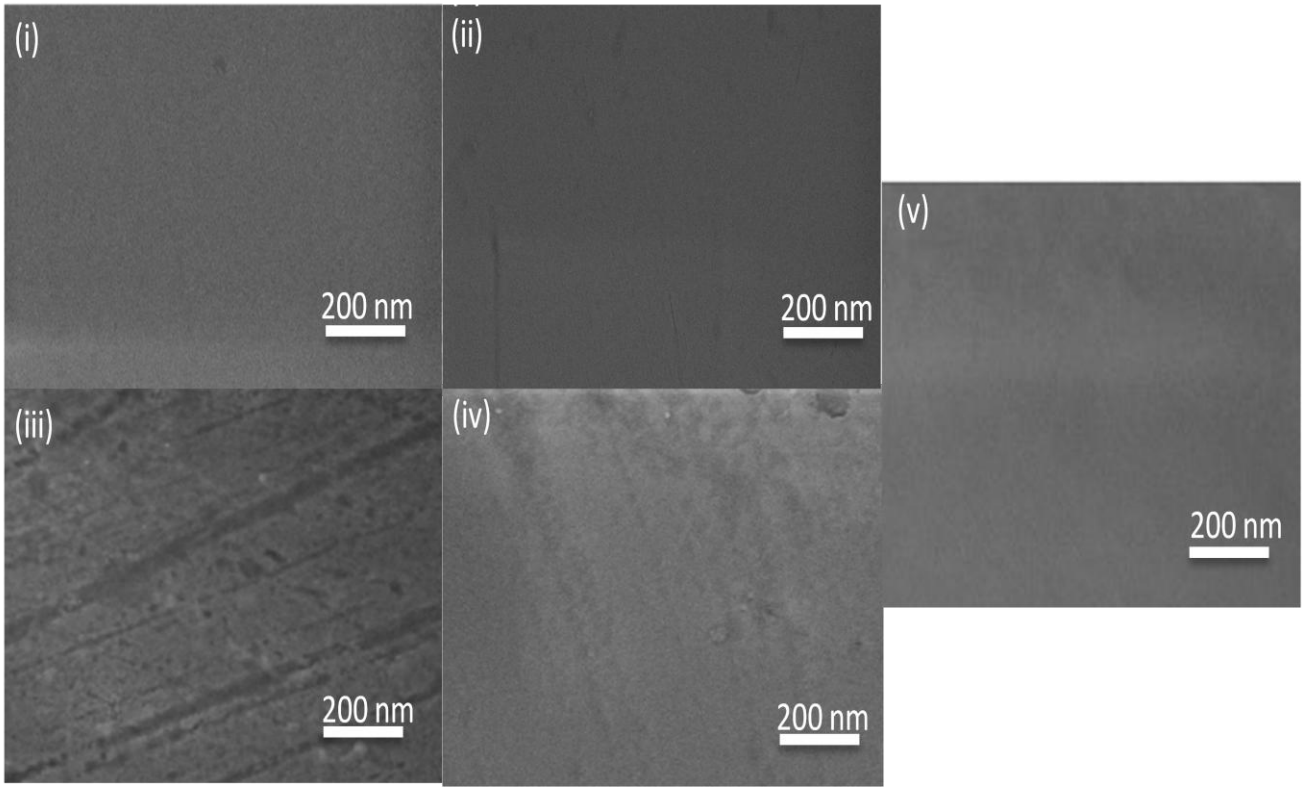

Fig. 4.6 (a): FESEM micrographs (i) $TBZEr_{0.0}$, (ii) $TBZEr_{0.5}$, (iii) $TBZEr_{1.0}$, (iv) $TBZEr_{2.0}$ and (v) $TBZEr_{2.5}$

FESEM micrographs of the glass-ceramics are given in **Fig. 4.6 (b)**. It is apparent from these micrographs that glasses have been converted to glass ceramics as crystalline phases have appeared in the matrix of glasses. These crystalline phases are uniformly distributed in the matrix of glasses. Their size is in the nano range. The uniform distribution of these nano-size precipitates will give isotropic properties of the glass-ceramics.

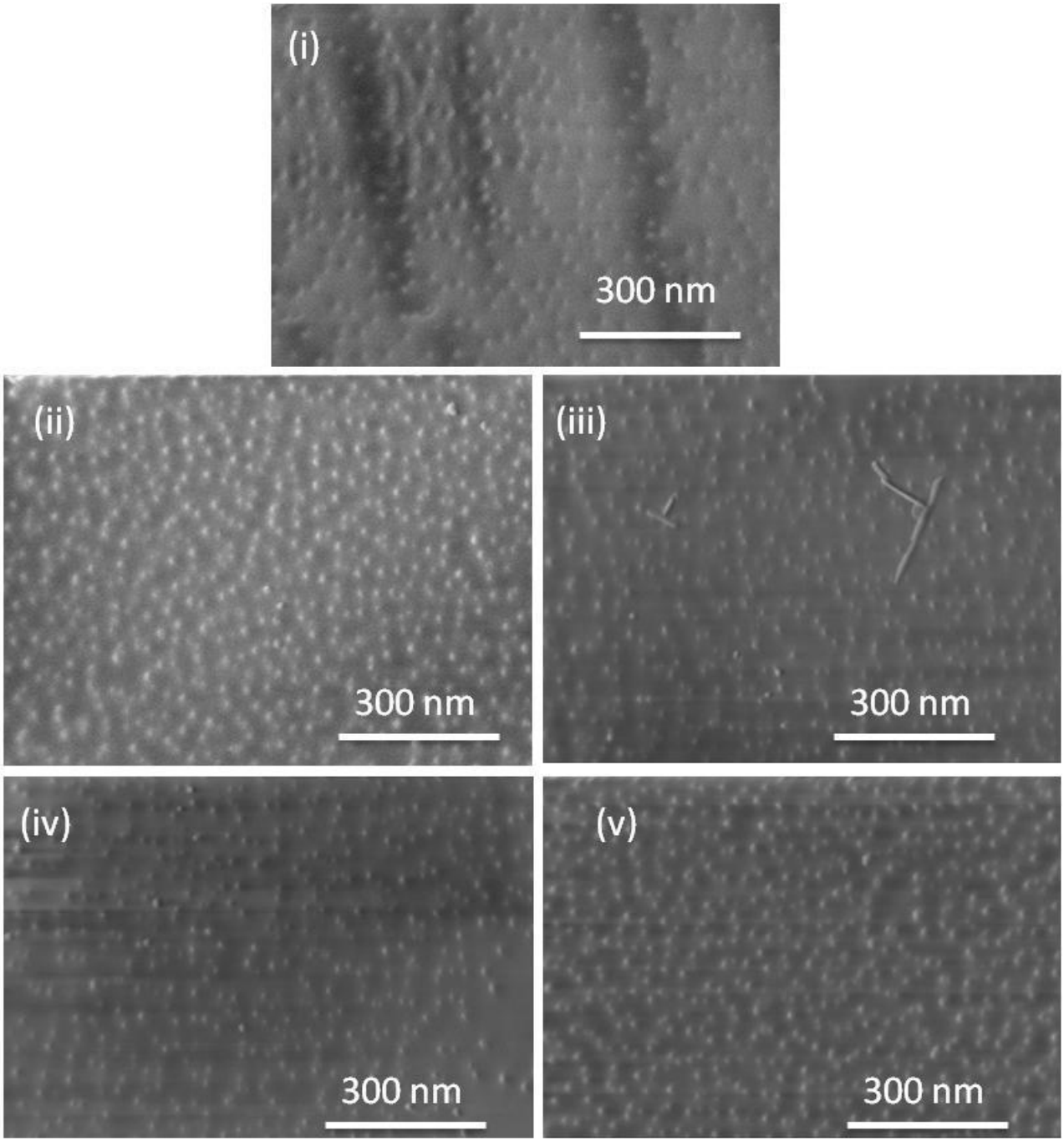

Fig. 4.6 (b): FESEM micrographs (i) $TBZEr_{0.0}GC$, (ii) $TBZEr_{0.5}GC$, (iii) $TBZEr_{1.0}GC$, (iv) $TBZEr_{2.0}$ GC and (v) $TBZEr_{2.5}GC$

The size of nano-particles is found to be in the rage of 35-40 nm. **Table 4.5** gives particle size observed for all glass ceramic samples.

Table 4.5: Particle size (nm) ±5 nm in glass ceramics

Sample ID	Particle Size
$TBZEr_{0.0}GC$	33
$TBZEr_{0.5}GC$	35
$TBZEr_{1.0}GC$	38
$TBZEr_{2.0}GC$	40
$TBZEr_{2.5}GC$	42

4.5 Absorption studies- Judd Ofelt (JO) analysis

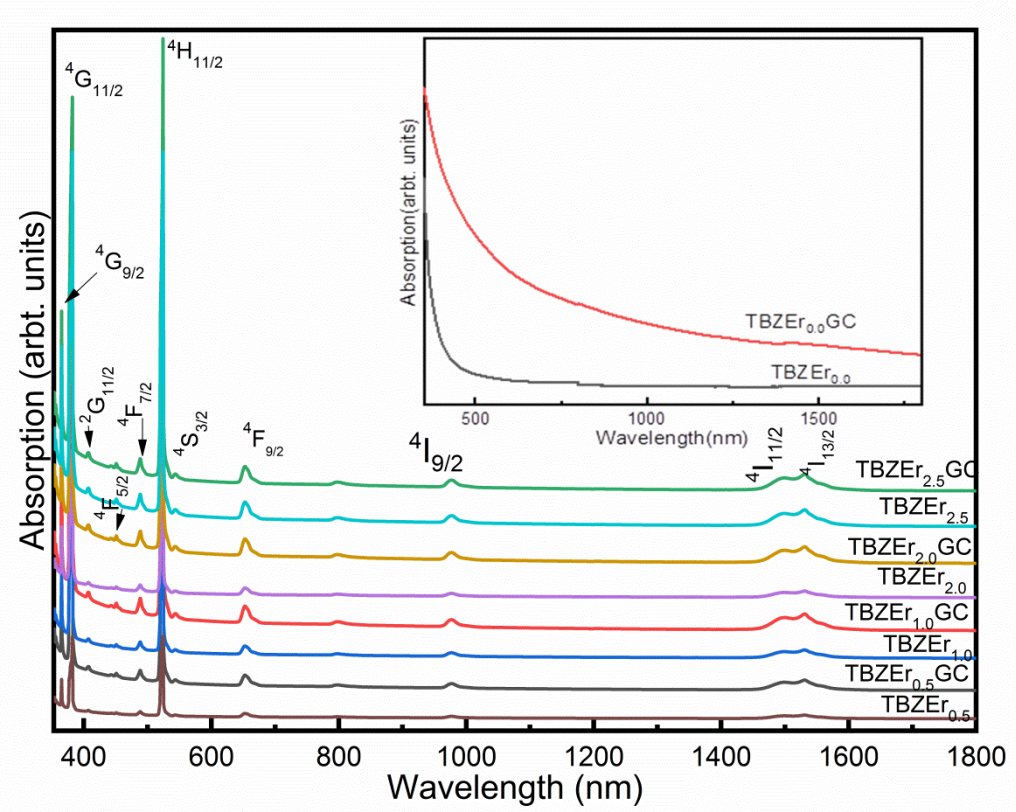

Fig. 4.7 (a): Absorption spectra of prepared samples in UV-Vis –NIR region

Fig. 4.7 (a) shows the absorption spectra of the prepared glasses and glass ceramics. It is evident from **Fig. 4.7 (a)**, there are total 11 absorption peaks observed in UV-Vis-NIR region. The absorption peaks are independent of the RE concentration but shows gradual change in the relative intensities. Absorption cross-section for the transition hypersensitive transition ($^4I_{15/2}$ to $^4H_{13/2}$) is determined according to:

$$\sigma_a(\lambda) = \frac{2.303 \times absorbance\ (\lambda)}{Nt} \qquad \textbf{(4.1)}$$

Where N is the concentration of Er^{3+} ions and 't' is the thickness (2.1±0.35 mm) of the sample. It is found that the absorption coefficient is increasing with the increase in rare earth concentration from 11.32 × 10^{-21} cm^2 ($TBZEr_{0.5}$) to 13.11 × 10^{-21} cm^2 ($TBZEr_{2.5}$). This may be due to the increase in the concentration of dopant which in turn increases the defect centers. It is also worth noting that in comparison to glasses, the absorption coefficient of nano-glass-ceramics decreases from 12.98 × 10^{-21} cm^2 ($TBZEr_{2.0}$) to 12.01 × 10^{-21} cm^2 ($TBZEr_{2.0}GC$) which in-turn is a clear indication of change in the environs of Er^{3+} ions after ceramization. The said change in environs is due to the incorporation of Er^{3+} ions in the TeO_2 crystals.

Table 4.6 gives the calculated (f_{cal}) and experimental (f_{exp}) oscillator strengths for different transitions of prepared samples. A good agreement between two said values is observed. The JO theory links the total absorbance of a transition and oscillator strength [32-34**].** It has been observed that the values of oscillator strengths increase for all transitions from glass to glass-ceramics in the UV-Vis-NIR region. It is probably due to the low-phonon energy environment formed after ceramization**.** The JO parameters of the prepared samples **(Table 4.7)** follows the trend, $\Omega_2>\Omega_4>\Omega_6$. Higher values of Ω_2 signify the high asymmetry in the surroundings of Er^{3+} ions. The Ω_2 of prepared samples is significantly higher than those of TZNE1 [3], TZNE2 [3], TZNE3 [3], PKAPbNEr 10 [35], SWNBEr [36], Er^{3+}:germanosilicate [37], germanate [38] and lower than those of Er^{3+} : $Li_2B_4O_7$ [39], Er^{3+}: CPZS [40], Er^{3+}:ZSP [41] and Er^{3+}:SFP [42] glasses. After heat treatment a decrease is observed in Ω_2 value which is due to the introduction of Ln^{3+} ions into the tellurite nanocrystals.

Table 4.6: Oscillator strengths (×10^{-6}), RMS deviation (δ_{rms}) and absorption cross-section of $TBZEr_x$ and $TBZEr_xGC$

Transition $^4I_{15/2}\rightarrow$	**$TBZEr_{0.5}$**		**$TBZEr_{1.0}$**		**$TBZEr_{2.0}$**		**$TBZEr_{2.5}$**		**$TBZEr_{0.5}GC$**		**$TBZEr_{1.0}GC$**		**$TBZEr_{2.0}GC$**		**$TBZEr_{2.5}GC$**	
	f_{cal}	f_{exp}	f_{exp}	f_{cal}	f_{cal}	f_{exp}	f_{cal}	f_{exp}	f_{cal}	f_{exp}	f_{exp}	f_{cal}	f_{exp}	f_{cal}	f_{exp}	f_{cal}
$^4I_{13/2}$	0.99	0.67	1.12	0.85	0.98	0.86	1.25	1.12	0.56	0.54	0.99	0.68	0.41	0.69	0.58	0.66
$^4I_{11/2}$	1.09	0.37	1.25	1.09	1.01	0.67	1.01	0.86	0.59	0.56	1.01	0.25	0.76	0.40	0.86	0.21
$^4I_{9/2}$	0.71	0.94	0.58	0.52	0.45	0.81	0.86	0.56	0.11	0.52	1.08	0.99	1.07	1.21	0.45	0.56
$^4F_{9/2}$	0.76	0.18	0.67	0.11	1.65	0.08	0.28	0.58	0.59	0.56	0.21	0.11	0.24	0.58	0.25	0.56

Transition $^4I_{15/2}\rightarrow$	$TBZEr_{0.5}$		$TBZEr_{1.0}$		$TBZEr_{2.0}$		$TBZEr_{2.5}$		$TBZEr_{0.5}GC$		$TBZEr_{1.0}GC$		$TBZEr_{2.0}GC$		$TBZEr_{2.5}GC$	
	f_{cal}	f_{exp}	f_{exp}	f_{cal}	f_{cal}	f_{exp}	f_{cal}	f_{exp}	f_{cal}	f_{exp}	f_{exp}	f_{cal}	f_{exp}	f_{cal}	f_{exp}	f_{cal}
$^4S_{3/2}$	0.63	0.58	0.38	0.62	1.52	1.01	0.25	0.23	0.56	0.48	0.23	0.58	0.67	0.69	0.18	0.19
$^2H_{11/2}$	0.84	0.22	0.13	0.26	0.62	0.44	0.29	0.31	0.71	0.18	0.08	0.14	0.14	0.23	0.15	0.26
$^4F_{7/2}$	4.04	3.03	4.32	3.99	4.36	4.56	2.99	3.65	6.96	5.65	4.95	4.29	5.19	5.17	3.14	4.98
$^4F_{5/2}$	4.17	4.39	3.25	3.58	4.85	4.24	4.98	4.58	5.19	4.56	4.28	3.98	5.99	5.06	5.87	5.26
$^4G_{11/2}$	11.30	11.21	10.69	10.56	11.01	11.25	10.56	10.68	10.98	10.68	10.21	10.11	10.08	10.28	10.86	10.50
$^2G_{11/2}$	1.21	1.75	1.12	1.68	1.06	1.23	1.54	1.45	1.86	1.95	1.93	1.99	1.48	2.56	1.68	1.65
$^4G_{9/2}$	3.17	3.39	2.25	2.58	3.85	3.24	3.98	3.58	4.19	3.56	3.28	2.98	4.99	4.06	4.87	4.26
δ_{rms}	0.60		0.56		0.65		0.32		0.35		0.48		0.16		0.24	
Absorption cross-section $^4I_{15/2}$ to $^4H_{13/2}$ ($\times 10^{-21}$ cm^2)	11.12± 1.21		12.45±0.98		12.01±1.24		13.05±1.98		11.32±1.99		12.87±2.12		12.98±2.22		13.11±2.37	

Table 4.7: JO intensity parameters (x 10^{-20} cm^2) and their trend

Sample ID	Ω_2	Ω_4	Ω_6	Trend
$TBZEr_{0.5}$	10.02±1.02	4.84±0.5	2.70±0.1	$\Omega_2 > \Omega_4 > \Omega_6$
$TBZEr_{1.0}$	9.20±0.99	2.74±0.5	2.55±0.2	$\Omega_2 > \Omega_4 > \Omega_6$
$TBZEr_{2.0}$	7.69±1.01	2.46±0.1	1.19±0.1	$\Omega_2 > \Omega_4 > \Omega_6$
$TBZEr_{2.5}$	6.17±0.98	4.32±0.3	3.27±0.3	$\Omega_2 > \Omega_4 > \Omega_6$
$TBZEr_{0.5}GC$	9.50±1.10	2.50±0.1	1.46±0.2	$\Omega_2 > \Omega_4 > \Omega_6$
$TBZEr_{1.0}GC$	8.60±1.01	5.83±0.3	4.82±0.2	$\Omega_2 > \Omega_4 > \Omega_6$
$TBZEr_{2.0}GC$	5.28±1.02	2.54±0.2	1.97±0.1	$\Omega_2 > \Omega_4 > \Omega_6$
$TBZEr_{2.5}GC$	4.32±0.99	4.64±0.1	2.64±0.3	$\Omega_2 > \Omega_4 > \Omega_6$

The energy gap (direct and indirect energy gap) values are determined by applying the relation proposed by Davis and Mott method [28]. The direct and indirect band gap values are given in **Table 4.8**.

Table 4.8: The optical properties of the prepared samples

Sample ID	Direct energy gap ± 0.51 (eV)	Indirect energy gap ± 0.51 (eV)	Urbach Energy ± 0.02 (eV)	Refractive index N ± 0.87
$TBZEr_{0.0}GC$	3.21	3.25	0.09	2.31
$TBZEr_{0.5}GC$	3.10	3.15	0.17	2.34

Sample ID	Direct energy gap ± 0.51 (eV)	Indirect energy gap ± 0.51 (eV)	Urbach Energy ± 0.02 (eV)	Refractive index N ± 0.87
$TBZEr_{1.0}GC$	3.09	3.08	0.18	2.41
$TBZEr_{2.0}GC$	2.79	2.90	0.21	2.44
$TBZEr_{2.5}GC$	2.22	2.59	0.35	2.58
$TBZEr_{0.0}$	3.42	3.32	0.19	2.29
$TBZEr_{0.5}$	3.28	3.24	0.20	2.32
$TBZEr_{1.0}$	3.19	3.21	0.21	2.38
$TBZEr_{2.0}$	2.89	3.18	0.36	2.42
$TBZEr_{2.5}$	2.34	2.79	0.59	2.56

Fig. 4.7 (b) and (c) gives the Tauc plots used to calculate the direct and indirect band gaps of the prepared glasses. The energy gap (direct and indirect) is observed to be in decreasing order with increase in the RE content. It may be due to the fact that concentration of Er^{3+} ion increases the number of TeO_{3+1} and BO_{3+1} units. Thus, there is reduction in average bond energy by the creation of NBOs and results in decrease of energy gap. [23,29].

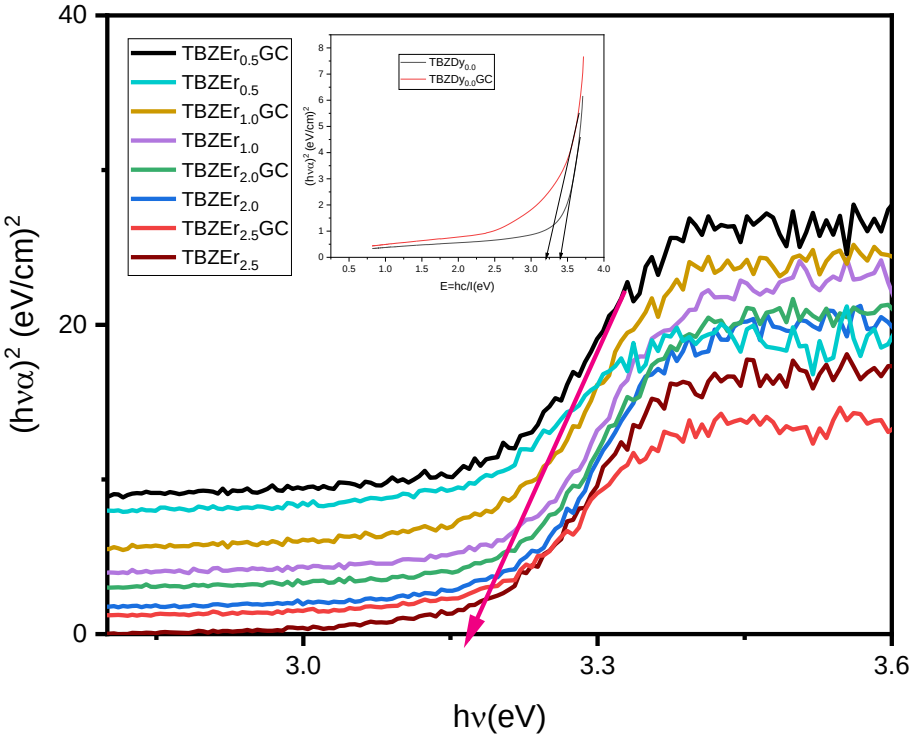

Fig. 4.7 (b) Tauc plot for direct band gap

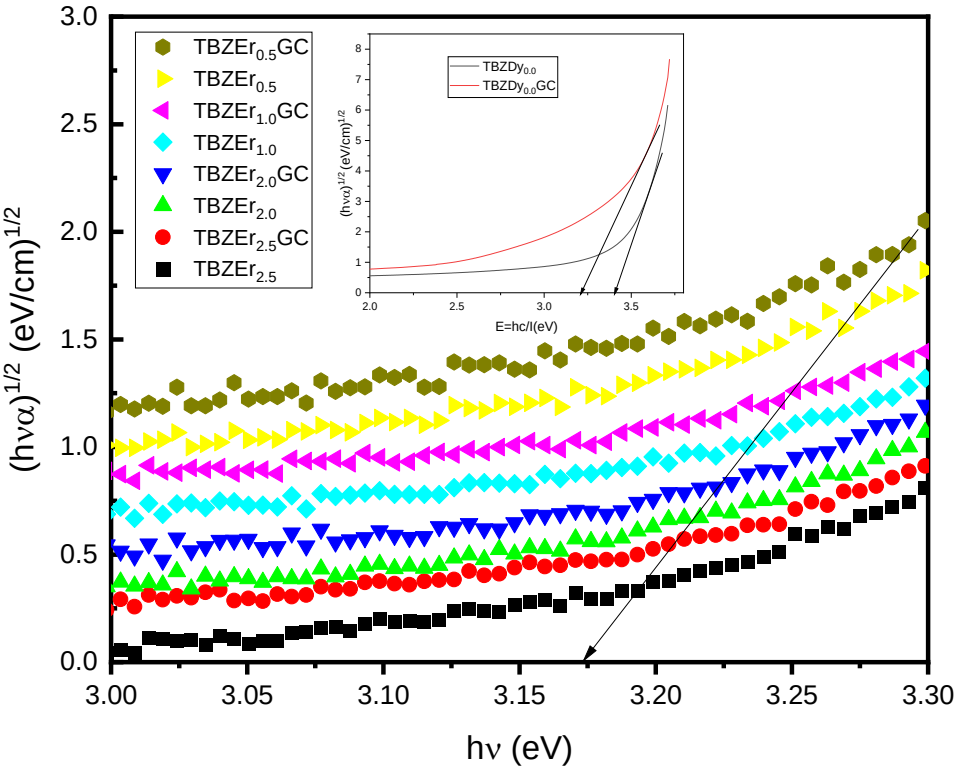

Fig. 4.7 (c) Tauc plot for indirect band gap

It is to note that the energy gap of present samples decreased after heat treatment. The decrease observed is due to the formation of new energy states in forbidden gap. The Urbach energy indicates the width of the band tails of the localized states and measures disorderness in materials. The absorption and the Urbach energy are related as following:

$$\alpha(\vartheta) = \alpha_0 e^{\frac{h\vartheta}{\Delta E}} \quad (4.2)$$

An increase in the Urbach energy is observed **(Table 4.8)** with increasing RE- content due to increase in the NBOs in the system lead to increase in the disorderedness. The decrease in the values of ΔE is observed due to the heat treatment.

4.6 Spectroscopic properties

4.6.1 Visible emssion studies

Fig. 4.8 shows excitation spectra of present glasses at 552 nm emission wavelength. Five bands are observed with bary-centers at 367, 380, 410, 457 and 488 nm [35]. The excitation intensity increases after the heat treatment. Maximum intensity has been found

for $TBZEr_{2.0}GC$. Since, the most prominent emission is observed at 380 nm hence, all the samples are excited at this wavelength for taking emission spectra.

Fig. 4.9 shows that visible emission spectrum of prepared samples in the range of 400-650 nm. The prominent green emission is observed at around 553 nm for all $TBZEr_x$ and $TBZEr_xGC$ which is assigned to transition from $^4S_{3/2}$ to $^4I_{15/2}$. It is observed that when Er^{3+} is excited with 380 nm excitation wavelength and because of this the ions go to the $^2G_{9/2}$ excited state. These excited ions then go to either $^4S_{3/2}$ or $^2H_{11/2}$ energy level via non-radiative transition [43]. Finally these ions come back to ground state by giving off green emission.

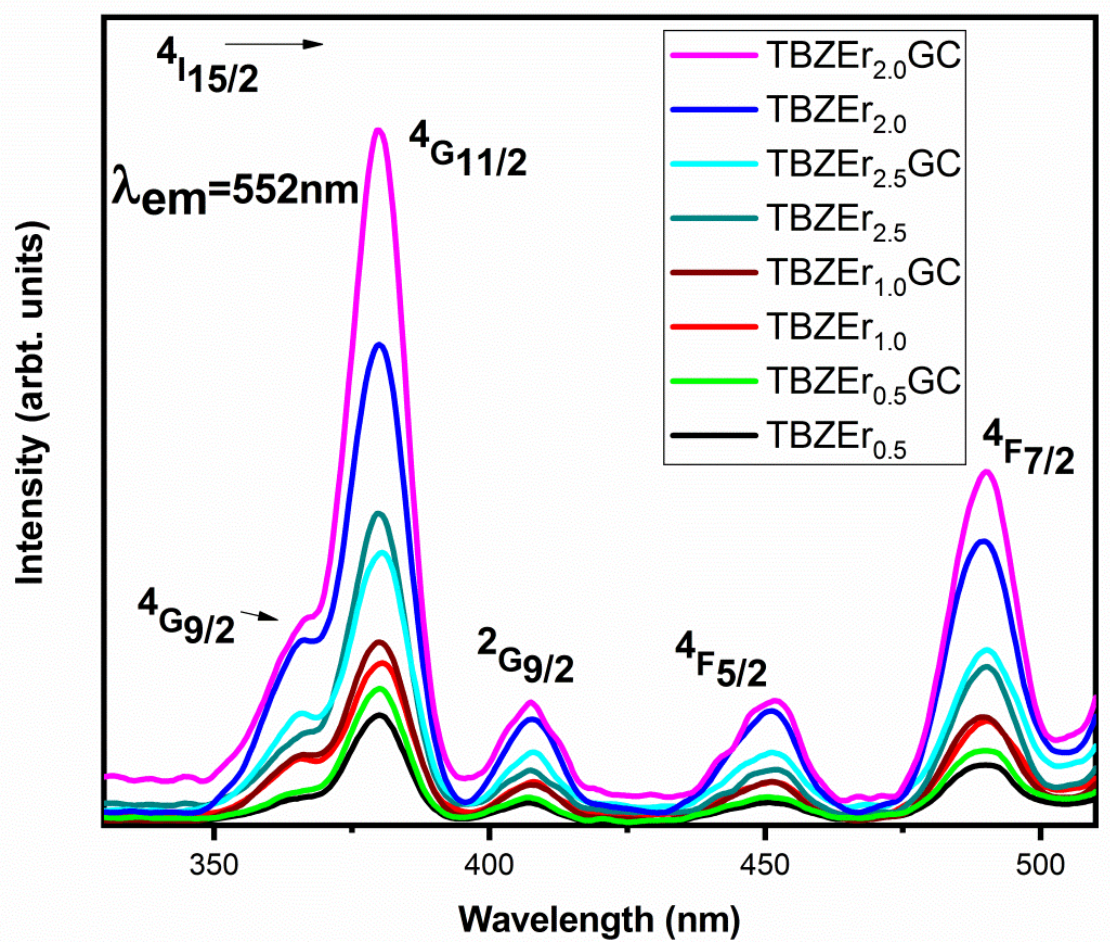

Fig. 4.8: Excitation spectra of $TBZEr_x$ glasses (λ_{em}=552 nm)

The appearance of two green peaks **(Fig. 4.9)** gives the evidence of thermal pairing between the levels ($^4S_{3/2}$ and $^2H_{11/2}$). Due to the less energy gap between these levels,

thermal disturbance rises the population of the $^2H_{11/2}$ level leading to appearance of a band at 528 nm. A weaker red band due to $^4F_{9/2} \rightarrow {}^4I_{15/2}$ is also found in the range of 623 nm – 648 nm. The emission intensity increases with increase in RE upto 2.0 mol %. Then decreases with further increase of RE (2.5 mol%) due to concentration quenching. It is worth noting that the PL intensity of glass ceramics is more than that of corresponding glasses. This is due to the decrease in the phonon energy with heat treatment as the Er^{3+} ions enter into the crystalline phases. This in turn decreases the non-radiative energy transfer and hence leads to increase in emission intensity. These results are in accordance with XRD results **(Fig. 4.3 (f))**.

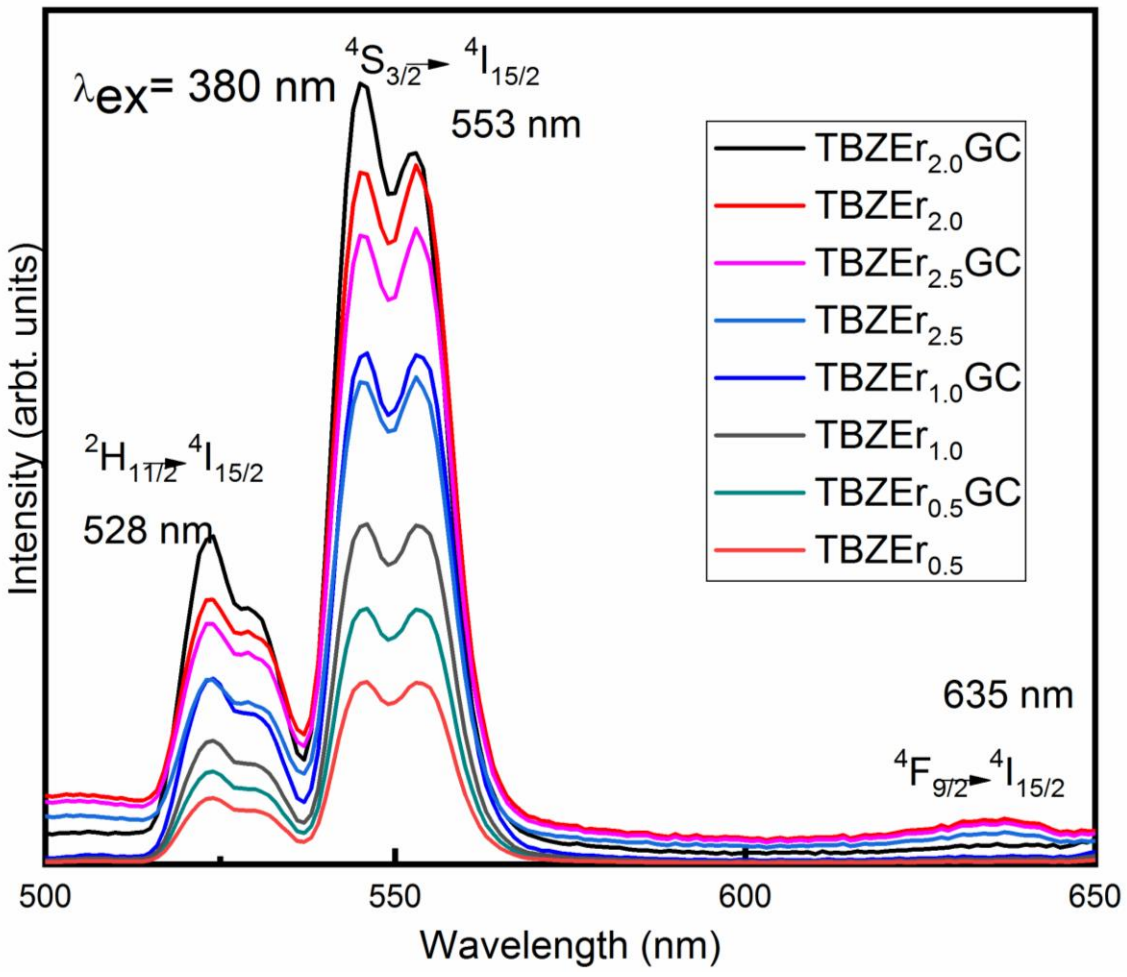

Fig. 4.9: Visible emission spectra (λ_{ex}=380 nm) of $TBZEr_x$ and $TBZEr_xGC$

The green emission of the samples is analyzed in terms of CIE chromaticity color coordinates. Fig. 4.9 shows the CIE 1931 chromaticity diagram for prepared samples. The said values are given in **Table 4.9**.

Table 4.9: CIE 1931 co-ordinates (x,y) of $TBZEr_x$ and $TBZEr_xGC$ (λ_{ex}=380 nm)

Concentration of Er^{3+} (mol%)	**(x,y) of $TBZEr_x$**	**(x,y) of $TBZEr_xGC$**
0.5	(0.331,0.580)	(0.335,0.551)
1.0	(0.341,0.578)	(0.332,0.533)
2.0	(0.340,0.581)	(0.325, 0.550)
2.5	(0.351,0.611)	(0.323,0.552)

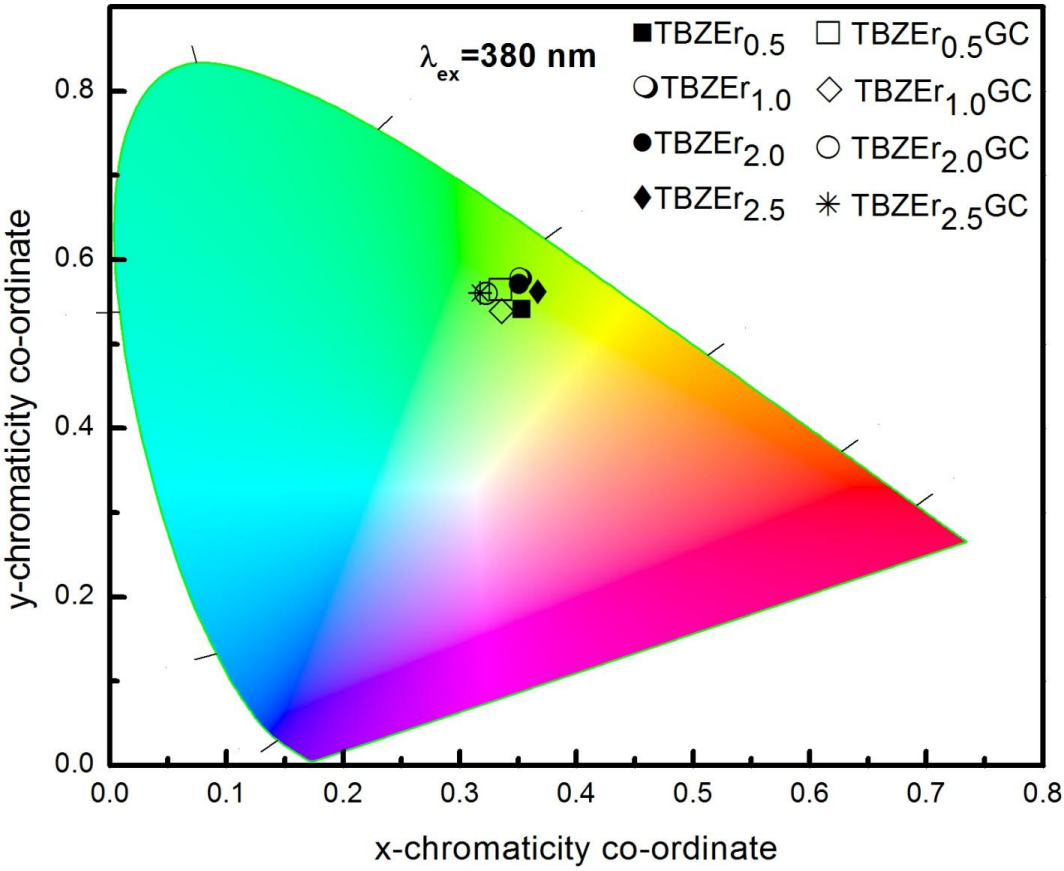

Fig. 4.10: CIE 1931 chromaticity diagram for $TBZEr_x$ and $TBZEr_xGC$, under 380 nm excitation

It is clear from **Table 4.8** that the prepared samples have chromaticity co-ordinates in the green region. Hence, the prepared samples can be used as green light emitting diodes in the display applications.

4.6.2 NIR emission studies

The NIR spectra of prepared samples are shown in **Fig. 4.11**. Er^{3+} ions in $^4I_{15/2}$ level goes into $^4I_{11/2}$ energy state when excited with 980 nm excitation wavelength. The excited Er^{3+}-ions then decays to $^4I_{13/2}$ level giving NIR emission at 1543 nm. It is worth noting that the PL intensity of glass ceramics is more than that of corresponding glasses. This is again due to the decrease in the phonon energy with heat treatment. The broadening of the NIR emission band is also observed which may be due to the local crystal-field generated in higher Er^{3+} concentration samples. It is found that the NIR emission intensity increases with increasing RE upto 2 mol% and then decreases for 2.5 mol% due to concentration quenching.

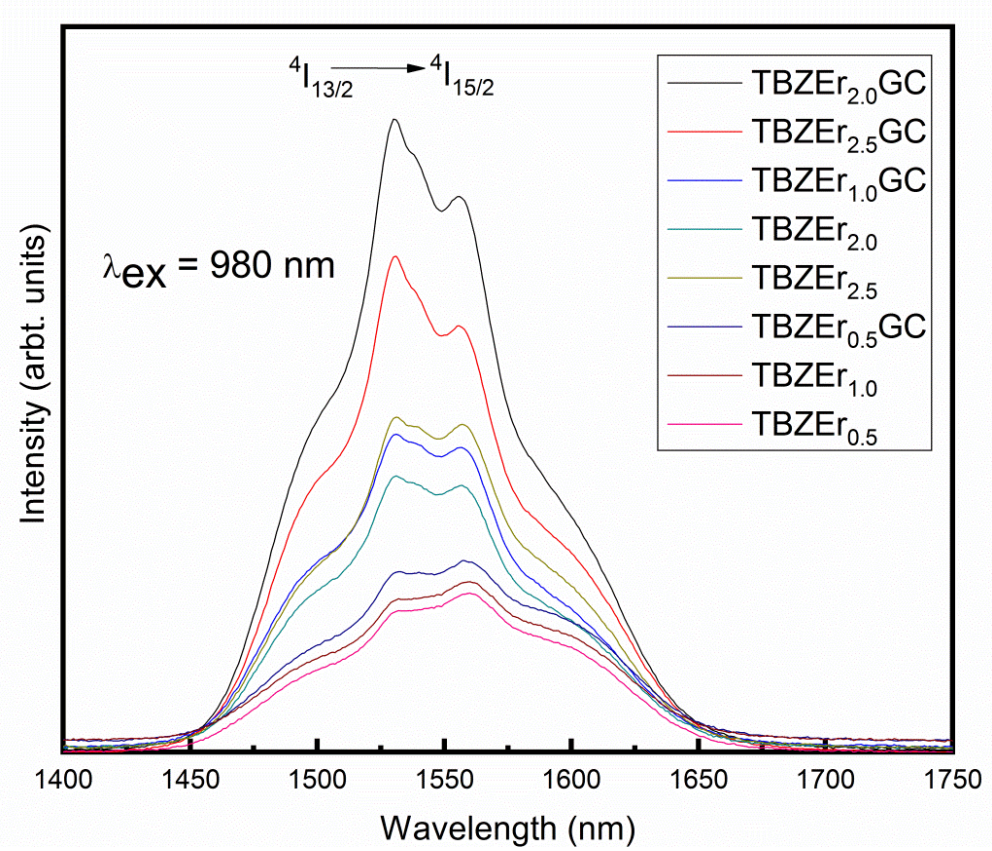

Fig. 4.11: NIR emission spectra of $TBZEr_x$ and $TBZEr_xGC$ (λ_{ex}=980 nm)

4.6.3 Radiative properties

Parameters like effective bandwidth ($\Delta\lambda_{eff}$) [32,45], lifetime (τ_{exp}) [32] and emission cross-section ($\sigma_{emi}(\lambda)$) [32,46,47] are calculated for the levels $^4S_{3/2}$ and $^4I_{13/2}$ **(Table 4.9)**. The branching ratio (β_{exp}) [32] for these levels is found to be $\beta_{exp} \geq 50\%$. It is observed from

Table 4.10 that there is an improvement in bandwidth with an increase in RE-concentration in prepared samples. It is due to the multiple interactions between the RE-ions, which enhances the Stark splitting between the energy levels of Er^{3+} ion. The large values of bandwidth observed for the prepared samples are favorable for wavelength division multiplexing [48]. Low quantum efficiencies observed for the $^4S_{3/2}$ level are due to less energy gap between $^4S_{3/2}$ and $^2H_{11/2}$ electronic energy states. Because of this there is loss of excited ions from $^4S_{3/2}$ state to lower energy states ($^2H_{11/2}$ and $^4F_{9/2}$) due to thermalization effect and multi-phonon relaxation.

The stimulated emission cross-section is calculated for $^4S_{3/2}\rightarrow{}^4I_{15/2}$ transition with the help of Füchtbauer-Ladenburg (FL) theory [47]. From **Table 4.9,** it can be seen that values of $\sigma_{emi}(\lambda)$ are more for TBZEr$_x$GC than TBZEr$_x$ samples. The increase in $\sigma_{emi}(\lambda)$ after heat treatment indicates that there is an increase in effective area of emission for $^4S_{3/2}\rightarrow{}^4I_{15/2}$ transition. It is also found that the studied systems have higher $\sigma_{emi}(\lambda)$ values than that of the Er^{3+}-doped TZNE1 (6.89×10^{-21}cm^2) [3] and PKSAEr10 (6.03×10^{-21} cm^2) [35] glasses for transition $^4S_{3/2}\rightarrow{}^4I_{15/2}$. Hence, the prepared samples can be considered as an active medium to achieve good lasing action in green region.

To estimate the emission cross-section of $^4I_{13/2}\rightarrow{}^4I_{15/2}$ the McCumber (MC) theory [46] and the Füchtbauer-Ladenburg (FL) theory [47] are applied. The emission cross-section derived from the FL theory ($\sigma_{FL}(\lambda)$) and MC theory ($\sigma_{MC}(\lambda)$) are maximum for TZEr$_{2.0}$GC, and are found to be 8.74×10^{-21} cm^2 and 7.49×10^{-21} cm^2, respectively. A difference in the two values ($\sigma_{FL}(\lambda)$ and $\sigma_{MC}(\lambda)$) is observed due to the re-absorption [35]. This is because of the spectral overlap of the emission and absorption bands of Er^{3+} ion **(Fig. 4.12)**. The $\sigma_{MC}(\lambda)$ is found to be 7.49×10^{-21} cm^2 at 1543 nm which is more than the absorption cross-section (6.89×10^{-21} cm^2) at 1543 nm.

It is known that the large $\sigma_{emi}(\lambda)$ gives low threshold and in turn high gain operation. From $\sigma_{abs}(\lambda)$ and $\sigma_{emi}(\lambda)$ values, the room temperature gain coefficient is studied [48].

Table 4.10: Effective bandwidth ($\Delta\lambda_{eff}$, nm), spontaneous emission probability (A, s^{-1}), experimental (β_{exp}, %) and calculated branching ratios (β_{cal}, %), emission cross-section ($\sigma_{FL}(\lambda)$, x 10^{-21} cm^2) and MC theory ($\sigma_{MC}\lambda(p)$, x 10^{-21} cm^2), radiative (τ_{rad}, ms) and experimental (τ_{exp}, ms) lifetime and quantum efficiency (η,%) of $TBZEr_x$ and $TBZEr_xGC$

Radiative parameters		$TBZEr_{0.5}$	$TBZEr_{1.0}$	$TBZEr_{2.0}$	$TBZEr_{2.5}$	$TBZEr_{0.5}$ GC	$TBZEr_{1.0}$ GC	$TBZEr_{2.0}$ GC	$TBZEr_{2.5}$ GC
$^4S_{3/2}\rightarrow{}^4I_{15/2}$	$\Delta\lambda_{eff}$ ± 4.21	13.82	15.51	17.38	18.33	12.30	15.64	16.91	17.93
	A ± 12	570	421	320	264	492	372	264	154
	β_{exp} ± 7	64	67	60	77	68	70	63	62
	β_{cal} ± 7	61	65	75	80	76	65	69	64
	$\sigma_{FL}(\lambda)$ ± 2.12	7.64	8.03	8.91	9.04	7.71	8.48	9.14	9.84
	τ_{exp} ± 0.21	0.56	0.46	0.39	0.12	0.77	0.53	0.45	0.25
	τ_{rad} ± 0.14	1.85	1.56	1.23	0.95	2.56	2.01	1.59	1.26
	η ± 4	30	25	21	19	39	35	29	20
$^4I_{13/2}\rightarrow{}^4I_{15/2}$	$\Delta\lambda_{eff}$ ± 4.21	8.58	10.25	11.54	12.36	9.35	12.55	14.16	15.86
	A ± 12	670	510	430	360	590	475	386	264
	β_{exp} ± 7	73	80	75	76	79	70	89	75
	β_{cal} ± 7	70	81	70	71	81	75	85	72
	$\sigma_{MC}(\lambda_p)$ ± 3.14	6.01	6.93	7.59	8.54	6.91	7.11	7.99	8.41
	$\sigma_{FL}(\lambda)$ ± 2.12	7.25	7.68	7.74	7.98	7.94	8.14	8.74	8.94
	τ_{exp} ± 0.21	0.48	0.39	0.26	0.10	0.56	0.50	0.42	0.13
	τ_{rad} ± 0.14	1.92	1.85	1.36	0.83	1.60	1.48	1.37	0.92
	η ± 4	70	65	60	55	75	72	69	61

Fig. 4.13 shows the gain cross-section spectra for $TBZEr_{2.0}GC$ with various population inversion rates. It is to noted that the gain coefficient becomes positive when 'p' becomes more than 0.4 which indicates that a low threshold is required for 1.54 μm laser operation in the prepared samples. It is clear from **Fig. 4.13** that the present samples have gain band-width in the range of 1450-1650 nm. It contains C (1530-1565 nm) and L (1565-1625 nm) communication bands. Hence a wide communication range of 1530-1650 nm is expected from the present samples whenever the population inversion is ≥ 40%.

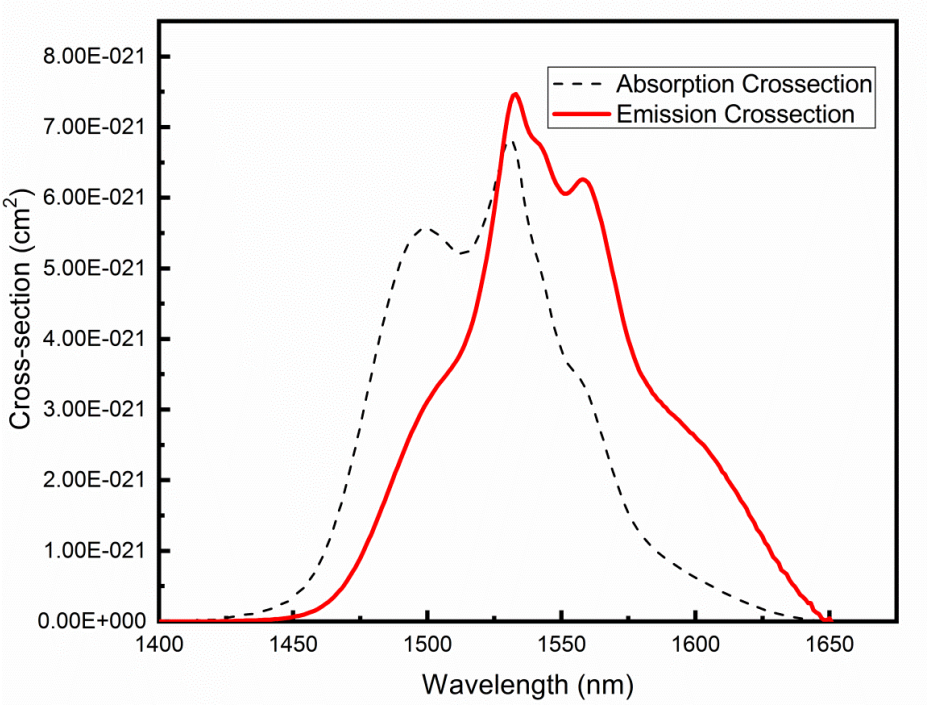

Fig. 4.12: The absorption and emission cross-section spectra of $TZEr_{2.0}GC$ for transition $^4I_{13/2}$ to $^4I_{15/2}$ of Er^{3+} ion

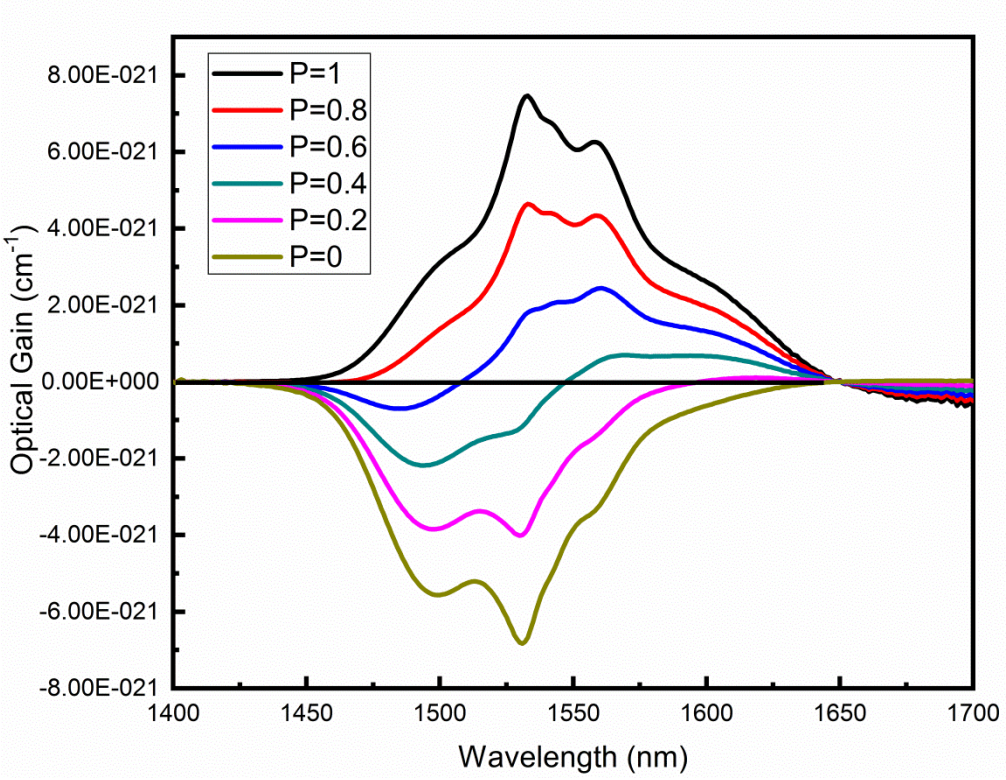

Fig. 4.13: The gain coefficient for transition $^4I_{13/2}$ to $^4I_{15/2}$ of Er^{3+} doped $TBZEr_{2.0}$ GC. Here, 'P' is the population inversion rate.

4.6.4 Decay curves

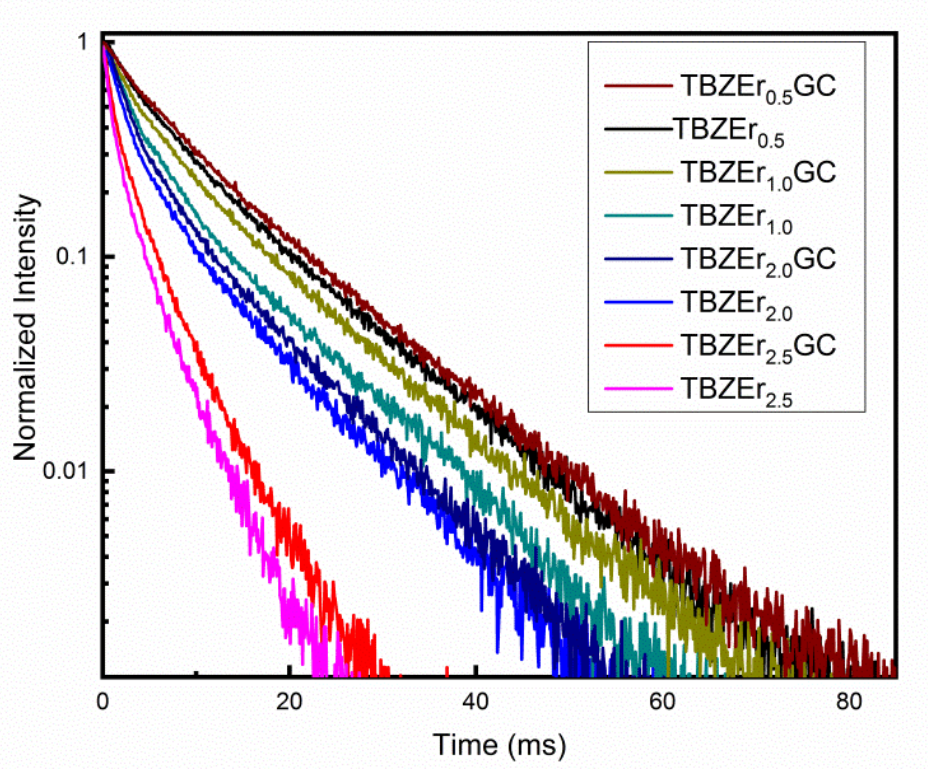

Fig. 4.14: Decay curve for the $^4S_{3/2}$ level in $TBZEr_x$ and $TBZEr_xGC$ samples

Fig. 4.14 shows the decay curves for the $^4S_{3/2}$ level obtained at emission wavelength of 553 nm and excitation wavelength of 380 nm. An increase in the non-exponential behavior is seen with increasing RE concentration. It clearly indicates the energy transfer between Er^{3+}-Er^{3+} ions is increasing thus decreasing the experimental lifetime.

It is to note that for the same RE concentration, an increase in the lifetime values are observed from the amorphous to crystalline state. This trend can be due to the decrease in non-radiative decay after the heat treatment of present glasses. The obtained lifetime curves for the $^4I_{13/2}$ state of Er^{3+} ions in $TBZEr_x$ and $TBZEr_xGC$ are shown in **Fig. 4.15**. It has been again observed that the lifetime of the $^4I_{13/2}$ level decreases with an increase in Er_2O_3 concentration. When RE (Er^{3+}) ion goes to $^4I_{15/2}$ (ground state) from $^4I_{13/2}$ (excited state), the energy radiated by this ion is transferred to another RE ion in the ground state which further goes to excited state [48]. This keeps on going until one Er^{3+} ion finally loses its energy to the quenching trap present in its close proximity [48].

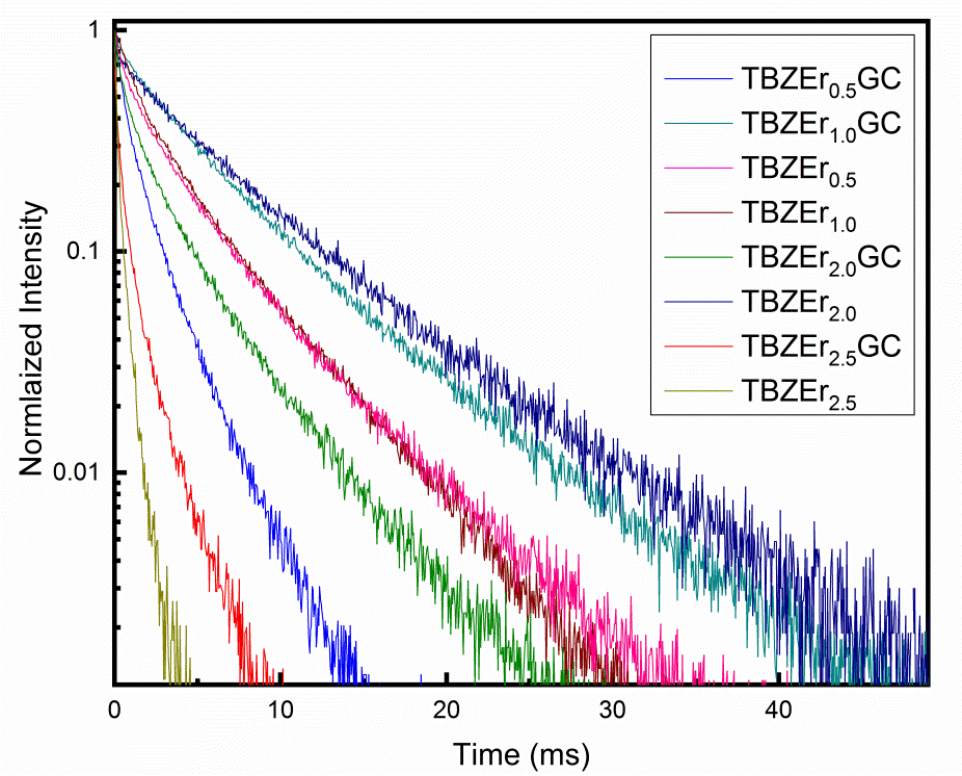

Fig. 4.15: Decay curve for the metastable state $^4I_{13/2}$ in $TBZEr_x$ and $TBZEr_xGC$

An increase in the lifetime values are observed after heat treatment. It indicates the presence of Er^{3+} ions in the nano-crystals due to which the chances of non-radiative transitions decreases which in-turn increases the lifetime [3]. The decrease in the non-radiative transitions occurs because of the expulsion of hydroxyl groups from the nano-crystals that are formed after heat treatment of glass and gives low phonon energy environment to Er^{3+} ions.

4.6.5 Up- conversion luminescence

The room temperature UC spectrum of prepared samples is presented in **Fig. 4.16**. The UC spectrum consists of three emission bands [49-51]. The partial energy diagram of Er^{3+} is given in **Fig. 4.17**. The basic UC mechanism in prepared samples can be understood as follows:

Step 1: With 980 nm near-infrared (NIR) excitation, the Er^{3+} ions present in the ground state ($^4I_{15/2}$) goes to the excited state ($^4I_{11/2}$) through ground state absorption (GSA).

Step 2: The electrons gets excited to higher excited state ($^4F_{7/2}$) by absorbing a photon via excited state absorption (ESA) or by energy transfer up-conversion (ETU).

After this the excited electrons can relax through two possible ways as described in **Step 3**:

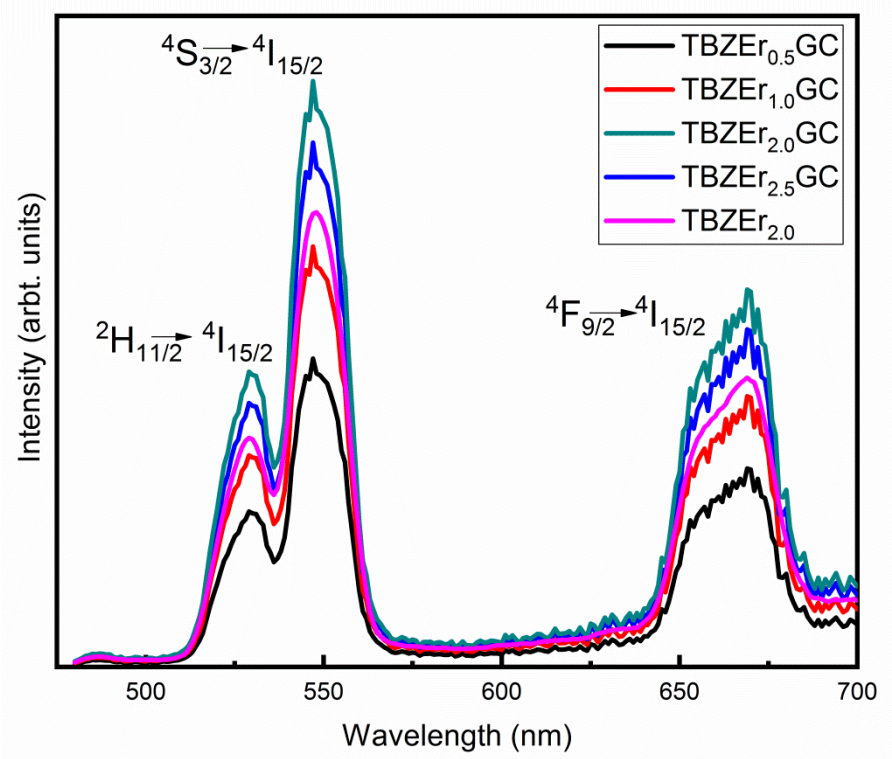

Fig. 4.16: Up-conversion spectra of Er^{3+}: $TBZEr_{2.0}$ and $TBZEr_xGC$ under 980 nm excitation

Step 3: As the Er^{3+} ions are unstable in the excited state ($^4F_{7/2}$), excited ions decay rapidly to the $^4S_{3/2}$ or $^2H_{11/2}$ levels and eventually goes back to the ground state ($^4I_{15/2}$) via $^2H_{11/2}$/$^4S_{3/2}$ to $^4I_{15/2}$ transitions, giving green emission.

Or

Step 3: The excited electrons in $^4F_{7/2}$ level relax rapidly to $^4F_{9/2}$ level by multi-phonon relaxation followed by the $^4F_{9/2}$ to $^4I_{15/2}$ transition, giving red luminescence.

It is clear from the **Fig. 4.16** that a significant increase in the UC intensity of $TBZEr_xGC$ glass ceramics takes place. It is due to decrease in energy transfer between the two neighboring RE ions which in turn is due to low phonon energy of the crystallites.

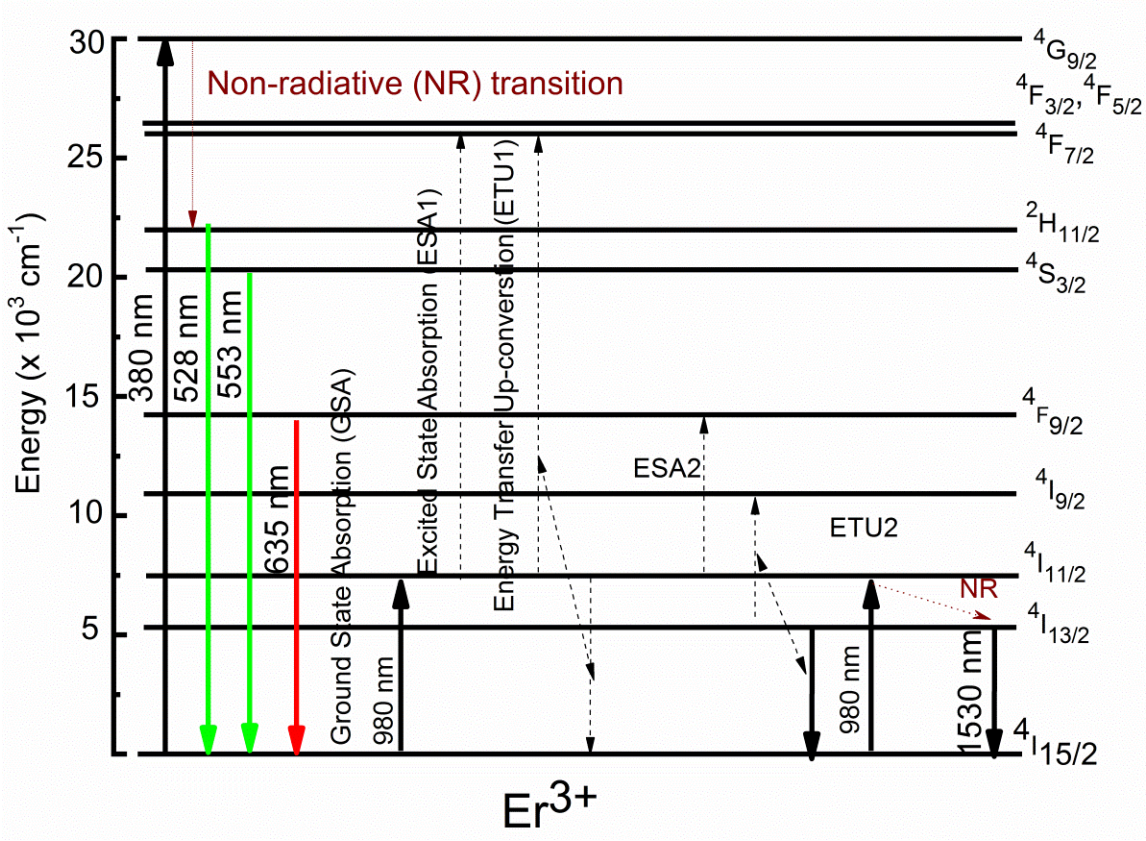

Fig.4.17: Possible partial energy level diagram for the prepared samples at excitation of 380 nm and 980 nm

References

1. K. Linganna, M. Rathaiah, N.Vijaya, Ch. Basavapoornima, C.K. Jayasankar, S. Ju, W.T. Han, V. Venkatramu, Ceram. Int., 41 (2015) 5765-5771.

2. Z. Pan, A. Ueda, R. Mu, S.H. Morgan, J. Lumin., 126 (2007) 251-256.

3. I. Jlassi, H.Elhouichet, S.Hraiech, M.Ferid, J. Lumin., 132 (2012) 832-840.

4. S. Marjanovic, J. Toulouse, H. Jain, C. Sandmann, V. Dierolf, A.R. Kortan, N. Kopylov, R.G. Ahrens, J. Non-Cryst. Solids, 322 (2003) 311-318.

5. D. Chen, Y. Wang, Y. Yu, E. Ma, F. Bao, Z.Hu, Y.Cheng, Mater. Chem. Phys., 95 (2006) 264-269.

6. P.H. González, I.R. Martín, L.L. Martín, S.F.L .Luis, C.P. Rodríguez, V. Lavín, Opt. Mater., 33 (2011) 742-745.

7. E. A. Ferreira, F.C. Cassanjes, G. Poirier, Opt. Mater., 35 (2013) 1141-1145.

8. E. Culea, I.V. Simiti, G. Borodi, E. N. Culea, R. Stefan, P. Pascuta, Ceram. Int., 40(2014) 11001-1007.

9. S. Xu, D. Fang, Z. Zhang, Z. Jiang, J. Solid State Chem., 178 (2005) 2159-2162.

10. R. J. Amjad, M.R. Sahar, S. K. Ghoshal, M.R. Dousti, S.Riaz, B.A.Tahir, J. Lumin., 132 (2012) 2714-2718.

11. S.K. Singh, N.K. Giri, D.K. Rai, S.B. Rai, Solid State Sci., 12 (2010) 1480-1483.

12. A. Jha, P. Joshi, S. Shen, Opt. Express, 16 (2008) 13526-13533.

13. H. Lin, S. Jiang, J. Wu, F.Song, N. Peyghambarian, E.Y.B. Pun, J. Phys. D: Appl. Phys., 36 (2003) 812-817.

14. V. K. Tikhomirov, D. Furniss, A. B. Seddon, J. Mater. Sci. Lett., 21(2002) 293-295.

15. Y. Guo, G. Gao, M. Li, L. Hu, J. Zhang, Mater. Lett., 80 (2012) 56-58.

16. F. Yang, C. Liu, D. Wei, Y. Chen, J. Lu, S.Yang, Opt. Mater., 36 (2014) 1040-1043.

17. S. K. Ahmmad, M.A. Samee, A. Edukondalu, S. Rahman, Results Phys., 2 (2012)175-181.

18. K.V. Raju, C.N. Raju, S. Sailaja, B.S. Reddy, Solid State Sci., 15 (2013) 102-109.

19. A.M. Noorazlan, H.M. Kamari, S.O. Baki, D.W. Mohamad, J. Nanomater., 2015 (2015) 1-9.

20. H. Fares, I. Jlassi, S. Hraiech, H. Elhouichet, M. Férid, J. Quant. Spectrosc. Radiat. Transf., 147(2014) 224-232.

21. I. Kabalci, G. Özen, M.L. Öveçoğlu, A. Sennaroğlu, J. Alloys Compd., 419 (2006) 294-298.

22. M.A. Villegas, J.M.F. Navarro, J. Eur. Ceram. Soc., 27 (2007) 2715-2723.

23. N. Chopra, S. Kaur, M. Kaur, S. Singla, R. Marwaha, G. Sharma, M. S. Heer, Phys. Status Solidi A, 215 (2018) 1700934 (1-7).

24. W. Widanarto, M.R. Sahar, S.K. Ghoshal, R. Arifin, M.S. Rohani K.Hamzah, J. Magn. Mater., 326 (2013) 123-128.

25. M. Sołtys, A. Górny, J. Pisarska, W. A. Pisarski, J. Non-Cryst. Solids, 498 (2018) 352-363.

26. A. E. Ersundu, G. Karaduman, M. Celikbilek, N. Solak, S. Aydın, J. Alloys Compds., 508 (2010) 266-272.

27. L. Jyothi, G. Upender, R. Kuladeep, D. Narayana Rao, **,** Mater. Res. Bull., 50 (2014) 424-431.

28. J. Tauc, Amorphous and liquid semiconductors, first ed., Plenum, London, 1974.
29. V. Khani, P. Alizadeh, M.S. Shakeri, Mater. Res. Bull., 48 (2013) 3579-3584.
30. S. Sakida, J. Am. Ceram. Soc., 84 (2001) 836-842.
31. M.A. Hassan, C.A. Hogarth, J. Mater. Sci., 23 (1988) 2500-2504.
32. C. Gorller-Walrand, K. Binnemans, Spectral intensities of f-f transitions in Handbook on the Physics and Chemistry of Rare Earths edited by K.A. Gscheneidner Jr. and L. Eyring (North Holland, Amsterdam, 1998), 25 (1998)101-264.
33. B.R. Judd, Phys. Rev., 127 (1962) 750-761.
34. G.S. Ofelt, J. Chem. Phys., 37 (1962) 511-520.
35. Ch. Basavapoornima, K. Linganna, C.R. Kesavulu, S. Ju, B.H. Kim, W.-T. Han, C.K. Jayasankar, J. Alloys Compd., 699 (2017) 959-968.
36. K. Ouannes, M.T. Soltani, M. Poulain, G. Boulon, G. Alombert-Goget, Y. Guyot, A. Pillonnet, K. Lebbou, J. Alloy. Compd., 603 (2014) 132-135.
37. T. Wei, F. Chen, Y. Tian, S. Xu, Opt. Commun., 315 (2014) 199-203.
38. T. Wei, F. Chen, X. Jing, F. Wang, Y. Tian, S. Xu, Solid State Sci., 31 (2014) 54-61.
39. B.V. Padlyak, R. Lisiecki, W. R. Romanowski, Opt. Mater., 54 (2016) 126-133.
40. Y. Subramanyam, L.R. Moorthy, S.V.J. Lakshman, Mater. Lett., 9 (1990) 277-283.
41. S.V.J. Lakshman, A. Suresh Kumar, Phys. Chem. Glasses, 29 (1988) 146-151.
42. S.V.J. Lakshman, A. Suresh Kumar, J. Phys. Chem. Solids, 49 (1988) 133-138.
43. M. Haouari, A. Maaoui, N. Saad, A. Bulou, Sensors and Actuators A, 261(2017)235-242.
44. Recueil des Travaux et Compte Rendu des Séance, Commission Internationale de l'Eclairage, Huitieme Session, Cambridge, September 1931, The University Press, Cambridge, 1932, pp. 19–32 Resolution 2 (1932).
45. M.J. Weber, Phys. Rev. B, 4 (1971) 2932-2939.
46. D.E. McCumber, , Phys. Rev. A, 136 (1964) 954-957.
47. B.F. Aull, H.P. Jenssen, IEEE J.Quantum Electron, QE-18 (1982) 925-930.
48. V.B. Sreedhar, N. Vijaya, D. Ramachari, C.K. Jayasankar, J. Mol. Struct., 1130 (2017) 1001-1008.
49. Z. Pan, A. Ueda, R. Mu, S.H. Morgan, J. Lumin., 126 (2007) 251-256.
50. H. K. Dan, Z. Dacheng, W. Rongfei, T. M. Hau, J. Qing, Y. Xue, Q. Jianbei, J. Rare Earth, 31 (2013) 843-848.
51. Y. Kawamoto, R. Kanno, J. Qiu, J.Mater. Sci., 33 (1998) 63- 67.

Effect of heat treatment on (70-x) TeO_2-20B_2O_3-10ZnO-xDy_2O_3

Overview

The present chapter deals with the variation in the radiative paramters of zinc borotellurite glasses and glass ceramics doped with Dy^{3+}. The optimization of the thermal parameters in order to covert glasses into glass ceramics is done as explained in the previous chapter. It has been observed that color co-ordinates of the glasses lie in the white light region. An increase in non-exponential decay has been observed with increasing RE concentration as well as after heat treatment.

5.1 Introduction

Glasses and glass ceramics (GCs) are materials used in different industrial applications. GCs are important functional materials formed by heat treatment of glasses. GCs have the advantages of both glasses (easy production) and crystals (optical activity) [1-3]. It also exhibits good chemical durability, mechanical strength and corrosion resistance. The doping of RE elements in glasses is done to achieve better optical properties when it is converted to glass ceramics. It offers several advantages such as excellent emission intensities and better optical gain as compared to the parent glasses [4-6]. These properties make the glass ceramics more efficient than the glasses for WLEDs, sensors and medical display devices [6,7].

Dysprosium ion (Dy^{3+}) is an efficient RE^{3+} ion for obtaining white light emission. It finds applications in solid state lasers, Q-Switch devices, and fiber optics telecommunication amplifiers [8-19]. Dy^{3+}-doped glasses show intense emissions in yellow (576 nm), blue (486 nm) and red (667 nm) region [20-22]. Tellurites are preferred as glass former because of its wide transmission range, high linear refractive indices (1.8–2.3) [23], lower phonon energy among oxide glass hosts (800 cm^{-1}), high solubility of dopant RE^{3+} ions [23-25], good thermal and mechanical stability [26], and low melting point. These properties make tellurite glasses promising materials for lasers, sensors, electronic devices, and optical amplifiers. As discussed in the **Chapter 2** TeO_2 is a conditional glass former and preparing pure tellurite glasses requires special quenching techniques. But with the addition of certain oxides like B_2O_3, NaO, ZnO, etc., these glasses can be obtained through melt quenching technique also [20-23]. The present composition of the tellurite glasses is chosen on the basis of literature survey where glass and glass ceramics of low phonon energy without using heavy metal fluorides like PbF_2 and CdF_2 can be easily obtained [5,6].

The present study deals with the structural and optical properties of the dysprosium doped zinc borotellurite glasses (TBZDy_x) and glass ceramics (TBZDy_xGC). Another objective of the present study is to optimize yellow/blue (Y/B) ratio for white light generation by varying the rare earth concentration and by heat treating the prepared glass samples.

5.2 Physical Properties

5.2.1 Appearance

Fig. 5.1 (a,b) shows the photographs of the glasses and glass ceramics with increasing Dy_2O_3 content. It is clear from the **Fig. 5.1 (a)** that the prepared glasses are transparent. There is no significant change in color with increasing rare earth concentration. However, glass ceramics as shown in **Fig. 5.1 (b)** became yellowish white after heat treatment due to possible ceramization.

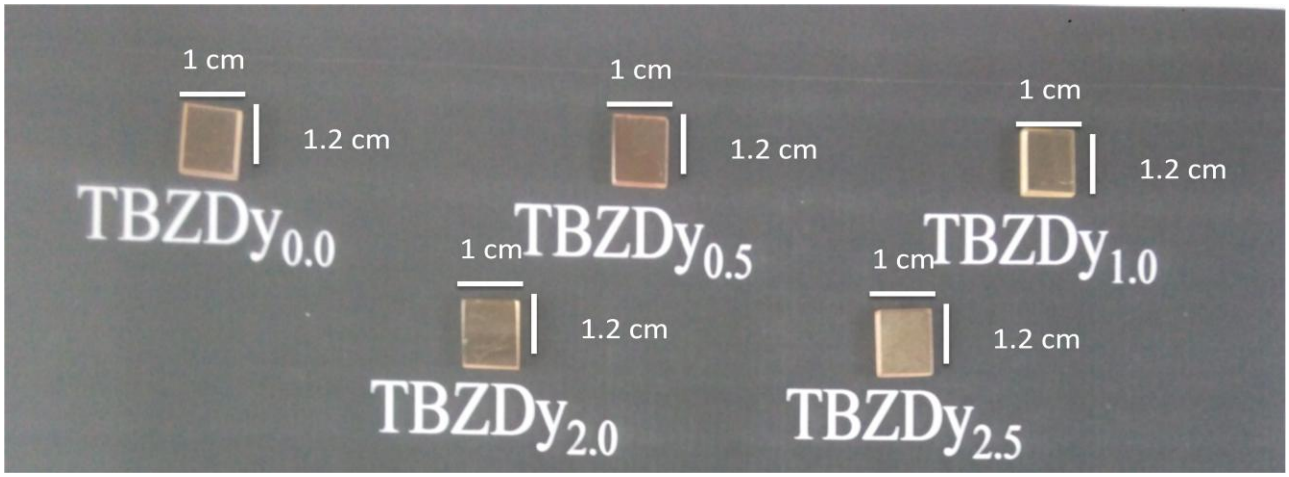

Fig. 5.1 (a): Phtograph of glasses with varying Dy_2O_3 content

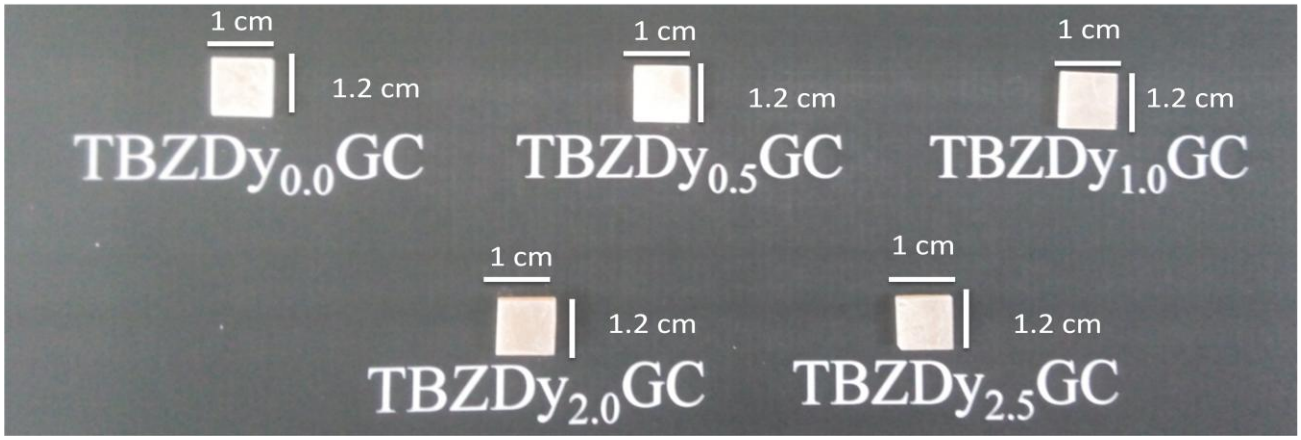

Fig. 5.1 (b): Phtograph of glass ceramics with varying Dy_2O_3 content

5.2.2 Density

Table 5.1 gives the values of density of the present samples. It is observed that density density increases with further increase of RE. It is due to addition of high molecular weight compound, Er_2O_3 (382.5g/mol) in place of comparatively lighter compound, TeO_2 (159.6

g/mol). An increase in the density values is observed after heat treatment which indicates that there is increase in the rigidity of the samples.

Table 5.1: Physical properties of the samples

Sample ID	Density (g/cm^3) ±2%
$TBZDy_{0.0}$	4.72
$TBZDy_{0.5}$	4.79
$TBZDy_{1.0}$	4.87
$TBZDy_{2.0}$	4.91
$TBZDy_{2.5}$	4.96
$TBZDy_{0.0}$GC	4.87
$TBZDy_{0.5}$GC	4.90
$TBZDy_{1.0}$GC	4.95
$TBZDy_{2.0}$GC	4.97
$TBZDy_{2.5}$GC	5.02

5.3 Thermal properties of the as-prepared glasses

Fig. 5.2 gives the DTA patterns of the as-prepared samples. The values of characteristics temperatures (Tg, T_{c1}, T_{c2} and ΔT) are given in **Table 5.2**. It is observed that there is an increase in T_g from 364 to 381 ^oC and T_{c1} from 424 to 458 ^oC with the increase in Dy^{3+} - concentration. Whereas, T_{c2} does not show any particular trend. This may be because of clustering of Dy^{3+} where clusters of different sizes may form during heating cycle.

The increase in the values of T_g and T_{c1} is because with the addition of rare earth (Dy_2O_3) in glass system B-O and Te-O bonds are repalced by Dy-O bonds. Also Dy-O bond is relatively stronger (615 kJ/mol), than B-O (536 kJ/mol) Te-O bond (377 kJ/mol). Therefore, the network connectivity in the glass matrix becomes stronger. Thus there is an increase in mean bond strength resulting in increase in T_g, and T_{c1} values [24]. The results are in agreement with that of Ersundu et al. [24] and Jyothi et al. [26] on Dy_2O_3 doped titanium-tungstate-tellurite glasses.

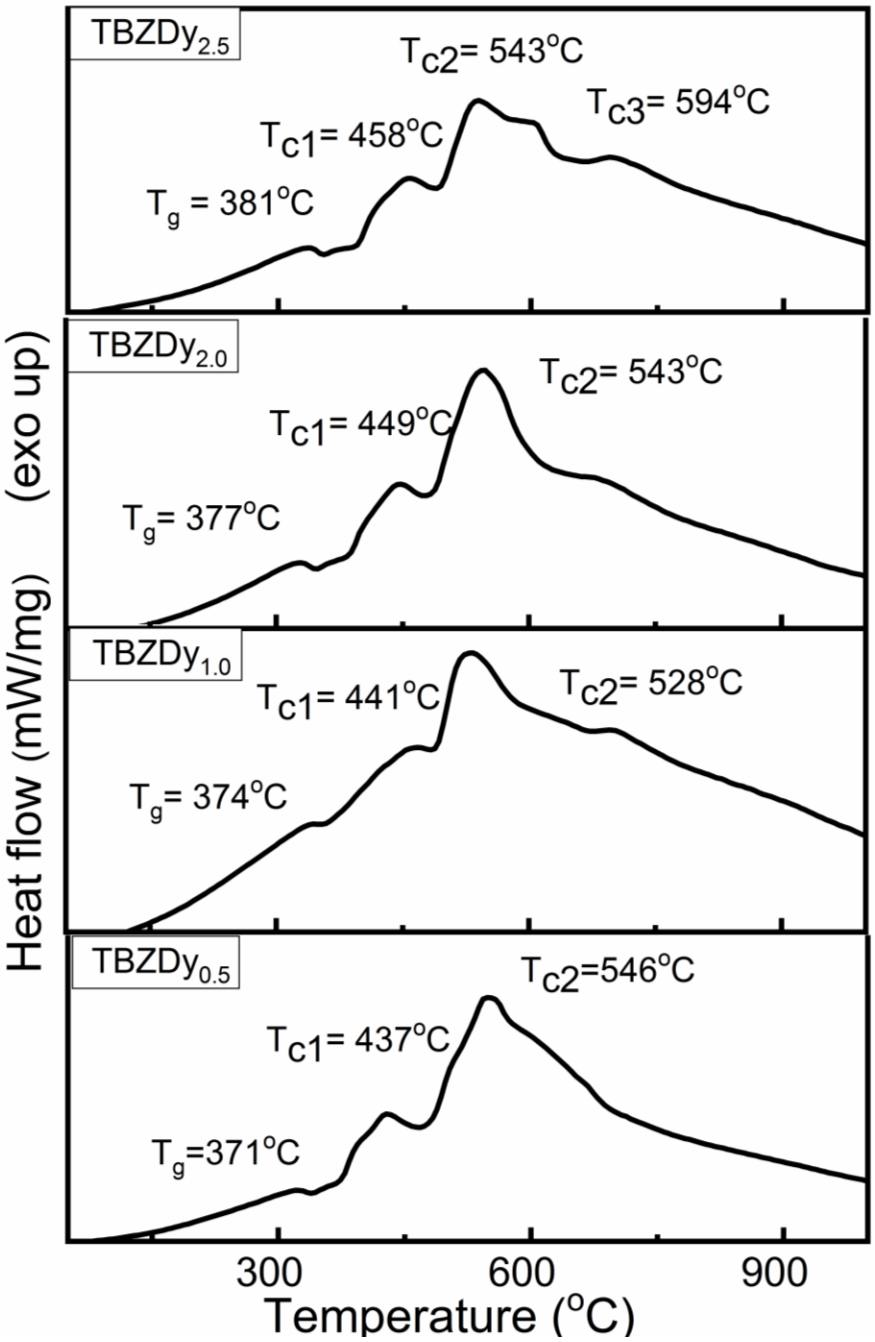

Fig. 5.2: DTA thermograph of Dy^{3+}:TBZDy glass where T_g is the glass transition, T_{c1} and T_{c2} are the peak crystallization temperatures

Table 5.2: Characteristic Thermal tempertaures (^oC) of Dy^{3+}:TBZDy glasses

Sample code	T_g±1 (^oC)	T_{c1}±1 (^oC)	T_{c2}±1 (^oC)	$\Delta T=T_{c1}-T_g$±1 (^oC)
$TBZDy_{0.5}$	371	437	546	66
$TBZDy_{1.0}$	374	441	528	67
$TBZDy_{2.0}$	377	449	540	72
$TBZDy_{2.5}$	381	458	542	77

5.4 Structural and morphological studies:

5.4.1 X-Ray diffraction (XRD)

5.4.1.1 X-Ray diffraction (XRD) of as-prepared glasses

XRD patterns of $TBZDy_x$ glasses is shown in **Fig. 5.3 (a)**. A broad hump is observed in the range of 20-35^o in the case of glass. It confirms that there is no noticeable crystallization in the glass matrix.

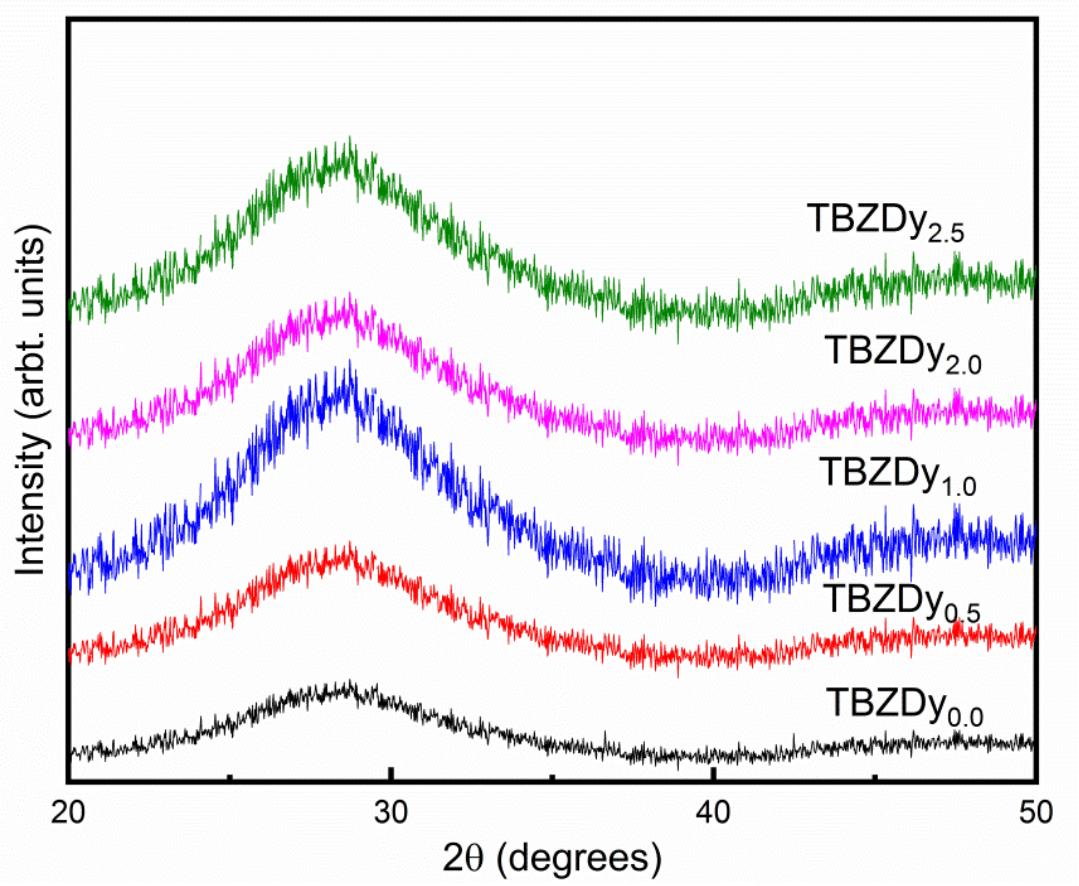

Fig. 5.3 (a): X-ray diffractograms of the as-prepared $TBZDy_x$ glasses

5.4.1.2 Optimization of temperature and time for preparing glass ceramics

The DTA studies which are shown in **Fig. 5.2** suggests that the T_g and T_{c1} of the as-prepared glasses lies in the range of 364 – 381 ^oC and 424 – 458 ^oC respectively. To prepare glass ceramics $TBZDy_{0.5}$ glass is given heat treatment at 375, 400 and 430 ^oC for 2, 4 and 6h respectively. The XRD patterns of the heat treated samples are shown in **Fig. 5.3 (b-d)**.

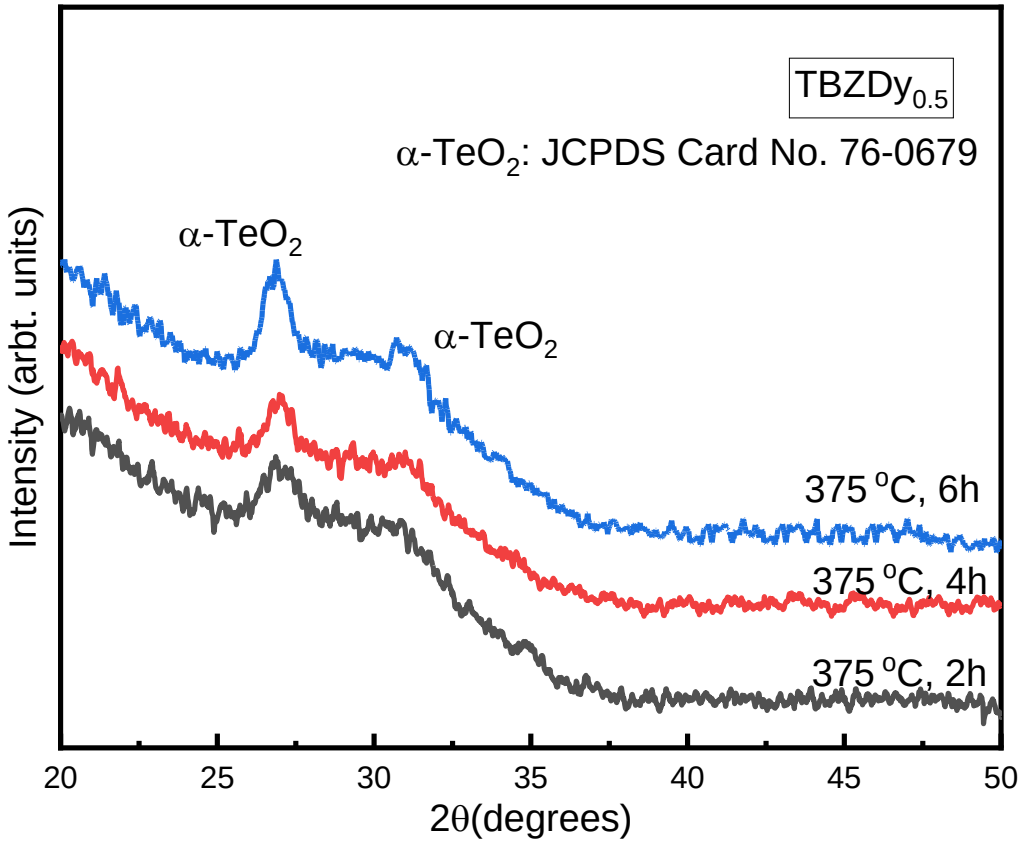

Fig. 5.3 (b): X-ray diffractograms of $TBZDy_{0.5}$ heat treated at 375 ^oC for 2, 4 and 6h

Fig. 5.3 (b) shows the XRD of the $TBZDy_{0.5}$ glass heat treated at 375 ^oC for 2, 4 and 6h respectively. The heat treated $TBZDy_{0.5}$ samples show background due to presence of amorphous phase. It was observed that the prepared samples show crystallization on heat treatment at 375 ^oC. The observed Bragg's peaks are due to the formation of α- TeO_2 (para-tellurite) phase.

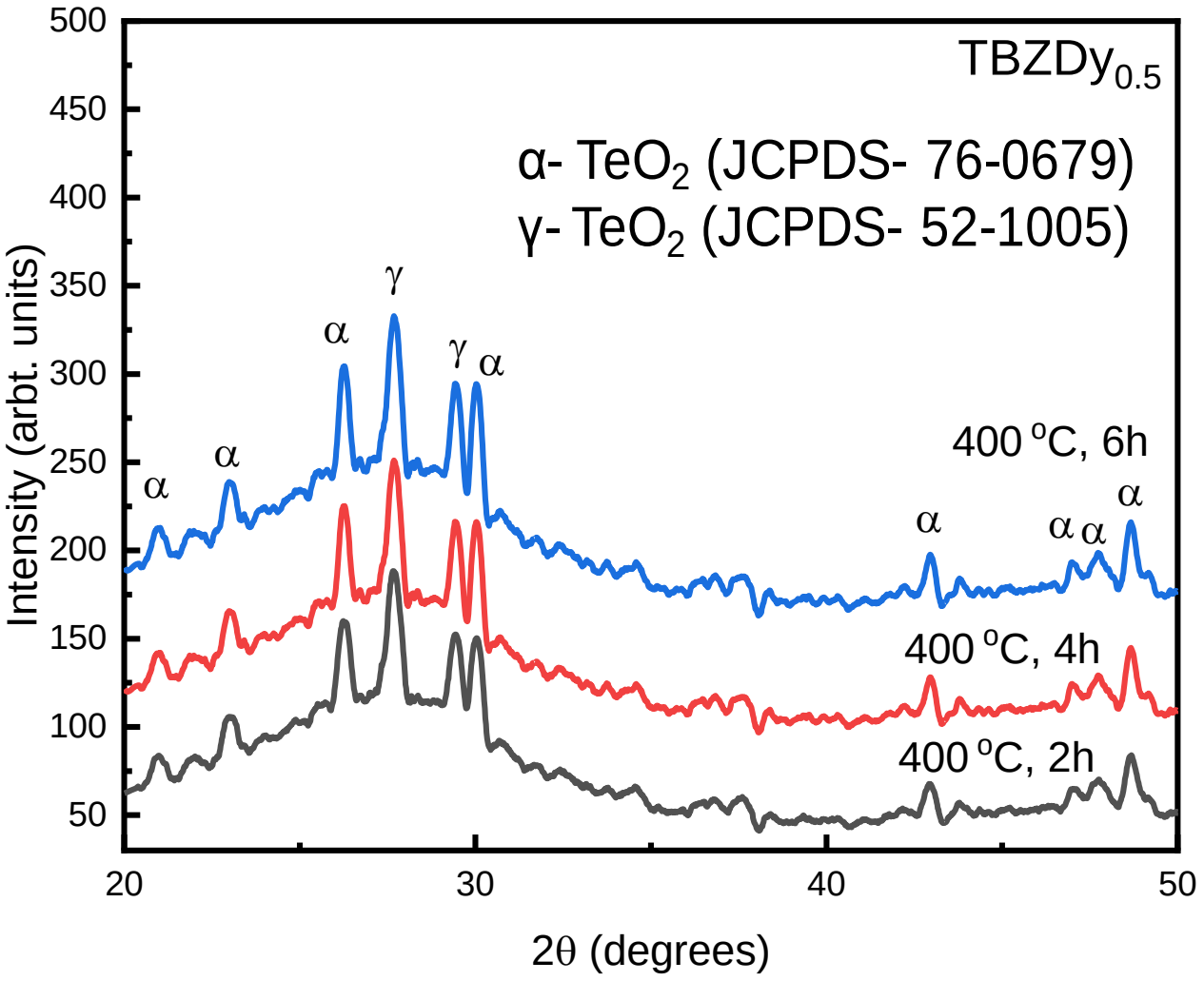

Fig. 5.3 (c): X-ray diffractograms of $TBZDy_{0.5}$ heat treated at 400 °C for 2, 4 and 6h

Fig. 5.3 (c) shows the XRD patterns of the $TBZDy_{0.5}$ sample heat treated at 400 °C for 2, 4 and 6h. It is observed that, along with α- TeO_2 another phase due to orthorhombic γ- TeO_2 appears. With an increase in time the intensity of the crystalline phases also increases.

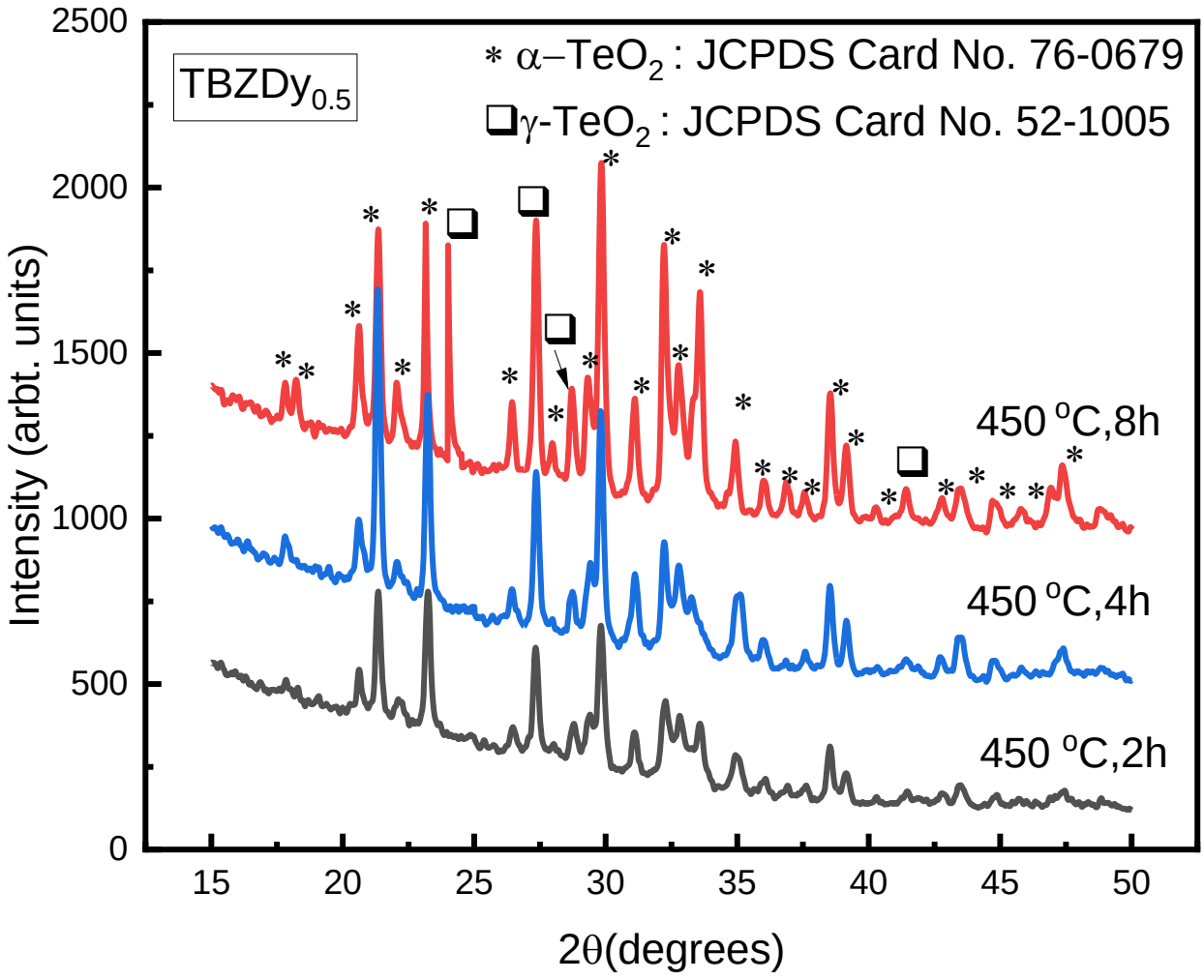

Fig. 5.3 (d): X-ray diffractograms of $TBZDy_{0.5}$ heat treated at 450 °C for 2, 4 and 6h

The $TBZDy_{0.5}$ glass has been further heat treated at 450 °C for 2, 4 and 6h. The observed XRD patterns are shown in **Fig. 5.3 (d)**. From the above results, it is observed that samples heat treated at 450 °C for 2, 4 and 6h are highly crystalline, with very small residual amorphous phase.

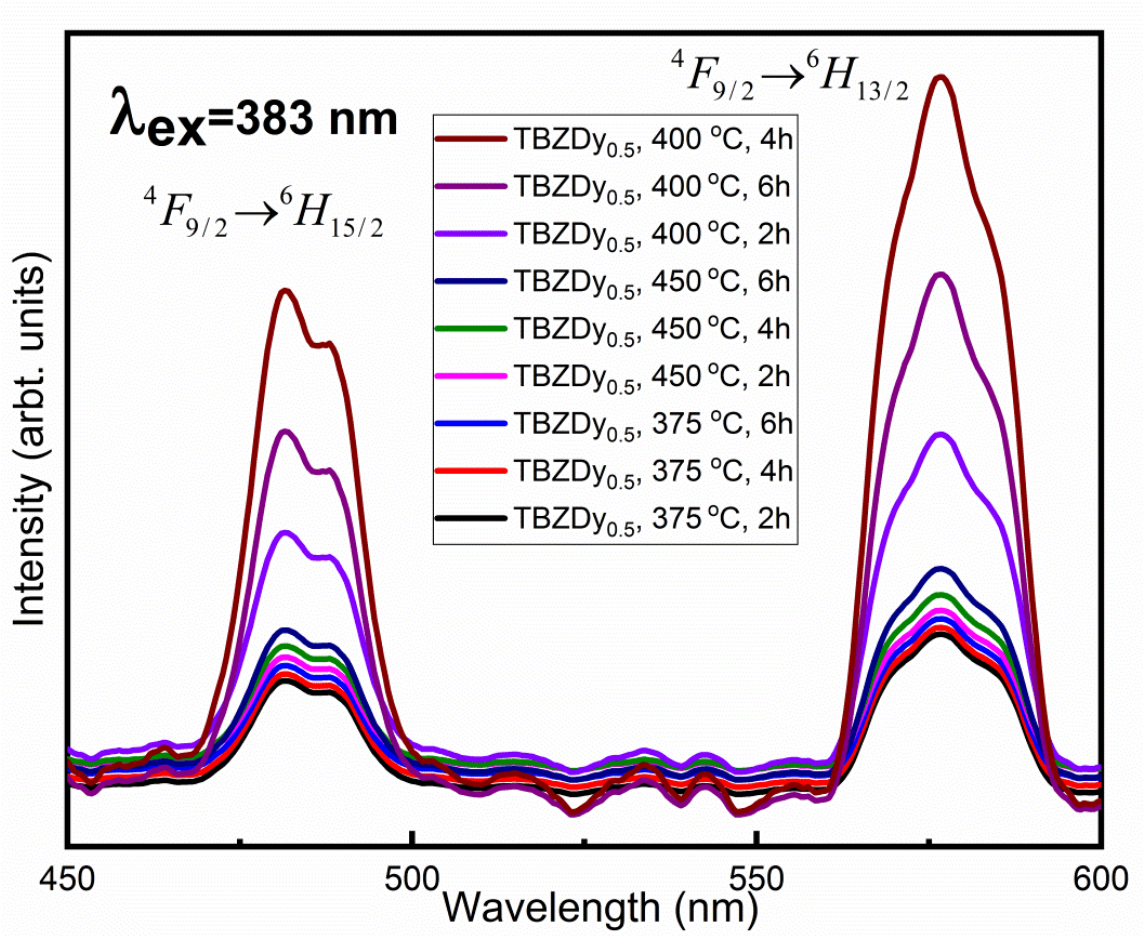

Fig. 5.3 (e): Photolumiescence spectra of the $TBZDy_{0.5}$ sample heat treated at 375, 400 and 450°C for 2, 4 and 6h respectively

The present study aims at the photoluminescence characteristics of the glasses and glass ceramics. In order to optimize the time and temperature conditions emission spectra has been studied. **Fig. 5.3 (e)** shows the emission spectra of heat treated samples. It is observed that the glass ceramics heat treated at 400 °C for 4h has highest emission intensity in Dy^{3+}- doped glasses. Therefore, in the order to prepare GCs, all the undoped and doped samples are heat treated at 400 °C for 4h in this study.

5.4.1.3 Effect of heat treatment on glasses with increasing Dy^{3+} concentration

The XRD patterns of all the RE-doped samples heat treated at 400 °C for 4h is shown in **Fig. 5.3 (f)**. The presence of several sharp diffraction peaks in the case of glass ceramics reveals presence of various phases. The JCPDS database has been used for phase identification of observed phases.

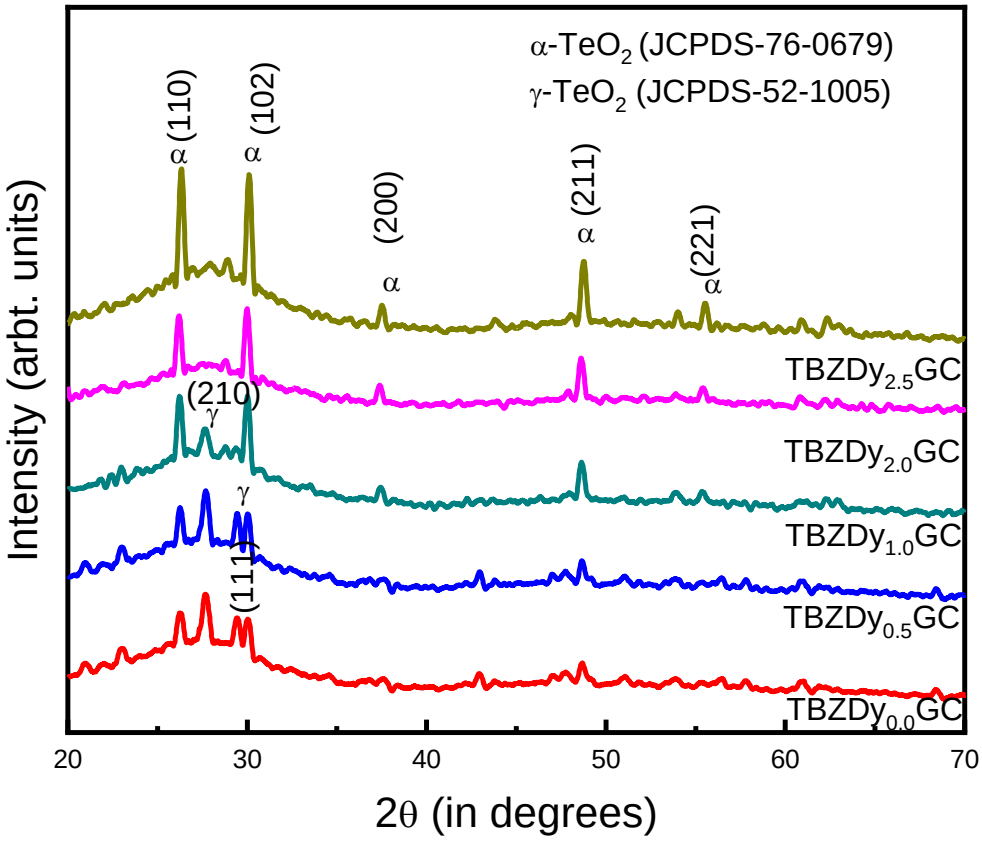

Fig. 5.3 (f): X-ray diffractograms pattern $TBZDy_xGC$ glass ceramics

The analysis of the XRD diffractograms of glass ceramics reveals presence of crystalline phases induced in the glass matrix after their heat treatment at 400 ^oC for 4h. The primary crystalline phase formed in the glass ceramics is tetragonal paratellurite α-TeO_2 phase (JCPDS reference code 76-0679) [47]. Another phase obtained in the present study is orthorhombic γ-TeO_2 (JCPDS reference code 52-1005) having chain structure. It is worth noting that at low rare earth concentration (upto 1mol%), γ-TeO_2 is dominating than the α-TeO_2 phase whereas with an increase in the RE content (upto 2.5 mol%) α-TeO_2 phase is dominating the former. Thus it is clear that with an increase in the RE - concentration, more stable α-TeO_2 is forming than metastable γ -TeO_2. The crystallite size has been found to be in the range 24 - 43 nm ± 5 nm and is given in **Table 5.3**.

Table 5.3: Average crystallite size (nm) ± 5 nm in glass ceramics after heat treatment

Sample ID	Crystallite Size ± 5 (nm)
TBZD$y_{0.0}$GC	21
TBZD$y_{0.5}$GC	26
TBZD$y_{1.0}$GC	32
TBZD$y_{2.0}$GC	35
TBZD$y_{2.5}$GC	43

5.4.2.1 Raman spectroscopy

To study the structural modifications in the glasses and glass ceramics, Raman measurements are carried out. To have detailed insight of glass structure, the de-convolution of the Raman spectrum has been done. **Fig. 5.4 (a)** shows de-convoluted Raman spectra of glass samples. The de-convoluted bands are centered at around 620, 664, 718, and 767 cm^{-1} [25,26]. The bands centered at 718 and 767 cm^{-1} **(Fig. 5.4 (a))** are due to symmetric bending and stretching vibrations of TeO_{3+1} trigonal pyramid (tp) units having NBOs. The other two bands centered at around 620 and 664 cm^{-1} are ascribed to asymmetric bending and stretching vibrations of TeO_4 trigonal bipyramidal (tbp) units having BOs [25,26,56]. With an increase in Dy^{3+}-concentration, a decrease in Raman intensity of bands at 620 and 664 cm^{-1} relative to bands at 718 and 767 cm^{-1} is observed**. Fig. 5.4 (b)** shows the variation in the structural units with increasing RE- content. This indicates that increase in RE content in glasses leads to rupture of Te-O-Te linkages and resuting into conversion of Q^4_4 to Q^3_4 structural groups [47] as shown in **Fig. 5.4 (c)**. Thus there is decrease of TeO_4 polyhedra structural units with BO and increase in TeO_4 structural units with NBOs [25].

The Raman spectra of the Dy^{3+}- doped zinc borotellurite glass ceramics is shown in **Fig.5.5**. The narrower bands in the heat treated sample are the consequence of the heat treatment of glasses. The bands at 653, 614 and 415 cm^{-1} are ascribed to α-TeO_2 at about 801 cm^{-1} belongs to γ-TeO_2 [47]. Assignment of Raman bands observed in glass ceramics is tabulated in **Table 5.4**. The peaks observed in the low frequency region of glass ceramics are attributed to α-TeO_2. No significant change is observed in the spectra after heat treatment with increase in RE content.

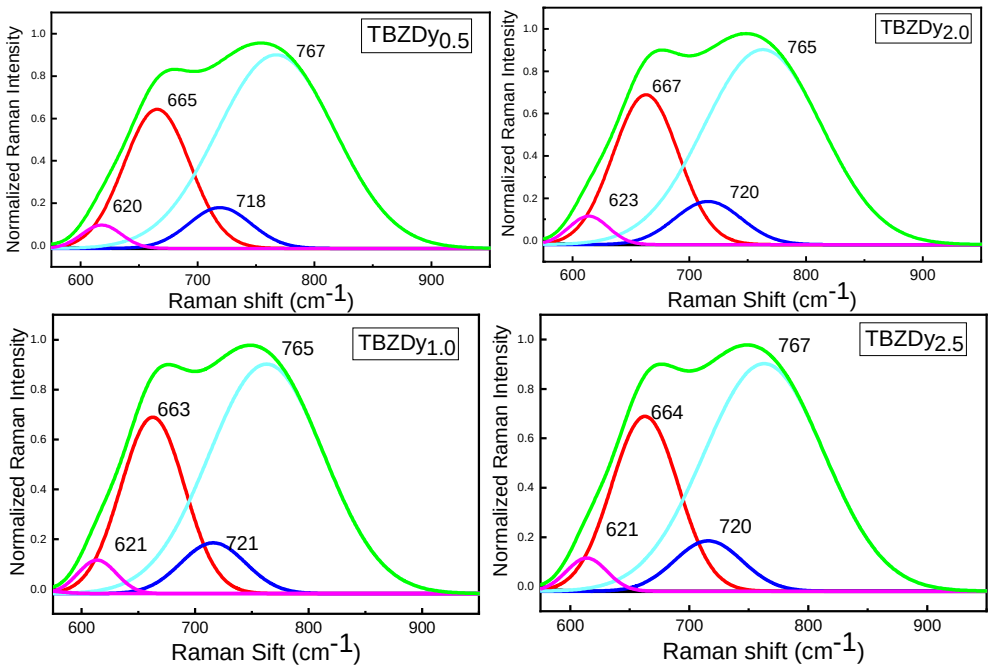

Fig. 5.4 (a): De-convoluted Raman spectra of present glasses

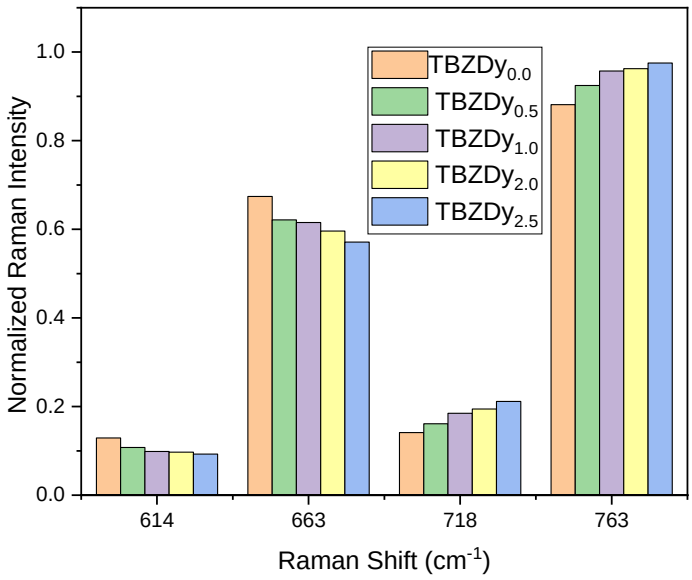

Fig. 5.4 (b): Normalized intensities of the raman bands after de-convolution at different RE-concentrations

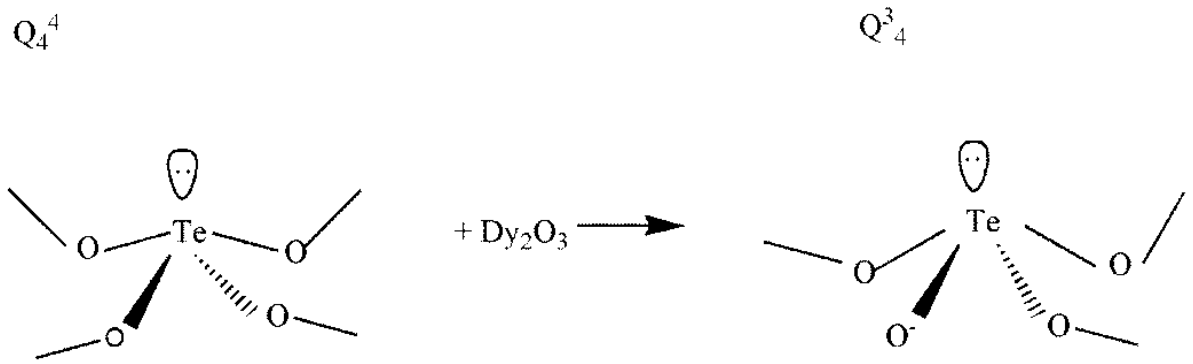

Fig. 5.4 (c): Possible structural change induced in the glasses with the introduction of Dy_2O_3. Where in notation Q_4^4 superscript gives the number of BOs and subscript gives number of NBOs

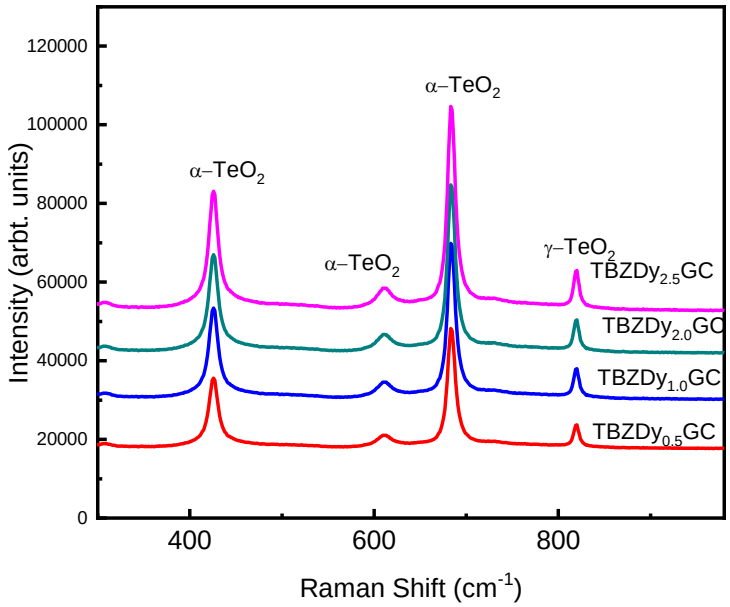

Fig. 5.5: Raman spectra of Dy^{3+}-doped zinc borotellurite glass ceramics

Table 5.4: Assignment of Raman bands in glass ceramics

Position (cm^{-1})	**Assignment**
119,142,173	TeO_4 unit's vibrational modes [56].
415	Stretching vibrations of Te-O-Te bonds in α -TeO_2 [56].
614	Anti- symmetric stretching vibrations of Te-O-Te linkages in α -TeO_2 [56].
653	Stretching vibrations of TeO_4 in α -TeO_2 [56].
801	γ -TeO_2 [47].

5.4.2.2 Fourier Transform Infrared spectroscopy (FTIR):

The changes in structure of BO_3 and BO_4 units with increase in concentration of Dy^{3+} content are analyzed with the FTIR. The fourier transform infrared spectra of prepared samples have been recorded in the wave number range 600 to 1500 cm^{-1} and shown in **Fig. 5.6 (a)**. The infrared vibrational bands are observed in 1500-1200 cm^{-1}, 1100-800 cm^{-1} and 800-680 cm^{-1} due to stretching vibrations of B-O bond in BO_3 units, B-O stretching vibrations of BO_4 tetrahedra of pentaborate, tetraborate and diborate structural units.

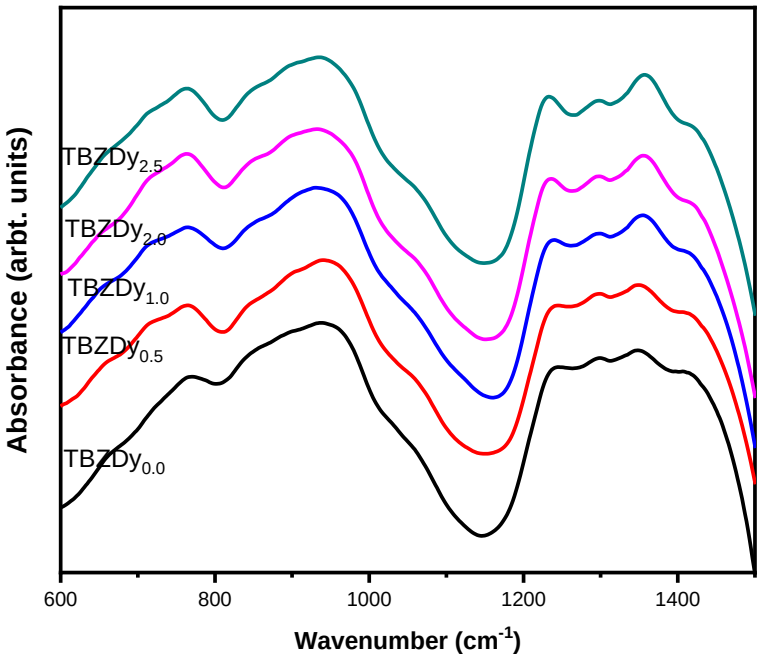

Fig.5.6 (a): Infrared Absorbance Spectra of the prepared glass system

The variations in the intensities of various structural units observed are shown in **Fig. 5.6 (b)**. It is clear from **Fig. 5.6 (b)** that with the increase in the Dy_2O_3 concentration an increase in the structural units having NBO's is observed. This result is in accordance with the Raman results which supports the formation of TeO_3 structural units.

Fig. 5.6 (c) represents the FTIR spectra of glass ceramics. It is worth noting that considerable changes are observed in the FTIR spectra of prepared glasses after heat treatment. The vibrational bands become sharper and narrower after the heat treatment. This may be due to

the ceramization of the glasses after heat treatment. Formation of new structural units at 1218 and 1335 cm^{-1} is observed. Also, bands at 579 and 622 cm^{-1} became more prominent due to heat treatment.

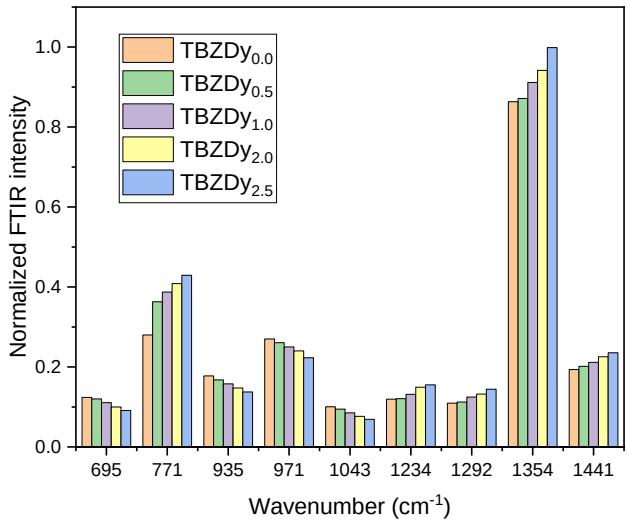

Fig. 5.6 (b): Normalized FTIR intensities of the prepared glasses

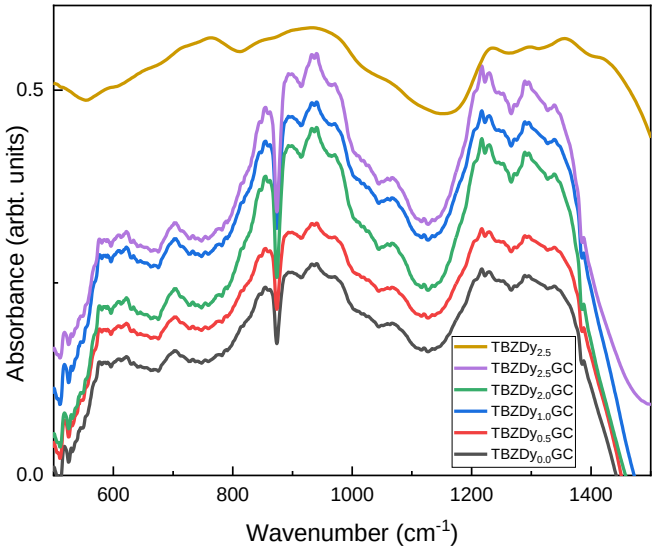

Fig. 5.6 (c): Infrared absorbance spectra of the Dy^{3+}-zinc borotellurite glass ceramics

5.4.3 Field Emission Scanning Electron Microscope (FESEM)

Fig. 5.7 (a) shows the micrographs of (i) $TBZDy_{0.5}$, (ii) $TBZDy_{0.5}$, (iii) $TBZDy_{1.0}$, (iv) $TBZDy_{2.0}$ and (v) $TBZDy_{2.5}$ glasses. The micrographs shows there is no crystalline phase present in as-prepared glass matrix.

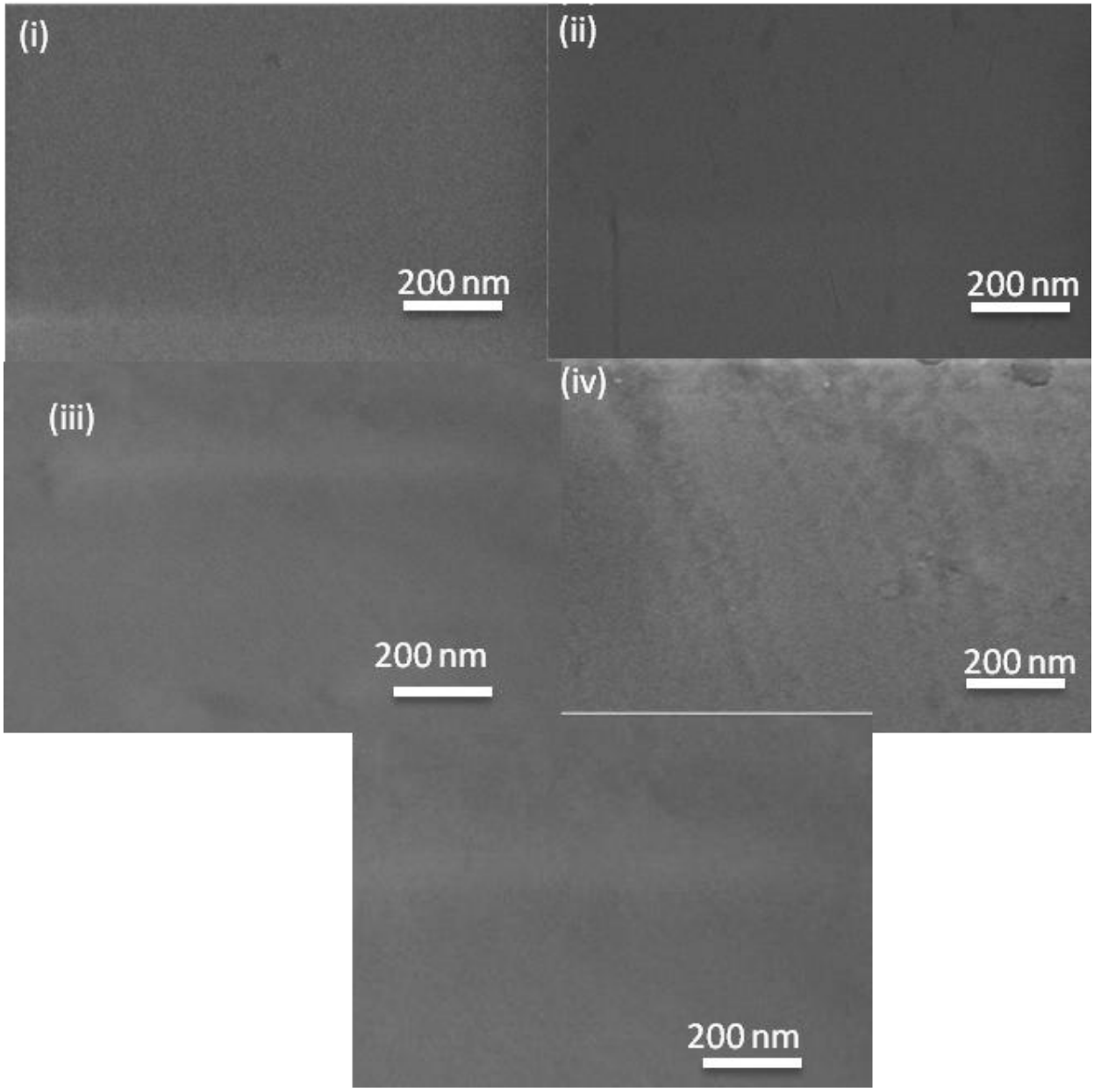

Fig. 5.7 (a): FESEM micrographs of Dy^{3+}-doped (i) $TBZDy_{0.0}$, (ii) $TBZDy_{0.5}$, (iii) $TBZDy_{1.0}$, (iv) $TBZDy_{2.0}$ and (v) $TBZDy_{2.5}$ glasses

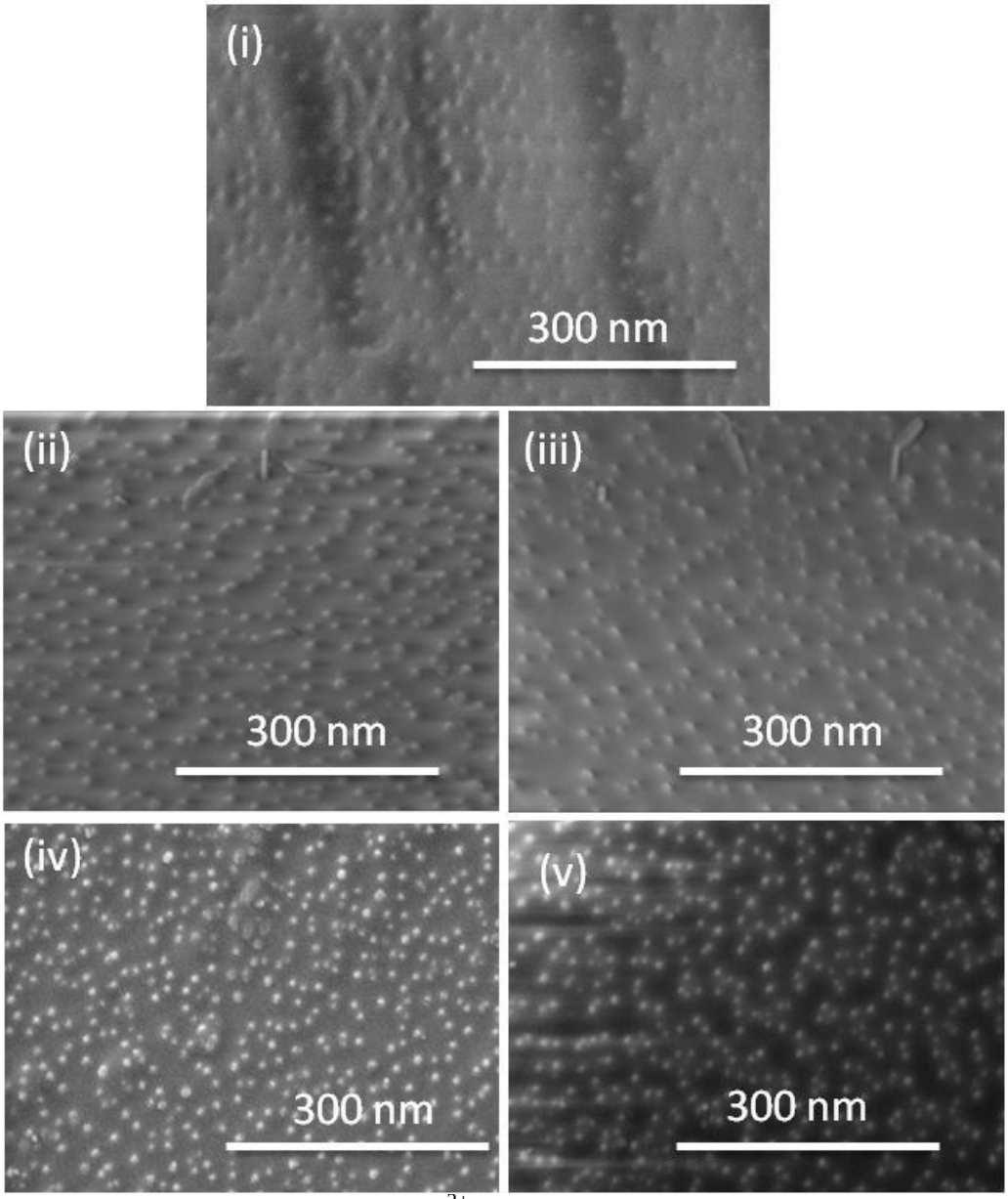

Fig. 5.7 (b): FESEM micrographs of Dy^{3+}-doped (i) TBZ$Dy_{0.0}$GC, (ii) TBZ$Dy_{0.5}$GC, (iii) TBZ$Dy_{1.0}$GC, (iv) TBZ$Dy_{2.0}$GC and (v) TBZ$Dy_{2.5}$GC glass ceramics

Fig. 5.7 (b) shows the micrographs of glass ceramics. It is clear from these micrographs that glasses got converted to glass ceramics as crystalline phases have appeared in the glass matrix. These crystalline phases are like spherulite and are uniformally produced in the glass matrix. The particle size lies in the nanometer range. The average size of the particles is in the range of 33 - 45 nm as given in **Table 5.5**. The uniform distribution of these nano particles in the glassy matrix will give isotropic properties of the glass ceramics.

Table 5.5: Particle size (nm) in glass ceramics after heat treatment

Sample ID	Particle Size±5 nm
$TBZDy_{0.0}GC$	33
$TBZDy_{0.5}GC$	36
$TBZDy_{1.0}GC$	40
$TBZDy_{2.0}GC$	42
$TBZDy_{2.5}GC$	45

5.5 Absorption studies - Judd-Ofelt (JO) analysis

The absorption spectra of present glasses and the corresponding glass-ceramics in UV-Vis-NIR (350-2000 nm) is shown in **Fig. 5.8 (a** and **b)**. Ten absorption bands have been identified from the ground state $^6H_{15/2}$ to excited states of Dy^{3+} [8,17,18,31].

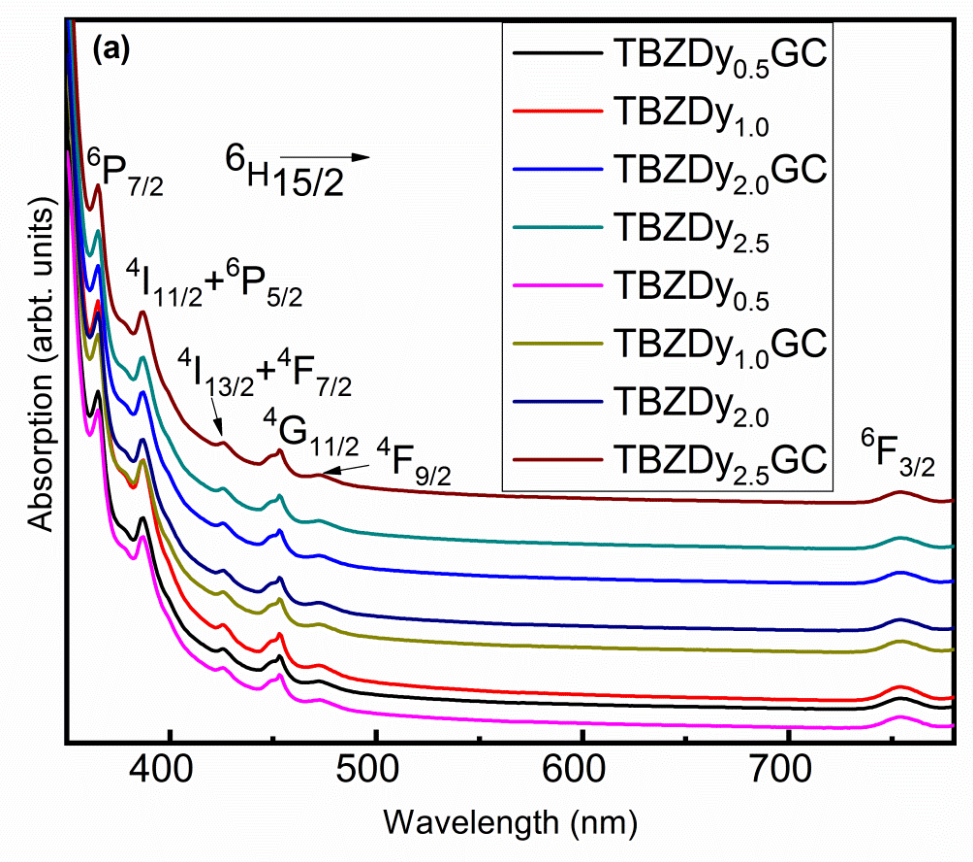

Fig. 5.8 (a): Absorption spectra of present samples in UV-Vis region

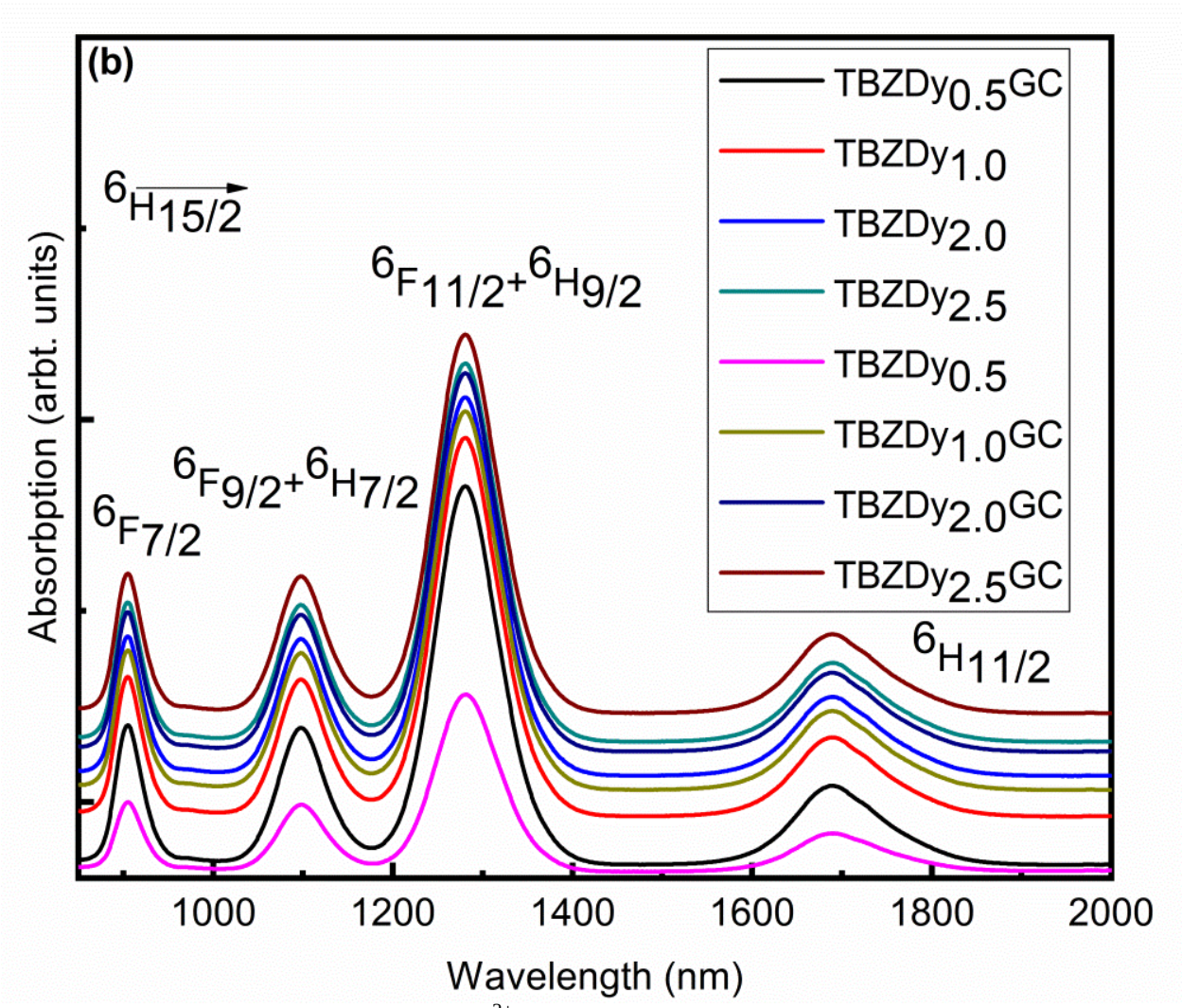

Fig. 5.8 (b): Absorption spectra of Dy^{3+}:TBZDy and TBZDy$_x$GC systems in NIR region

The absorption cross-section is calculated for the hypersensitive absorption peak at 1280 nm using the following expression:

$$\alpha(h\vartheta) = \frac{1}{Nd} ln(\frac{I_0}{I}) \quad (5.1)$$

Where, 'N' is the concentration of rare earth,'d' is the thickness of the sample, 'I_o' and 'I' are the incident intensity and transmitted intensity. The thickness of the prepared samples is 2±0.3 mm. The concentration of rare earth in the prepared samples is 2.9× 10^{20} ions per cm^3, 5.8× 10^{20} ions per cm^3, 11.5× 10^{20} ions per cm^3 and 14.8× 10^{20} ions per $cm^3$for 0.5, 1.0, 2.0 and 2.5 Dy^{3+}- mol%, respectively. It is found that the values of absorption coefficient increases gradually with increase in RE ion concentration and with heat treatment **(Table**

5.6). To find the oscillator strengths standard procedures are used [13,17,18]. The oscillator strengths ($\times 10^{-6}$) of different transitions of Dy^{3+} for TBZDy and TBZDy$_x$GC are given in **Table 5.6**. As we know that the oscillator strengths are the measure of probability of a absorption. It is found that the values of oscillator strengths decrease for all transitions from glass to glass-ceramics in the UV-Vis region but increase in the NIR region except for hypersensitive transition ($^6H_{15/2} \rightarrow {}^6F_{11/2}+{}^6H_{9/2}$). Similar results are reported for Dy^{3+}-doped oxyflouride glass ceramics [4-6]. The JO parameters for TBZDy$_x$ and TBZDy$_x$GC systems along with some reported Dy^{3+}: glasses [19-21, 31-36] are given in **Table 5.7 (a,b)**. The decrease in the value of Ω_2 after the crystallization of the precursor glass is observed. It indicates a decrease of covalent character between the RE^{3+} ions and surrounding ligands.

Table 5.6: Oscillator strengths ($\times 10^{-6}$), RMS deviation (δ_{rms}) between experimental and calculated values and absorption cross-section for Dy^{3+}:TBZDy$_x$ and TBZDy$_x$GC systems

Transition $^6H_{15/2}\rightarrow$	**TBZDy$_{0.5}$**		**TBZDy$_{1.0}$**		**TBZDy$_{2.0}$**		**TBZDy$_{2.5}$**		**TBZDy$_{0.5}$GC**		**TBZDy$_{1.0}$GC**		**TBZDy$_{2.0}$GC**		**TBZDy$_{2.5}$GC**	
	f_{exp}	f_{cal}	f_{exp}	f_{cal}	f_{exp}	f_{cal}	f_{exp}	f_{cal}	f_{exp}	f_{cal}	f_{exp}	f_{cal}	f_{exp}	f_{cal}	f_{exp}	f_{cal}
$^6P_{7/2}$	0.99	0.67	1.12	0.85	0.98	0.86	1.25	1.12	0.56	0.54	0.99	0.68	0.41	0.69	0.58	0.66
$^4I_{11/2}+{}^6P_{5/2}$	1.09	0.37	1.25	1.09	1.01	0.67	1.01	0.86	0.59	0.56	1.01	0.25	0.76	0.40	0.86	0.21
$^4I_{13/2}+{}^4F_{7/2}$	0.71	0.94	0.58	0.52	0.45	0.81	0.86	0.56	0.11	0.52	1.08	0.99	1.07	1.21	0.45	0.56
$^4G_{11/2}$	0.76	0.18	0.67	0.11	1.65	0.08	0.28	0.58	0.59	0.56	0.21	0.11	0.24	0.58	0.25	0.56
$^4F_{9/2}$	0.63	0.58	0.38	0.62	1.52	1.01	0.25	0.23	0.56	0.48	0.23	0.58	0.67	0.69	0.18	0.19
$^6F_{3/2}$	0.84	0.22	0.13	0.26	0.62	0.44	0.29	0.31	0.71	0.18	0.08	0.14	0.14	0.23	0.15	0.26
$^6F_{7/2}$	4.04	3.03	4.32	3.99	4.36	4.56	2.99	3.65	6.96	5.65	4.95	4.29	5.19	5.17	3.14	4.98
$^6F_{9/2}+{}^6H_{7/2}$	4.17	4.39	3.25	3.58	4.85	4.24	4.98	4.58	5.19	4.56	4.28	3.98	5.99	5.06	5.87	5.26
$^6F_{11/2}+{}^6H_{9/2}$	11.3	11.2	10.69	10.56	11.01	11.25	10.56	10.68	10.98	10.68	10.21	10.11	10.08	10.28	10.86	10.50
$^6H_{11/2}$	1.21	1.75	1.12	1.68	1.06	1.23	1.54	1.45	1.86	1.95	1.93	1.99	1.48	2.56	1.68	1.65
δ_{rms}	±0.60		±0.56		±0.65		±0.32		±0.35		±0.48		±0.16		±0.24	
Absorption Cross-section ± 0.98 ($\times 10^{-20}$ cm^2)	5.26		5.81		5.95		6.02		6.06		6.11		6.19		6.24	

Table 5.7 (a): JO intensity parameters in present Dy_2O_3 systems (x 10^{-20} cm^2)

Sample ID	Ω_2 ±1.05	Ω_4 ±.09	Ω_6 ±0.04	Trend	Reference
$TBZDy_{0.5}$	14.32	5.64	2.64	$\Omega_2 > \Omega_4 > \Omega_6$	Present Work [PW]
$TBZDy_{1.0}$	13.91	4.99	2.01	$\Omega_2 > \Omega_4 > \Omega_6$	[PW]
$TBZDy_{2.0}$	13.66	3.84	2.17	$\Omega_2 > \Omega_4 > \Omega_6$	[PW]
$TBZDy_{2.5}$	14.73	3.72	2.08	$\Omega_2 > \Omega_4 > \Omega_6$	[PW]
$TBZDy_{0.5}GC$	10.53	3.13	2.77	$\Omega_2 > \Omega_4 > \Omega_6$	[PW]
$TBZDy_{1.0}GC$	9.05	3.30	2.19	$\Omega_2 > \Omega_4 > \Omega_6$	[PW]
$TBZDy_{2.0}GC$	10.66	3.44	2.27	$\Omega_2 > \Omega_4 > \Omega_6$	[PW]
$TBZDy_{2.5}GC$	8.73	3.72	2.18	$\Omega_2 > \Omega_4 > \Omega_6$	[PW]

Table 5.7 (b): JO intensity parameters in reported Dy_2O_3 systems (x 10^{-20} cm^2)

Sample ID	Ω_2	Ω_4	Ω_6	Trend	Reference
TCZNB	11.30	3.30	2.60	$\Omega_2 > \Omega_4 > \Omega_6$	[20]
CBTCdD	5.87	0.27	1.32	$\Omega_2 > \Omega_6 > \Omega_4$	[33]
BTKA0.05D	3.34	0.20	0.68	$\Omega_2 > \Omega_6 > \Omega_4$	[31]
LSBP0.5Dy	5.73	2.19	1.92	$\Omega_2 > \Omega_4 > \Omega_6$	[35]
DZCTFB	10.64	1.51	2.50	$\Omega_2 > \Omega_6 > \Omega_4$	[32]
0.5LBTPD	10.9	3.68	2.86	$\Omega_2 > \Omega_4 > \Omega_6$	[19]
0.5DZTFB	8.28	2.79	1.89	$\Omega_2 > \Omega_4 > \Omega_6$	[34]
BTLN0.05D	7.13	2.16	1.44	$\Omega_2 > \Omega_4 > \Omega_6$	[21]
Dy0.5	4.90	0.94	2.07	$\Omega_2 > \Omega_6 > \Omega_4$	[36]

Energy gap is used to obtain information about the modifications in the energy levels brought by heat treatment and RE addition. The energy gap of the present glasses is calculated using Mott and Davis formulation [42].

Table 5.8: The direct and indirect energy gap and refractive index of $TBZDy_x$ and $TBZDy_xGC$

Sample ID	Direct energy gap ± 0.21 (eV)	Indirect energy gap ± 0.32 (eV)	Urbach Energy ± 0.02 (eV)	Refractive index N ± 0.87
$TBZDy_{0.0}GC$	3.21	3.25	0.09	2.31
$TBZDy_{0.5}GC$	3.21	3.24	0.18	2.33
$TBZDy_{1.0}GC$	3.16	3.18	0.20	2.40
$TBZDy_{2.0}GC$	2.89	3.09	0.23	2.43
$TBZDy_{2.5}GC$	2.31	2.56	0.31	2.57
$TBZDy_{0.0}$	3.42	3.32	0.19	2.29
$TBZDy_{0.5}$	3.32	3.26	0.21	2.31
$TBZDy_{1.0}$	3.25	3.22	0.23	2.37
$TBZDy_{2.0}$	2.91	3.19	0.29	2.41
$TBZDy_{2.5}$	2.36	2.81	0.32	2.54

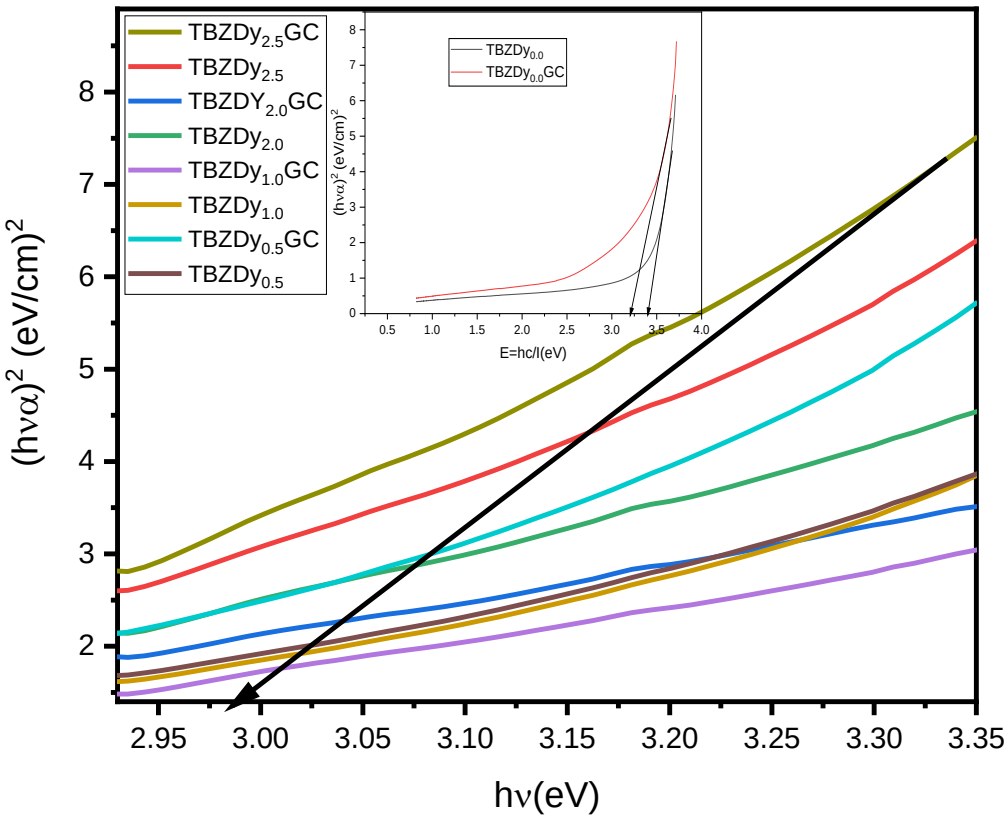

Fig. 5.8 (c) Tauc plot for direct band gap

Fig. 5.8 (c) and (d) gives the graphs of direct and indirect energy band gap. The values of energy gap and refractive index are tabulated in **Table 5.8**. A decrease in the energy gap of the samples is observed with increasing RE concentration. It can be due to increase in the number of NBOs. The refractive index values are calculated with the help of direct band gap. It is worth noting that the refractive index increases with increasing RE content as given in **Table 5.8**. The energy gap of the samples also decreases with heat treatment. The Urbach energy indicates the width of the band tails of the localized states and measures disorderness in materials. The absorption and the Urbach energy are related as following:

$$\alpha(\vartheta) = \alpha_0 e^{\frac{h\vartheta}{\Delta E}} \quad (5.2)$$

An increase in the Urbach energy is observed **(Table 5.8)** with increasing RE- content due to increase in the NBOs in the samples, whereas a decrease in the values of ΔE is observed due to the heat treatment.

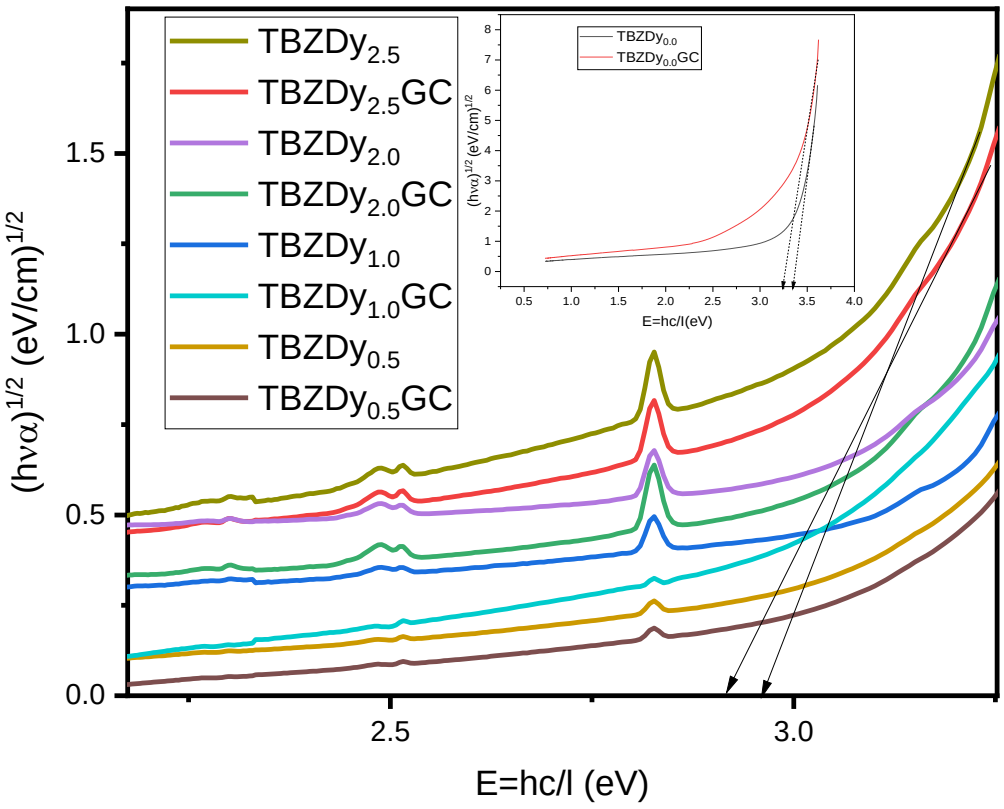

Fig. 5.8 (d) Tauc plot for indirect band gap

5.6 Spectroscopic properties

5.6.1 Excitation and emission studies

The excitation spectra of present samples in range of 300-500 nm at 575nm is given in **Fig. 5.9**. A number of peaks are observed in the excitation spectra of the glasses. The transitions are assigned from ground state $^6H_{15/2}$ to $^6P_{5/2}$, $^6P_{7/2,}$ $^4P_{3/2}$, $^4I_{13/2}$, $^4G_{11/2}$, $^4I_{15/2}$ and $^4F_{9/2}$ [9-12,19-21]. **Fig. 5.9** depicts that glasses can be excited by several wavelengths in the ultraviolet and visible region. However, 383 nm is chosen as the excitation wavelength for the present study because the maximum intensity is found at this excitation wavelength.

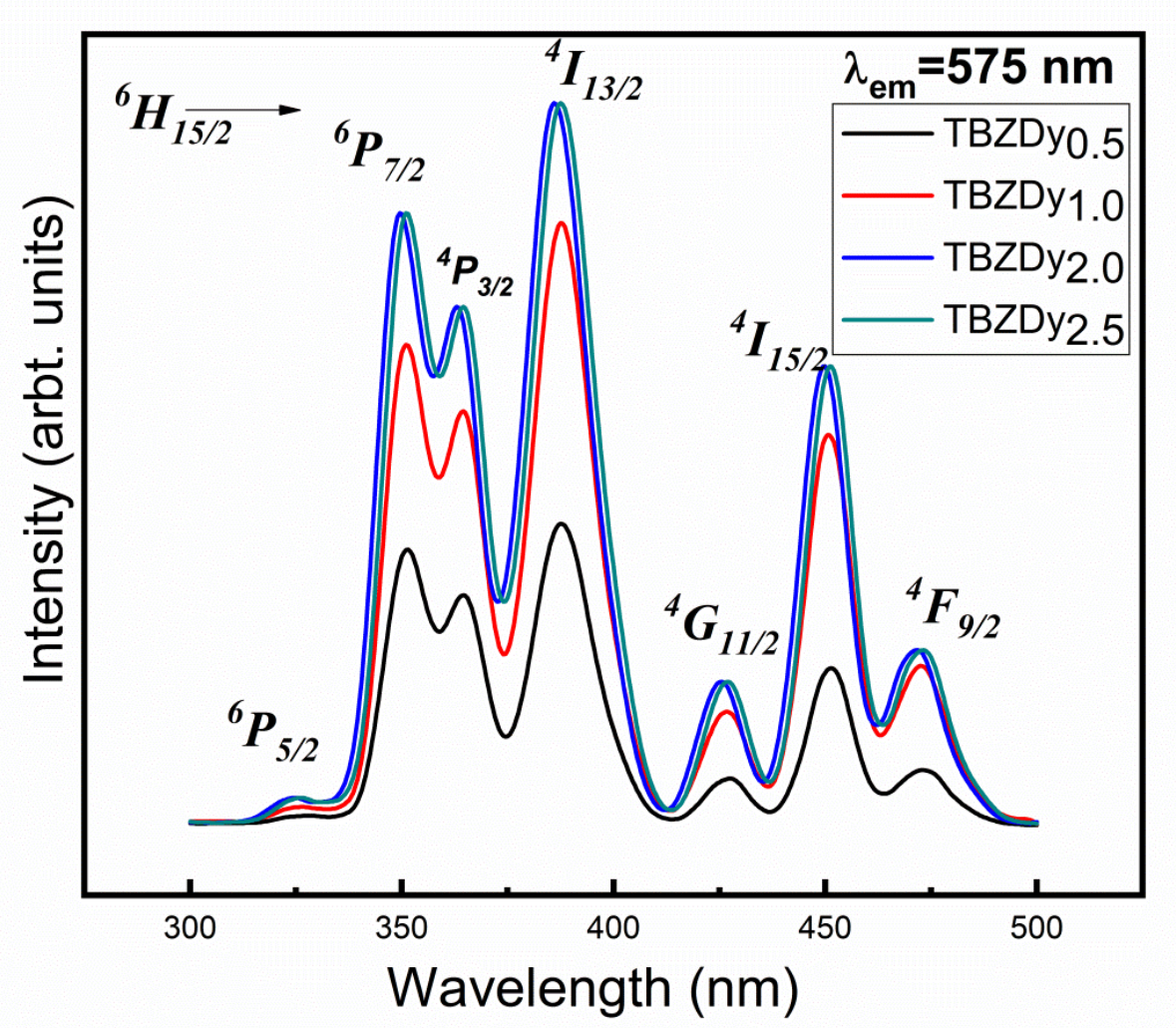

Fig. 5.9: Excitation spectra of Dy^{3+}:$TBZDy_x$ glasses at 575 nm emission

Fig. 5.10 shows visible emission spectra taken in 450-700 nm range at 383 nm for glasses and glass-ceramics. The Dy^{3+}-doped glasses show emission at 482 (blue) and 575 nm (yellow) corresponding to the transitions $^4F_{9/2} \rightarrow {}^6H_{15/2}$ and $^4F_{9/2} \rightarrow {}^6H_{13/2}$, respectively [32-40]. A weak emission is observed around at 663 nm (red) which is attributed to the transition $^4F_{9/2} \rightarrow {}^6H_{11/2}$ [37-40]. For the present glasses and glass-ceramics, yellow band located at 575 nm is more intense than the blue band which suggests that the Dy^{3+} ion is located at a lower symmetry local site [5].

It is worth noting that there is considerable variation in the emission intensities after heat treatment. Hence, to quantify these variations in the emission intensities due to different

concentration of Dy^{3+} in glasses and glass-ceramics a quantity is introduced. The Y/B ratio is the ratio of emission intensities of two dominant bands, i.e., yellow (electric dipole transition) and blue (magnetic dipole transition). The modifications in the Y/B ratio with increasing Dy^{3+} content are given in **Table 5.9**. From **Table 5.9** it is observed that there is a decrease in the value of Y/B ratios from 5.5 ($TBZDy_{2.5}$) to 1.57 ($TBZDy_{2.5}GC$). A reduction in the Y/B ratios of glass-ceramics can be understood by considering the structural changes that occur locally because of Dy^{3+} ions additions in the TeO_2 nano-crystals. These results are also supported by the decrease in the Ω_2 values after heat treatment. Similar results are found in Dy^{3+} doped oxyfluoride glasses and glass ceramics [4-6].

The emission spectra is further analyzed with the help of CIE 1931 colour coordinates [41]. The quality of the light source is studied in terms of the CCT values. **Fig. 5.10** depicts the CIE chromaticity color co-ordinates of Dy-doped glasses and the glass-ceramics at 383 nm excitation. **Fig. 5.11** shows that the CIE coordinates for glasses and glass ceramics lies in yellowish white and white light region respectively. The CIE –coordinate values along with CCT values are given in **Table 5.9**. The colour coordinates of glass samples after heat treatment are closer to Blue LED + YAG:Ce, HT-P278BPV (x = 0.32, y = 0.33), which is a commercial pc-LED [51]. Thus, by changing the environment of RE ions, the tuning of color co-ordinates can be done. The correlated color temperature values obtained for the glasses are in the range of fluorescent tube and day light i.e. 3935-5500 K, whereas, the CCT values of the glass-ceramics are closer to that of the cool sources.

Table 5.9: Yellow/Blue ratios, (x,y) and CCT, K at 383 nm excitation for Dy^{3+}:$TBZDy_x$ and $TBZDy_xGC$ systems

Sample ID →	**$TBZDy_{0.5}$**	**$TBZDy_{1.0}$**	**$TBZDy_{2.0}$**	**$TBZDy_{2.5}$**	**$TBZDy_{0.5}GC$**	**$TBZDy_{1.0}GC$**	**$TBZDy_{2.0}GC$**	**$TBZDy_{2.5}GC$**
Y/B	3.7:1	3.8:1	4.1:1	5.5:1	1.40:1	1.43:1	1.49:1	1.57:1
(x,y)	(0.43,0.44)	(0.42,0.43)	(0.43,0.43)	(0.42,0.43)	(0.32,0.34)	(0.32,0.34)	(0.32,0.35)	(0.33,0.32)
CCT	4776	4608	4698	4702	5609	6037	6071	6001

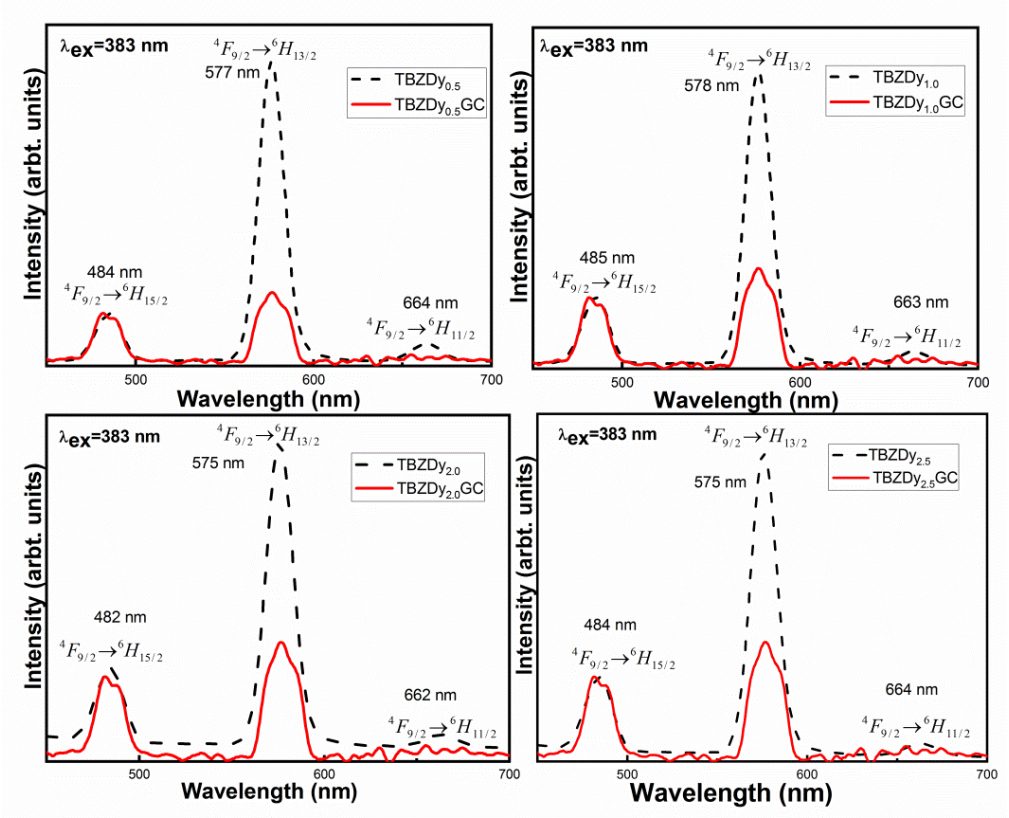

Fig. 5.10: Visible emission spectra of Dy^{3+}:$TBZDy_x$ and $TBZDy_xGC$ systems

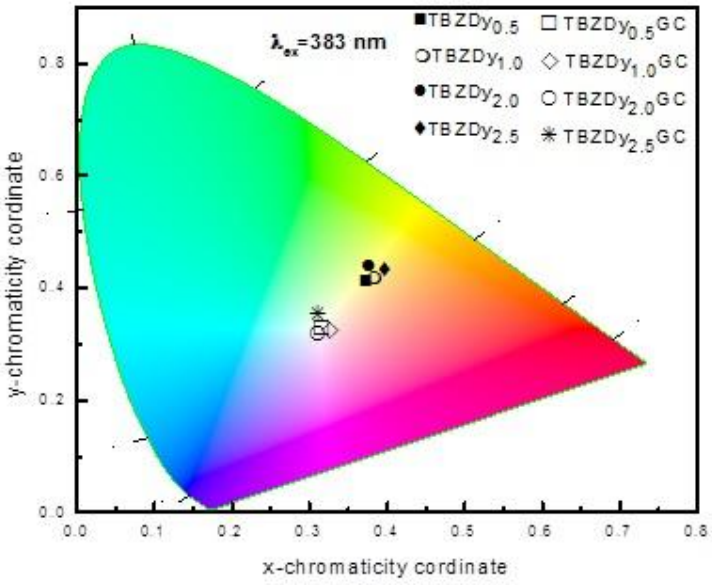

Fig. 5.11: CIE chromaticity colour co-ordinate diagram for Dy^{3+}:$TBZDy_x$ and $TBZDy_xGC$ systems at 383 nm excitation

5.6.2 Radiative properties

Radiative parameters have been determined for $^4F_{9/2} \rightarrow {}^6H_{13/2}$ transition with the help of Fuchtbauer-Ladenburg (FL) theory [13,43,44]. The radiative paramters of the present samples are given in **Table 5.10**.

Table 5.10: Radiative parameters of Dy^{3+}-doped glasses and glass-ceramics

Radiative parameter		TBZDy$_{0.5}$	TBZDy$_{1.0}$	TBZDy$_{2.0}$	TBZDy$_{2.5}$	TBZDy$_{0.5}$ GC	TBZDy$_{1.0}$ GC	TBZDy$_{2.0}$ GC	TBZDy$_{2.5}$ GC
$^4F_{9/2} \rightarrow {}^6H_{13/2}$	β_{exp} (%) ± 7	76	80	74	61	57	59	75	57
	β_{cal} (%) ± 7	64	78	60	53	58	69	67	65
	$\Delta\lambda_{eff\ (nm)}$ ± 0.79	8.58	10.25	11.54	12.36	9.35	12.55	14.16	15.86
	A_R (s^{-1}) ± 19	670	510	430	360	590	475	386	264
	σ_{emi} (10^{-22} cm^2) ± 7.21	67.25	67.94	68.91	70.53	36.13	37.21	38.25	39.35

The effective line width ($\Delta\lambda_{eff}$) of the emission transition is the measure of sharpness of a transition. The values of $\Delta\lambda_{eff}$ for glasses and glass-ceramics are found to be lower than Dy^{3+}:CBTZnD (14.176 nm) [33], Dy^{3+}:TZPPN (14.81 nm) [52] and Dy^{3+}:1CdBiB (24.484 nm) [53] glasses, and higher than Dy^{3+}:1DZTFB (7.225 nm) [22] glass. The transition having branching ratio, $\beta \geq 0.5$, could be considered for the possible lasing action. Hence, σ_{emi} is calculated and discussed for $^4F_{9/2} \rightarrow {}^6H_{13/2}$ transition having $\beta > 0.5$. From **Table 5.10**, it can be seen that the values of σ_{emi} decrease with the increasing in RE content as well as from glass to glass-ceramics. It is observed from **Table 5.10** that the σ_{emi} of the prepared samples is found to be higher than the reported Dy^{3+} doped 0.05DZTFB (6.275×10^{-22} cm^2) [22], Dy^{3+} doped CBTZnD ($4.992\times10^{-22}cm^2$) [33], Dy^{3+} doped BaF_2-B_2O_3 ($2.74\times10^{-22}cm^2$) [34], Dy^{3+} doped TZPPN (6.09×10^{-22} cm^2) [52] and PKBAF10 ($4.76\times10^{-22}cm^2$) [54] glasses. However, it is lower than the Dy^{3+} doped 1CdBiB ($24.38\times10^{-21}cm^2$) [53] and Dy^{3+} doped ZnO-PbO-P_2O_5 (8.80×10^{-21} cm^2) [55] glasses. The higher σ_{emi}, β and lower $\Delta\lambda_{eff}$ values of present samples imply their potential for the fabrication of WLEDs.

5.6.3 Decay curve analysis

Lifetime measurements for the $^4F_{9/2}$ level of dysprosium are shown in shown **Fig. 5.12**. The non-exponential nature of decay curves is observed for all the samples. It increases with increase in RE content. This can be due to resonant energy transfer and cross-relaxations

between RE-ions as shown in **Fig. 5.13.** With increase in the dysprosium content, increase in the non-exponential behavior is also observed.

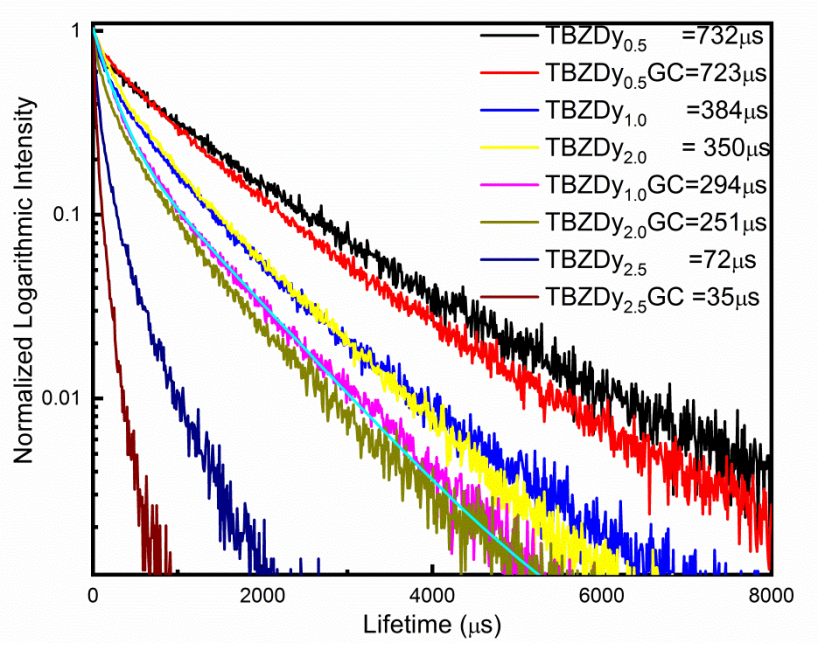

Fig. 5.12: Decay curves of prepared glasses and glass-ceramics (λ_{ex}=383nm, λ_{em}= 575 nm). Solid line IH fitting

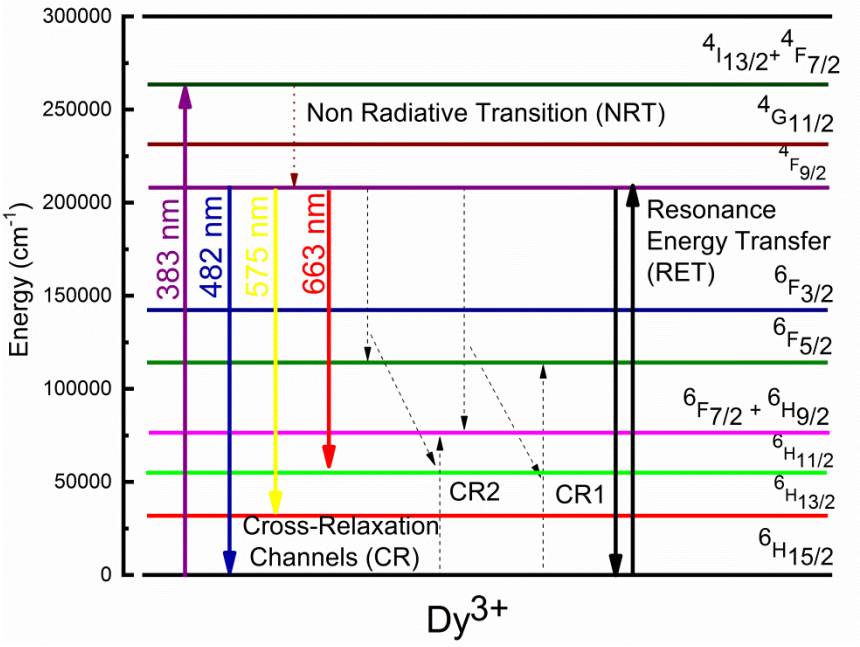

Fig. 5.13: Partial energy level diagram of Dy^{3+}:TBZDy_x and TBZDy_xGC systems

The ion–ion interaction and microscopic energy transfer mechanisms are studied with the help of Inokuti–Hirayama (IH) model [46]. The experimental lifetime (τ_{exp}) for the $^4F_{9/2}$ level are found to be 732, 384, 350, 72 μs of glasses and 723, 294, 251, 35 μs of glass-ceramics for the 0.5, 1.0, 2.0, 2.5 mol% of Dy^{3+}, respectively. It is worth noting that a there is a decrease in the lifetime values with an increase in RE content as well as with heat treatment. The decrease in the lifetime values is because of concentration quenching which inturn indicates an increase in the energy transfer rates between RE^{3+}- ions.

The energy transfer between RE^{3+}-ions can be calculated from the energy transfer parameter (Q) [46]. Results of the fitting for Dy^{3+}:$TBZDy_x$ and $TBZDy_xGC$ systems using IH model are given in **Table 5.11**. A good fit is obtained with Q = 2.36 and τ_0= 732 μs for $TBZDy_{0.5}$ glass and Q= 1.70 and τ_0= 723 μs for $TBZDy_{0.5}GC$ glass-ceramic **(Fig. 5.12)**. An increase in the magnitude of Q from 2.36 ($TBZDy_{0.5}$) to 6.05 ($TBZDy_{2.5}$) and 2.70 ($TBZDy_{0.5}$ GC) to 8.33 ($TBZDy_{2.5}GC$) with an increase in the rare earth content and heat treatment, respectively, is observed.

Table 5.11: Lifetime, quantum efficiency, and IH fitting paramters of Dy^{3+}:$TBZDy_x$ and $TBZDy_xGC$ systems

Sample ID	**τ_{rad} ± 45 (μs)**	**τ_{exp}± 32 (μs)**	**η ± 2 (%)**	**Q± 0.45**	**R_0 ± 1.5 (Å)**	**$C_{DA} \times 10^{-42}$ ± 1.25 cm^6 s^{-1}**	**W_{NR} ± 0.51**
$TBZDy_{0.5}$	1060	732	69	2.36	8.28	8.22	3.56
$TBZDy_{1.0}$	619	384	62	3.23	7.71	10.45	3.69
$TBZDy_{2.0}$	603	350	58	5.35	6.98	11.56	4.25
$TBZDy_{2.5}$	138	72	52	6.05	5.89	54.94	5.56
$TBZDy_{0.5}GC$	1205	723	60	2.70	7.95	10.22	4.01
$TBZDy_{1.0}GC$	498	294	59	3.90	6.25	13.52	4.25
$TBZDy_{2.0}GC$	482	251	52	6.44	4.12	16.49	4.89
$TBZDy_{2.5}GC$	61	35	57	8.33	2.95	23.91	6.23

Table 5.11 shows that the non-radiative transitions rate also increases with increasing RE content and heat treatment. Quantum efficiencies (η) are calculated for all the prepared samples as given in **Table 5.11**. The τ_{rad} are calculated with the help of JO parameters. The τ_{exp} and τ_{rad} for $^4F_{9/2}$ level of Dy^{3+} glasses and glass-ceramics are reported in **Table 5.11**. An inconsistency between the values of τ_{exp} and τ_{rad} has been observed. A decrease in the values of η is observed with increasing RE content. The decrease can be because of enhanced energy transfer between RE^{3+} ions. The decrease in η is further supported by increase in the non-exponential character of decay curves. The obtained quantum efficiency 'η' for the

$TBZDy_x$ glass and glass ceramics is given in **Table 5.11**. The results suggests that present glass samples have good lasing action. It is to noted that 'η' for the present glasses and glass-ceramics is relatively higher than those reported for GC1 (41%) [4], GC2 (23%) [4], BTLN0.25D (45%) [21], BTLN2D (38%) [21], BTKA0.05D (34%) [31], BTKA0.5D (40%) [31], BTKA2.0D (26%) [31], CBTZnD (44%) [33] LSBP0.5Dy (57%) [35], LSBP1Dy (39%) [35] and is low compared to those reported for 0.5LBTPD (85%) [19], 0.25LBTPD (89%) [19], 0.01DZCTFB (71%) [33], 0.05DZTFB (73%) [34], LSBP0.1Dy (74%) [35], BTLN0.05D (74%) [21] glasses.

References

1. C. Yu, J. Zhang, L. Wen, Z. Jiang, Mater. Lett., 61(2007) 3644-3646.
2. O. Maalej, M. El Jouad, N. Gaumer, S. Chaussedent, B. Boulard, M. D. B. Ameur, M. D. B. Tijani, J. Non. Cryst. Solids, 420 (2015) 48-54.
3. J. Xie, Q. Zhang, Y. Zhuang, X. F. Liu, M. Guan, B. Zhu, R. Yang, J. Qiu, J. Alloys Compd., 509 (2011) 3032-3037.
4. P. Babu, K. H. Jang, E. S. Kim, L. Shi, R. Vijaya, V. Lavin, C.K. Jayasankar, H. J. Seo, J. Non. Cryst. Solids, 350 (2010) 236-243.
5. R. Bagga, V. G. Achanta, A. Goel, J. M.F. Ferreira, N. P. Singh, D. P. Singh, M. Falconieri, G. Sharma, Mater. Sci. Eng., B 178 (2013) 218-224.
6. P. Babu, K. Hyuk Jang, Ch. S. Rao, L. Shi, C. K. Jayasankar, V. Lavín, H. J. Seo, Opt. Express, 19 (2011) 1836-1841.
7. M. Jayasimhadri, L.R. Moorthy, K. Kojima, K. Yamamoto, N. Wada, J. Phys. D: Appl. Phys., 39 (2006) 635-641.
8. W.T. Carnall, P.R. Fields, K. Rajnak, J. Chem. Phys. 49 (1968) 4424-4442.
9. I. Arul Rayappan, K. Marimuthu , S. Surendra Babu , M. Sivaraman, J. Lumin., 130 (2010) 2407-2412.
10. M. V. S. Kumar, D. Rajesh, A. Balakrishna and Y. C. Ratnakaram, J. Mol. Struct., 1041 (2013) 100-105.
11. R. V. Kumar, S.B. Rai, Sol. State. Commun., 132 (2004) 647-652.
12. P. Chimalawong, K. Kirdsiri, J. Kaewkhao, P. Limsuwan, Procedia Engin., 32 (2012) 690 – 698.
13. C. Gorller-Walrand, K. Binnemans, Spectral intensities of f-f transitions in Handbook on the Physics and Chemistry of Rare Earths edited by K.A. Gscheneidner Jr. and L. Eyring (North Holland, Amsterdam, 1998), 25 (1998)101-264.
14. C.K. Jayasankar, M.F. Reid, F.S. Richardson, Phys. Stat. Sol. (b), 155(2) (1989) 559-569.
15. C.K. Jayasankar, K. R. Setty, P. Babu, Th. Troster, W.B. Holzapfel, Phys. Rev. B., 69 (2004) 214108 (1-7).
16. K. S. Lim, N. Vijaya, C.R. Kesavulu ,C.K. Jayasankar, Opt. Mater., 35(8) (2013)1557-1563.
17. C.K. Jayasankar, V. Venkatramu, S. Surendra Babu, P. Babu, J. Alloys Compds., 374 (2004) 22-26.
18. C.R. Kesavulu ,C. K. Jayasankar, Mater. Chem. Phys., 130 (2011) 1078-1085.
19. S. Selvi, G. Venkataiah, S. Arunkumar, G. Muralidharan, K. Marimuthu, Physica B, 454 (2014) 72-81.
20. O. Ravi, C. M. Reddy, B. S. Reddy, B. D. P. Raju, Opt. Comm., 312 (2014) 263-268.
21. V. Uma, K. Maheshvaran, K. Marimuthu, G. Muralidharan, J. Lumin., 176 (2016) 15–24.
22. M. N. Ami Hazlin, M.K. Halimah, F.D. Muhammad, J. Lumin., 196 (2018) 498-503.
23. N. Chopra, S. Kaur, M. Kaur, S. Singla, R. Marwaha, G. Sharma, M. S. Heer, Phys. Status Solidi A, 215 (2018) 1700934 (1-7).
24. A. E. Ersundu, G. Karaduman, M. Celikbilek, N. Solak, S. Aydın, J. Alloys Compds., 508 (2010) 266-272.

25. N. Jaba, A. Mermet, E. Duval, B. Champagnon, J. Non-Cryst. Solids, 351 (2005) 833-837.
26. L. Jyothi, G. Upender, R. Kuladeep, D. Narayana Rao, Mater. Res. Bull., 50 (2014) 424-431.
27. F. M. Fudzi, H. M. Kamari, A. A. Latif, A. M. Noorazlan, J. Nanomater., 2017 (2017) 4150802 (1-8).
28. P.G. Pavani, K. Sadhana, V. C. Mouli, Physica B, 406 (2011) 1242-1247.
29. S. Surendra Babu, K. Jang, E. J. Cho, H. Lee, C. K. Jayasankar, J. Phys. D: Appl. Phys., 40 (2007) 5767-5774.
30. A. Kaur, A. Khanna, C. Pesquera, F. González, V. Sathe, J. Non. Cryst. Solids, 356 (2010) 864–872.
31. K. Annapoorani, P. Karthikeyan, Ch. Basavapoornima, K. Marimuthu, J. Non. Cryst. Solids, 476 (2017) 128-136.
32. P. Karthikeyan, S. Arunkumar, K. Annapoorani, K. Marimuthu, Spectrochim Acta A Mol Biomol Spectrosc., 193 (2018) 422-431.
33. P. Karthikeyan, R. Vijayakumar, K. Marimuthu, Physica B, 521 (2017) 347-354.
34. P. S. Kumar, K. Marimuthu, J. Mole. Struct., 1125 (2016) 443-452.
35. R. Vijayakumar, G. Venkataiah, K. Marimuthu, J. Alloys Compds., 652 (2015) 234-243.
36. J. Pisarska, J. Phys.: Condens. Matter, 21 (2009) 285101(1-7).
37. K. V. Krishnaiah, K.U. Kumar, C. K. Jayasankar, Mater. Express, 3 (2013) 61-70.
38. L. Gomes, J. Lousteau, D. Milanese, E. Mura, S. D. Jackson, J. Opt. Soc. Am. B: Opt. Phys., 31(2014) 429-435.
39. S. Tanabe, T. Hanada, M. Watanabe, T Hayashi, N. Soga, J. Am. Ceram. Soc., 78 (1995) 2917-2922.
40. A. M. Babu, B.C. Jamalaiah, J. Suresh Kumar, T. Sasikala, L. Rama Moorthy, J. Alloys Compds., 509 (2011) 457–462.
41. "Commission Internationale de l'Eclairage, Huitieme Session, Cambridge, September 1931", Recueil des Travaux et Compte Rendu des Séance, The University Press, Cambridge 1932, Resolution 2 (1932) 19-32.
42. C. S. McCamy, COLOR research and application 17, (1992)142-144.
43. B. F. Aull, H. P. Jenssen, IEEE J. Q. Ele., 18 (1982) 925-930.
44. T. Schweizer, D. W. Hewak, B. N. Samson, D. N. Payne, Opt. Lett., 21(1996)1594-1596.
45. D. C. Yeh, W. A. Sibley, M. Suscavage, M. G. Drexhage, J. Appl. Phys., 62 (1987) 266-275.
46. M. Inokuti, F. Hirayama, J. Chem. Phys., 43 (1965) 1978-1989.
47. I. Jlassi, H. Elhouichet, S. Hraiech, M. Ferid, J. Lumin., 132 (2012) 832-840.
48. U. Hoppe, E.Yousef, C. Russel, J. Neuefeind, A.C. Hannon, J, Phy: Condens. Mater., 16 (2004) 1645-1663 .
49. M. C. Gonçalves, L. F. Santos, R. M. Almeida, C. R. Chimie, 5 (2002) 845–854.
50. D.K. Sardar, J.B. Gruber, B. Zandi, J.A. Hutchinson, C.W. Trussell, J. Appl. Phys., 93 (2003) 2041-2046.
51. T. Erdem, S. Nizamoglu, X. W. Sun, H. V. Demir, Opt. Express, 18 (2010) 340-347.

52. K. Damak, E. S. Yousef, C. Rüssel, R. Maâlej, J. Quant. Spectrosc. Radiat. Transfer, 134 (2014) 55–63.
53. S. Sailaja, C. Nageswara Raju, C. Adinarayana Reddy, S. Hemasundara Raju, U. Rambabu, B. Sudhakar Reddy, Ferroelectric Lett. Sec., 40 (2013) 30-40.
54. R. Praveena, R. Vijaya, C. K. Jayasankar, Spectrochim. Acta Pt A, 70 (2008) 577–586.
55. R. J. Amjad, M. R. Sahar, S. K. Ghoshal, M. R. Dousti, R. Arifin, Opt. Mater., 35 (2013) 1103–1108.
56. N. Gupta, A. Kaur , A. Khanna, F. Gonzàlez, C. Pesquera , R. Iordanova , B. Chen, J. Non. Cryst. Solids, 470 (2017) 168-177.

Effect of gamma irradiation on (70-x)TeO_2-20B_2O_3-10ZnO-xEr_2O_3

Overview

The present chapter deals with variations in thermal and spectroscopic properties of the Er_2O_3 glasses after 50 kGy gamma irradiation. The structural analysis of the irradiated glass samples showed some structural changes in terms of formation of new structural units after irradiation. Emission intensity decreases after irradiation because of increase in non-radiative transitions. The chapter also discusses about the characteristic shielding properties of as- prepared TBZEr_x samples in detail. It has been observed that the shielding properties of the samples improved with the RE addition.

6.1 Introduction

Influence of different types of harmful radiations on living bodies are of major concern to our society [1-5]. These radiations originate from different sources like nuclear medicines, nuclear power plants, space etc. According to a report by NASA, astronauts are exposed to different ionizing radiation with effective doses in the range from 50 to 2 Sv. Such high energy radiations with large penetration depth can cause threat to the living beings. Therefore, researchers are trying to develop different types of shielding materials. The shielding materials can reduce the penetration of such radiations, thereby decreasing its harmful impact. The commonly used shielding materials are concrete, polymers, alloys, bricks, etc. However, these materials are opaque. The present situation demands to develop transparent shielding materials for reactors and medical applications.

Among various available shielding materials, glasses are the potential candidates for the same. This is because of their cost effectiveness, homogeneity, good chemical stability, transparency and high attenuation coefficients [6-15]. Glasses can also be fabricated in different shapes and sizes. Hence, it enables researchers to tune their physical and optical properties [16-27]. Many researchers are trying to improve the shielding properties of the glasses. Sayeed et al. [7] studied tellurite glasses and found that these glasses possess good shielding properties due to high mass attenuation coefficients. RE- doped glasses have also gained interest for their shielding properties. In a study, Saidu et al. [4] incorporated terbium ions into zinc lithium borate glasses which enhanced the dosimetry properties of the glasses by many folds. Hegde et al. [6] studied bismuth borate glasses doped with Eu_2O_3 and reported that rare earth ions cause shielding effect against the high dosage radiations.

Motive of this work is to analyze impact of 50 kGy gamma rays on structural and spectroscopic properties of TBZEr_x samples. The 50 kGy dosage is used for the reason that according to various studies it is an optimized dosage that can be used to sterilize medical instruments and pathogen inactivation [2,3]. Moreover, shielding properties like MAC, HVL and Z_{eff} are studied and presented in this chapter.

6.2 Physical Studies: Density

The effect of gamma irradiation on density has been analyzed to understand the extent of modifications occurred in the glasses after gamma irradiation. It has been observed from **Table 6.1** that there is a decrease in density of the undoped sample after irradiation. It may be because of the irradiation induced defects like generation of electron-hole pairs, breaking of bonds present between already existing structural groups in matrix, etc. These defects allow the glass structure to open up and hence decrease the density. It is also observed that there is no significant effect of irradiation on density of glasses doped with rare earth. This indicates that the doped samples are radiation resistant and can have better shielding properties than the un-doped sample.

Table 6.1: Density of the as prepared and gamma irradiated glasses

Sample	**Density (g/cm^3) ±2%**
$TBZEr_{0.0}$	4.72
$TBZEr_{0.5}$	4.79
$TBZEr_{1.0}$	4.86
$TBZEr_{2.0}$	4.90
$TBZEr_{2.5}$	4.95
$TBZEr_{0.0}$50kGy	4.67
$TBZEr_{0.5}$50kGy	4.76
$TBZEr_{1.0}$50kGy	4.84
$TBZEr_{2.0}$50kGy	4.88
$TBZEr_{2.5}$50kGy	4.93

6.3 Thermal studies of the gamma irradiated glasses

Fig. 6.1 shows DTA patterns of $TBZEr_x$50kGy glasses. The transition (T_g), crystallization temperatures (T_{c1} and T_{c2}) along with thermal stability are given in **Table 6.2.** A decrease in the transition temperature of the as-prepared glasses is observed after gamma irradiation. This decrease in the characteristic temperatures can be understood on the basis of number of TeO_{3+1} and BO_{3+1} units. Because of irradiation there is an increase in such units. It results into opening up of glass structure. Also gamma irradiation creates large number of defects in system which weakens the structure leading to decrease in the characteristic temperatures.

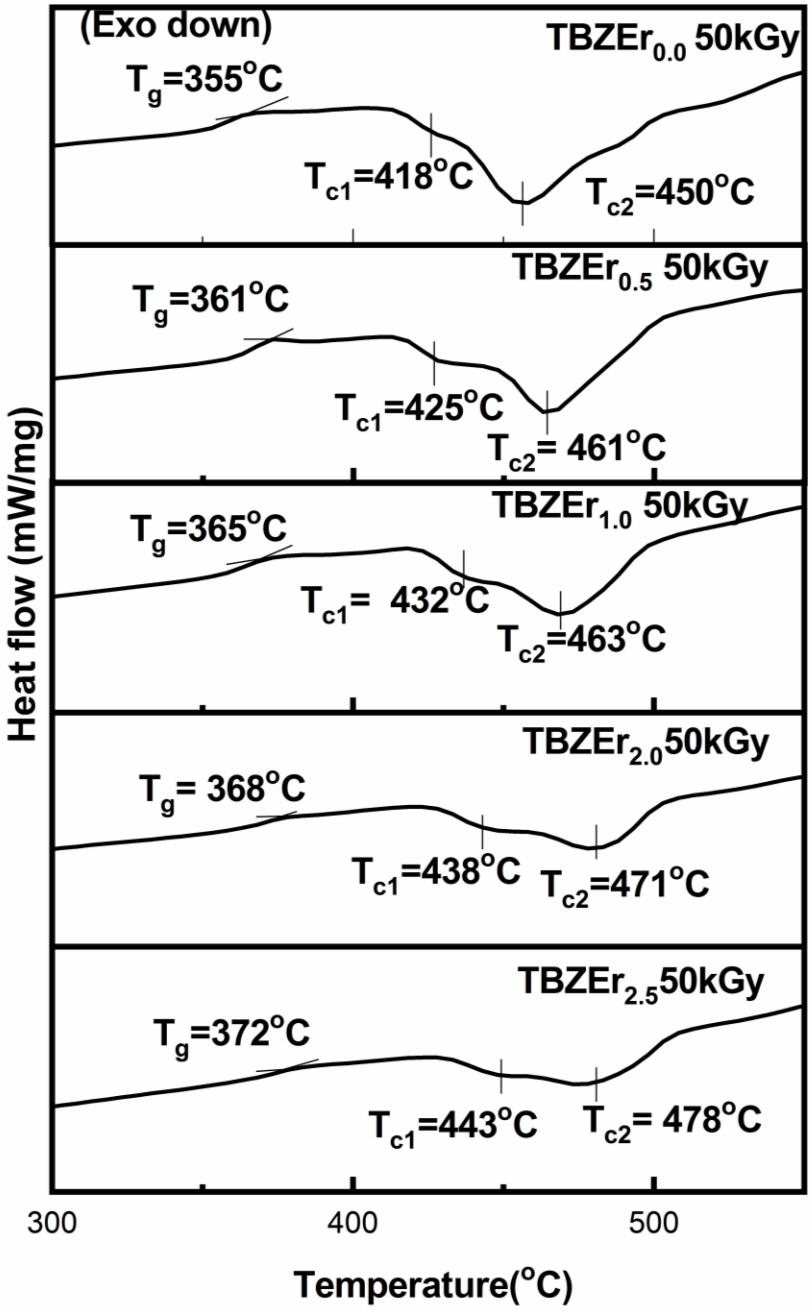

Fig. 6.1: DTA graphs of gamma irradiated glasses

Table 6.2: Thermal parameters of $TBZEr_x$ glasses before and after gamma irradiation

Sample code	T_g±1 (^oC)		T_{c1}±1 (^oC)		T_{c2}±1 (^oC)		$\Delta T=T_{c1}-T_g$ (^oC)	
	Before	**After**	**Before**	**After**	**Before**	**After**	**Before**	**After**
$TBZEr_{0.0}$	364	355	424	418	455	450	60	54
$TBZEr_{0.5}$	369	361	432	420	466	461	63	59
$TBZEr_{1.0}$	370	365	438	432	469	463	68	67
$TBZEr_{2.0}$	375	368	444	438	479	471	69	70
$TBZEr_{2.5}$	378	372	449	443	481	478	71	71

6.4 Structural Studies

6.4.1 X-ray diffraction (XRD):

The XRD diffractograms of irradiated $TBZEr_x$50kGy glasses are given in **Fig. 6.2**. All glass samples exhibit similar XRD patterns. The absence of Bragg's peaks confirms amorphous nature of samples even after gamma irradiation.

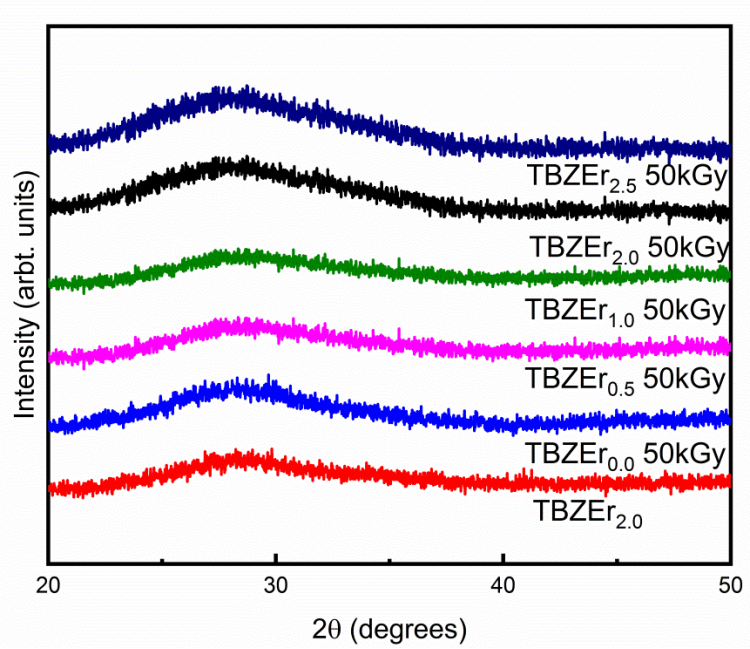

Fig. 6.2: X-ray diffraction pattern of glasses after gamma irradiation. Bottom graph shows XRD pattern of $TBZEr_{2.0}$ before irradiation

6.4.2 Raman Spectroscopy

The modifications in structure after irradiation are studied by Raman measurements. **Fig. 6.3(a)** shows the Raman spectra of the irradiated glasses. In order to have a detailed insight at the Raman bands associated with TeO_2 structural units, the de-convolution of the spectrum has been done. **Fig. 6.3(b)** shows the deconvoluted spectra of $TBZEr_{0.5}$ 50kGy. No significant effect of irradiation and RE doping on the number of band and band positions is observed.

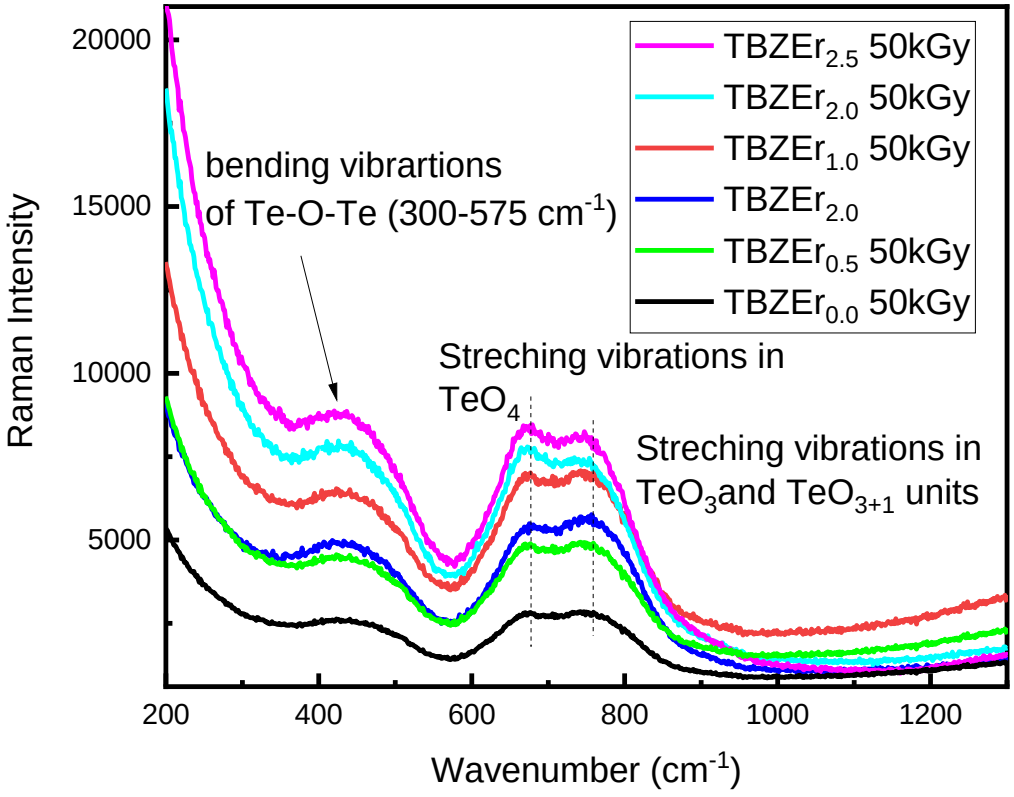

Fig. 6.3(a): Raman spectra of samples irradiated at 50 kGy

The 300-500 cm^{-1} region belongs to stretching and bending vibrations of the Te–O–Te bonds [29]. Bands centered at 615 and 666 cm^{-1} are attributed to asymmetric bending and stretching vibrations of TeO_4 units with BOs respectively [30]. Bands centered at 720 and 770 cm^{-1} are due to symmetric bending and stretching vibrations of TeO_3 and TeO_{3+1}trigonal pyramid (tp)

units having NBOs [31]. **Fig. 6.3 (c)** gives the normalized intensities of the Raman bands after de-convolution at different RE- concentrations.

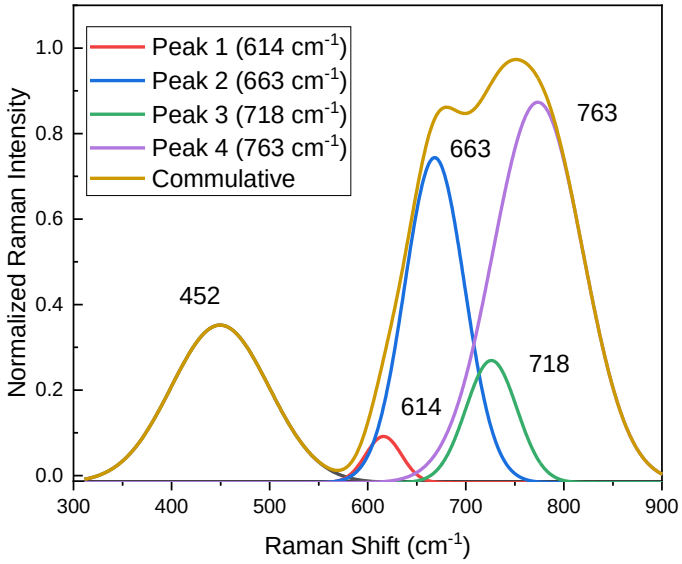

Fig. 6.3(b): De-convoluted Raman spectrum of $TBZEr_{2.0}$ 50kGy after irradiation

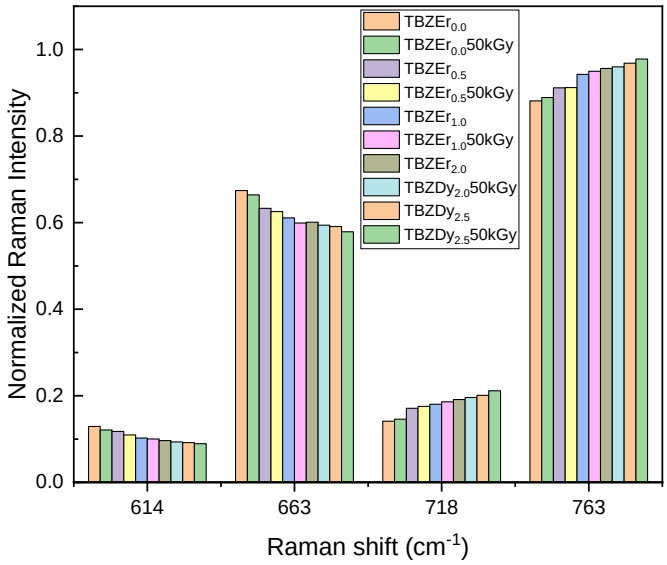

Fig. 6.3(c): Normalized intensities of the Raman bands after de-convolution at different RE-concentrations

It is observed that there is a decrease in the amplitude of the bands at 615 and 666 cm^{-1} w.r.t. bands at 720 and 770 cm^{-1} after irradiation **(Fig. 6.3 (c))**. It may be due to the breakage of Te-O-Te bonds which in turn leads to systematic conversion TeO_4 structural groups to TeO_{3+1} units [15]. Thus there is increase in TeO_3 structural units with NBOs [15].

6.4.3Fourier Transform Infrared spectroscopy (FTIR):

The FTIR spectra of the present glasses (post and pre gamma irradiation) in the region 450–1500 cm^{-1} are presented in **Fig. 6.3 (d,e)**. The observed vibrational modes are divided into three distinct frequency regions of 1500-1200 cm^{-1}, 1100-700 cm^{-1} and 700-500 cm^{-1}. The FTIR spectrum shows the presence of trigonal pyramidal TeO_3 and TeO_4 units in the region 700-600 cm^{-1} [28]. A band at 768 cm^{-1} is attributed to TeO and TeO^- bonds of trigonal pyramidal TeO_3 units [29]. The intermediate region (1100-700 cm^{-1}) belongs to B-O stretching vibrations of BO_4, whereas the bands observed in the higher wavenumber region i.e. 1500-1200 cm^{-1} are due to stretching vibrations of B-O bond in BO_3 units [30,31]. **Table 6.3** represents the observed functional vibration groups (in cm^{-1}) of Er^{3+}-doped zinc borotellurite glasses.

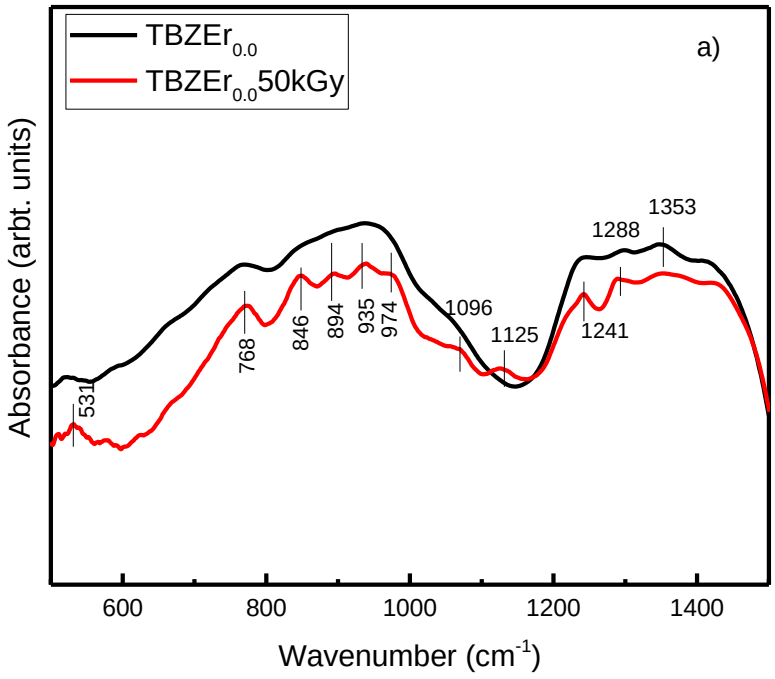

Fig. 6.3(d): Infrared absorbance spectra of the base glass ($TBZEr_{0.0}$) before and after gamma irradiation

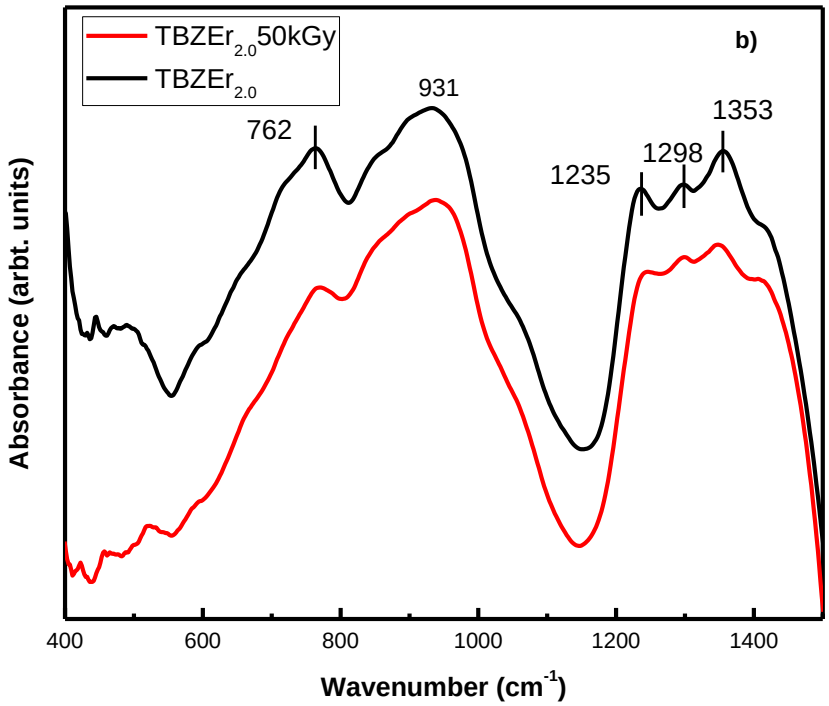

Fig. 6.3 (e): Infrared absorbance spectra of $TBZEr_{2.0}$ before and after irradiation

Table 6.3: Assignment of IR bands present in the samples

S.No.	Band position	Assignment of bands
1.	575-639	Trigonal bipyramidal TeO_4 units [28]
2.	762	TeO and TeO^- bonds of TeO_3 units [28]
3.	806-1152	B-O stretching vibrations of BO_4 tetrahedra due to B-O vibrations of pentaborate, tetraborate and diborate structural units [29]
4.	1155-1258	Stretching vibrations of BO_3 tetrahedra due to B-O involving mainly the linkage of oxygen connecting different groups [29]
5.	1260-1316	Assigned to stretching vibrations of the B-O of trigonal $(BO_3)^{3-}$ units in metaborate, pyroborates and orthoborates [30]
6.	1353	Due to anti- symmetric stretching vibrations with three NBOs of B-O-B groups [31]

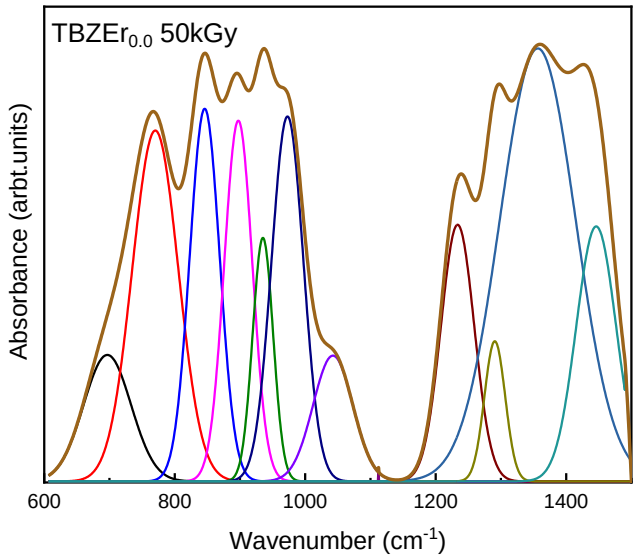

Fig. 6.3(f): The deconvoluted FTIR spectra of $TBZEr_{0.0}$50kGy

Fig. 6.3(f) shows the deconvoluted graph of $TBZEr_{0.0}$50kGy. **Fig. 6.3(g)** gives the variations in the intensity of Er^{3+}-doped zinc borotellurite glasses before and after gamma irradiation. It is clear from **Fig. 6.3(g)** that the base glass shows distinct changes after the gamma ray irradiation. The FTIR spectrum of the glasses is deconvoluted in order to see the structural modifications. It is clear from the **Fig. 6.3(g)** that new bands appear at 845 and 897 cm^{-1} for the $TBZEr_{0.0}$50kGy. It may due to the fact that the energy transferred by gamma rays can break some bonds in the glass network. This leads to the weakening of the already disordered glass system. Another band at 1125 cm^{-1} is observed after irradiation corresponds to B-O vibrations of the BO_{3+1} structural units. On the other hand, it is observed from the **Fig. 6.3(g)** that the glass samples containing Er^{3+}- ion do not show the appearance of the new bands except for some intensity variations. It has been observed that after gamma irradiation the intensity of structural units having NBO's has increased. This can be related to the increase in the cross linking of the glass network with the RE addition. The FTIR results suggest that the rare earth ions present in the system act as shielding materials.

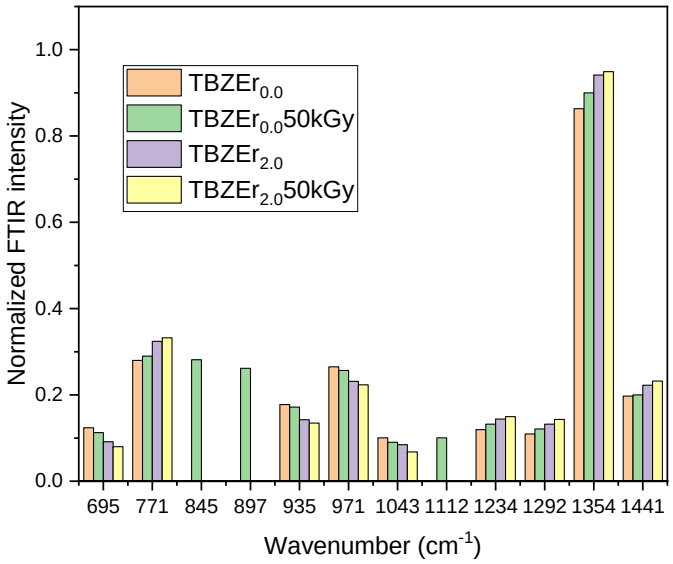

Fig. 6.3(g): Normalized intensities of the FTIR bands after de-convolution at different RE-concentrations

6.5 Absorption Spectroscopy: Judd Ofelt (JO) studies

The absorption spectrum for the present samples is shown in **Fig. 6.4**. Bands observed are due to absorption from of ground state of Er^{3+} ($^4I_{15/2}$) to different excited states. The position of absorption bands has been found to be independent of irradiation and increasing RE concentration. The absorption cross-section $\alpha_a(\lambda)$ for the transitions from $^4I_{15/2}$ to $^4H_{11/2}$ (hypersensitive transition) has been calculated using following relation:

$$\alpha_a(\lambda) = \frac{2.303 \times absorbance\ (\lambda)}{Nt} \quad (6.1)$$

Where, 'N' is the concentration of the Er^{3+} ions and 't' is the thickness of the samples. It is a well known fact that some transitions in REs are sensitive to their local environment in the matrix. Such transitions are known as hypersensitive transitions and follows the selection rules $\Delta S = 0$, $|\Delta L| = \leq 2$ and $|\Delta J| = \leq 2$. The values of absorption cross-section for the hypersensitive transition are tabulated in **Table 6.4**. It is clear from **Table 6.4** that the absorption cross-section has increased after gamma irradiation. This is because when glasses are irradiated, the electrons and holes are produced which increases the absorption coefficient of glasses.

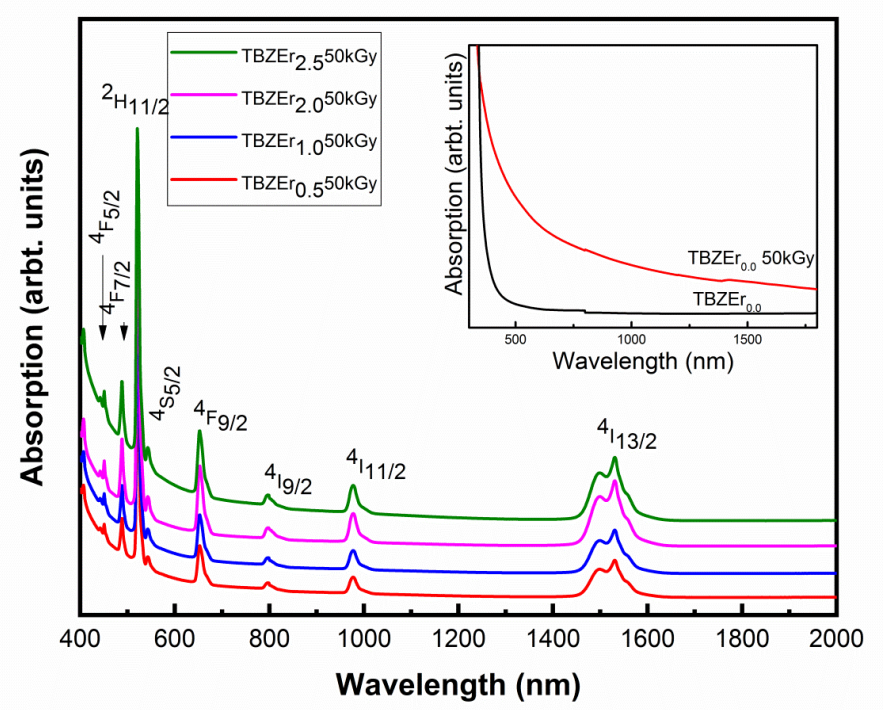

Fig. 6.4: Absorption spectra of $TBZEr_x$ samples after 50kGy at irradiation

Table 6.3 gives the energy gap and refractive index values of present samples**.** From **Table 6.4** it can be seen that there is a decrease in the energy gap (direct and indirect) because of irradiation due to modifications/induced defects in energy levels. These defects can generate localized energy states in forbidden gap of materials. The electronic transitions between the newly formed these states in turn reduce the energy gap.

Table 6.4: The band gap, Urbach energy, refractive index and absorption cross-section of the present samples

Sample ID	Direct energy gap ± 0.21 (eV)	Indirect energy gap ± 0.32 (eV)	Urbach Energy ± 0.02 (eV)	Refractive index N ± 0.87	Absorption Cross-section ± 2 (× 10^{-21} cm^2)
$TBZEr_{0.0}$50kGy	3.31	3.18	0.26	2.26	-
$TBZEr_{0.5}$50kGy	3.21	3.17	0.24	2.30	11.98
$TBZEr_{1.0}$50kGy	3.11	3.15	0.26	2.36	12.96
$TBZEr_{2.0}$50kGy	2.85	3.09	0.40	2.40	13.12
$TBZEr_{2.5}$50kGy	2.29	2.68	0.63	2.53	13.24
$TBZEr_{0.0}$	3.42	3.32	0.19	2.29	-
$TBZEr_{0.5}$	3.28	3.24	0.20	2.32	11.32
$TBZEr_{1.0}$	3.19	3.21	0.21	2.38	12.87
$TBZEr_{2.0}$	2.89	3.18	0.36	2.42	12.98
$TBZEr_{2.5}$	2.34	2.79	0.59	2.56	13.11

The energy gap of irradiated samples further decreases with increase in RE concentration. It is because with increasing RE content TeO_{3+1} and BO_{3+1} units also increase. It is noted that the energy gap values of glasses containing RE are less affected by gamma irradiation as compare to base sample ($TBZEr_{0.0}$50kGy). This happens because REs acts as shielding agents for the glass structure against irradiation. The refractive index calculated with the help of Dimitriov and Sakka relation. Another important feature of amorphous materials is Urbach energy also known as Urbach tail (ΔE). The increase observed in ΔE values **(Table 6.4)** of the irradiated samples indicates the creation of defects in the glasses. The values of refractive index follow opposite trend as that of energy gap. The changes are because of structural changes. **Table 6.5(a)** gives the oscillator strengths of the samples after gamma irradiation. It has been observed from **Table 6.5(a)** that the oscillator strengths increases after gamma irradiation which in-turn predict a decrease in the emission intensities due to the local defects generated due to gamma irradiation. The calculated (f_{cal}) and experimental (f_{exp}) oscillator strengths prepared samples are given in **Table 6.5 (a)**. The root mean square deviation (δ_{rms}) between two oscillator strengths is ≤ 1. It suggests good agreement between calculated and experimental f-values. The values of oscillator strength are found to be maximum for the transition from $^4I_{15/2}$ to $^4G_{11/2}$ in case of $TBZEr_x$50kGy which is also a hypersensitive transition.

Table 6.5 (a): Oscillator strengths ($\times 10^{-6}$) and RMS deviation (δ_{rms}) for $TBZEr_x$50kGy

Transition $^4I_{15/2}\rightarrow$	**$TBZEr_{0.5}$ 50kGy**		**$TBZEr_{1.0}$kGy**		**$TBZEr_{2.0}$kGy**		**$TBZEr_{2.5}$kGy**	
	f_{cal}	**f_{exp}**	**f_{cal}**	**f_{exp}**	**f_{cal}**	**f_{exp}**	**f_{cal}**	**f_{exp}**
$^4I_{13/2}$	0.92	0.62	1.15	0.84	0.91	0.84	1.24	1.54
$^4I_{11/2}$	1.07	0.33	1.26	1.04	1.04	0.62	1.09	0.82
$^4I_{9/2}$	0.65	0.90	0.54	0.55	0.46	0.84	0.84	0.62
$^4F_{9/2}$	0.71	0.49	0.64	0.36	0.62	0.29	0.24	0.21
$^4S_{3/2}$	0.68	0.54	0.34	0.64	1.54	1.04	0.21	0.19
$^2H_{11/2}$	0.85	0.24	0.14	0.23	0.65	0.45	0.24	0.21
$^4F_{7/2}$	4.01	3.01	4.34	3.46	4.35	4.58	2.12	1.65
$^4F_{5/2}$	4.14	4.32	3.25	3.52	4.84	4.25	4.91	2.89
$^4G_{11/2}$	11.39	11.24	10.60	10.51	10.41	10.24	10.50	10.61
$^2G_{11/2}$	1.24	1.79	1.15	1.66	1.04	1.25	1.51	1.48
$^4G_{9/2}$	3.14	3.31	2.24	2.54	3.88	3.25	3.92	3.51
δ_{rms}	0.56		0.60		0.61		0.52	

To obtain additional information about site to site variations and symmetry around Er^{3+} ions in the host matrix, JO theory has been applied [33-36]. The calculated values of oscillator strengths and JO parameters are given in **Table 6.5 (b)**. The present glasses follow trend as $\Omega_2 > \Omega_4 > \Omega_6$ **(Table 6.5 (b))**. It is noted that a marginal decrease in the value of Ω_2 is observed after irradiation. The decrease can be due to the decrease in the covalent character after irradiation. It is observed that Ω_2 values of present samples are higher than TZF35 (30.2×10^{-21} cm^2) [37], ZBE1 (39.4×10^{-21} cm^2) [38], ZBZE2 (36.9×10^{-21} cm^2) [38], ZBZE3 (30.2×10^{-21} cm^2) [38], N3BEr (20.24×10^{-21} cm^2) [39], B0TEr (38.43×10^{-21} cm^2) [40], Er: NAPT (35.0×10^{-21} cm^2) [41].

Table 6.5 (b): JO parameters (x 10^{-21} cm^2) and their trend

Sample Code	$\Omega_2 \pm 10.2$	$\Omega_4 \pm 5.5$	$\Omega_6 \pm 2.5$	Trend
$TBZEr_{0.5}$	100.2	48.4	27.0	$\Omega_2 > \Omega_4 > \Omega_6$
$TBZEr_{1.0}$	92.0	27.4	25.5	$\Omega_2 > \Omega_4 > \Omega_6$
$TBZEr_{2.0}$	76.9	24.6	11.9	$\Omega_2 > \Omega_4 > \Omega_6$
$TBZEr_{2.5}$	61.7	43.2	32.7	$\Omega_2 > \Omega_4 > \Omega_6$
$TBZEr_{0.5}$ 50Gy	99.1	45.0	23.6	$\Omega_2 > \Omega_4 > \Omega_6$
$TBZEr_{1.0}$ 50kGy	91.7	26.5	17.2	$\Omega_2 > \Omega_4 > \Omega_6$
$TBZEr_{2.0}$50kGy	75.8	23.4	11.9	$\Omega_2 > \Omega_4 > \Omega_6$
$TBZEr_{2.5}$50kGy	61.1	42.4	30.4	$\Omega_2 > \Omega_4 > \Omega_6$

Higher Ω_2 values of present samples indicate large asymmetry around Er^{3+}. The large values of Ω_2 in the present case are due to the large polarization of Te^{4+} ions and asymmetry in the vicinity of the Er-ions [16].

6.6 Spectroscopic Studies

6.6.1 Visible emission studies

Fig. 6.5 shows excitation spectrum of irradiated glass samples taken at 552 nm. The excitation spectra of present samples exhibit many excitation bands [42]. The excitation wavelength chosen for the present study is 380 nm because its corresponding band is most pronounced. **Fig. 6.6 (a)** shows emission spectra for present samples. The three emission bands at 528 nm, 552 nm and 660 nm are observed. The emission spectra **(Fig. 6.6 (a))** give green emission at 528 nm and 552 nm. The reasons for the appearance of these two bands are already explained in **Chapter 4**.

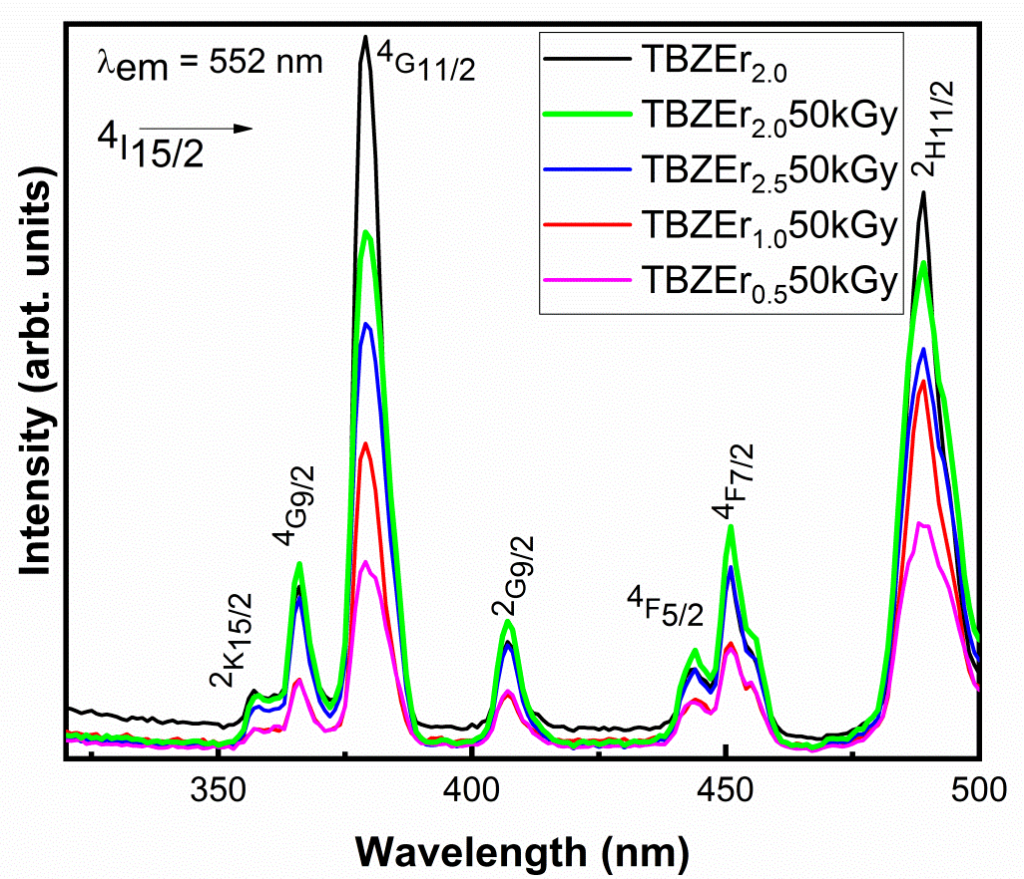

Fig. 6.5: Excitation spectra of Er^{3+}- doped zinc borotellurite glasses after irradiation

As explained in **Chapter 4** samples with 2.0 mol% of Er^{3+} content has maximum emission intensity, hence, $TBZEr_{2.0}$ glass is used for comparison with the irradiated glasses in the graphs. It can be seen from **Fig. 6.6 (a)** that after irradiation there is no significant variation in position and shape of the bands except for changes in the intensity. The emission intensity of the present glasses decreases after the gamma irradiation. This is because when the glasses are irradiated there is generation of secondary electron and hole pairs. The secondary electrons act as quenching traps and hence decrease the emission intensity.

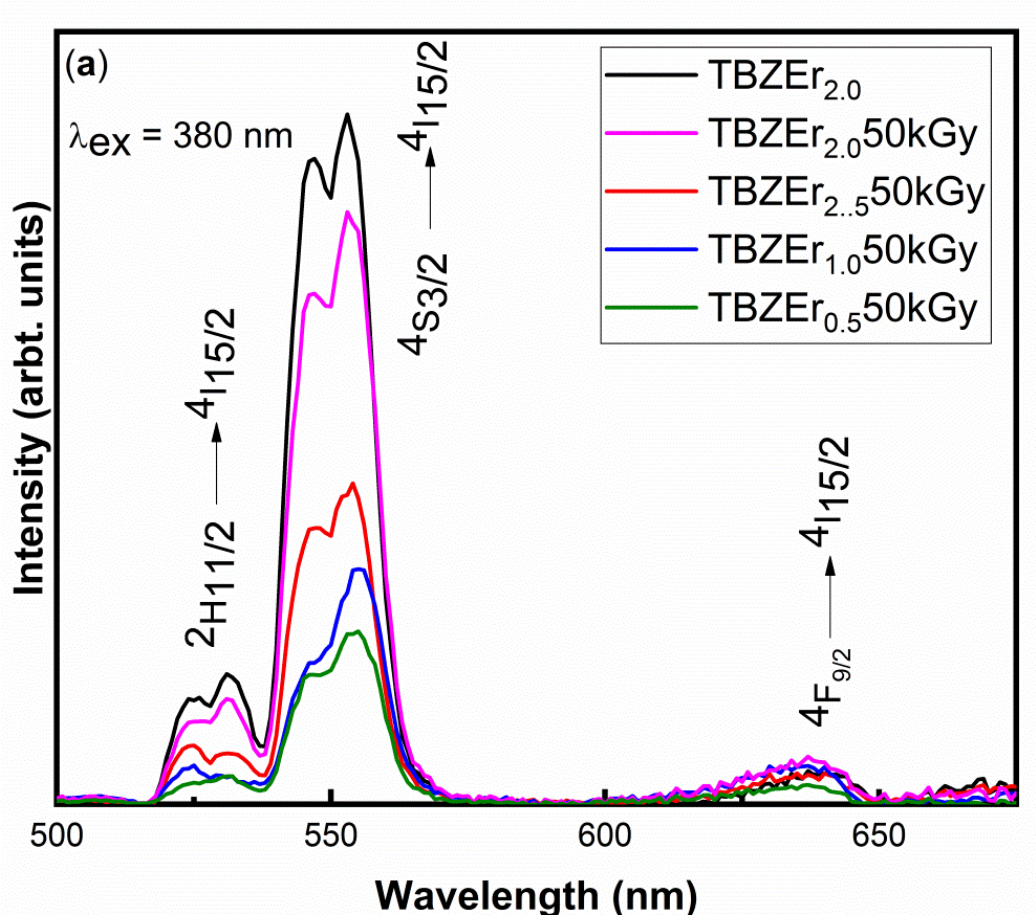

Fig. 6.6 (a): The visible emission spectra of Er^{3+}-zinc borotellurite glasses after irradiation

The maximum emission intensity is again found at 2.0 mol% of Er^{3+} after irradiation. A decrease is observed with further increase in Er^{3+}- content. The decrease can be explained on basis of concentration quenching. It happens because distance between the neighboring RE ions also decreases as the RE concentration is increased. This in turn increases the energy transfer between the ions and hence the emission intensity decreases.

Table 6.6: CIE co-ordinates for different concentrations of Er^{3+}-doped zinc borotellurite glass after and before gamma irradiation at 380 nm excitation

Concentration of Er^{3+} (mol%)	**CIE co-ordinates (x,y) after irradiation**	**CIE co-ordinates (x,y) before irradiation**
0.5	(0.338,0.585)	(0.331,0.580)
1.0	(0.343,0.583)	(0.341,0.578)
2.0	(0.336, 0.586)	(0.340,0.581)
2.5	(0.346,0.614)	(0.351,0.611)

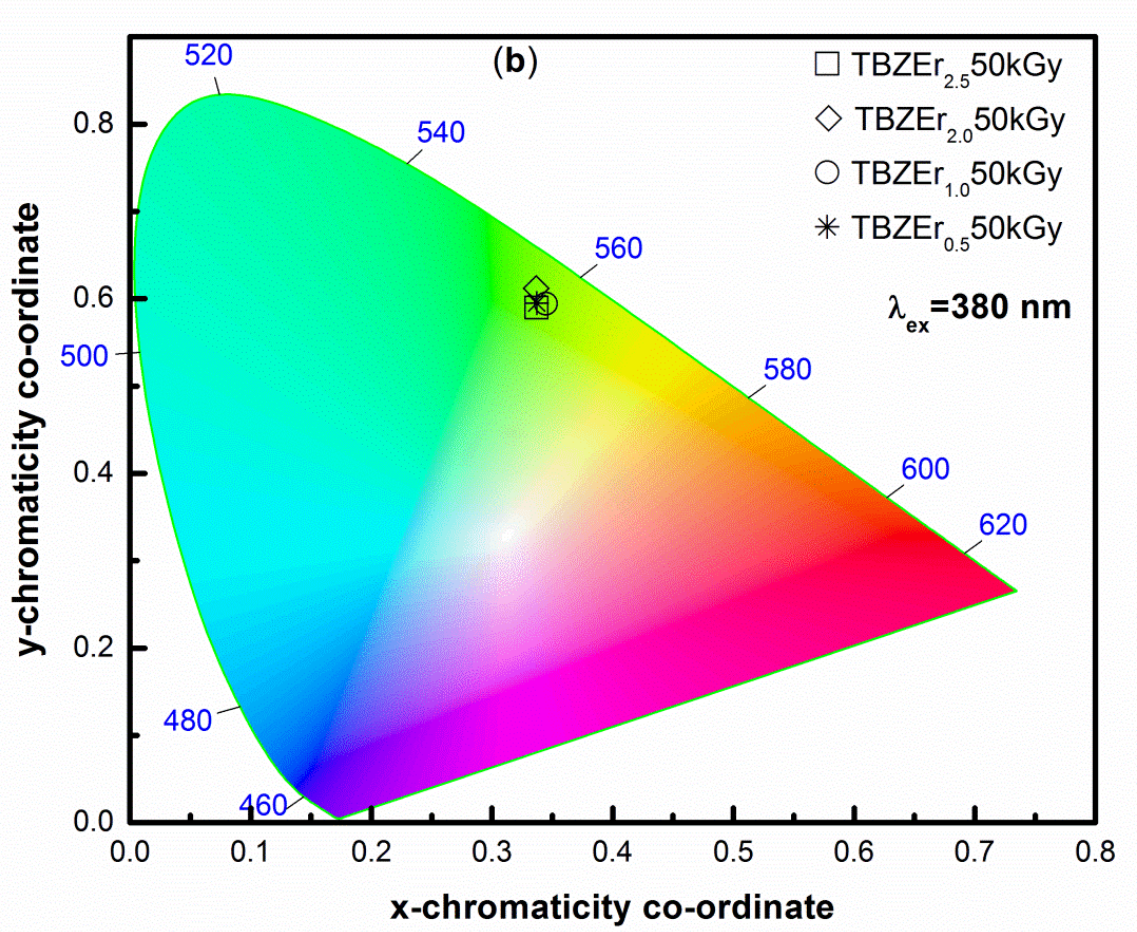

Fig. 6.6 (b): CIE 1931 diagram of $TBZEr_x$ samples after irradiation

The observed visible emission is further studied in terms of CIE color coordinates [44]. **Fig. 6 (b)** represents the CIE 1931 color co-ordinates and the values of same are given in **Table 6.6**. It is clear from **Fig 6.6 (b)** that CIE co-ordinates of the irradiated samples also lie in the green region.

6.6.2 NIR emission studies

The near-infrared emission at 1550 nm is seen for all irradiated samples when excited with 980 nm in 1350-1750 nm spectral range. **Fig. 6.6 (c)** shows the NIR emission in the glasses. With 980 nm excitation ions goes to $^4I_{11/2}$ excited level through ground state absorption. The excited ions relax via non-radiative emission to $^4I_{13/2}$ (meta stable level). These ions further go back to the ground state ($^4I_{15/2}$) by giving NIR emission at 1.53μm. It is observed that the NIR emission also decreases after irradiation.

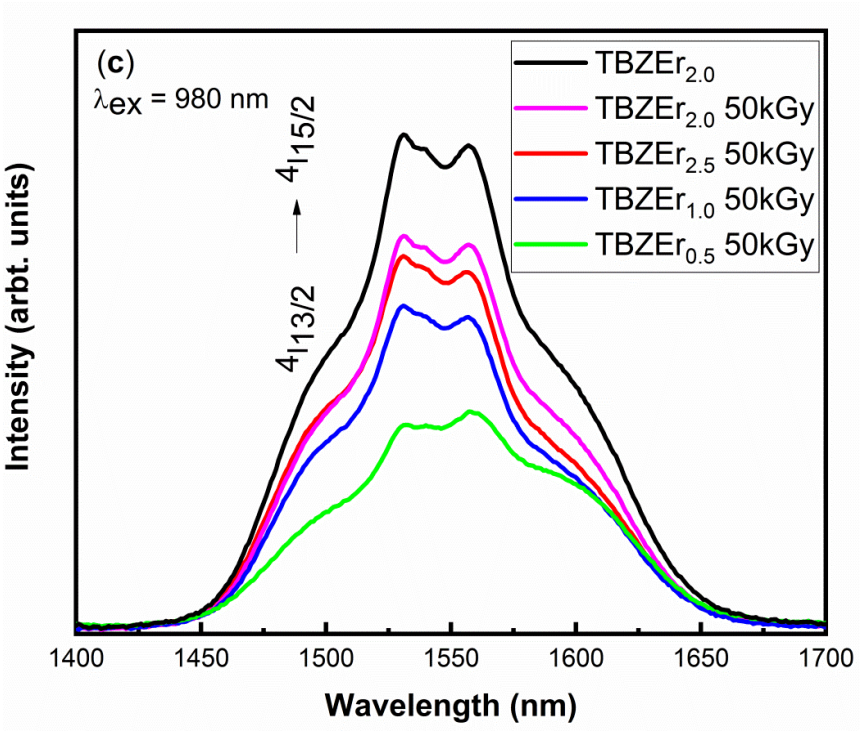

Fig. 6.6 (c): NIR emission spectra of Er^{3+}-zinc borotellurite glass after irradiation

Table 6.7: Effective bandwidth ($\Delta\lambda_{eff}$, nm), experimental (β_{exp}, %) and calculated branching ratios (β_{cal}, %), stimulated emission cross-section from ($\sigma_{MC}(\lambda)$, x 10^{-21} cm^2) and FL-theory ($\sigma_{FL}\lambda(p)$, x 10^{-21} cm^2, experimental lifetime (τ_{exp}, ms) for level $^4S_{3/2}$ and $^4I_{13/2}$ of Er^{3+}-doped zinc borotellurite glasses

Radiative parameters		TBZEr$_{0.5}$ 50kGy	TBZEr$_{1.0}$ 50kGy	TBZEr$_{2.0}$ 50kGy	TBZEr$_{2.5}$ 50kGy	TBZEr$_{0.5}$	TBZEr$_{1.0}$	TBZEr$_{2.0}$	TBZEr$_{2.5}$
$^4S_{3/2}\rightarrow{}^4I_{15/2}$	$\Delta\lambda_{eff}$	13.45	15.26	17.20	18.09	13.82	15.51	17.38	18.33
	β_{exp}	62	65	59	75	64	67	60	77
	β_{cal}	63	64	76	81	61	65	75	80
	τ_{exp}	0.51	0.42	0.31	0.09	0.56	0.46	0.39	0.12
	$\sigma_{FL}(\lambda_p)$ ± 2.12	7.51	7.95	8.84	8.94	7.64	8.03	8.91	9.04
$^4I_{13/2}\rightarrow{}^4I_{15/2}$	$\Delta\lambda_{eff}$	8.54	10.01	11.51	12.31	8.58	10.25	11.54	12.36
	β_{exp}	71	79	75	77	73	80	75	76
	β_{cal}	68	83	71	69	70	81	70	71
	$\sigma_{MC}(\lambda_p)$	5.22	5.99	6.39	7.13	6.01	6.93	7.59	8.54
	$\sigma_{FL}(\lambda_p)$	7.01	7.56	7.64	7.89	7.25	7.68	7.74	7.98
	τ_{exp}	0.41	0.35	0.25	0.08	0.48	0.39	0.26	0.10

6.6.3 Radiative Properties

Understanding of radiative parameters is essential to describe the functionality of a material as a laser active medium. **Table 6.7** gives radiative parameters of $TBZEr_x$ 50kGy samples. The branching ratios of $^4S_{3/2}$ and $^4I_{13/2}$ levels are found to be >50%. Hence, the radiative parameters are calculated and analyzed for these two levels only. From **Table 6.7**, it is observed that after γ-irradiation there is small decrease in the effective bandwidth due to radiation induced defects. On the other hand, an increase in same is observed with increasing RE content. This is due to increase in the Stark splitting between the energy levels of Er^{3+} with increase in its concentration.

The stimulated emission cross-section $\sigma_{emi}(\lambda_p)$ for level $^4I_{13/2}$ is calculated with the help of McCumber (MC) [45] and Füchtbauer–Ladenburg (FL) theory [46]. The said values are given in **Table 6.7**. The maximum value of emission cross-section derived from the FL theory ($\sigma_{FL}(\lambda)$) and MC theory ($\sigma_{MC}(\lambda)$) is found to be 7.64×10^{-21} and 6.39×10^{-21} cm^2, respectively. The difference in the two calculated values of $\sigma_{MC}(\lambda_p)$ and $\sigma_{FL}(\lambda_p)$ is because of reabsorption of the energy emitted by the excited Er^{3+}- ions. The reabsorption leads to spectral overlap of emission and absorption bands as shown in **Fig. 6.7**. It has been seen that $\sigma_{MC}(\lambda_p)$ and $\sigma_{FL}(\lambda_p)$ decrease after irradiation. This is due to increase in factors like radiative trapping, reabsorption etc. It is noted that $\sigma(\lambda_p)$ of present samples is higher than Al/P silica (5.50×10^{-21} cm^2) [47], ZrF4 (4.9×10^{-21} cm^2) [47], 46TeO_2-9P_2O_5-15ZnO-30$LiNbO_3$-4000ppm Er_2O_3 (0.494×10^{-20} cm^2) [48] and PbO-PbF_2-B_2O_3 ($4.6\pm0.7\times10^{-21}$ cm^2) [49] glasses.

Fig. 6.8 shows calculated gain cross-section as a function of P, where P is the inversion rate. It is worth noting that the gain cross-section becomes positive for P > 0.5. This suggests that with population inversion above 50%, bandwidth in the range of 1450-1650 nm can be obtained. As already known, the above mentioned spectral range covers optical communication window from S- to L- bands. This allows present samples to find applications in wavelength division multiplexing (WDM) networks even after gamma irradiation.

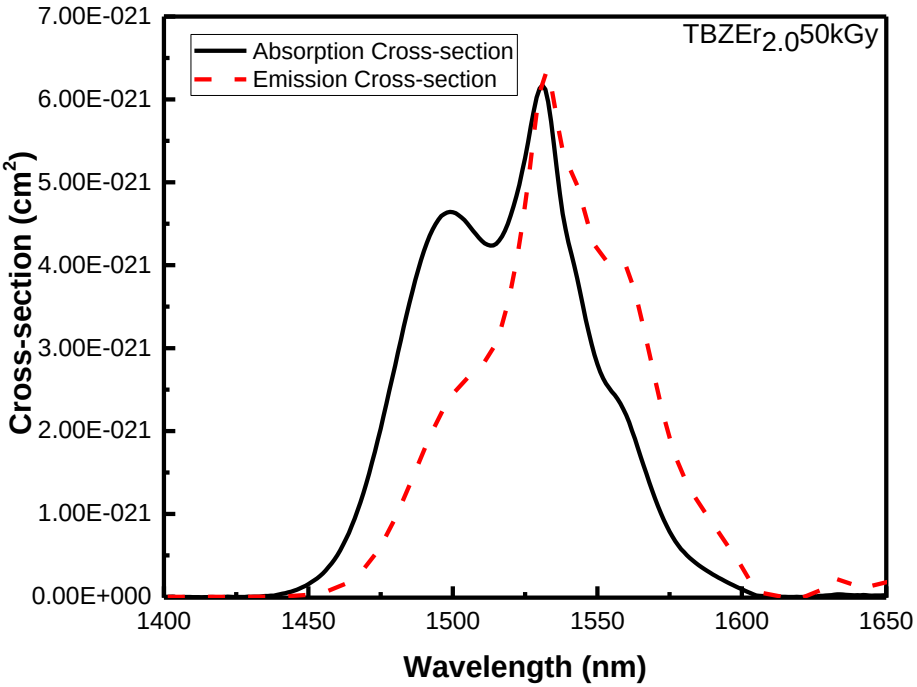

Fig. 6.7: The absorption and emission cross-section spectra of $TZEr_{2.0}50kGy$ for transition $^4I_{13/2}$ to $^4I_{15/2}$ of Er^{3+} ion

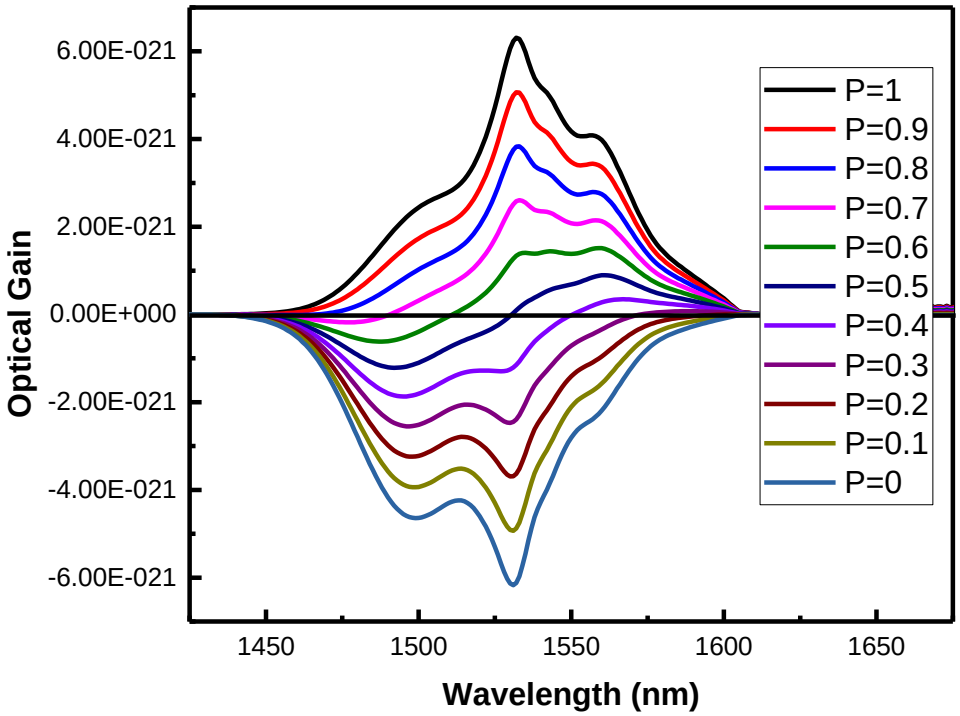

Fig. 6.8: The gain coefficient for transition $^4I_{13/2}$ to $^4I_{15/2}$ of Er^{3+} doped $TBZEr_{2.0}50kGy$

6.6.4 Decay Curves

It is a well known fact that lifetime an imperative parameter for light emitting devices. The luminescence decay curves of levels giving green and NIR emissions are shown in **Fig. 6.9 (a and b)**. **Fig. 6.9** shows the non- exponential behavior of the decay curves of the samples for all concentrations. The experimentally observed values of lifetime are given in **Table 6.7**. Decay curves analysis suggests that lifetime values decrease after γ-ray irradiation. This is because of increase in energy transfer through non-radiative decays to quenching traps (defects). Another decrease in the decay time is observed as content of RE ions increases.

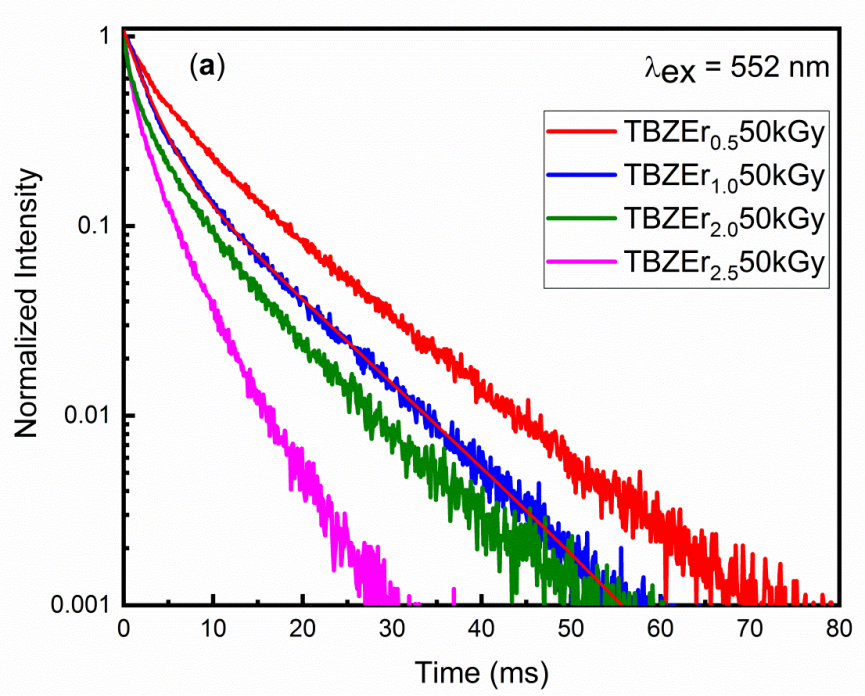

Fig. 6.9 (a): Decay curve for the $^4S_{3/2}$ to $^4I_{15/2}$ transition of Er^{3+} ions in zinc borotellurite glasses after 50kGy gamma irradiation

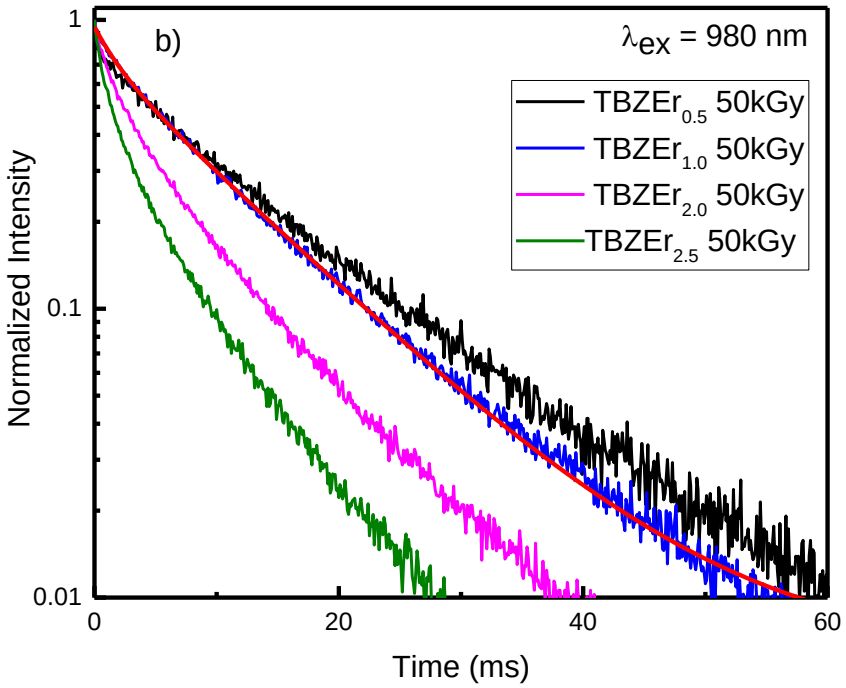

Fig. 6.9 (b): Decay curve for the metastable state $^4I_{13/2}$ of Er^{3+} ions in zinc borotellurite glasses after 50kGy gamma irradiation

6.6.5 Upconversion Luminescence

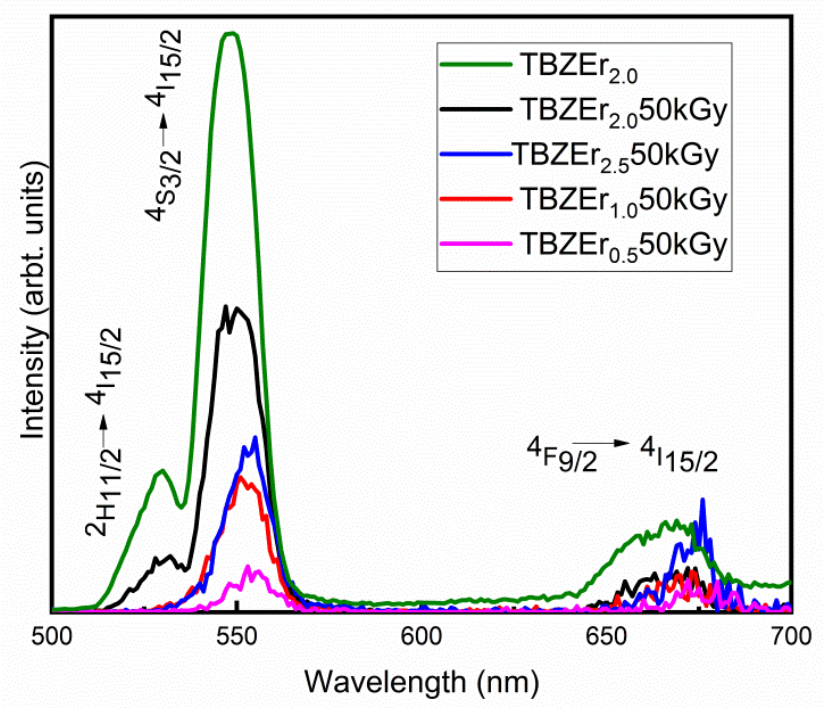

Fig. 6.10: Upconversion spectra of Er^{3+}: TBZEr2$_{.0}$ and TBZEr$_x$50kGy samples at 980 nm excitation

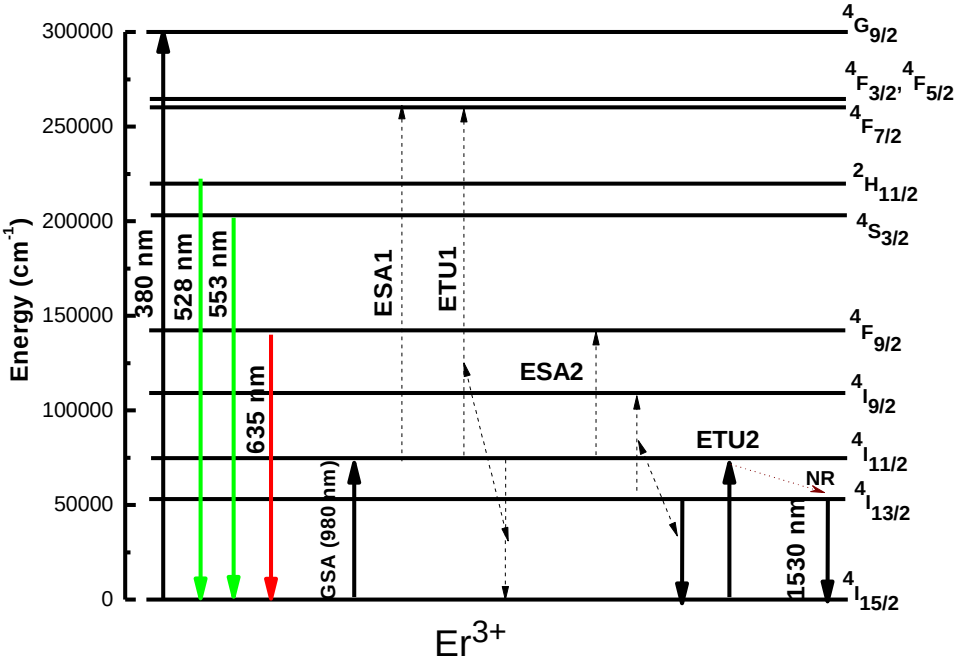

Fig. 6.11: Possible partial energy level diagram for the Er^{3+} at excitation of 380 nm and 980 nm

Fig. 6.10 shows UC observed in irradiated samples at 980 nm excitation. The upconversion profile of the irradiated samples is similar to that of emission profile observed at 380 nm excitation. The upconversion spectra of present samples consist of green (530 and 552 nm) and red (660 nm) emission bands [50-52]. **Fig. 6.10** shows the upconversion spectra observed for $TBZEr_{1.0}$50kGy. The UC emission decreases after irradiation. It is interesting to see that the red UC band is more prominent than red down conversion band observed with 380 nm excitation. This indicates the presence of another efficient channel which populates the $^4F_{9/2}$ level. All the energy transfer processes involved in the UC mentioned processes are also shown in **Fig. 6.11**.

The green upconversion is observed when the energy level $^2H_{11/2}$ or higher have necessary population inversion. This is achieved by ESA and ETU processes. The process of UC is already explained in **Chapter 4**.

6.7 Shielding Properties

The characteristic shielding properties e.g. mass attenuation coefficient (MAC) for the $TBZEr_x$ glasses has been computed using the PSD/Phy-X program [53]. The values of MAC are graphically given in **Fig.6.12**. As observed from **Fig. 6.12**, the mass attenuation

coefficient (MAC) decreases exponentially between 0.015 MeV to 0.03 MeV except for 0.004MeV. K-absorption edge of the tellurium element is observed at 0.004 MeV. The MAC decreases due to photoelectric interactions between photons and matter in 0.015 MeV to 0.03 MeV range.

Another decrease in the 0.03 MeV to 0.2 MeV is observed which is due to the Compton scattering. Finally the MAC values become almost constant from 0.2 MeV onwards due to photoelectric production. It is also observed that the maximum value of MAC is found at 15keV and it increases from 38.02 ± 1.05 cm^2/g ($TBZEr_{0.0}$) to 43.01cm^2/g ± 1.05 cm^2/g ($TBZEr_{2.5}$). It is observed that the change in MAC of samples with increasing RE concentration is more significant at lower energies than at higher photon energies.

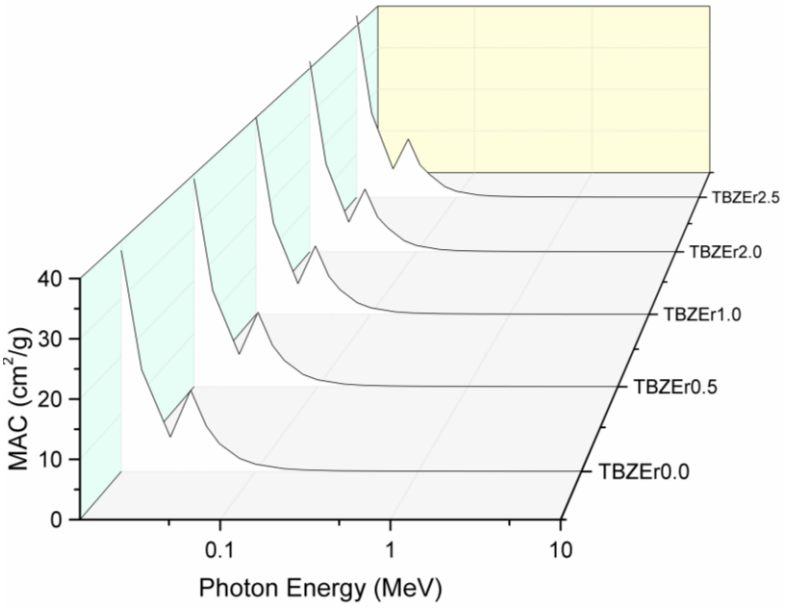

Fig. 6.12: The variations in MAC (cm^2/g) of as-prepared samples with Photon energy (MeV)

In order to study the transmission of gamma photons in the absorber material half HVL and MFP are studied. HVL is measure of the thickness the material which decreases intensity of incident photon to half of its value, whereas MFP is distance travelled by photons between two successive collisions. The error estimated in the HVL, MFP and Z_{eff} values is ±2%. The HVL and MFP for all as-prepared samples are given in **Fig 6.13 and 6.14**. As seen from **Fig. 6.13 and Fig. 6.14** the HVL and MFP values decrease with increase in the doping. Therefore, if the $TBZEr_{2.5}$ sample is used as γ- shielding material at higher energy, a thinner specimen

of $TBZEr_{2.5}$ will be used. It leads to conclusion that $TBZEr_{2.5}$ will show better γ radiation shielding properties than the other present samples.

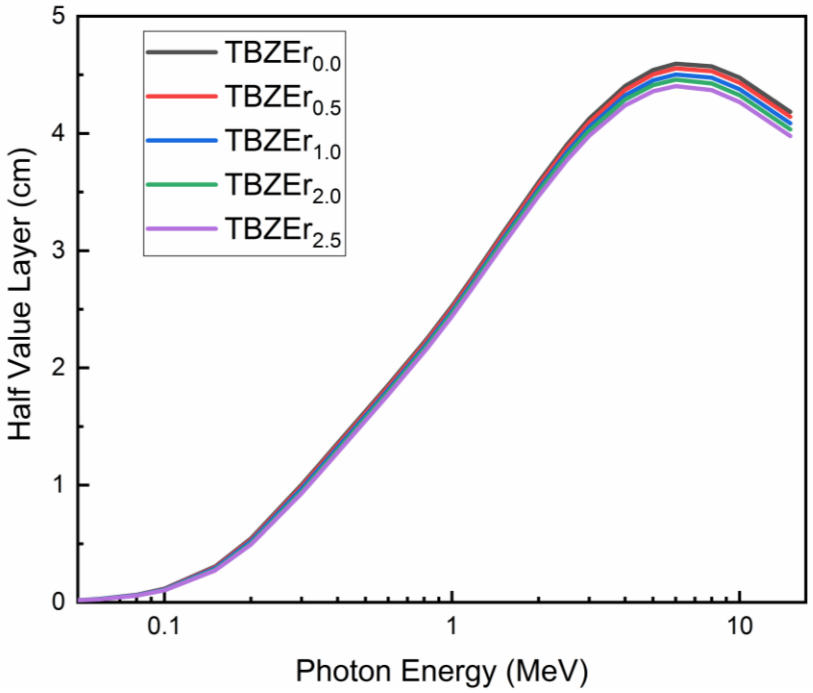

Fig. 6.13: The variations in HVL (cm) of as-prepared samples with Photon energy (MeV)

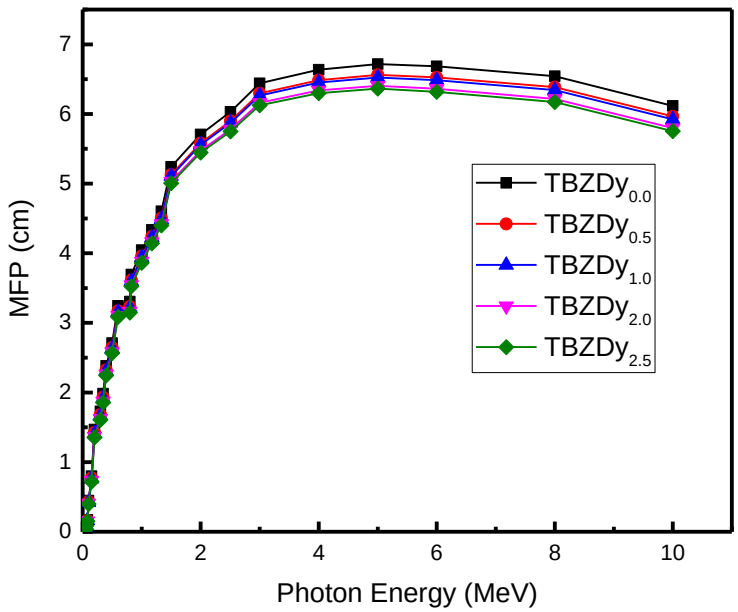

Fig. 6.14: The variations in MFP (cm) of as-prepared samples with Photon energy (MeV)

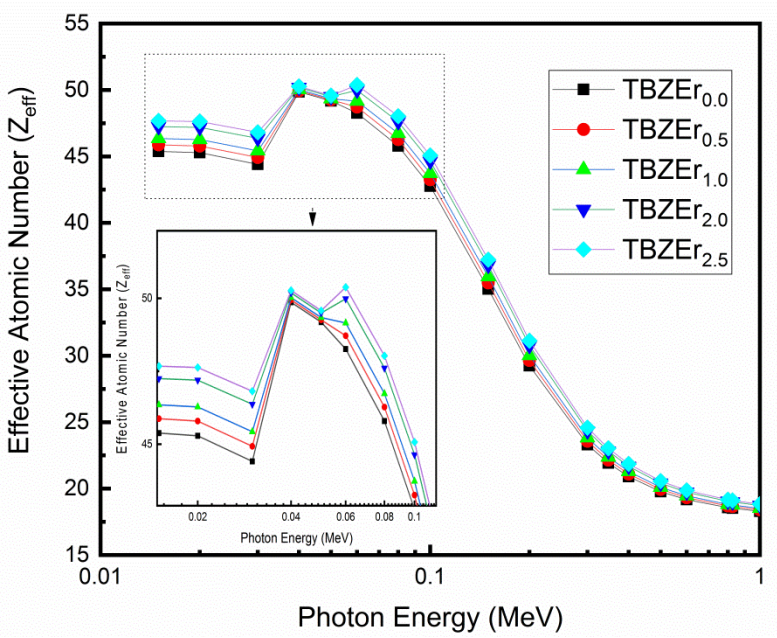

Fig. 6.15: The effective atomic number (Z_{eff}) with the photon energy (MeV)

Fig. 6.15 shows the Z_{eff} of the as-prepared samples with increasing RE concentration. It is observed from the **Fig. 6.15** that Z_{eff} decreases from 0.015 MeV - 4 MeV. Discontinuity is observed at 0.004MeV and 0.0059 MeV due to absorption edge of Te and Er respectively. On the other hand, an increase in the Z_{eff} values is observed from 4MeV to 15MeV due to the pair production. It is noted that that Z_{eff} increases with increase in the RE content. Hence $TBZEr_{2.5}$ will be able to absorb more photon than $TBZEr_{0.0}$.

References

1. B.M. Fideler, C.T. Vangsness, B. Lu, C. Orlando, T. Moore, Am. J. Sports Med., 23 (1995) 643-646.
2. S. Kim, J. O. Jeong, S. Lee, J. S. Park, H. J. Gwon, S. I. Jeong, J. G. Hardy, Y. M. Lim, J. Y. Lee, Sci. Reports, 8 (2018) 3721.
3. T. A. Grieb, R. Y. Forng, R. E. Stafford, J. Lin, J. Almeida, S. Bogdansky, C. Ronholdt, W. N. Drohan, W. H. Burgess, Biomater., 26 (2005) 2033–2042.
4. A. Saidu, H. Wagiran, M.A. Saeed, H.K. Obayes, A. Bala, F. Usman, Radiat. Phys. Chem., 144 (2018) 413–418.
5. G. Lakshminarayana, S.O. Baki, K.M. Kaky, M.I. Sayyed, H.O. Tekin, A. Lira, I. V. Kityk, M.A. Mahdi, J. Non. Cryst. Solids., 471 (2017) 222–237.
6. V. Hegde, N. Chauhan, V. Kumar, C.S.D. Viswanath, K.K Mahato, S. D. Kamath, J. Lumin., 207 (2019) 288-300.
7. M. Sayyed, G. Lakshminarayana, I. Kityk, M. Mahdi, Radiat. Phys. Chem., 139 (2017) 33-39.
8. M.S. Al-Buriahi, K.S. Mann, Mater. Res. Express., 6(10) (2019) 105206.
9. P. Kaur, K. Singh, S. Thakur, P. Singh, B. Bajwa, Spectrochim. Acta, Part A, 206 (2019) 367–77.
10. H. Gomaa, M. Sayyed, H. Tekin, G. Lakshminarayana, A. EL-Dosokey, Physica B, 567 (2019) 109–112.
11. P. Fuochi, U. Corda, M. Lavalle, A. Kovács, M. Baranyai, A. Mejri. K. Farah, 54 (2009) 39–43.
12. M. Sayyed, J. Alloys Compd., 695 (2017) 3191–3197.
13. P. Vani, G. Vinitha, M. Sayyed, B. Elbashir, N. Manikandan, J. Non. Cryst. Solids, 511 (2019) 194–200.
14. N. Chopra, S. Kaur, M. Kaur, S. Singla, Ritika, G. Sharma, M. S. Heer, Phys. Status Solidi (a), 215 (2018)1700934
15. S. Kaur, O. P. Pandey, C.K.Jayasankar, N. Chopra, J. Non-Cryst. Solids, 521 (2019) 119472.
16. S. Kaur, O. P. Pandey, C.K.Jayasankar, N. Chopra, J. Non-Cryst. Solids, 530 (2020) 119842.
17. S. Y. El-Kameesy, S. A. El-Ghany, M. A. El-H. Azooz, Y. A. A. El-Gammam, World J. Cond. Matt. Phys., 3 (2013) 198-202.
18. H. M. Zakaly, A. S. Abouhaswa, S. A MIssa, M. Y. A Mostafa, M. Pyshkina, R.El-Mallawany, Non-Cryst. Solids, 543 (2020) 120151
19. S. A. M. Issa, G. Susoy, A. M. Ali, H. O. Tekin, Y. B. Saddeek, Ali Al-Hajry, H. Algarni, P. S. Anjana, O. Agar, App. Phys. A, 125:867(2019) 1-19
20. I. Boukhris, I. Kebaili, M.S. Al-Buriahi, B. Tonguc , M. M. Al Shammari, M.I. Sayyed, Ceram. Inter., 46 (2020) 22883-22888
21. N. Y. Yorgun, Radiochim. Acta, 107(8) (2019) 755–765.
22. H. A. Saudi, S. U. El-Kameesy, Radiat. Det. Tech. Methods, 44 (2018) 1-7.
23. M.H.A. Mhareb, M. Alqahtani, F. Alshahri, Y.S.M. Alajerami , N. Saleh , N. Alonizan, M.I. Sayyed, M.G.B. Ashiq, T. Ghrib, S. I. Al-Dhafar , T. Alayed , M. A. Morsy, J. Non-Cryst. Solids, 541(2020) 120090.

24. N. S. Prabhu, V. Hegde, M.I. Sayyed, O. Agar, S. D. Kamath, Mater. Chem. Phys., 230 (2019) 267–276.
25. K.M. Mahmoud, Y.S. Rammah, Physica B: Cond. Matt., 577 (2020) 411756.
26. A.M. Noorazlan, H.M. Kamari, S.O. Baki, D.W. Mohamad, J. Nanomater., 2015 (2015) 1-9.
27. E. Culea, I. Vida-Simiti, G. Borodi, E.N. Culea, R. Stefan, P. Pascuta, J.Mater.Sci., 49 (2014) 4620–4628.
28. E. Mansour, J. Mol. Struct., 1014 (2012) 1–6.
29. M. Leśniak, R. Szal, B. Starzyk, M. Gajek, M. Kochanowicz, J. Żmojda, P. Miluski, J. Dorosz, M. Sitarz, D. Dorosz, J. Therm. Anal. Calorim., 138 (2019) 4295–4302.
30. M. Lesniak, G. Mach, B. Starzyk, A. Baranowska, M. Bik, M. Kochanowicz, J. Zmojda, P. Miluski, M. Sitarz, D. Dorosz, J. Mole. Struct. 1217 (2020) 128452
31. K. Pach-Zawada, M. Le_sniak, K. Filipecka, E. Golis, El S. Yousef, P. Pawlik, D. Dorosz, M. Sitarz, J. Filipeck, J. Mole. Struct., 1224 (2021) 128787.
32. M.A. Marzouk, J. Mole. Struct., 1019 (2012) 80-90.
33. B.R. Judd, Phys. Rev., 127 (1962) 750-761.
34. G.S. Ofelt, J. Chem. Phys., 37 (1962) 511-520.
35. C. Gorller-Walrand, K. Binnemans, edited by K.A. Gscheneidner Jr. and L. Eyring (North Holland, Amsterdam, 1998), 25 (1998)101-264.
36. W.T. Carnall, P.R. Fields, K. Rajnak, , J. Chem. Phys. 49 (1968) 4424-4442.
37. A. Miguel, R. Morea, J. Gonzalo, M.A. Arriandiaga, J. Fernandez, R. Balda, J. Lumin., 140 (2013) 38–44.
38. I. Pal, S. Sanghi, A. Agarwal, M.P. Aggarwal, J. Mater. Chem. Phys., 133 (2012) 151.
39. I. Arul Rayappan, K. Marimuthu, J. Phys. Chem. Solids, 74(2013) 1570–1577.
40. K. Selvaraju, K. Marimuthu, Physica B, 407 (2012) 1086–1093.
41. A.A. Reddy, S.S. Babu, G. Vijaya Prakash, Opt. Commun., 285 (2012) 5364-5367.
42. Ch. Basavapoornima, K. Linganna, C.R. Kesavulu, S. Ju, B.H. Kim, W.T. Han, C.K. Jayasankar, J. Alloys Compds., 699 (2017) 959-968.
43. M. Haouari, A. Maaoui, N. Saad, A. Bulou, Sensors and Actuators A, 261 (2017) 235-242.
44. William B. Cowan, Computer Graphics, 17 (1983) 315-321.
45. D.E. McCumber, Phys. Rev. A, 136 (1964) 954-957.
46. B.F. Aull, H.P. Jenssen, IEEE J. Quantum Electron, QE-18 (1982) 925-930.
47. Q. Wang and N. K. Dutta, J. Appl. Phys., 95(2004) 4025-4028.
48. El Sayed Yousef, J. Alloys Compds., 561 (2013) 234-240.
49. L.R.P. Kassab, L.C. Courrol, R. Seragioli, N.U. Wetter, S.H. Tatmi, L. Gomes, J. Non-Cryst. Solids, 348 (2004) 94–97.
50. Z. Pan, A. Ueda, R. Mu, S.H. Morgan, J. Lumin. 126 (2007) 251-256.
51. H. K. Dan, Z. Dacheng, W. Rongfei, T. M. Hau, J. Qing, Y. Xue, Q. Jianbei, J. Rare Earth. 31 (2013) 843-848.
52. Y. Kawamoto, R. Kanno, J. Qiu, J.Mater. Sci. 33 (1998) 63- 67.
53. E, Şakar, Ö. Özpolat, B. Alım, M.I. Sayyed, M. Kurudirek, J. Phys. Chem. Solids 166 (2020), 108496

Effect of gamma irradiation on (70-x)TeO_2-20B_2O_3-10ZnO-xDy_2O_3

Overview

The present chapter discusses the effect of 50 kGy gamma irradiation on the thermal, structural and spectroscopic properties of glasses doped with Dy_2O_3. Studies of radiative properties reveal that the present samples can be used for optoelectronic purposes even after subjected to heavy gamma dosage. The chapter further discusses about the effect of increasing Dy_2O_3 concentration on the shielding properties of the present glasses in detail. The results suggested that the shielding properties improved with the increasing RE concentration.

7.1 Introduction

Recently the interest in radioactive materials is growing because of their applications in industry, medicine, power plants etc [1-12]. It is imperative to develop materials that can be safely used during high nuclear exposure and can act as shielding material [13-25]. Numerous conventional materials like concrete, bricks, polymers etc. are already in use [26-30]. But these conventional materials suffer from drawbacks like toxicity, transparency, durability etc. The scientists are trying to develop shielding materials which have characteristics like minimal impact on environment, economical, easy preparation, transparent, durable etc. Among the various materials, glasses fulfill the required conditions which makes them good candidate for shielding materials. Several reports suggest that glasses with REs as dopants are potential candidates for shielding materials [31-36]. Monisha et al. [38] studied the Dy^{3+} doped SiO_2-B_2O_3-Al_2O_3-NaF-ZnF glasses and stated that Dy^{3+} doped (1.5 mol%) sample showed good shielding properties. Wagh et al. [39] found that the mass attenuation coefficient increases as the content of RE increases in flouroborate glasses.

Present chapter deals with variation in thermal and spectroscopic properties of $TBZDy_x$ 50kGy glasses after 50 kGy γ-irradiation. It also includes theoretical studies of the various shielding parameters of the as-prepared glasses. The theoretical calculations have been done with the help of Phy-X/PSD software.

7.2 Physical properties

Density is sensitive to the structural softening, compactness, cross-linking density and interstitial spacing of the materials. **Table 7.1** gives the density of present samples. It is seen that there is a marginal decrease in the density values after gamma irradiation. It may be due to increase in the defects like electron-hole pair, vacancies etc. [12].

Table 7.1: Density of the samples before and after irradiation

Sample	Density (g/cm^3) ±2%
$TBZDy_{0.0}$	4.72
$TBZDy_{0.5}$	4.79
$TBZDy_{1.0}$	4.87
$TBZDy_{2.0}$	4.91
$TBZDy_{2.5}$	4.96
$TBZDy_{0.0}$50kGy	4.67
$TBZDy_{0.5}$50kGy	4.77
$TBZDy_{1.0}$50kGy	4.85
$TBZDy_{2.0}$50kGy	4.89
$TBZDy_{2.5}$50kGy	4.94

7.3 Thermal studies

The DTA thermographs of $TBZDy_x$50kGy glasses are shown in **Fig. 7.1**. **Table 7.2** gives the characteristic temperatures along with thermal stability of the present samples. A decrease is observed in characteristic temperatures after gamma irradiation. It can be understood on the basis of number of TeO_{3+1} and BO_{3+1} units.

Because of irradiation there may be an increase in the number of TeO_{3+1} and BO_{3+1} units containing non-bridging Oxygens (NBO's) leading to opening up of the glass structure. Another reason could be high energy gamma irradiation creates defects in the glasses. The defects produced weaken the glass structure leading to decrease in the characteristic temperatures.

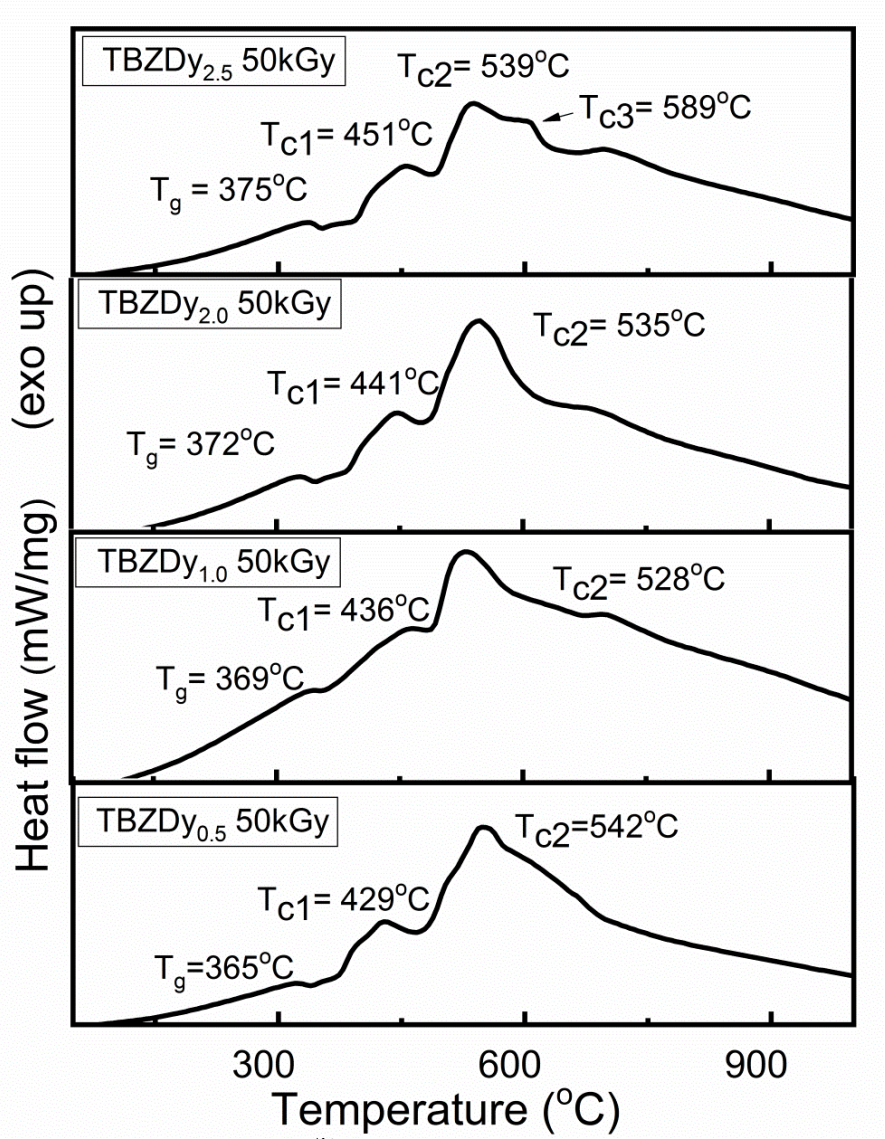

Fig. 7.1: DTA thermographs of Dy^{3+}:TBZDy glasses where T_g is the glass transition, T_{c1} and T_{c2} are the peak crystallization temperatures

Table 7.2: Thermal parameters of $TBZDy_x$ glasses before and after gamma irradiation

Sample label	T_g±1 (°C)		T_{c1}±1 (°C)		T_{c2}±1 (°C)		ΔT=T_{c1}-T_g (°C)	
	Before	After	Before	After	Before	After	Before	After
$TBZDy_{0.5}$	371	365	437	429	546	542	66	64
$TBZDy_{1.0}$	374	369	441	436	528	520	67	67
$TBZDy_{2.0}$	377	372	449	441	540	535	72	69
$TBZDy_{2.5}$	381	375	458	451	542	539	77	76

7.4 Structural studies

7.4.1 X-Ray Diffraction analysis

Fig. 7.2 shows the XRD diffractograms of irradiated samples. The XRD patterns of the un-irradiated samples are given in **Chapter 5**. Broad humps obtained in the XRD are the characteristics of the disorderness. Hence, it confirms absence of long range order and presence of amorphous nature in glasses even after γ-irradiation.

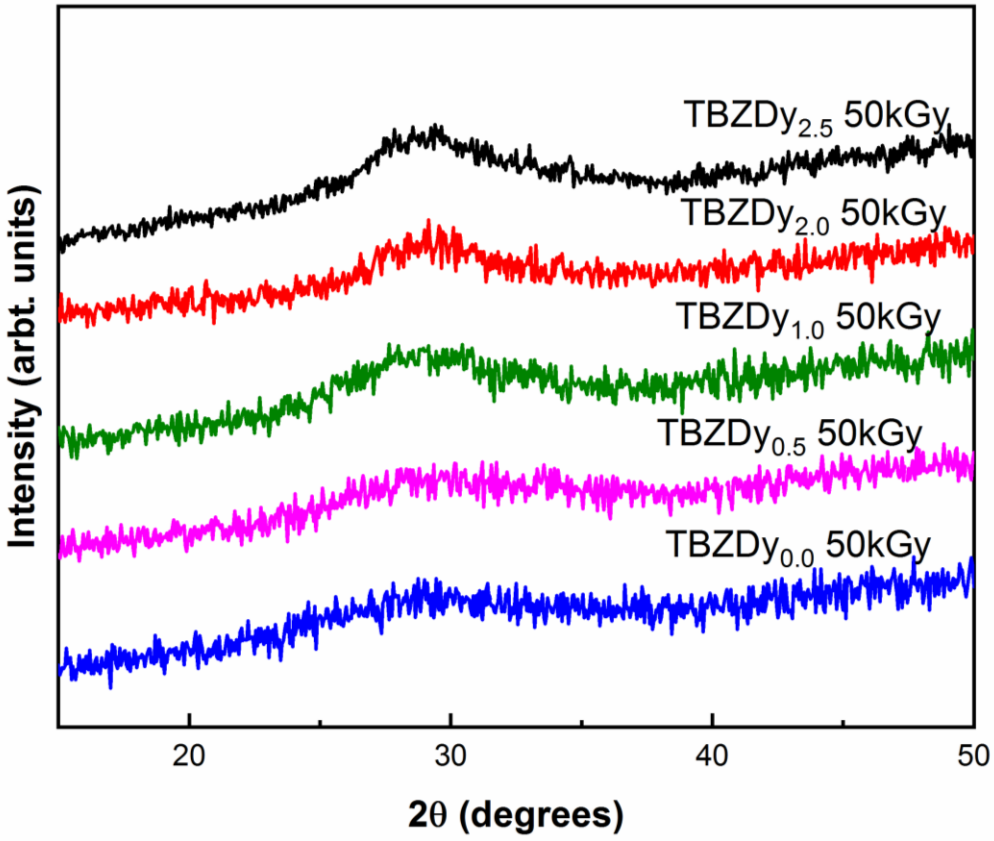

Fig 7.2: X-ray diffraction pattern of the irradiated glasses

7.4.2 Raman Spectroscopy

To study the modifications in structure of glasses after gamma irradiation, Raman measurements have been carried out. Raman spectra of gamma irradiated $TBZDy_x$ samples is given in **Fig. 7.3(a)**. The Raman study of the as-prepared samples is given in **Chapter 5**. **Fig. 7.3 (b)** shows the deconvoluted spectrum of $TBZDy_{2.5}$ 50kGy. It has been observed that even after irradiation the number of band and band positions remains un-altered.

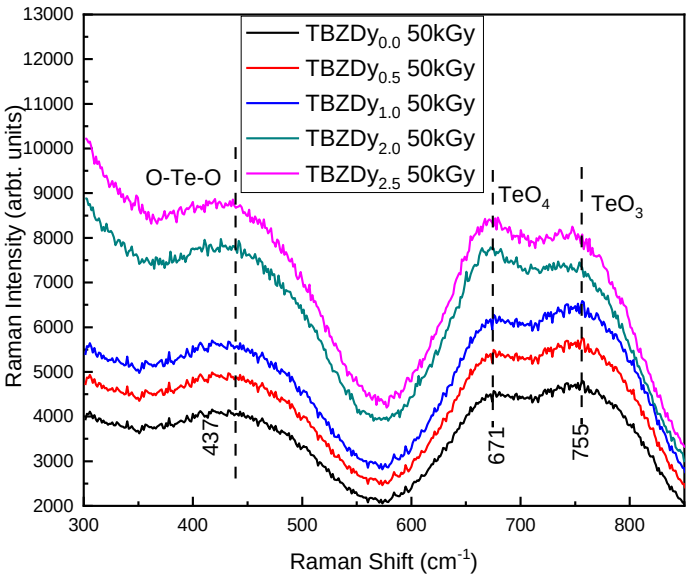

Fig. 7.3 (a): Raman spectra of irradiated glasses

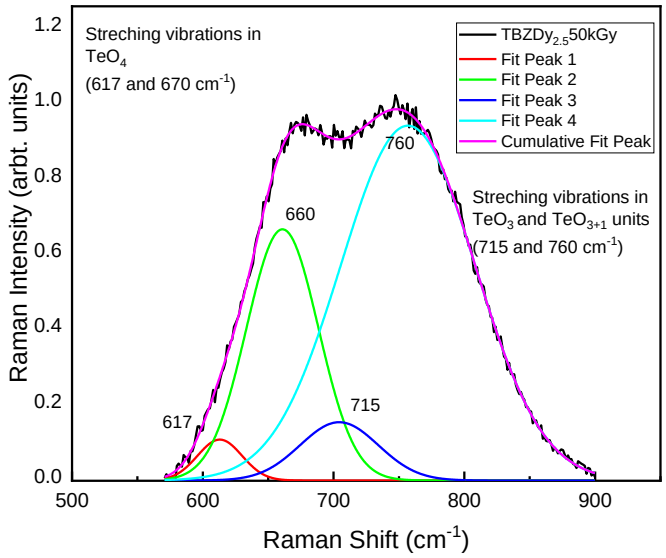

Fig. 7.3 (b): De-convoluted spectrum of $TBZDy_{2.5}$ 50kGy glass

The literature studies suggest that the 300-500 cm^{-1} region corresponds to stretching and bending vibrations of the Te–O–Te bonds [11,12,18,19]. The Raman bands centered at approximately at 660 and 617 cm^{-1} corresponds to TeO_4 units having BOs [11]. The

Raman bands centered at approximately 760 and 715 cm^{-1} corresponds to TeO_3 and TeO_{3+1} units [18]. These units contain non-bridging oxygen atoms (NBOs**).** It has been observed from **Fig. 7.3 (c)** that after irradiation there is a decrease in the amplitude of the bands at 617 and 667 cm^{-1} w. r. t. Raman bands at 723 and 760 cm^{-1}.

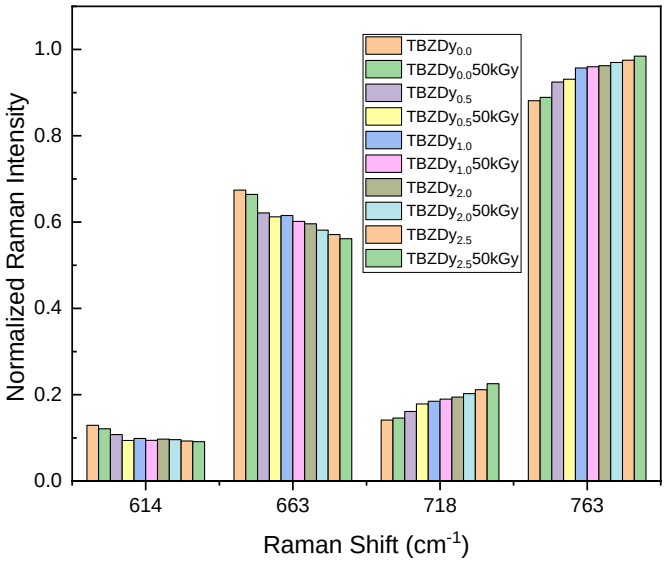

Fig. 7.3(c): Normalized intensities of the Raman bands after de-convolution at different RE- concentrations

It can be due to breakage of Te-O-Te bond linkages and this leads to systematic conversion TeO_3 structural groups to TeO_{3+1} unit because of irradiation [12]. Thus there is an increase in TeO_{3+1} structural unit with NBOs.

7.4.3 Fourier Transform Infrared spectroscopy (FTIR):

The FTIR spectra of the present glasses (before and after gamma irradiation) in the region 400–1500 cm^{-1} are given in **Fig. 7.3 (d)**. A band at around 695 cm^{-1} belongs to TeO_4 structural unit. Another band at around 768 cm^{-1} is attributed to TeO and TeO^- bonds of trigonal pyramidal TeO_3 units [29]. The intermediate region (1100-700 cm^{-1}) belongs to B-O stretching vibrations of BO_4. Whereas, the bands observed in the 1500-1200 cm^{-1} are due to stretching vibrations of B-O bond in BO_3 units [30,31]. **Fig. 7.3(e)** shows the variations in the intensity of Dy^{3+}-doped zinc borotellurite glasses before and after gamma irradiation. It is observed from the **Fig. 7.3(e)** that the glass samples containing Dy^{3+}- ion

do not show the appearance of the new bands except for some intensity variations. The FTIR results suggest that samples having RE ions show some resistance against gamma irradiation.

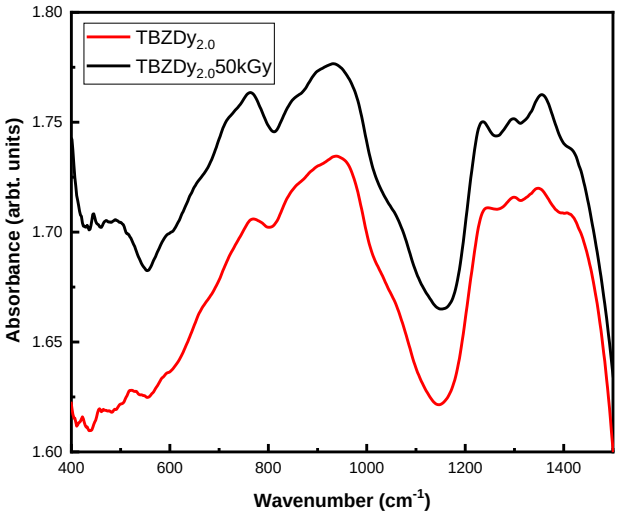

Fig. 7.3 (d): Infrared absorbance spectra of $TBDy_{2.0}$ before and after irradiation

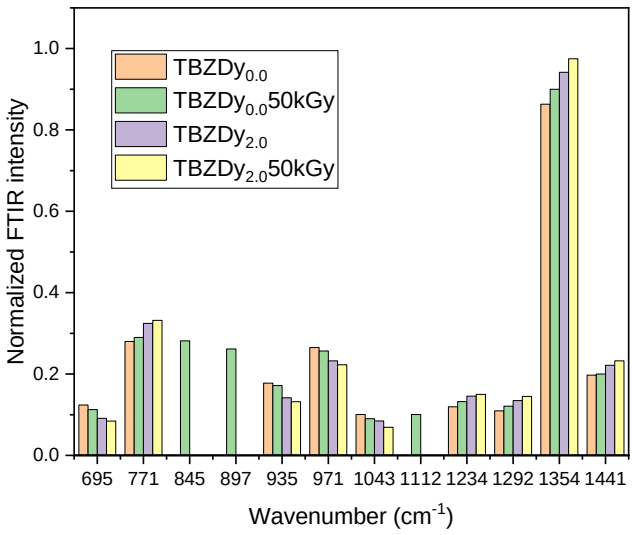

Fig. 7.3(e): Normalized intensities of the FTIR bands after de-convolution of the prepared samples

7.4 Absorption studies: Judd-Ofelt (JO) Analysis

The absorption spectrum of γ-irradiated glasses doped with Dy_2O_3 is shown in **Fig. 7.4**. The absorption spectra of the γ- irradiated samples with Dy_2O_3 showed absorption bands of Dy^{3+} [41]. For Dy_2O_3 transition at 1280 nm is hypersensitive. **Table 7.3** gives the values of absorption cross-section, α(υ) for the said transition. A marginal increase in the values of α(υ) after γ-irradiation is observed. It can be attributed to the radiation induced defects like NBOs, vacancies and increase in the number of free electron-hole pair. These defects increase the absorption due to increase in collisions of free electron generated after irradiation. The increase in intensities of absorption peaks is also reported by Marzouk and Ghoneim et al. [41] on Dy^{3+}- doped soda lime flourophospates in their recent report.

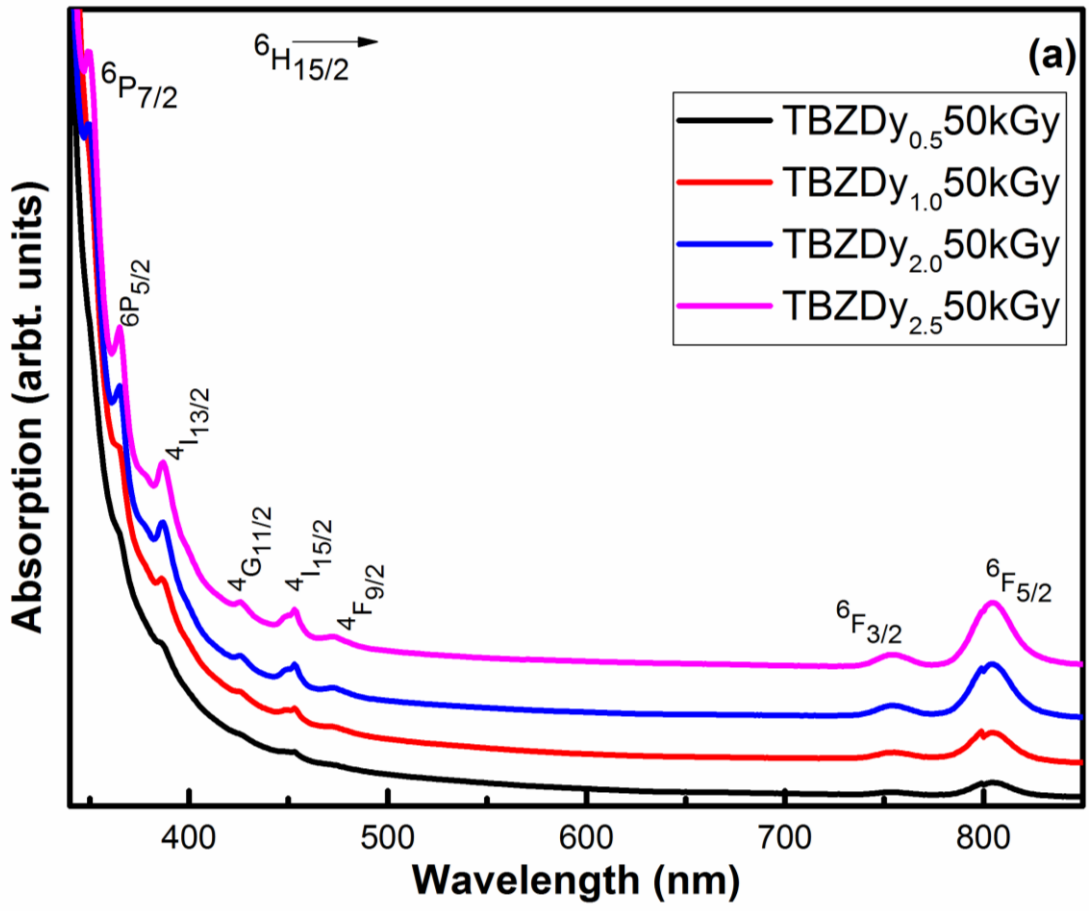

Fig.7.4 (a): Absorption spectra of $TBZDy_x$ 50kGy in UV-Vis

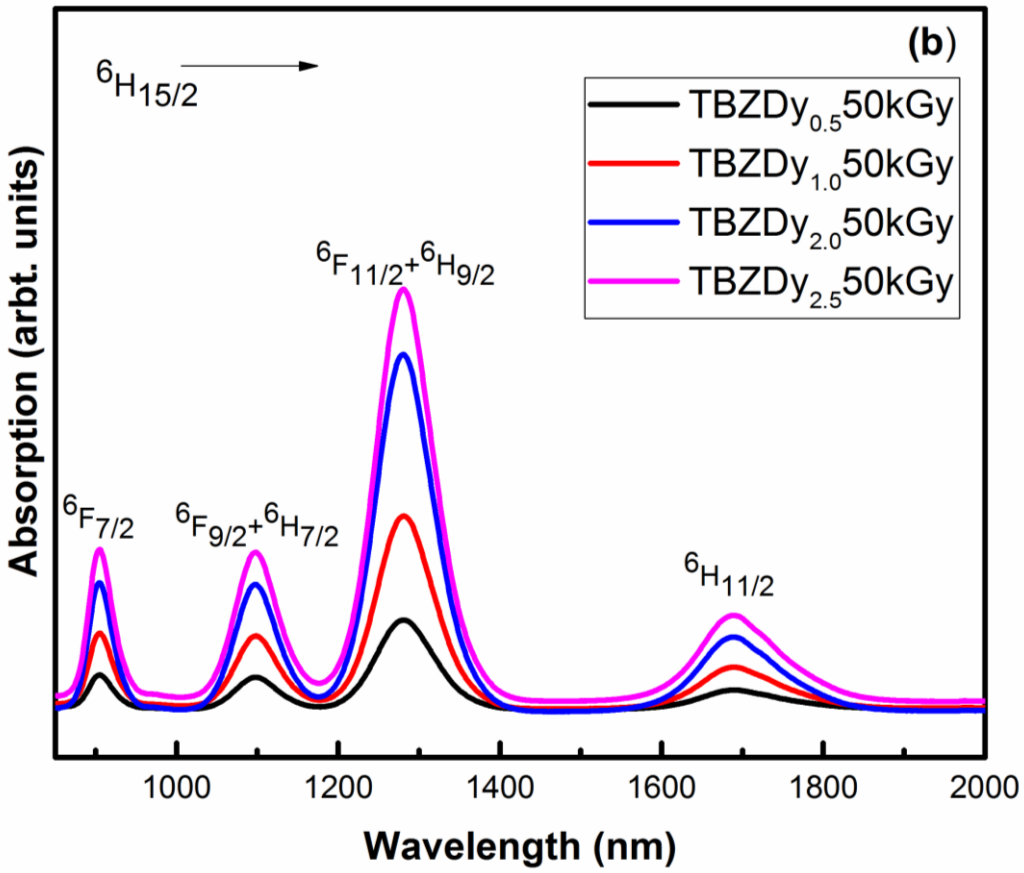

Fig.7.4 (b): Absorption spectra of TBZDy$_x$ 50kGy in NIR region

Table 7.3: The absorption cross-section (α(υ)) for peak at 1280 nm

Sample ID	α(υ) ±0.54 cm^2 (×10^{-20} cm^2) (Before)	α(υ) ±0.54 cm^2 (×10^{-20} cm^2) (After)
TBZDy$_{0.0}$	-	-
TBZDy$_{0.5}$	5.26	6.06
TBZDy$_{1.0}$	5.81	6.11
TBZDy$_{2.0}$	5.95	6.19
TBZDy$_{2.5}$	6.02	6.24

The localized bonding and symmetry in surrounding of RE ions is studied with help of JO-theory [43-46]. The variations in the JO-parameters indicate the structural modifications surrounding the RE^{3+}- ions. JO values for the present samples and other Dy^{3+} -doped samples are given in **Table 7.4 (a,b)**.

Table 7.4 (a): JO intensity parameters (x 10^{-20} cm^2) of present glasses

Sample ID	$\Omega_2 \pm 1.05$	$\Omega_4 \pm 0.05$	$\Omega_6 \pm 0.04$	Trend	Reference
$TBZDy_{0.5}$ 50kGy	14.23	5.59	2.52	$\Omega_2 > \Omega_4 > \Omega_6$	Present Work (PW)
$TBZDy_{1.0}$ 50kGy	13.80	4.88	1.98	$\Omega_2 > \Omega_4 > \Omega_6$	[PW]
$TBZDy_{2.0}$ 50kGy	13.59	3.81	2.09	$\Omega_2 > \Omega_4 > \Omega_6$	[PW]
$TBZDy_{2.5}$ 50kGy	14.61	3.67	2.01	$\Omega_2 > \Omega_4 > \Omega_6$	[PW]
$TBZDy_{0.5}$	14.32	5.64	2.64	$\Omega_2 > \Omega_4 > \Omega_6$	[PW]
$TBZDy_{1.0}$	13.91	4.99	2.01	$\Omega_2 > \Omega_4 > \Omega_6$	[PW]
$TBZDy_{2.0}$	13.66	3.84	2.17	$\Omega_2 > \Omega_4 > \Omega_6$	[PW]
$TBZDy_{2.5}$	14.73	3.72	2.08	$\Omega_2 > \Omega_4 > \Omega_6$	[PW]

Table 7.4 (b): JO intensity parameters (x 10^{-20} cm^2) of reported glasses

Sample ID	Ω_2	Ω_4	Ω_6	Trend	Reference
TSWD15	11.359	3.087	2.663	$\Omega_2 > \Omega_4 > \Omega_6$	[48]
TTWD20	3.39	0.27	1.05	$\Omega_2 > \Omega_6 > \Omega_4$	[50]
Dy: KLTB	9.86	3.31	2.41	$\Omega_2 > \Omega_4 > \Omega_6$	[49]
TWLD2	11.036 ± 0.42	1.708 ± 0.26	2.664 ± 0.32	$\Omega_2 > \Omega_6 > \Omega_4$	[47]

It is observed that the γ-irradiated samples follows trend $\Omega_2 > \Omega_4 > \Omega_6$ which is same as that of the glasses. A decrease in Ω_2 after irradiation indicates decrease in the covalency. The Ω_2 values of the present samples are higher as compared to that of some cases reported in the literature [47-50].

Table 7.5 gives the energy gap (direct and indirect) and refractive index. It is worth noting that RE- doped irradiated samples have comparable values of energy gap with that of un-irradiated doped samples. It suggests that the doped samples have some resistance against γ- irradiation. In a study Maheshwari et al. [43] reported similar results in gamma irradiated Er^{3+}-doped phosphate glasses. Authors suggested that it may be because of the capturing of released electron-hole pairs by the RE-ions. The Urbach energy is calculated for the present samples and the values are given in **Table 7.5**. A small increase in the Urbach energy values is observed with γ- irradiation. It suggests that there is increase in the degree of disorderness in the glass system after irradiation. The small increase in

disorderness is may be due to increase in the imperfections in the localized states with irradiation. Another increase is observed with increasing RE concentration, suggesting increase in the number of NBOs in the glass matrix. The refractive index values are calculated with the help of Dimitriov and Sakka relation [42]. The refractive index values follows opposite trend as that of energy gap (**Table 7.5**).

Table 7.5: The Energy gap and refractive index of glass samples

Sample ID	**Direct energy gap ± 0.21 (eV)**	**Indirect energy gap ± 0.32 (eV)**	**Urbach Energy ± 0.02 (eV)**	**Refractive index N ± 0.87**
TBZ$Dy_{0.0}$50kGy	3.31	3.18	0.26	2.26
TBZ$Dy_{0.5}$50kGy	3.28	3.21	0.28	2.30
TBZ$Dy_{1.0}$50kGy	3.19	3.18	0.31	2.35
TBZ$Dy_{2.0}$50kGy	2.89	3.11	0.42	2.39
TBZ$Dy_{2.5}$50kGy	2.31	2.69	0.56	2.52
TBZ$Dy_{0.0}$	3.42	3.32	0.19	2.29
TBZ$Dy_{0.5}$	3.32	3.26	0.25	2.31
TBZ$Dy_{1.0}$	3.25	3.18	0.29	2.37
TBZ$Dy_{2.0}$	2.91	3.09	0.37	2.41
TBZ$Dy_{2.5}$	2.36	2.56	0.51	2.54

7.5 Spectroscopic properties

7.5.3 Excitation and emission studies

The excitation spectra of irradiated glasses with varying Dy^{3+}- content at emission wavelength of 575nm are shown in **Fig.7.5**. The excitation band at 383 nm wavelength is chosen for exciting the samples to take emission spectra as corresponding excitation band is most prominent.

The emission spectra of the irradiated samples are shown in **Fig. 7.6**. Emission spectra show three bands at 482, 575 and 663 nm. It is observed that the emission characteristics such as shape of the bands and band positions are unaltered even after gamma irradiation. The emission spectra of the irradiated samples have more intense yellow band than the blue band.

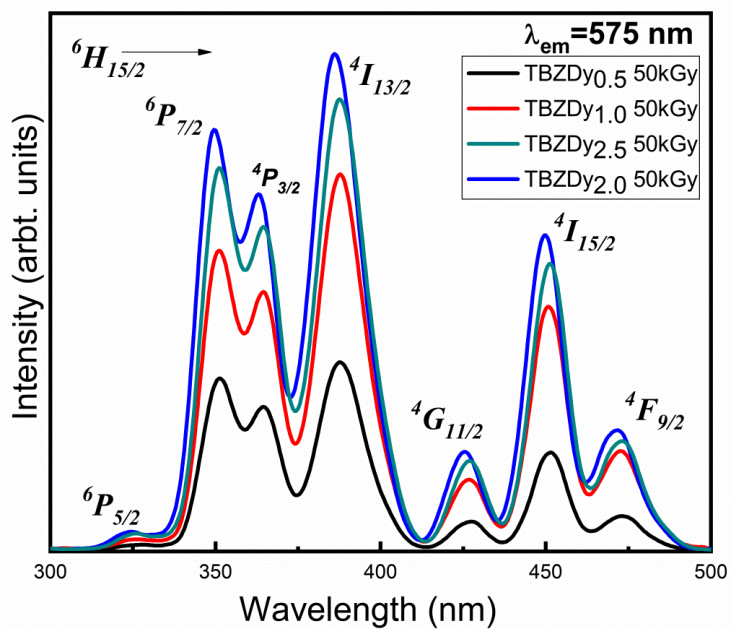

Fig.7.5: Excitation spectra of irradiated Dy^{3+}:$TBZDy_x$ glasses

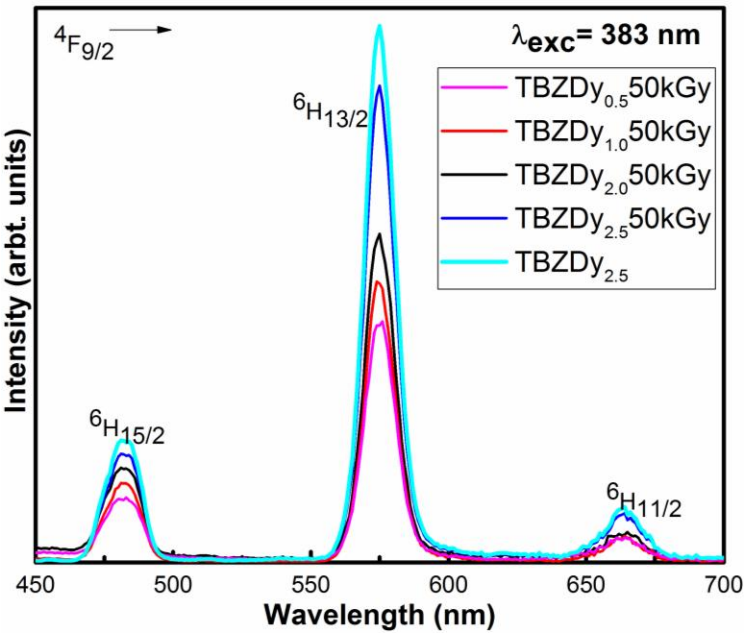

Fig 7.6: Emission Spectra of irradiated $TBZDy_x$ samples

Change in emission intensity is observed and analyzed in terms of Y/B values. **Table 7.6** gives Y/B values of present and as-prepared samples. Reduction in the Y/B values is

observed after gamma irradiation. It can be understood that the structural changes occur locally because of the gamma irradiation.

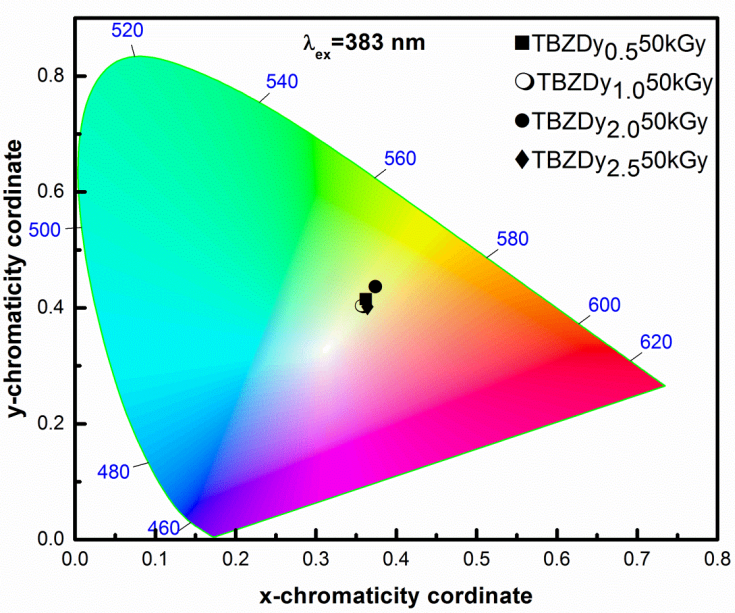

Fig. 7.7: CIE 1931 co-ordinates diagram of irradiated $TBZDy_x$ glasses

In the present study the emission is varied by changing the environment around RE ions. The emission of TBZDy 50kGy is studied in terms of CIE color-coordinates [47]. **Fig. 7.7** depicts the CIE color co-ordinates of Dy-doped glasses at 383 nm excitation. **Table 7.6** gives the CIE coordinates for the present samples. The color coordinates for the present glasses falls in yellowish white region **(Fig. 7.7)**.

Table 7.6: Y/B, CIE color co-ordinates and characteristic radiative parameters of $TBZDy_x$ glasses

Radiative parameters		**$TBZDy_{0.5}$ 50kGy**	**$TBZDy_{1.0}$ 50kGy**	**$TBZDy_{2.0}$50kGy**	**$TBZDy_{2.5}$ 50kGy**	**$TBZDy_{0.5}$**	**$TBZDy_{1.0}$**	**$TBZDy_{2.0}$**	**$TBZDy_{2.5}$**
Y/B		(3.4:1)	(3.6:1)	(3.9:1)	(5:1)	3.7:1	3.8:1	4.1:1	5.5:1
(x,y)		(0.43,0.42)	(0.43,0.41)	(0.42,0.43)	(0.41,0.43)	(0.43,0.44)	(0.42,0.43)	(0.43,0.43)	(0.42,0.43)
$^4F_{9/2} \rightarrow {}^6H_{13/2}$	**$\Delta\lambda_{eff\ (nm)}$ ± 0.79**	8.61	10.29	11.59	12.41	8.58	10.25	11.54	12.36
	A_R (s^{-1}) ± 19	668	508	427	358	670	510	430	360
	β_{exp} (%) ± 7	76	80	75	62	76	80	74	61
	β_{cal} (%) ± 7	64	79	62	55	64	78	60	53
	σ_{emi} (10^{-22} cm^2) ± 7.2	65.6	66.7	67.9	68.9	67.2	67.9	68.9	70.5

7.6.2 Radiative properties

The radiative parameters are determined with the help of Fuchbauer- Ladenburg (FL) theory [51]. **Table 7.6** gives radiative parameters of $TBZDy_x$ 50kGy. The branching ratio characterizes lasing power of particular transition [52-54]. In present case, $\beta > 50\%$ for yellow transition. Hence the radiative parameters are calculated for $^4F_{9/2} \rightarrow {}^6H_{13/2}$ transition. The $\Delta\lambda_{eff}$ is measure of the sharpness of the transition. Linewidth $\Delta\lambda_{eff}$ of present samples is found to be lower than the Dy^{3+}: P_2O_5–Al_2O_3–Na_2O (16 nm) [52], Dy^{3+}:NAP (15.71 nm) [53] and Dy^{3+}: PKBAFD10 (13 nm) [54] glasses, and higher than Dy^{3+}: BTLN0.5D (4.09 nm) glasses [55]. The materials having large σ_{emi} requires low-threshold and have high gain. From **Table 7.6**, it is observed that values of σ_{emi} decrease after irradiation. It is due to the defects induced by irradiation which in turn increases in the non-radiative decay. It can be observed from **Table 7.6** that $TBZDy_{2.5}$50kGy has the highest σ_{emi} for $TBZDy_x$ 50kGy glasses. The σ_{emi}, of the irradiated samples is found to be higher than NAP ($4.4\times10^{-22}cm^2$) [53], PKBAFD10 (4.76×10^{-22} cm^2) [54], Dy^{3+} doped 2D ZTFB ($5.284\times10^{-22}cm^2$) [56], 1D ZTFB (5.628×10^{-22} cm^2) [56] and 0.5D ZTFB ($5.483\times10^{-22}cm^2$) [56] glasses. However, it is lower than the Dy^{3+} doped TSWD15 ($47.01\times10^{-22}cm^2$) [48] glass.

7.6.3 Decay curves

The decay time are observed at 575 nm emission and 383 nm excitation wavelength [11]. The decay curves for all irradiated samples are given in **Fig. 7.8**. Non-exponential behavior is because of due to cross relaxation (CR) channels and resonant energy transfer (RET). The CR channels which are responsible for non-radiative relaxations are shown in **Fig.7.9** [11].

The lifetime curves are fitted with the help of IH model by taking dipole-dipole interactions into consideration. **Table 7.7** gives the fitting parameters. The value of τ_0 is taken from $TBZDy_{0.5}$ 50kGy glass sample. A decrease in the decay time is obtained with gamma irradiation as well as increase in RE- content. The results indicated an energy transfer between the RE- increases via CR channels as indicated by energy transfer parameter (Q) [50]. Decrease observed in critical transfer distance (R_o) also suggest increase in RET and IH parameters.

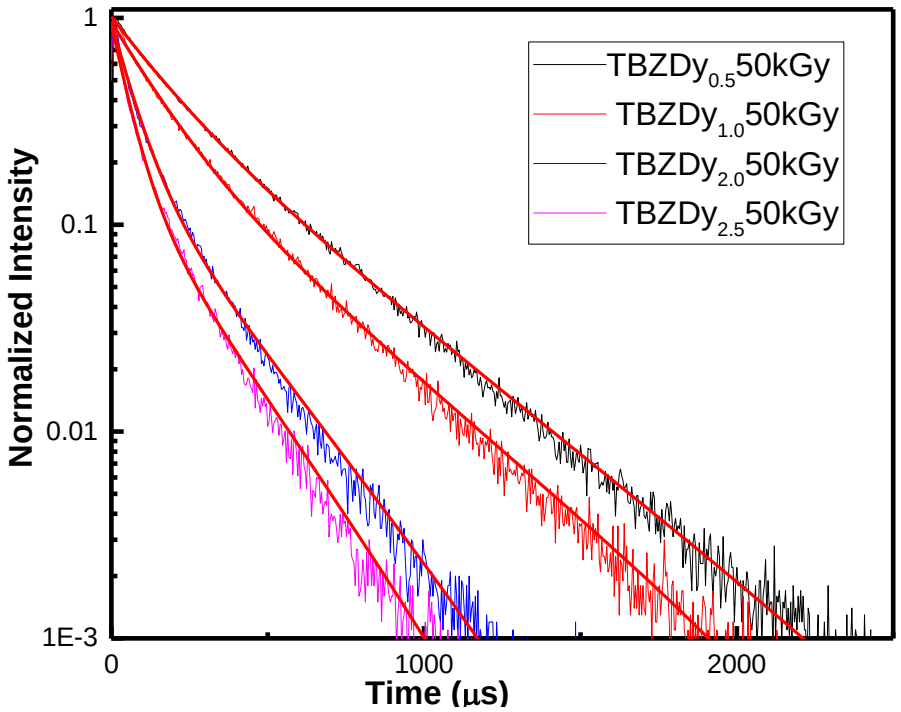

Fig. 7.8: Decay curves for prepared glasses (λ_{ex}=383nm and λ_{em}= 575 nm).

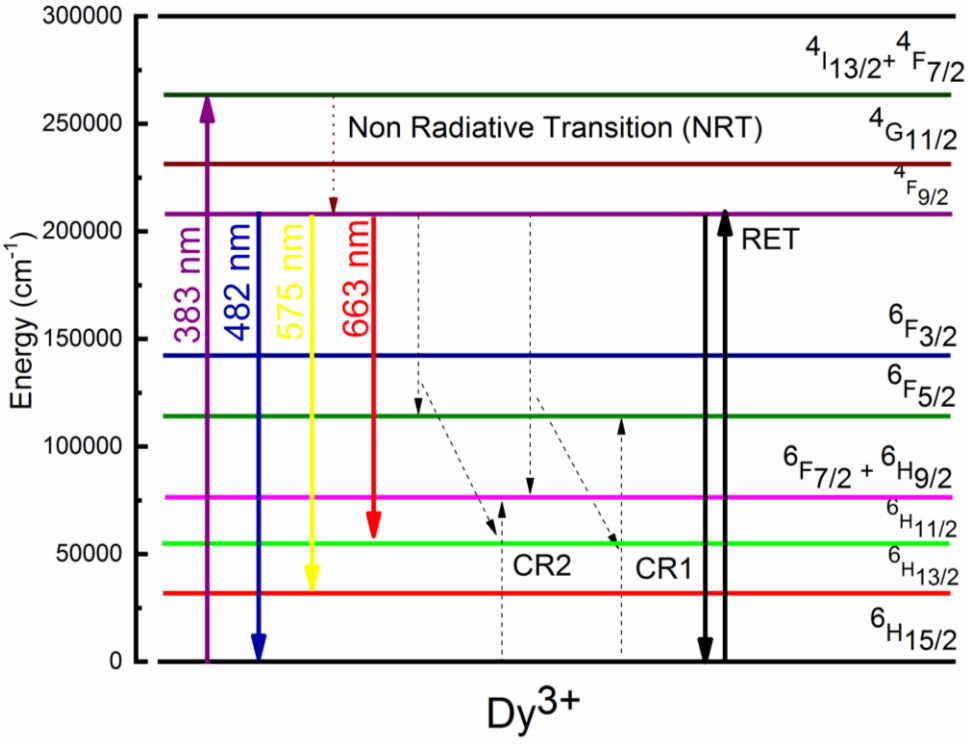

Fig. 7.9 Partial energy level diagram of Dy^{3+} ions

Table 7.7: Lifetime and IH fitting parameters of Dy^{3+}: TBZDy_x50kGy systems

Sample Label	τ_{rad} ± 45 (μs)	τ_{exp} ± 32 (μs)	η ± 2 (%)	Q± 0.45	R_0 ± 1.5 (Å)	$C_{DA} \times 10^{-42}$ ± 1.25 $cm^6 s^{-1}$	W_{NR} ± 0.51
TBZ$Dy_{0.5}$50kGy	1051	725	68	2.39	8.26	8.23	3.57
TBZ$Dy_{1.0}$50kGy	601	379	62	3.21	7.69	10.48	3.69
TBZ$Dy_{2.0}$50kGy	591	345	58	5.36	6.95	11.59	4.27
TBZ$Dy_{2.5}$50kGy	132	69	52	6.08	5.86	54.94	5.59
TBZ$Dy_{0.5}$	1060	732	69	2.36	8.28	8.22	3.56
TBZ$Dy_{1.0}$	619	384	62	3.23	7.71	10.45	3.69
TBZ$Dy_{2.0}$	603	350	58	5.35	6.98	11.56	4.25
TBZ$Dy_{2.5}$	138	72	52	6.05	5.89	54.94	5.56

The τ_{rad} values are calculated with the help of JO parameters. An increase in the W_{NR} is observed after gamma irradiation due to irradiation induced defects. The values of τ_{rad} for TBZDy_x50kGy glasses are reported in **Table 7.7**. A variation between the two values has been observed because of relaxations through non-radiative transitions. The quantum efficiency (η) of the present irradiated samples is calculated [47] and given in **Table 7.7**. A decrease in the values of 'η' is observed after irradiation and with increasing RE content. The decrease in η values is expalined by increase of non-exponential behavior. The η value is found to be maximum for TBZ$Dy_{0.5}$ 50kGy (68%) (Table7). It is noted that η for the irradiated glasses is higher than those reported for TWLD01 (12%) [47], TWLD025 (29%) [47], TWLD05 (47%) [47], TSWD10 (39%) [48], TSWD20 (32%) [48], 2wt% Dy_2O_3-doped NAP glass (55%) [53], and is low compared to those reported for TWLD1 (88%) [47], TTWD10 (90%) [50], 1 wt% Dy_2O_3-doped NAP glass (93%) [53], glasses.

7.6 Shielding Properties

The gamma ray shielding properties of the as-prepared samples were obtained via Phy-X/PSD software [58]. The Mass Attenuation Coefficient (MAC) profile of TeO_2-B_2O_3-ZnO glasses is given in **Fig. 7.10**.

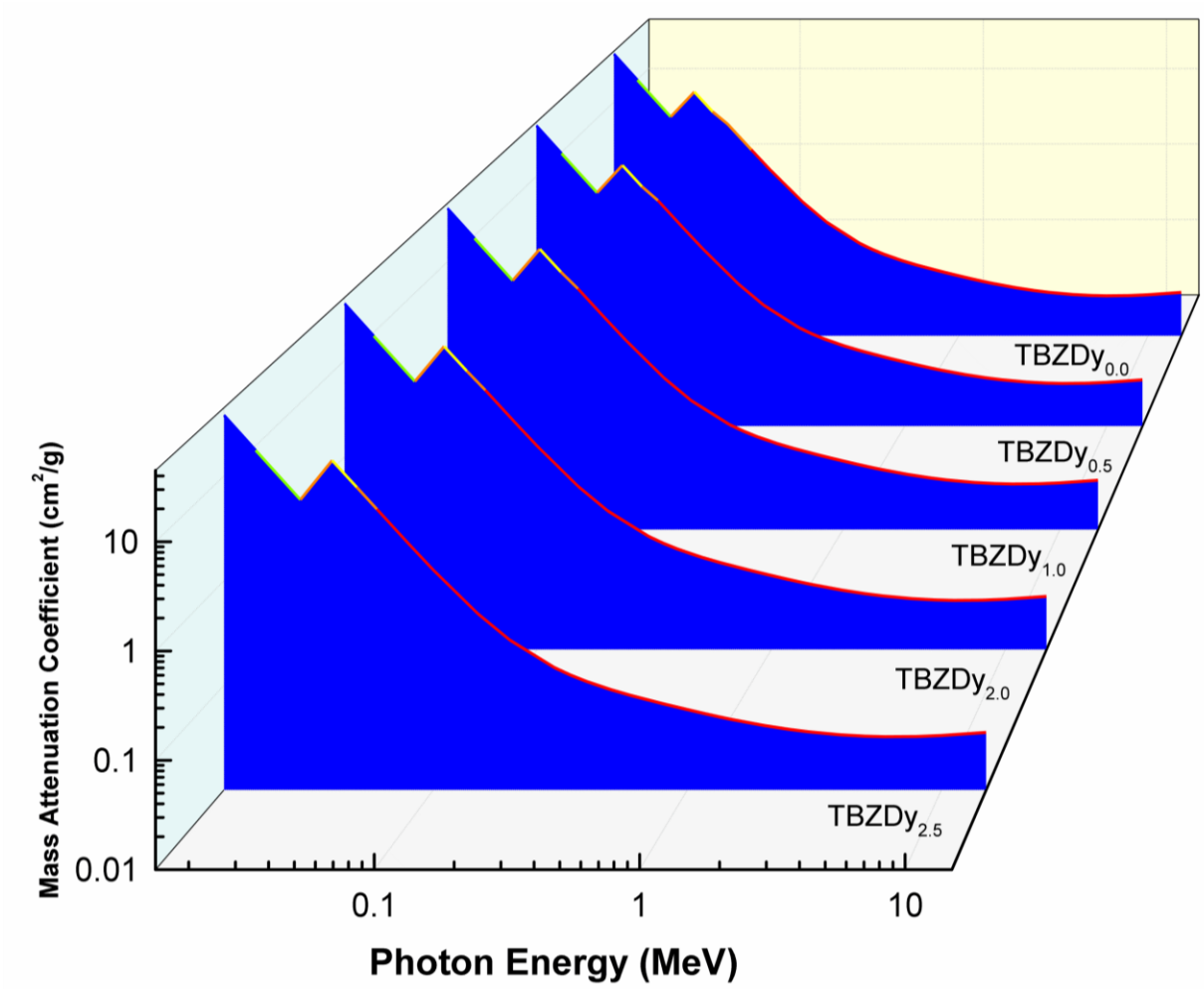

Fig. 7.10: The mass attenuation coefficient (MAC, cm^2/g) of the samples with Photon energy (MeV)

It is observed that The MAC profiles for all the samples shows similar behavior at all the energies. The MAC decreases when energy increases with increase in the photon energy 0.015MeV to 0.8MeV. This sharp decrease is due to the photoelectric absorption. A discontinuity in this trend is observed at 0.004 MeV. This happens because of the K-absoprtion edge of the tellurium (Te). The MAC values remains almost constant in the energy range 0.8MeV to 3MeV due to Compton Scattering (CS). It is because CS is independent of the chemical composition. The maximum MAC value has been obtained at 0.015 MeV. The MAC values increased with increasing RE from 38.34 ±.1.05 cm^2/g ($TBZDy_{0.0}$) to 41.65 ± 1.05 cm^2/g ($TBZDy_{2.5}$) at 0.015 MeV.

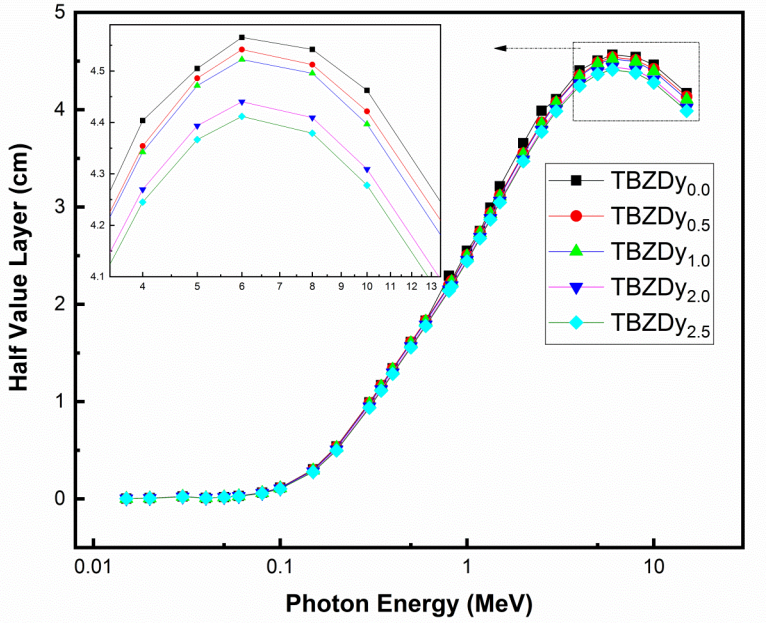

Fig. 7.11: The HVL (cm) of samples with Photon energy (MeV)

The gamma ray transmission in the samples is further analyzed with the help of HVL and MFP. **Fig. 7.11** shows that HVL increases with increasing photon energy. HVL values decreases at high photon energies as RE content increases. It suggests that the higher energy photons will lose their energy at smaller distance in $TBZDy_{2.5}$ than in $TBZDy_{0.0}$.

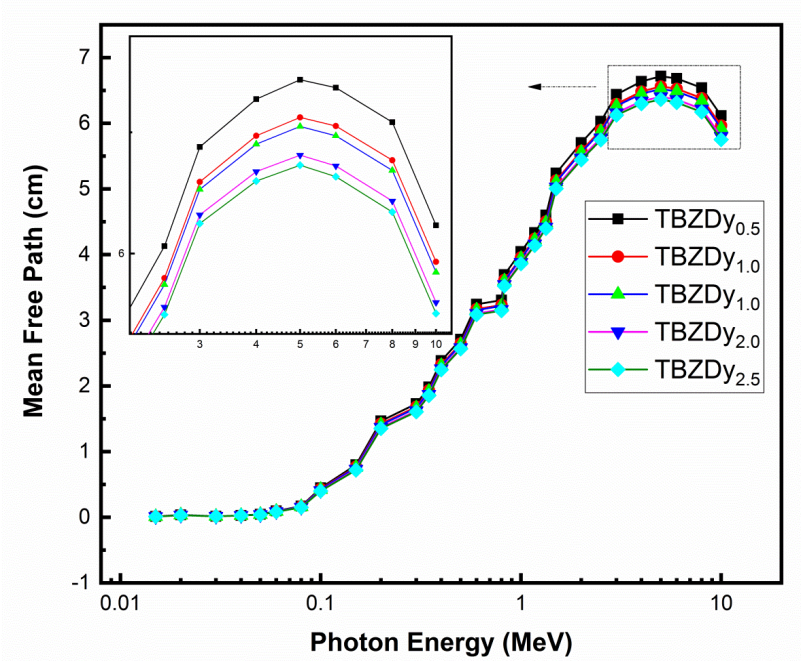

Fig. 7.12: The MFP (cm) in samples with Photon energy (MeV)

Fig. 7.12 shows the MFP results of the present samples. MFP values follow similar trend as that of HVL values. It is noted that better shielding properties are observed when these two factors (HVL and MFP) are small.

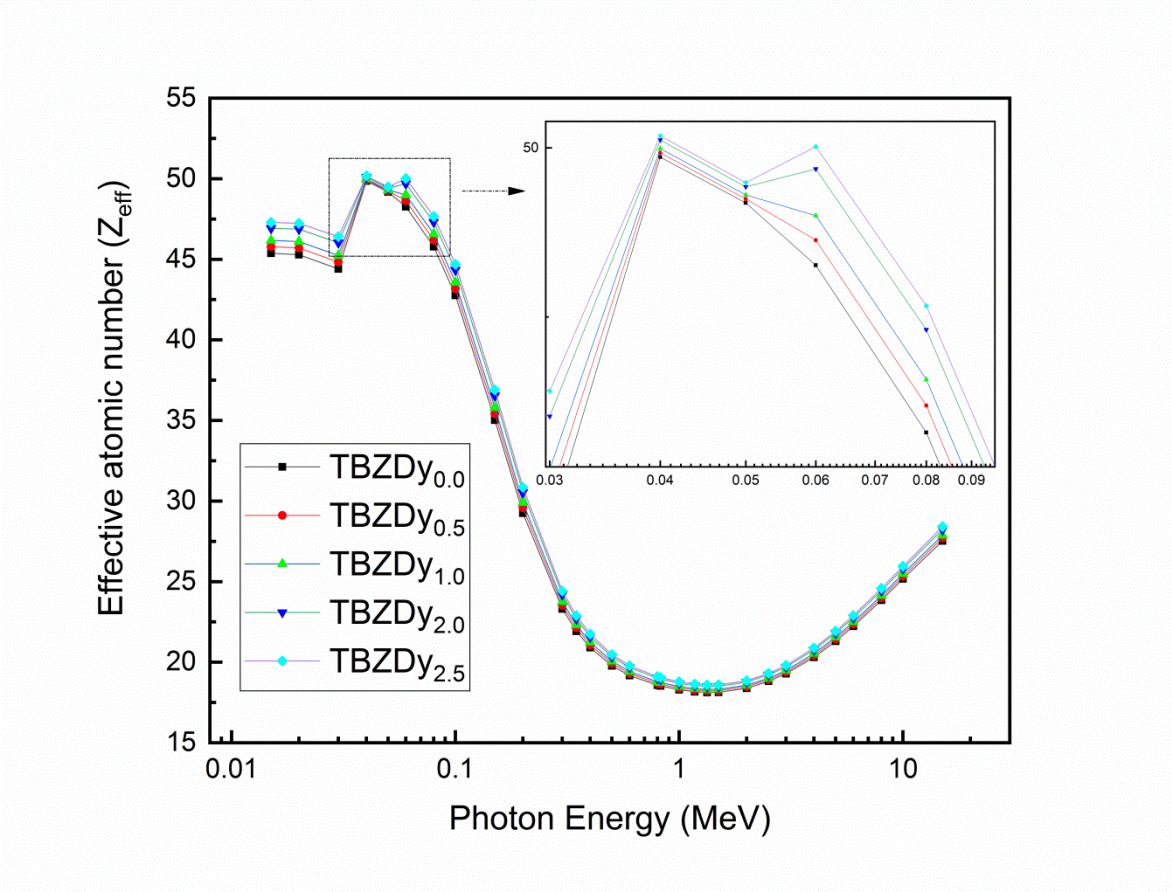

Fig. 7.13: The effective atomic number (Z_{eff}) with the photon energy (MeV)

Another important quantity in the radiation physics is Z_{eff}. The large values of Z_{eff} are required for the shielding materials. This is due to the fact that for higher Z_{eff}, higher is the collision probability and better is the attenuation. **Fig. 7.13** shows the Z_{eff} of the as-prepared samples with increasing RE concentration. It is observed from the **Fig. 7.13** that Z_{eff} decreases from 0.015 MeV - 4 MeV. Discontinuity is observed at 0.004MeV and 0.006 MeV due to absorption edge of Te and Dy respectively. On the other hand, an increase in the Z_{eff} values is observed from 4MeV to 15MeV due to the pair production. It is noted that that Z_{eff} increases with increase in the RE content. Hence $TBZDy_{2.5}$ will be able to absorb more photon than $TBZDy_{0.0}$. The estimated error in the HVL, MFP and Z_{eff} is ± 2%.

References

1. M. Elisa, S. M. Iordache, A.M. Iordache , I.C. Vasiliu, C.E.A. Grigorescu, B.A. Sava, L. Boroica, A.V. Filip, M.C. Dinca, C. Bartha, N. Acha, C. E. Aguado, J. Non. Cryst. Solids, 556 (2021) 120569

2. A. Jose, T. Krishnapriya, T. Jose, C. Joseph, N.V. Unnikrishnan, P.R. Biju, Ceram. Int., 47 (2021) 6790-6799

3. Li Feng, L. Bian, J. Nie, H. He , C. Liu, Optik , 169 (2018) 118–124

4. G.C. Righini, F. Enrichi , L. Zur, M. Ferrari, IOP Conf. Series: J.Phys.: Conf. Series 1221 (2019) 012028

5. C. Doerenkamp, E. Carvajal, C. J. Magon, W. J. Faria, J. P. Donoso, Y. G. Gobato, A. S. Camargo, H. Eckert, J. Phys. Chem. C , 123(2019) 22478−22490

6. G.V. Honnavar, K. P. Ramesh, Bull. Mater. Sci., 40 (2017) 991–997

7. Y. Al-Hadeethia, M. Ahmed, S. Heniti , M.I. Sayyed , Y.S. Rammah, Ceram. Int. 46 (2020) 19198-19208

8. L. Marcondes, L. Rodrigues , C. Cunha , R. Gonçalves, A. Camargo , F. Cassanjes, G. Poirier, J. Lumin., 213 (2019) 224-234

9. K. Han, J. Heo, W. Chung, Opt. Mater., 111 (2021) 110545

10. B. I. Denker, V. V. Dorofeev, B. I. Galagan, V. V. Koltashev, S. E. Motorin, S. E. Sverchkov, V. G. Plotnichenko, Appl. Phys. B, 124:235 (2018) 1-8

11. S. Kaur, O. P. Pandey, C.K. Jayasankar, N. Chopra, J. Non-Cryst. Solids, 521 (2019) 119472.

12. S. Kaur, O. P. Pandey, C.K. Jayasankar, N. Chopra, J. Lumin, 235 (2021) 118031

13. M.K. Halimah, M.F. Faznny, M.N. Azlan, H.A.A. Sidek, Results Phys., 7(2017) 581-589

14. K. M. Kaky, M. I. Sayyed, F. Laariedh, A. H. Abdalsalam, H. O. Tekin, S. O. Baki, App. Phys. A 125:32 (2019) 1-12

15. U. Abdullahi, M.K. Halimah, A.A. Latif , F. D. Muhammad , A.I. Abubakar, J. Non. Cryst. Solids, 483 (2018)18-25

16. M. N. Ami Hazlin, M.K. Halimah, F.D. Muhammad, M.F. Faznny, Physica B**,** 510 (2017) 38-42

17. S. Rani, N. Ahlawat, R. Parmar, S. Dhankhar, R. S. Kundu, Indian J. Phys., 92 (2018) 901–909

18. M. Lesniak, G. Mach, B. Starzyk, A. Baranowska, M. Bik, M. Kochanowicz, J. Zmojda, P. Miluski, M. Sitarz, D. Dorosz, J. Mol. Struct. 1217 (2020) 128452

19. K. Pach-Zawada, M. Le_sniak, K. Filipecka, E. Golis, El S. Yousef, P. Pawlik, D. Dorosz, M. Sitarz, J. Filipeck, J. Mol. Struct., 1224 (2021) 128787.

20. L. Gholamzadeh, N. A. Shik, M. K. Aminian, M. G. Nejad, Nuc. Inst. Meth. Phys. Res. A, 973 (2020) 164174.

21. F. Akman, I. Ozkan, M.R. Kaçal, H. Polat, Shams A.M. Issa, H.O. Tekin, O. Agar, App. Radia. Isotopes 167 (2021) 109470.

22. J. P. McCaffrey, H. Shen, B. Downton, E. M. Hing, Med. Phys, 34 (2007) 530-537.

23. S. Nambiar, J. T. W. Yeow, ACS Appl. Mater. Interfaces, 4 (2012) 5717−5726.

24. H. S. Alorfi, M. A. Hussein, S.A. Tijani, Construction and Building Materials, 251 (2020) 118908.

25. H. O. Tekin, T. Manici, Nuc. Sci. Tech. 28:95 (2017) 1-4.

26. C. G. Murillo, J. R. Contreras, L. A.Velasco, H. A. Martínez, J. A. Rodriguez, H. R. Carrillo, Nuc. Engin. Tech. 52 (2020) 1792-1797.
27. L.A. Velascoa, J.R. Contrerasa, C.G. Murillob, H.A. Martíneza, H.R. Carrilloc, J.A. Rodríguezd, I.A. Salas, Appl. Rad. Isotopes, 161 (2020) 109167.
28. M.I. Sayyed, H.O. Tekin, O.Kilicoglu, O. Agar, M.H.M. Zaid, Results. Phys., 11 (2018) 40-45.
29. K. S. Mann, B. Kaur, G. S. Sidhu, A. Kumar, Rad. Phys. Chem., 87 (2013) 16–25.
30. M.I. Sayyed, Chin. J. Phys., 54 (2016) 408 - 415.
31. G. Lakshminarayana, A. Kumar, H. O. Tekin, S. A. M. Issa, M. S. Al-Buriahi, D. E. Lee, J. Yoon, T. Park, J. Mater. Research. Tech., 9 (2020) 14549-14567.
32. M. Kurudirek, J. Alloys Compds., 727(2017) 1227-1236.
33. Y.S. Alajerami , D. Drabold , M.H.A. Mhareb , K. L. Cimatu , G. Chen , M. Kurudirek, Ceram. Intern., 46 (2020) 12718–12726.
34. H.O. Tekin, L.R.P. Kassab, Shams A.M. Issa, C.D.S. Bordon, E.E. Guclu, G.R. Mattos, O. Kilicoglu, Ceram. Intern., 45 (2019) 24664–24674.
35. F.I. El-Agawany, O.L. Tashlykov, K.A. Mahmoud, Y.S. Rammah, Ceram. Int., 46(2020) 23369-23378.
36. H.O. Tekin, E.E. Altunsoy, E. Kavaz, M.I. Sayyed, O. Agar, M. Kamislioglu, Results Phys., 12 (2019) 1457–1464.
37. G. Lakshminarayana, M.G. A. Kumar, M.I. Dong, N.V. Sayeed, M.A. Long, J. Non- Cryst. Solids, 481 (2018) 65-73.
38. M. Monisha, A. N. DSouza, V. Hegde, N. S. Prabhu, M.I. Sayyed, G. Lakshminarayana, S. D. Kamath, Curren. Appl. Phys., 20(2020) 1207-1216.
39. A. Wagh, M.I. Sayyed , A. Askin, Ö. F. Özpolat, E. Sakar, G. Lakshminarayana, Sudha D. Kamath, Solid State Sci., 96(2019) 105959.
40. Neetu Chopra, Sandeep Kaur, Manpreet Kaur, Shivani Singla, Ritika, Gopi Sharma, Manmohan Singh Heer, Optical, Phys. Status Solidi (a), 215 (2018)1700934
41. M.A. Marzouk, N.A. Ghoneim, Rad. Phys. Chem., 174 (2020) 108893.
42. M.A. Marzouk, J. Mole. Struct., 1019 (2012) 80-90.
43. W.T. Carnall, P.R. Fields, K. Rajnak, , J. Chem. Phys. 49 (1968) 4424-4442.
44. B.R. Judd, Phys. Rev., 127 (1962) 750-761.
45. G.S. Ofelt, J. Chem. Phys., 37 (1962) 511-520.
46. C. Gorller-Walrand, K. Binnemans, edited by K.A. Gscheneidner Jr. and L. Eyring (North Holland, Amsterdam, 1998), 25 (1998)101-264
47. O. Kıbrısl, A.E. Ersundu, M. Çelikbilek Ersundu, J. Non – Cryst. Solids 513 (2019) 125–136
48. V. Himamaheswara Rao, P. Syam Prasad, M. Mohan Babu, P. Venkateswara Rao, T. Satyanarayana, Luís F. Santos, N. Veeraiah, Spectrochimica Acta Part A: Mol. Biomolecular Spectr. ,188 (2018) 516–524.
49. S.A. Saleem, B.C. Jamalaiah, M. Jayasimhadri, A. Srinivasa Rao, K. Jang, L. Rama Moorthy, J. Quant. Spectrosc. Radiat. Transf. 112 (2011) 78–84.
50. L. Jyothi, G. Upender, R. Kuladeep, D. Narayana Rao, Mater. Research Bull., 50 (2014) 424–431
51. B.F. Aull, H.P. Jenssen, IEEE J. Quantum Electron, QE-18 (1982) 925-930.

52. G. Lakshminarayana, R. Yang, M. Mao, J. Qiu, Opt. Mater., 31 (2009) 1506–1512
53. A. A. Reddy , M. C. Sekhar, K. Pradeesh, S. S. Babu, G. V. Prakash, J Mater Sci, 46(2011),2018–2023
54. R. Praveena, R. Vijaya, C.K. Jayasankar, Spectrochimica Acta Part A 70 (2008) 577–586.
55. V. Uma, K. Maheshvaran, K. Marimuthu, G. Muralidharan, J. Lumin., 176 (2016) 15–24.
56. P. S. Kumar, K. Marimuthu, J. Mole. Struct., 1125 (2016) 443-452.
57. M. Inokuti, F. Hirayama, J. Chem. Phys., 43 (1965) 1978-1989.
58. E, Şakar, Ö. Özpolat, B. Alım, M.I. Sayyed, M. Kurudirek, J. Phys. Chem. Solids 166 (2020), 108496.

Conclusions and Future Perspectives

Overview

This chapter deals with the conclusions drawn from Chapter 4, 5, 6 and 7. The effect of different processing conditions like gamma irradiation and heat treatment on the spectroscopic properties of glasses Er_2O_3/Dy_2O_3 is discussed in detail. Also the suggestions to carry out future work in this research are given in the chapter.

8.1 Conclusions

In the present work glasses doped with Er_2O_3/Dy_2O_3 were synthesized with the help of melt-quenching. The effect of gamma irradiation and heat treatment on the spectroscopic properties of as-prepared glasses was studied.

The amorphous nature of zinc borotellurite glasses doped with Er_2O_3 was confirmed with the help of XRD results. The structural analysis revealed presence of TeO_{3+1} and TeO_3 structural units in the glass system. The absorption spectra consisted of f-f transitions of Er^{3+} ions from ground state $^4I_{15/2}$ to different excited states. The decrease observed in Ω_2 parameter with increase in the Er^{3+} content may be because of increase in the asymmetry around the Er^{3+} ions. It was further observed that the doping of Er^{3+} ions into borotellurite glasses resulted into the decrease in band gap and increase in refractive index. The visible and NIR emission intensity of the glasses increased with increasing RE concentration from 0.5 to 2.0 mol% and then decreased due to concentration quenching. The stimulated emission cross-section decreased with increase in RE concentration. The CIE coordinates of the glasses lie in the green region. The decay time of the as-prepared samples decreased from 0.56 ms to 0.12 ms with increase in the RE concentration.

The Differential thermal analysis (DTA) of the Er^{3+} doped glasses suggested that the T_g lies in the range of 364 - 378^oC and T_{c1} 424 - 449^oC. So in order to optimize the time and temperature conditions for the heat treatment, sample containing 0.5 mol% of Er^{3+} was heat treated at 375, 400 and 450 ^oC for 2, 4 and 6h. It was observed that the optimized time and temperature condition was 400 ^oC for 4h. Hence, in order to convert glasses into glass-ceramics all as-prepared glass samples were heat treated at 400 ^oC for 4h. After heating of the glasses at 400 ^oC for 4h, the XRD results confirmed the presence of α- TeO_2 and $Er_2(TeO_3)_3$ phase. FESEM results confirmed induction of nano-particles having size of around 33 - 40 ± 5 nm after heat treatment. The JO parameters of the heat treated samples showed deviation with respect to as prepared glasses, due to structural changes occurred in the vicinity of Er^{3+} ions. It was observed that the lifetime of the samples increases after heat treatment. An increase in the photoluminescence emission and up-conversion intensity was observed after ceramization. The aforementioned results suggest that the prepared glass ceramics act as good active medium for laser fabrication.

A broad hump obtained in the Dy^{3+}- doped glasses confirmed the absence of noticeable crystallization in the glass matrix. The structural and optical studies confirmed an increase in the NBOs with increasing Dy^{3+}- content. The absorption spectra of the samples showed the presence of bands due to different electronic transitions of Dy^{3+}. The JO parameters of the present samples followed the trend as $\Omega_2 > \Omega_4 > \Omega_6$. The Ω_2 deceased with increase in the RE- concentration. It could attribute to decrease in the covalency between the Dy^{3+} and their ligands. The band gap and refractive index values showed similar trend as that of Er^{3+}-doped glasses. The emission spectra showed luminescence at 482, 575 and 663 nm. Emission intensity of samples increases with the Dy^{3+}-content. The changes in the emission intensities were quantified with the help of Y/B ratios. The CIE-coordinates of doped glasses with Dy_2O_3 lie in the yellowish- white region. Decay time shows non-exponential character.

In continuation, the DTA results suggested the characteristic temperatures of $TBZDy_x$ glasses lies in 364 - 381^oC and T_{c1} 424 – 458 ^oC as there is increase in rare earth content. For optimization of time and temperature conditions, sample containing 0.5 mol% of Dy^{3+} was heat treatment at 375 ^oC for 2, 4 and 6h and same was repeated at 400 and 450 ^oC. It was observed that in the present case the optimized time and temperature condition were 400 ^oC for 4h. Hence, to convert glasses into glass-ceramics Dy^{3+}-doped as-prepared glass samples were heat treated at 400 ^oC for 4h. The XRD results of glass-ceramics revealed the presence of α- and γ- TeO_2 phases with α-TeO_2 as the major phase. FESEM confirmed the formation of 33-45nm ± 5nm sized nano-particles. The Judd–Ofelt parameters of Dy^{3+} ions in glass-ceramics, showed large deviation with respect to glass. It clearly indicates that there was structural change in the local environment of the Dy^{3+} ions from covalent glassy to more ionic oxide nanocrystals. This effect was also observed on the Y/B values of glass-ceramics. CIE coordinates of glass-ceramics were found to be closer to that of commercial pc-LED. The CCT values of glass-ceramics were closer to that of the cool sources.

The as-prepared glasses were given 50 kGy γ- irradiation to study its effect on physical, optical and spectroscopic properties. XRD diffractograms represent the absence of long range order even after 50kGy gamma irradiation. The Raman results of glass sample showed some structural changes in terms of formation of new structural units after irradiation. The irradiation had small effect on energy gap and Urbach energy values of the samples doped with rare earth. The radiative properties revealed that the prepared samples can be used for

optoelectronic purposes even after subjected to heavy gamma dosage. The CIE values suggested that the present glass samples emit green light after irradiation also. The shielding properties of present samples glasses were analyzed with Phy-X/PSD software. The shielding properties of the glass samples were improved after RE doping. The present study shows that the prepared doped samples can be used as possible entrant in nuclear field.

Further, the effect of 50 kGy γ-rays on the spectroscopic of Dy^{3+}-zinc borotellurite glasses was studied. The samples retained their amorphous character even after irradiation. Absorption coefficient increased after gamma irradiation. The band gap and refractive index values of the doped samples showed small effect of irradiation. The radiative properties revealed that the present samples can be used for optoelectronic purposes even after being subjected to heavy dosage. The values of MAC and Z_{eff} increased with RE concentration. Moreover, the values of HVL and MFP decreased with the increase in RE amount. The shielding properties of the glasses get improved with increase in RE concentration. The present study showed that the prepared doped samples can be used in optoelectronic devices even in presence of heavy gamma dosage.

8.1.1 Comparison of different properties between Erbium and Dysprosium zinc borotellurite glasses under different processing conditions:

The studies done show that studied compositions provide low- phonon energy environment to REs even in the absence of toxic materials like PbF_2. This section contains a comparison between the physical, optical and spectroscopic properties of the dysprosium and erbium doped glasses and glass ceramics.

a) Density

A comparison between density values of the prepared samples at different rare earth concentrations is given in **Fig. 8.1**. It is worth noting that there is very less or no variation in the density values of the two systems (Dy^{3+} and Er^{3+}-doped samples). It may be due to their lesser quantity and similar electronic configuration of Dy ([Xe] $4f^{9}$) and Er ([Xe] $4f^{11}$). Along with that, the two systems (Dy-doped and Er-doped) follow similar trends after heat treatment and gamma irradiation. It may be because the rare earth ions effect the structural properties of the host systems in a similar manner. It is worth noting that the density increases with increase in RE concentration and heat treatment. An increase in density with RE addition may be due to addition of high molecular weight compound, Er_2O_3 (382.5g/mol)

in place of comparatively lighter compound, TeO_2 (159.6 g/mol). The non- linear increase in the density observed at 1.0mol% and 2.5 mol% may be due to the clustering of the RE ions. The RE^{3+}- ions goes into the interstitial spaces within the glass network, increasing the packing density of the glass structure and decreasing the molar volume [18]. An increase in density with heat treatment may be due to increase in the rigidity of the samples after ceramization. A small variation in the density with heat treatment and gamma irradiation is observed because of same experimental conditions.

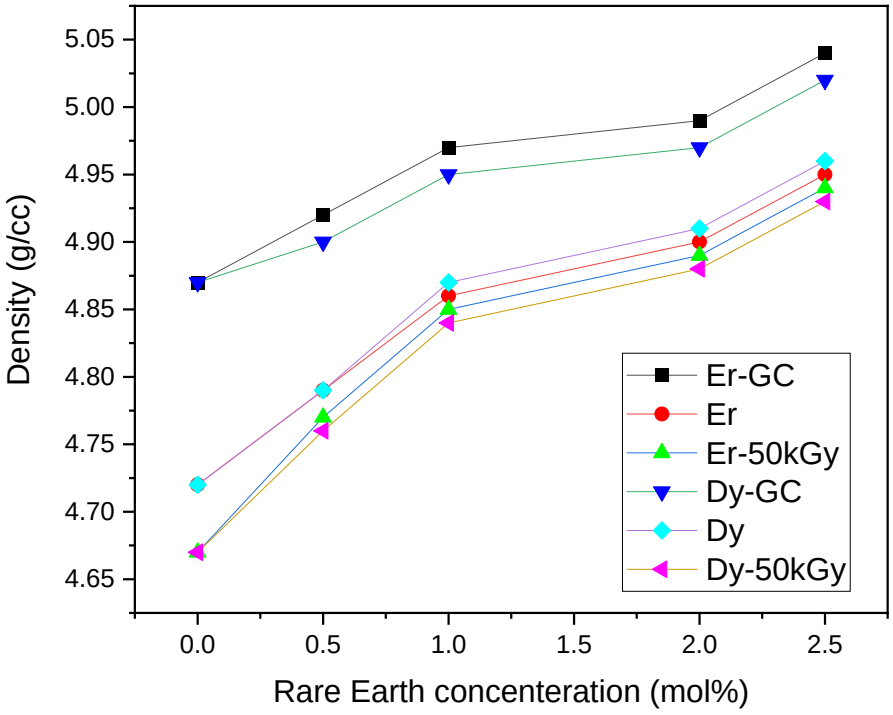

Fig. 8.1: Comparison between observed densities of the prepared samples

b) Refractive Index:

Fig. 8.2 gives a comparison between the refractive index values of the prepared glasses and glass ceramics. It is to be noted that there is small difference in the refractive index values observed for both the glasses containing rare earth ions. It is probably due to similar density values. It is worth noting that the refractive index increases with the RE addition and heat treatment. It may be due increase in the compactness of the prepared samples. However, the refractive index decreases after gamma irradiation probably due to decrease in the number of

non-bridging oxygens. Overall studies indicate that the refractive index increases linearly (in general) upto 2 mol% doping. However, a higher increment is observed for 2.5 mol% doping. This may be due to the non-linear increase in the density due to the clustering of the RE ions.

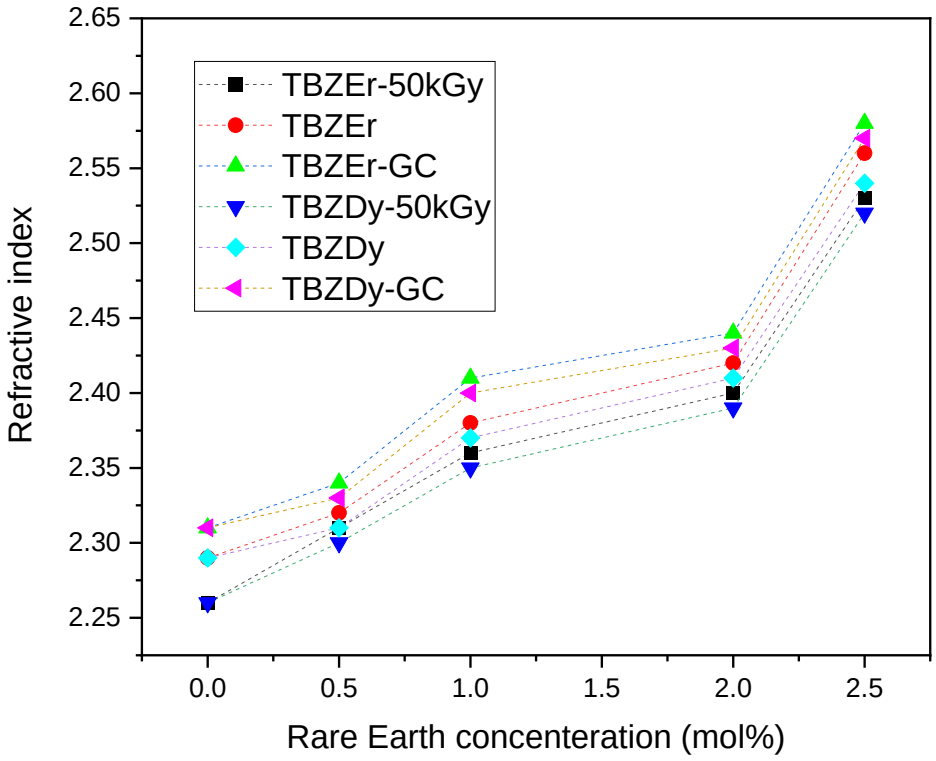

Fig. 8.2: Comparison between refractive index of the prepared samples

c) Stimulated emission cross-section:

Stimulated emission cross-section (σ_e) is an important parameter from spectroscopic view-point. **Fig. 8.3** gives a comparison between stimulated emission cross-sections observed for two different rare earth containing glasses. It is worth noting that value of σ_e for dysprosium doped samples lie in the range of 10^{-23} cm^2 ($^4F_{9/2} \rightarrow {}^6H_{13/2}$) on the other hand it lies in the range of 10^{-21} cm^2 in case of Er^{3+} doped samples. It is due to the presence of metastable level ($^4I_{13/2} \rightarrow {}^4I_{15/2}$) in Er^{3+} which has large emission cross-section. It is also worth noting that the stimulated emission cross-section do not follow any particular trend as the rare earth content is increased in case of Er^{3+}-doped samples. It may be because of an overlap between the emission and absorption bands of Er^{3+} ions.

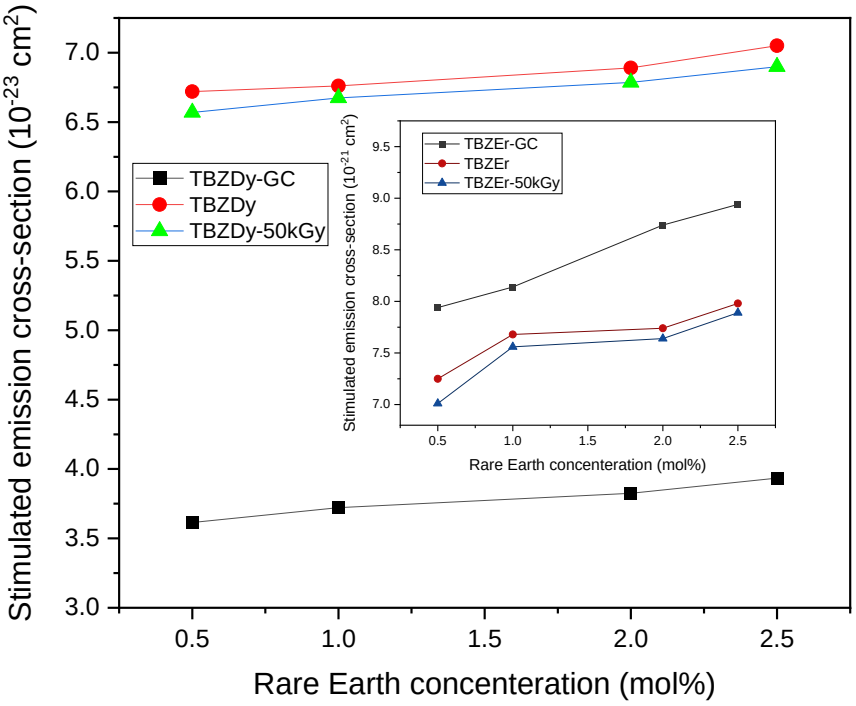

Fig. 8.3: Comparison between stimulated emission cross-section of the prepared samples

d) Time Decay:

Fig. 8.4 gives a comparison between the decay times observed for the lifetime values for Dy^{3+} - doped samples for $^6H_{13/2}$ level that lies in μs - range. Moreover, for Er^{3+}- doped samples it lies in ms range which is again due $^4I_{13/2}$ level present in case of Er^{3+} is the meta-stable level. Hence the corresponding glasses show higher decay time. It is also worth noting that the lifetime values after heat treatment increases in case of Er^{3+}- doped samples. However, it decreases in case of Dy^{3+}- doped samples. It is because of increase in the radiative losses which is shown by the increase in the non-exponential nature of the decay curves.

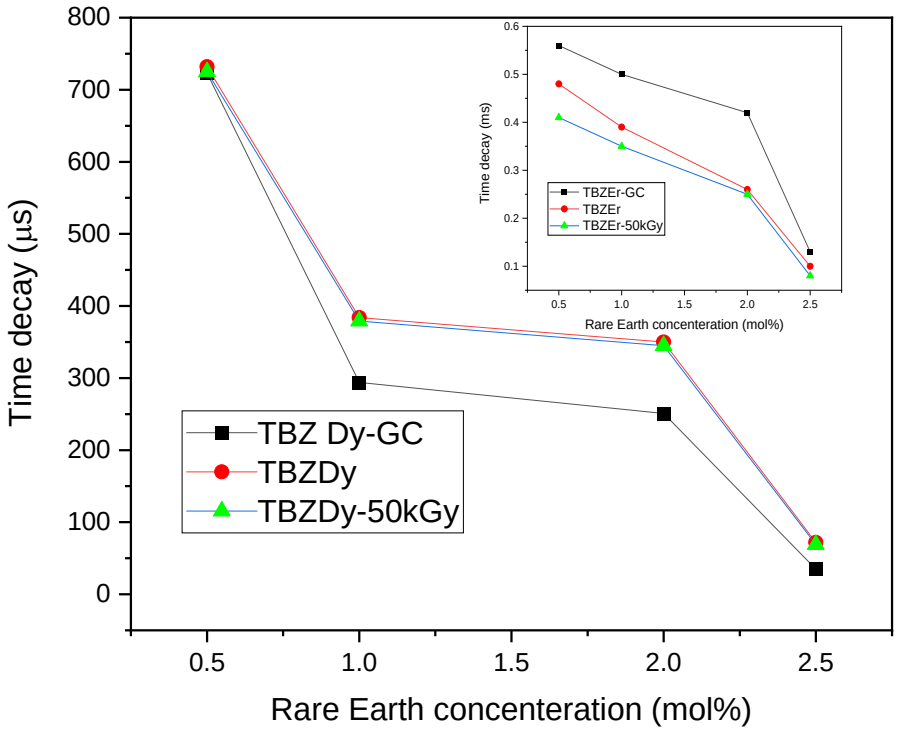

Fig. 8.4: Comparison between decay time of the prepared samples

e) CIE- coordinates

Table 8.1: CIE co-ordinates prepared samples.

Concentration of RE-ion (Er^{3+}/Dy^{3+}) (mol%)	**(x,y) of $TBZEr_x$**	**(x,y) of $TBZEr_xGC$**	**(x,y) of $TBZEr_x$ 50kGy**	**(x,y) of $TBZDy_x$**	**(x,y) of $TBZDy_xGC$**	**(x,y) of $TBZDy_x$ 50kGy**
0.5	(0.331,0.580)	(0.335,0.551)	(0.338,0.585)	(0.43,0.44)	(0.32,0.34)	(0.43,0.42)
1.0	(0.341,0.578)	(0.332,0.533)	(0.343,0.583)	(0.42,0.43)	(0.32,0.34)	(0.43,0.41)
2.0	(0.340,0.581)	(0.325, 0.550)	(0.336, 0.586)	(0.43,0.43)	(0.32,0.35)	(0.42,0.43)
2.5	(0.351,0.611)	(0.323,0.552)	(0.346,0.614)	(0.42,0.43)	(0.33,0.32)	(0.41,0.43)

Table 8.1 gives the CIE-coordinates obtained for both the glass systems. It is observed that there is marginal variation in the (x,y) for the Er^{3+}-doped samples but after heat treatment and

gamma irradiation the chromaticity co-ordinates lie in the green region. Hence, the prepared samples can be used as green light emitting diodes in the display applications. However, it is worth noting that the CIE-coordinates of Dy^{3+}-doped samples moved from yellowish white region to white region after heat treatment. Hence, it can be said that the present Dy^{3+}- doped glass ceramics are good host materials for white light emitting phosphors.

8.2 Future Perspectives

In the present thesis various parameters were optimized to achieve high emission cross-sections and decay time under different conditions like heat treatment and irradiation with high energy gamma radiations. On the basis of present work the future possible study that can be undertaken could be directed towards manufacturing high performance phosphors and optical fibers. Since the tellurite glasses have excellent non-linear optical properties, doping in these glasses with metal nano particles can make them suitable for various optical devices. As the study deals with only one modifier (i.e. zinc oxide) attempts should be made by varying the modifiers. Since the present glasses show radiation shielding properties even without the addition of heavy metal ions like Pb and Bi, there is scope to study these samples as radiation shielding windows.